Prospects for Measuring the Differential High p_{T} b-Jet Cross Section with the ATLAS Detector

DISSERTATION
zur Erlangung des akademischen Grades eines
Doktors der Naturwissenschaften

vorgelegt von
Diplom-Physiker Kai Karsten Grybel
geb. am 30.07.1977 in Köln

eingereicht beim Fachbereich Physik
der Universität Siegen

Dezember 2010

Gutachter der Dissertation: Prof. Dr. P.Buchholz
Prof. Dr. C.Grupen

Datum der Disputation: 21. Januar 2011

Abstract

Currently, the Large Hadron Collider (LHC) at CERN in Geneva accelerates protons up to an energy of 3.5 TeV resulting in collisions of a center-of-mass energy of $\sqrt{s} = 7\,\text{TeV}$. To study the production of b-quarks in proton-proton collisions is part of the physics program of the ATLAS experiment, which is one of the experiments at the LHC. The b-quarks produced in the hard scattering of the protons are measured as jets in the ATLAS detector. The aim of this PhD thesis is to study prospects of a differential p_{T} b-jet cross section measurement in the jet p_T range of $p_{\text{T}_{jet}} > 30\,\text{GeV}$. This study is based on simulated Monte Carlo (MC) data assuming a center-of-mass energy of $\sqrt{s} = 10\,\text{TeV}$.

The trigger selection is based on a combination of single jet triggers considering the different prescale factors of the different jet triggers. The MC data samples contain signal b-jets and background jets from other QCD physics processes in the proton-proton collision. In order to identify the b-jets and to reject background jets, b-tagging algorithms based on the on average longer lifetime of particles containing a b-quark compared to other hadrons, which decay before reaching the detector, are used. Since the b-tagging performance is not uniform over the jet p_{T} region considered, different b-tagging efficiency scenarios are studied. The jet p_{T} independent b-tagging efficiency scenarios of $\epsilon_{Tag} = 0.5$ and $\epsilon_{Tag} = 0.6$ as well as an optimized b-tagging efficiency scenario in order to minimize the statistical uncertainty of the measurement in each jet p_{T} bin are presented.

An unfolding algorithm is applied to the measured b-jet spectrum in order to correct for detector effects due to the measuring process. The expected systematic uncertainties for different jet p_{T} regions are studied and an estimate for the evolvement of the statistical uncertainties as a function of the integrated luminosity is given. Once an integrated luminosity of at least $100\,\text{pb}^{-1}$ has been collected the differential b-jet cross section at the ATLAS experiment can be measured up to $p_{\text{T}_{jet}} < 750\,\text{GeV}$. For $750\,\text{GeV} < p_{\text{T}_{jet}} < 1.1\,\text{TeV}$ an integrated luminosity of approximately $400\,\text{pb}^{-1}$ is needed to reduce the statistical uncertainty to the level of the systematic uncertainty. The systematic uncertainty is dominated by the uncertainty of the jet energy scale calibration of the calorimeters. The systematic uncertainties vary from about 25% in the lower jet p_T region to about 50% in the higher jet p_{T} region.

Zusammenfassung

Gegenwärtig werden am Large Hadron Collider (LHC) am CERN bei Genf Protonen auf eine Energie von 3.5 TeV beschleunigt und bei einer daraus resultierenden Schwerpunktsenergie von $\sqrt{s} = 7\,\text{TeV}$ zur Kollision gebracht. Die Untersuchung von b-Quarks in den Proton-Proton-Kollisionen sind ein Teil der physikalischen Fragestellungen, denen am ATLAS-Experiment am LHC nachgegangen wird. Die b-Quarks, die im harten Streuprozess der Protonen produziert werden, werden als Teilchenstrahlbündel (Jets) im Detektor registriert und vermessen. In dieser Doktorarbeit wird eine Messung des differentiellen p_{T}-Wirkungsquerschnittes von b-Jets mit $p_{\text{T}_{Jet}} > 30\,\text{GeV}$ vorbereitet. Die Studie basiert auf Monte Carlo (MC) generierten Ereignissen, bei einer angenommenen Schwerpunktsenergie von $\sqrt{s} = 10\,\text{TeV}$. Bei der Selektion der Ereignisse während der Datennahme (Trigger-Selektion) werden Jet-Signaturen im Detektor verwendet, wobei bei der Kombination der Jet-Trigger verschiedene Prescale-Faktoren zu berücksichtigen sind. Die generierten MC Ereignisse beinhalten sowohl b-Jet-Signalereignisse wie auch Untergrundereignisse, die aus weiteren QCD-Prozessen in den Proton-Proton-Kollisionen stammen. Zur Identifikation von b-Jets sowie zum Unterdrücken von Untergrundereignissen werden b-Tagging-Algorithmen verwendet, die auf der im Durchschnitt längeren Lebensdauer von b-Quark-haltigen Hadronen, verglichen mit anderen Hadronen, die zerfallen bevor sie den Detektor erreichen würden, beruhen. Die Güte der Separation des Signals vom Untergrund mit Hilfe dieser Algorithmen ist vom betrachteten Jet-p_{T}-Bereich abhängig. Aus diesem Grunde werden Szenarien mit verschieden gewählten b-Tagging-Effizienzen untersucht. Zum einen werden Szenarien mit einer über den betrachteten Jet-p_{T}-Bereich konstanten b-Tagging-Effizienz von $\epsilon_{Tag} = 0.5$ sowie $\epsilon_{Tag} = 0.6$ verwendet und zum anderen wird eine optimierte b-Tagging-Effizienz untersucht, die die statistische Unsicherheit pro betrachtetem Jet-p_{T}-Bereich minimiert.
Das gemessene b-Jet-Spektrum wird entfaltet, um auf Detektoreffekte, die beim Messprozess auftreten, zu korrigieren. Die systematischen Unsicherheiten der Messung des differentiellen b-Jet-Wirkungsquerschnittes in den einzelnen Jet-p_{T}-Bereichen sowie die zu erwarteten statistischen Unsicherheiten der Messung als Funktion der integrierten Luminosität werden abgeschätzt.
Bereits mit einem Datensatz entsprechend einer integrierten Luminosität von etwa $100\,\text{pb}^{-1}$ wird es möglich sein, den differentiellen Wirkungsquerschnitt bis zu $p_{\text{T}_{jet}} < 750\,\text{GeV}$ zu messen. Für den Jet-p_{T}-Bereich von $750\,\text{GeV} < p_{\text{T}_{jet}} < 1.1\,\text{TeV}$ wird eine Datenmenge von ungefähr $400\,\text{pb}^{-1}$ benötigt, um den Wirkungsquerschnitt mit einer statistischen Unsicherheit zu messen, die in etwa der erwarteten systematischen Unsicherheit der Messung entspricht. Die systematischen Unsicherheiten variieren dabei von ca. 25% im niedrigeren Jet-p_{T}-Bereich, bis hin zu ca. 50% im höheren Jet-p_{T}-Bereich.

Contents

Chapter 1

Introduction

The main question of elementary particle physics is to study the properties of the particles, which are the constituents of matter, and to understand the interactions between them. Currently the knowledge about elementary particles may be summarized in the Standard Model of Elementary Particles (SM). The SM describes all available experimental results and particle properties. Although the SM is a very successful theory, many questions cannot be answered and extensions of the SM are expected (New Physics). In order to further test the SM and possible extensions, the next generation of elementary particle physics experiments has been built. The Large Hadron Collider (LHC), built at CERN (European Laboratory for Particle Physics) in Geneva accelerates protons up to an energy of 7 TeV per beam (in the beginning 3.5 TeV per beam). Two multi-purpose experiments are located at the LHC: A Toroidal LHC Apparatus (ATLAS [1], Chapter 2) and the Compact Muon Solenoid (CMS [2]).

One of the aspects of the physics program of the ATLAS experiment is the study of heavy quarks like the b-quark. The cross section of b-jet production depends on the energy. The differential p_{T} b-jet cross section has already been measured at lower energies. Currently, the b-jet cross section is extrapolated to the higher center-of-mass energy available at the LHC. As the next step, the b-jet cross section has to be measured at this higher energy and will then be used to check theoretical predictions by the SM and as important input to other analyses.

Within this thesis, the measurement of the differential p_{T} b-jet cross section $\frac{d\sigma_{b-jet}}{dp_{\mathrm{T}}}$ with the ATLAS detector will be prepared, i.e. the measurement of the cross section of jets initiated by a b-quark as a function of the jet p_{T}. At the time this study was started, a data taking run at a center-of-mass energy of $\sqrt{s} = 10\,\mathrm{TeV}$ was planned. Therefore, within this thesis, this center-of-mass energy is assumed.

After the description of the ATLAS detector, an introduction to the SM as well as to the theory of production of the b-quarks is given. Their fragmentation and hadronization to b-hadrons (hadrons containing a b-quark) are explained in Chapter 3. In Chapter 4 previous experiments measuring the differential b-jet cross section are discussed and the strategy of measuring the differential b-jet cross section with the ATLAS experiment is given.

The ATLAS experiment started data taking at the end of 2009. When this thesis

started, no data from the ATLAS detector was available. Therefore the measurement of the differential b-jet cross section is prepared using Monte Carlo (MC) events (Chapter 5). In this MC data, the production of b-quarks in the proton-proton collisions and the expected background events are simulated. The simulated events are reconstructed to find the objects relevant for the physics analysis in the measured information of the detector (Chapter 6). In Chapter 7 an introduction to the measurement of the (integrated) luminosity is given, which is one of the input variables to determine the differential b-jet cross section.
The measurement of the differential b-jet cross section entails several steps (Chapter 8). In order to identify the b-jets b-tagging algorithms are used, which are based on the on average longer lifetime of b-hadrons compared to other hadrons, which decay before reaching the detector. The precision of the differential b-jet cross section measurement depends on the ability to identify b-jets and to reject background jets. In order to correct for detector effects due to the measuring process, an unfolding algorithm is applied to the measured b-jet p_{T} spectrum. Furthermore, estimated systematic uncertainties of the measurement are provided as well as extrapolations of the expected statistical uncertainties for the differential b-jet cross section measurement for different values of the integrated luminosity.
In Chapter 9 a summary and prospects for the results of the differential b-jet cross section measurement are given.

Chapter 2

ATLAS Experiment

ATLAS is one of the experiments of the LHC (Large Hadron Collider), which is located at CERN (European Laboratory for Particle Physics), Geneva. In the start-up phase of the LHC the energy of the accelerated protons will be about 3.5 TeV resulting in a center-of-mass energy of 7 TeV. The design center-of-mass energy is $\sqrt{s} = 14$ TeV. The protons are accelerated in bunches of about 10^{11} protons each, which collide every 25 ns. This corresponds to an instantaneous luminosity of 10^{29} cm^{-2}s^{-1}. The luminosity will be ramped up to the design luminosity of 10^{34} cm^{-2}s^{-1} (high luminosity) later on. In the case of high luminosity on average 23 proton-proton collisions will occur in every bunch crossing.

In this chapter the design of the ATLAS experiment [1] is described. A schematic overview of the detector is shown in Fig. 2.1 and its main performance goals are listed in Tab. 2.1.

detector component	**required resolution**
tracking	$\sigma_{p_T}/p_{\mathrm{T}} = 0.05\% p_{\mathrm{T}} \oplus 1\%$
EM calorimetry	$\sigma_E/E = 10\%/\sqrt{E} \oplus 0.7\%$
hadronic calorimetry (jets)	
barrel and end-cap	$\sigma_E/E = 50\%/\sqrt{E} \oplus 3\%$
forward	$\sigma_E/E = 100\%/\sqrt{E} \oplus 10\%$
muon spectrometer	$\sigma_{p_T}/p_{\mathrm{T}} = 10\%$ at $p_{\mathrm{T}} = 1$ TeV

Table 2.1: List of the main performance goals of the ATLAS detector. The energy E and the transverse momentum p_{T} are given in GeV.

This chapter starts with the definition of the ATLAS coordinate system and units followed by an overview of the different detector parts. The main detector parts are the Inner Detector (2.2), the calorimeters (2.3) and the Muon System (2.5). The luminosity measurements will be performed using mostly the forward detectors described in Section 2.4. In addition the designs of the magnet and the trigger system are explained in Sections 2.6 and 2.7.

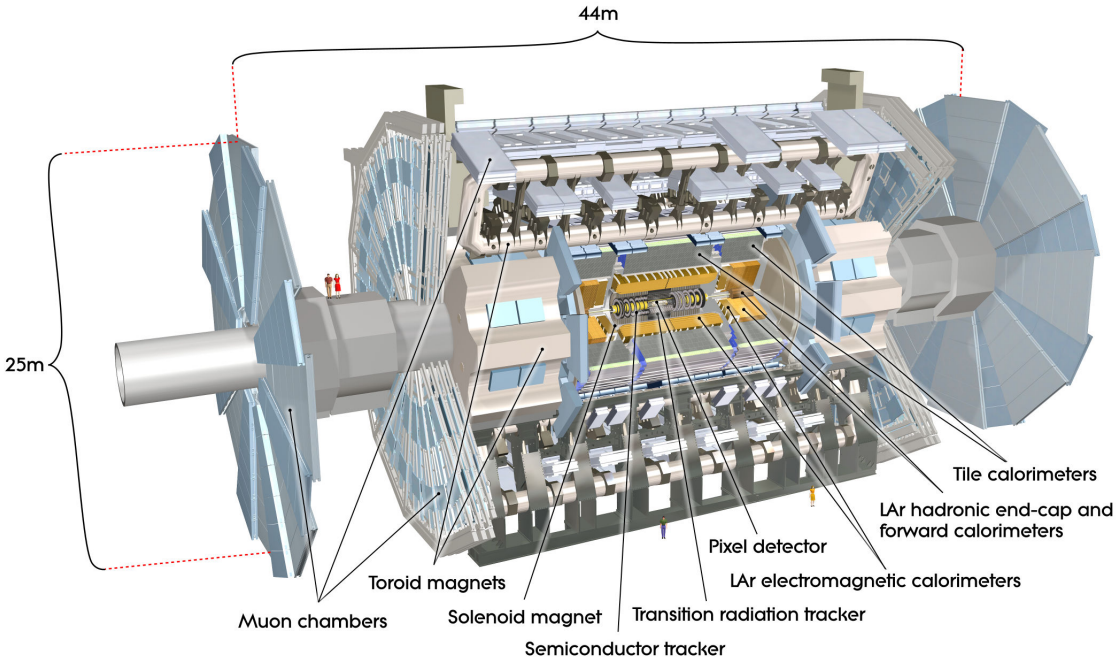

Figure 2.1: Schematic overview of the ATLAS detector [1].

2.1 ATLAS Units and Coordinate System

The nominal interaction point of the proton-proton collision is defined as the origin of the coordinate system. The z-axis points in the beam direction. The x-y plane is transverse to the proton beam. The positive x-axis points to the center of the LHC ring, while the positive y-axis points upwards. The azimuthal angle ϕ is the angle w.r.t. the x-axis in the x-y plane, with values in the range of $[-\pi, \pi]$. The polar angle θ is the angle from the beam direction measured in the y-z plane and covers the range $[0, \pi]$. Instead of the angle θ the Lorentz invariant pseudo rapidity η is used. η is defined as:

$$\eta = -\ln\left(\tan\left(\frac{\theta}{2}\right)\right). \tag{2.1}$$

The distance ΔR in the azimuthal-angle-pseudorapidity space between e.g. two tracks or jets, is defined as

$$\Delta R = \sqrt{(\Delta\phi)^2 + (\Delta\eta)^2}. \tag{2.2}$$

As unit of energy MeV is used, so that the momentum is given in $\frac{\text{MeV}}{\text{c}}$. In the following the definition $c = 1$ is used. E.g. the momentum is given in MeV. The standard unit of the length is mm.

2.2 Inner Detector

The Inner Detector is the innermost part of the ATLAS experiment and is shown in Fig. 2.2. The main purpose of this detector part is the measurement of possible

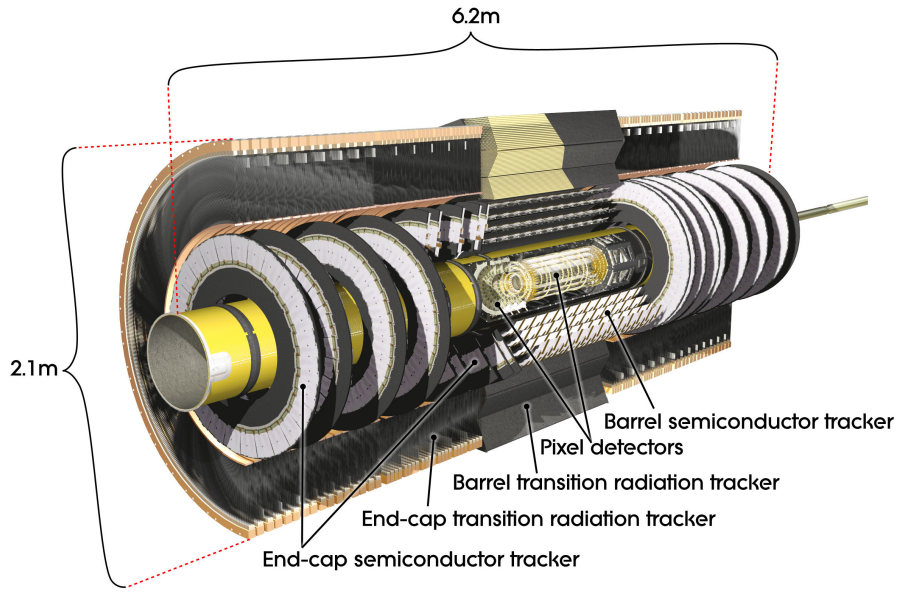

Figure 2.2: Design of the ATLAS Inner Detector [1], which consists of the Pixel Detector, the SCT and TRT.

particle hits with high precision in order to reconstruct the tracks of the particles and the primary interaction point of the two protons. Therefore the contribution of the detector material to the interaction length λ or radiation length X_0 has to be as small as possible, while the detector has to have cooling, a readout system etc.. The overall material contribution of the Inner Detector varies from about $X_0 \approx 0.5$ ($\lambda \approx 0.2$) for $|\eta| = 0$ to $X_0 \approx 2.4$ ($\lambda \approx 0.7$) for $|\eta| = 1.8$. This will lead to e.g. electrons loosing their energy through Bremsstrahlung or due to photon conversion ($\approx 40\%$) before they reach the electromagnetic calorimeter.
The Inner Detector is subdivided into three detector parts. The first detector part is the Pixel Detector followed by a Semiconductor Tracker (SCT) and the Transition Radiation Tracker (TRT). In the next sections the different detector parts and their principles of measuring particle hits are explained. From these particle hits, tracks and vertices will be reconstructed (see 6.2).

2.2.1 Pixel Detector

The Pixel Detector is closest to the interaction point of the protons. A high granularity is necessary to fulfill the requirement of precision hit measurements.
This detector part uses semiconductor detectors. Semiconductors have a small energy gap between the valence and the conducting band. Additional atoms are brought into the semiconductor by diffusion (doping). These atoms have one additional weakly-bound valence electron (n-doped semiconductor) or one electron less (p-doped semiconductor) compared to the regular semiconductor material. This electron (hole) in the n-type (p-type) semiconductor behaves like a free charge carrier.
At a p-n junction a p-type and a n-type semiconductor are placed next to each other.

The additional electrons from the n-type part diffuse to the p-doped semiconductor. This results in a depletion region void of charge carriers. An additional applied external voltage (in blocking direction) increases the size of the depletion zone. A particle traveling through the depletion zone ionizes the atoms and produces free charge carrier in the depletion zone. The signal is measured as a current of these free charge carriers in the depletion zone.
The sensor of one module of the ATLAS Pixel Detector is working like a semiconducting n^+-implanted detector with a thickness of 250 μm, divided into pixels with a size of 50×400 μm^2 and connected via 46 080 read-out channels. In the barrel region 13 of the modules are mounted on one stave. The staves are mounted on the barrel layers tilted by an angle of -20^0 w.r.t. a tangent vector at the given radius of the barrel layers. In total the Pixel Detector has 80.4×10^6 readout channels.
The Pixel Detector is symmetric w.r.t. to the interaction point and built with three barrel layers in the central region (0 mm $< |z| <$ 400.5 mm) in addition to three disks each in the forward and backward direction (495 mm $< |z| <$ 650 mm) mounted perpendicular to the beam axis.
The first layer (called b-layer) at a radius of $r = 5.05$ cm is centered around the interaction point. The second layer is located at $r = 8.85$ cm and the outermost layer at $r = 12.25$ cm. The Pixel Detector is designed to measure particle hits with an intrinsic accuracy of 10 μm in r-ϕ and 115 μm in z direction.

2.2.2 Semiconductor Tracker

The Semiconductor Tracker (SCT) surrounds the Pixel Detector. Due to a lower expected hit occupancy in the SCT area compared to the Pixel Detector region, the SCT granularity does not need to be as high as in the Pixel Detector. The SCT is also a semiconductor detector and is working according to the same basic principle as the Pixel Detector (see Section 2.2.1).
The sensors of the SCT are divided into strips of 80 μm $\times$ 6.4 cm with a thickness of about 285 μm.
The SCT consists of four cylindrical layers in the central region (0 mm $< |z| <$ 749 mm) and nine disks each in the forward and backward direction (839 mm $< |z| <$ 2735 mm). Every module contains two active sensors, which are tilted by 40 mrad w.r.t. the geometrical center of the sensor. Every particle has to pass eight strip sensors to obtain four precisely measured space points. About 6.4×10^6 readout channels are available.
The SCT is designed for an intrinsic accuracy of 17 μm in r-ϕ and 580 μm in z direction.

2.2.3 Transition Radiation Tracker

The Transition Radiation Tracker (TRT) is based on the transition radiation effect. Relativistic charged particles, which pass the interface of materials with different dielectrical constants, emit photons. The emitted photons are mostly X-ray photons

and the average energy of these photons is proportional to the Lorentz factor γ, which can be used for particle (e.g. electron) identification.

The TRT consists of gaseous straw tubes, each with a diameter of 4 mm, to detect the radiation photons. The tubes are arranged parallel to the beam axis in the barrel region ($|\eta| < 1.0$) and radially in the end-cap region ($1.0 < |\eta| < 2.0$). They are filled with a gas mixture of 70% xenon, 27% CO_2 and 3% O_2 and use tungsten wires as anodes in the middle of the tubes. As transition radiation material, polypropylene foils and fibers are located between the tubes.

The radial (length) extension of the TRT is 554 mm $< R <$ 1082 mm (0 mm $< |z| <$ 780 mm) in the barrel and 617 mm $< R <$ 1106 mm (827 mm $< |z| <$ 2744 mm) in the end-cap region. Due to the geometry, the TRT provides only information in r-ϕ with an intrinsic accuracy of about 130 μm. With approximately 351 000 readout channels, the TRT will measure typically 36 hit points in radial direction per crossing particle.

2.3 Calorimeters

The purpose of a calorimeter is to absorb and to measure the energies of particles. Incoming particles interact with the calorimeter material and produce secondary particles, which themselves interact with the material. A particle shower is created this way, until the energies of all shower particles are small enough to be absorbed completely (or they escape from the detector). The shapes of the showers are different for hadrons and electrons or photons. The radiation length X_0 for electrons is smaller then the interaction length λ of hadrons. Therefore electromagnetic showers are shorter and broader in comparison to hadron showers. Hence two different types of calorimeters are existing in ATLAS (Fig. 2.3). The electromagnetic calorimeter (EMC) will be described in Section 2.3.1. The EMC is enclosed by the hadron calorimeter (Section 2.3.2).

The calorimeters in ATLAS are sampling calorimeters, which measure only part of the energies of the incoming particles. In order to reduce the size of the calorimeters, they consist of alternating layers of absorbers. Passive material, with a high material density, is used to reduce the energy. The energy deposition of the particles in the active material due to interactions, is measured. Afterward the energy measurement will be corrected for the energy lost in the passive material.

The calorimeters cover a range of $|\eta| < 4.9$. The EMCs have a thickness of $> 22\ X_0$ in the barrel and $> 24\ X_0$ in the end-cap region. The interaction length of the calorimeters is about 9.7 λ in the barrel part of ATLAS and about 10 λ in the end-cap region. The total thickness of the calorimeter provides a sufficient reduction of punch-throughs (particles entering the muon system) well below the irreducible rate of prompt or decay muons.

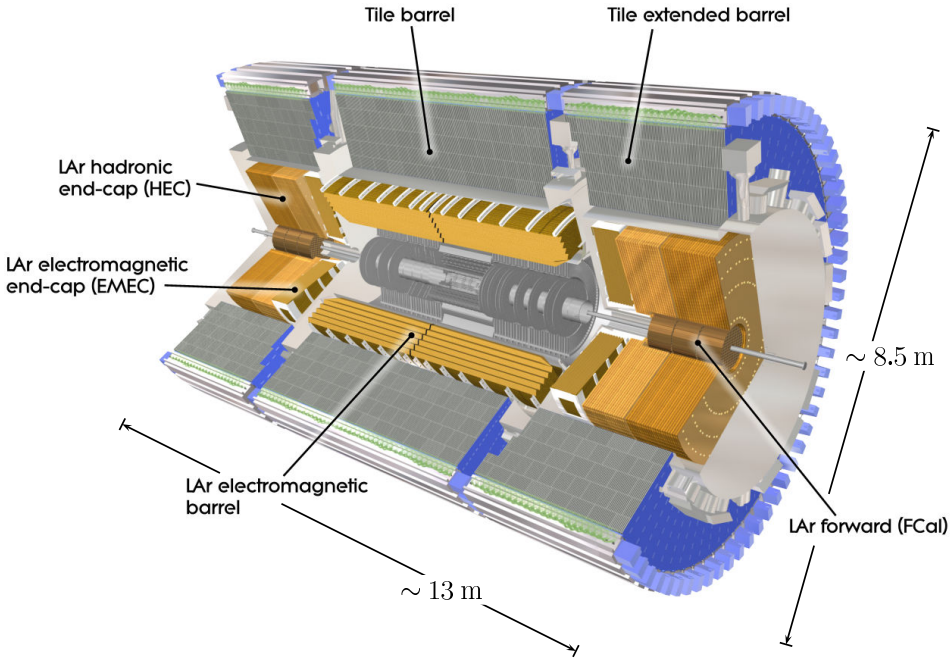

Figure 2.3: Layout of the electromagnetic and the hadron calorimeter. Both calorimeters are segmented in a barrel and an end-cap region [1].

2.3.1 Electromagnetic Calorimeter

The EMC is build in an accordion geometry with full ϕ symmetry and coverage. It is divided in three parts, the barrel part ($|\eta| < 1.475$) and the outer end-cap parts ($1.375 < |\eta| < 3.2$). The EMC consists of layers of liquid argon (LAr) as active material and lead absorber plates, to which two steel plates are glued. Incoming particles will cause a shower in the lead plates. The produced particles will interact with the LAr and produce additional secondary electrons, which will be measured by means of accordion-shaped polyimide electrodes. The radiation length X_0 of electrons in lead is about 0.56 cm in comparison to the interaction length λ of hadrons, which is about 17 cm. Therefore, electrons and photons will typically be absorbed in the EMC, while hadrons will reach the hadron calorimeter.

2.3.2 Hadron Calorimeter

Due to different physics requirements like radiation hardness or spatial precision of the measurement of the energy deposition, the hadron calorimeter uses different technologies in three different regions in η:

- **Tile calorimeter:**
  This sampling calorimeter consists of an almost periodic structure of layers of steel as absorber material and scintillating tiles as active material, which are read out by wavelength shifting fibers and photomultipliers. The tiles are arranged radially and normal to the beam line. The barrel part covers

the η range of $|\eta| < 1.0$, while the extended barrel tile calorimeter's range is $0.8 < |\eta| < 1.7$.

- **LAr hadron end-cap calorimeter (HEC):**
  In order to adjust the material density in the transition between the end-cap and the forward calorimeter, the HEC overlaps in $|\eta|$ with the tile calorimeter and the forward calorimeter. It covers the η range of $1.5 < |\eta| < 3.2$. It is arranged in two independent wheels per end-cap. As passive material, copper plates with a thickness of 25 mm (further away 50 mm) is chosen, whilst the gaps of 8.5 mm between the plates are filled with liquid argon, used as active material.

- **LAr forward calorimeter (FCal):**
  In the very forward region of $3.1 < |\eta| < 4.9$ the FCal has to work in an environment of very high radiation. Therefore, it is built with high material density and has a depth of about 10 hadronic interaction lengths. The FCal consists of three modules. The first module is made of copper and measures mostly the electromagnetic components of incoming particles. The two other modules measure mostly the energy of hadronic interactions. These modules consist of a tungsten metal matrix with tubes arranged parallel to the beam axis with rods in between. The small gap of about 0.25 mm is filled with liquid argon.

2.4 Forward Detector

Three detector types cover the forward region of ATLAS. The aim of two of these detectors is to measure and monitor the actual luminosity of ATLAS. The first one is LUCID (LUminosity measurement using Cerenkov Integrating Detector) for relative luminosity measurements and the second one is ALFA (Absolute Luminosity For ATLAS) for an absolute luminosity determination. Details of the principle of the luminosity measurements are given in Chapter 7. The third forward detector is the ZDC (Zero-Degree Calorimeter) and is monitoring the centrality of heavy-ion collisions, which is not covered in this thesis and will therefore not be explained in detail.
The LUCID detector consists of two aluminum vessels, 1.5 m long, arranged parallel to and centric around the beam axis. There is one vessel in each end-cap region of ATLAS at about $z = \pm 17$ m from the interaction point. Each vessel consists of 20 aluminum tubes of 15 mm diameter filled with C_4F_{10} gas at a pressure of 1.2−1.4 bar, which results in a Cerenkov threshold of 2.8 GeV for pions and 10 MeV for electrons. Particles passing the tubes will produce Cerenkov light, which will be reflected on average three times and then detected by photomultipliers (PM). The readout of the PM signal is fast enough for associating the signal to a bunch crossing. The luminosity measurement will then be performed by counting particles or signals per bunch crossing.

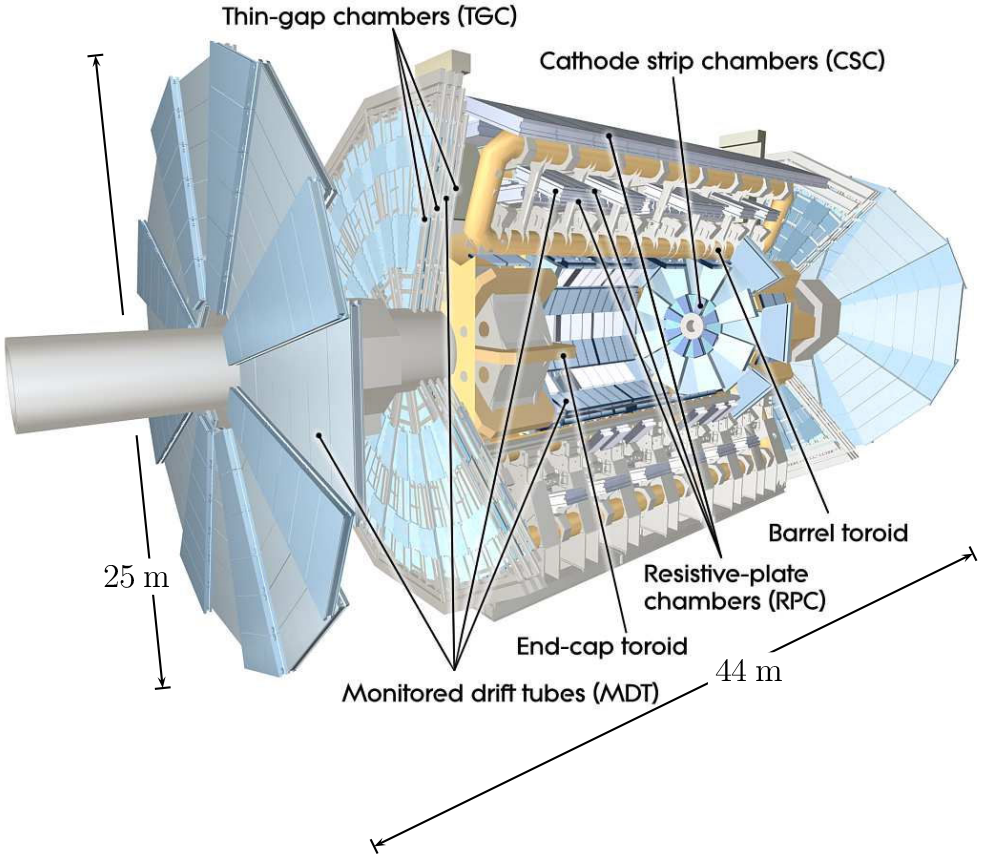

Figure 2.4: Sketch of the ATLAS Muon System. MDT and CSC are used to measure charged track particles while RPC and TGC are mainly trigger detectors [1].

The measurement of the absolute luminosity with the ALFA detector is based on the optical theorem, which relates the elastic scattering rate at small angles to the total cross section and the luminosity. ALFA consists of plastic scintillating fibers, which are arranged in a Roman Pot. A Roman Pot is a vacuum vessel with the detector mounted on a movable carrier. Here the Roman Pot contains a detector made of ten ceramic plates, each connected with 64 scintillating fibers, which are readout by photomultipliers. On each side of ATLAS two Roman Pot units, separated by 4 m, are installed in about 240 m distance from the interaction point. The detectors are attached to a movable frame. In case of a luminosity measurement the detectors will be moved close (≈ 1 mm) to the beam.

2.5 Muon System

The Muon System is the outermost part of the ATLAS detector (Fig. 2.4). The purpose of the Muon System is the measurement of hits caused by particles coming from the primary interaction region. These hits are used to reconstruct tracks as well as to trigger on events containing tracks in the Muon System.
Muons are interacting with material only via the electromagnetic or weak interaction. So energy loss due to hadronic interactions does not occur and the energy loss

in the calorimeter is smaller. Due to their higher mass in comparison to the electron, which also only experiences the electromagnetic and weak force, their energy loss via Bremsstrahlung is a factor of $\left(\frac{m_e}{m_\mu}\right)^2$ smaller. Therefore, muons are the only particles, which enter the Muon System.
The Muon System of ATLAS is designed to measure charged particle tracks with high precision as well as to trigger on events containing a muon signal. To measure the hits of charged particles, two different detectors are used.
In the η range of $|\eta| < 2.7$ (except for the innermost layer in the end-cap region) Monitored Drift Tube chambers (MDT) are installed. In the barrel part, the chambers are arranged in three double-layers while in the end-cap region, the chambers are arranged in three wheels perpendicular to the beam axis. Each MDT chamber consists of three to eight layers of drift tubes. These proportional counters are filled with 93% argon and 7% CO_2 and use a tungsten-rhenium wire in the middle of the tube as anode, which has a diameter of 50 μm. The stand-alone point resolution per tube is about 80 μm and 35 μm per chamber.
In the innermost layer of the end-cap the MDT is replaced by a Cathode Strip Chamber (CSC) due to the expected higher particle flux in that detector region. CSCs are multi-wire proportional chambers filled with a gas mixture of 30% Argon, 50% CO_2 and 20% CF_4. The point resolution of the CSCs is about 40 μm in the bending and about 5 mm in the transverse plane.
The second aim of the Muon System is to trigger on muonic events. Therefore dedicated trigger detectors have to deliver signals in a time window of $15 - 25$ ns, which have to be fast enough to tag bunch crossings.
In the barrel part of the detector ($|\eta| < 1.05$) Resistive Plate Chambers (RPC) are deployed as trigger chambers. These chambers are arranged in three concentric cylindrical layers and therefore provide three trigger stations measuring ϕ and η of a penetrating particle. The chambers consist of two resistive plates, made of phenolic-melaminic plastic laminate. The gaps of 2 mm between the electrodes are filled with a gas mixture of 94.7% $C_2H_2F_4$, 5% Iso-C_4H_{10} and 0.3% SF_6, which a traversing particle can ionize. The signal produced by the free electrons will be measured as signal on the electrodes.
In the η range of $1.05 < |\eta| < 2.4$ Thin Gap Chambers (TGC) are deployed and will be used as trigger stations as well as to measure the azimuthal coordinate ϕ to complement the MDT measurement. The TGCs are also a multi-wire proportional chambers filled with a gas mixture of CO_2 and n-C_5H_{12}. A high electrical field provides a fast trigger signal and a tagging efficiency for bunch crossings of above 99%.

2.6 Magnet System

The magnet system of ATLAS is intended to bend the trajectory of a charge particle in order to measure the momentum of particles with $p_T > 0.5\,\text{GeV}$. Particles with lower p_T cannot leave the Inner Detector due to too small bending radii. The magnetic system is divided in four different magnet systems. The schematic overview

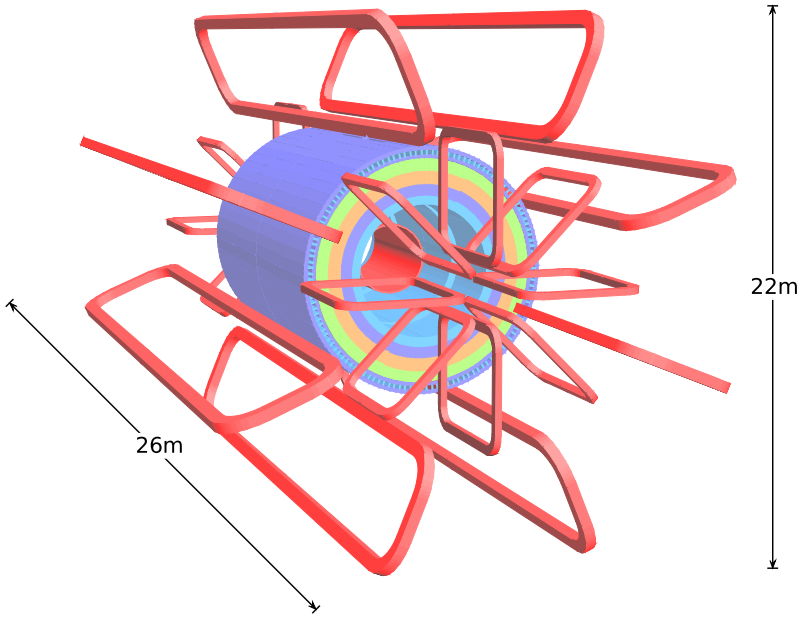

Figure 2.5: The geometry of the ATLAS magnet coils. The inner part is the Central Solenoid, which produces a solenoidal magnetic field of 2 T in the Inner Detector. The toroids in the outer part produce a toroidal magnetic field, which is used for measuring the momenta of muons in the Muon System [1].

is shown in Fig. 2.5.
In the barrel region, the Central Solenoid (CS) with an inner diameter of 2.46 m and an outer diameter of 2.56 m is arranged around the Inner Detector. It produces a magnetic field of about 2 T. The layout of the magnet system is tuned to keep the impact on the calorimeter performance as low as possible. It is contributing only about 0.66 radiation lengths to the material budget. The magnetic flux is returned by the steel in the hadron calorimeter. Due to the geometry, the tracks in the Inner Detector are bend in the r-ϕ plane.
The outer magnet system consists of the barrel toroid, which is interleaved by two toroids in the end-cap regions. The barrel toroid consists of eight superconducting coils with a length of 25.3 m, an inner diameter of 9.4 m and an outer diameter of 20.1 m. The coils are arranged symmetrically along the beam axis. The barrel toroid produces a magnetic field of about 0.5 T, which causes tracks in the Muon System to bend in the r-z plane. The end-cap toroids have a length of 5 m, an inner and outer radius of 1.65 m and 10.7 m. They are also constructed as eight superconducting coils, which are arranged symmetrically around the beam axis. The magnetic field has a strength of about 1 T.

2.7 Trigger

The nominal bunch crossing rate of the LHC is 40 MHz, which means on average one event of a data size of approximately 1.6 Mb every 25 ns. The amount of data

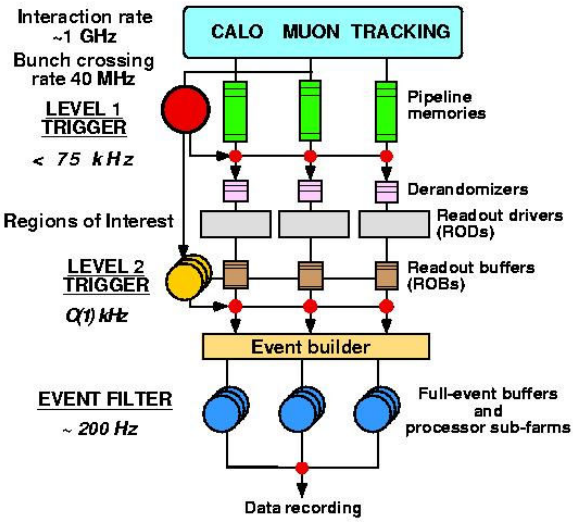

Figure 2.6: The three stage ATLAS trigger system [3].

to be stored on tape is too large in case every collision is recorded. Also, the cross section of interesting physics processes, i.e. contained in the physics program of ATLAS, is at least two orders of magnitude lower compared to the cross section of inelastic proton-proton scattering. Therefore ATLAS has developed a three-stage trigger system to preselect physics events of interest with high efficiency. The general structure of the ATLAS trigger is shown in Fig. 2.6.
The first level trigger (L1) will use information of the Muon System as well as the calorimeters. Trigger objects are high p_{T} muons, electrons and photons, jet energy, τs decaying into hadrons, missing energy (E_{T}^{miss}) or total transverse energy. The L1 trigger will reduce the event rate to $\leq 75\,\mathrm{kHz}$. The latency of the L1 trigger decision is at most $2.5\,\mu\mathrm{s}$ after the bunch-crossing. For this time event data of the different contributing detector parts has to be stored in memory pipelines.
The high level trigger (HLT) refines the decision of the L1 trigger. The HLT consists of the level 2 (L2) trigger and the event filter (EF). The L2 trigger is seeded by Regions-of-Interest (RoI), which are defined by the L1. The L2 uses more detector information in order to reduce the event rate to $\leq 3.5\,\mathrm{kHz}$. The average event processing time is 40 ms. The EF uses more sophisticated offline-like analysis algorithms to refine the L2 trigger decision. Hereby the event rate will be reduced to $\leq 200\,\mathrm{Hz}$. This is the rate of event information, which will be written to the data storage for further offline physics analysis. The average EF processing time is in the order of 4 seconds.

2.7.1 Level 1 Trigger

The L1 trigger is a hardware-based trigger and tuned to cover the whole physics program of ATLAS. Therefore, the L1 is looking for trigger objects in the Muon System and the calorimeters. Information of both trigger subsystems is send to the Central Trigger Processor (CTP), which combines the information. In total 256

different trigger items can be defined and prescale factors may be set for a given threshold in order to balance the rate of interesting physics events with different cross sections. A prescale factor of n means that statistically only every n^{th} event with a positive trigger decision for a certain (prescaled) signature will be accepted. The event is also associated to a particular bunch-crossing.
The L1 calorimeter trigger consists of approximately 7200 analog trigger towers with a granularity of 0.1×0.1 in $\eta \times \phi$. Firstly the information of the trigger towers is sent to the pre-processor. The pre-processor associates the event with a particular bunch crossing and digitizes the analog signal from the trigger towers. Secondly the information is sent to the Cluster Processor (CP) and the Jet/Energy-sum Processor (JEP) in parallel.
The CP identifies electrons, photons and τ objects above a given transverse energy threshold. The trigger algorithm is looking for 2×2 clusters of trigger towers in the EMC using a 4×4 trigger tower window and the sum of 1×2 or 2×1 trigger towers. In case, that the 2×2 core towers of the sliding window locates a local E_{T} maximum in the EMC and the hadronic calorimeter, three isolation cuts are applied:

- total E_{T} of the hadronic trigger cluster located behind the core EMC trigger cluster is less than the isolation threshold,
- total E_{T} of the 12 trigger towers surrounding the core EMC trigger cluster is less than a programmable threshold,
- total E_{T} of the 12 trigger towers surrounding the core hadron trigger cluster is less than a programmable threshold.

The JEP subsystem identifies jet elements as the sum of 2×2 trigger towers in the EMC and 2×2 trigger towers in the hadron calorimeter. This results in an overall granularity of 0.2×0.2 in $\eta \times \phi$. The algorithm uses a sliding window of adjustable size of 2×2 up to 4×4 jet elements. If the energy deposition in a region of 2×2 jet elements constitutes an isolated local maximum above a given energy threshold, the algorithm forms a reconstructed trigger jet object.
Both subsystems (CP and JEP) send the information to the Central Trigger Processor (CTP), which defines the RoI, which is passed to the HLT as a seed.
The muon trigger is divided into two trigger regions. In the barrel region (Fig. 2.7(a)) for $|\eta| < 1.05$, the muon trigger uses the RPCs (Section 2.5). Each station consists of a RPC doublet. The middle layer (RPC2) is the pivot station. If a hit is measured in RPC2, a corresponding hit in the inner layer (RPC1) is searched for within a road from the RPC2 hit pointing to the primary interaction region. The width of the road depends on the desired p_{T} threshold and is pre-defined in a look-up table (LUT). Simultaneously, three low and three high p_{T} thresholds can be applied. For low p_{T} (approximately 6 to 9 GeV) 3-out-of-4 possible coincidence hits out of the two RPC doublets are required. For high p_{T} thresholds (approximately 9 to 35 GeV) also information of the outer RPC double layer (RPC3) is used. In addition to the trigger result of RPC1 and RPC2, at least one out of two possible hits in RPC3 has to be inside the road.

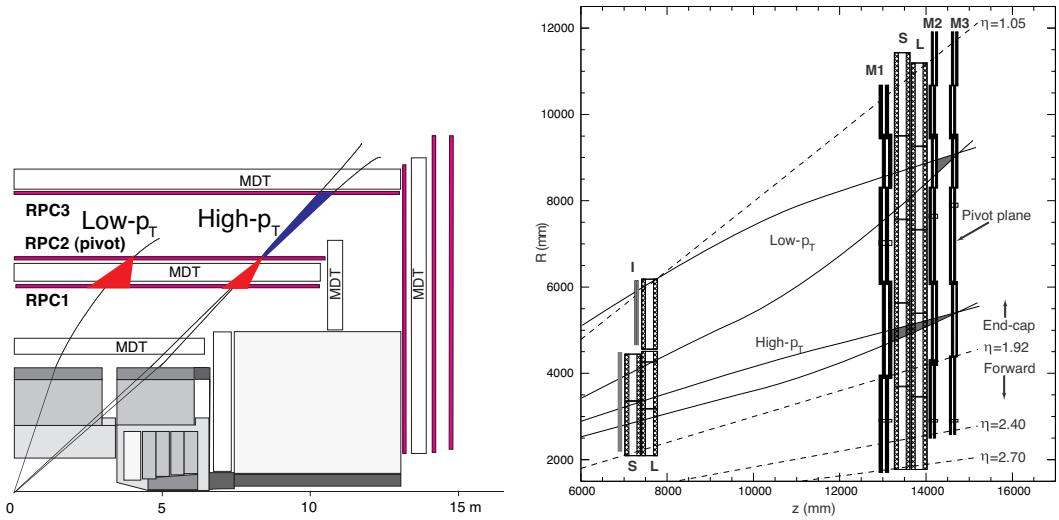

Figure 2.7: Trigger stations and sketch of trigger roads of the muon L1 trigger (a) in the barrel and (b) in the end-cap region [1].

In the end-cap region the TGCs are used as trigger stations. Here the trigger is working according to the same principle as in the barrel part. The TGC detectors are arranged in four different layers (Fig. 2.7(b)). The outermost layer acts as the pivot plane. A hit in this plane seeds a road of a width defined by LUT entries (depends on the applied p_{T} threshold). Within this road, pointing from the hit to the interaction point, hits in the other trigger layers will be searched for. Three different low and three different high p_{T} thresholds are available.

2.7.2 High Level Trigger

The HLT consists of two software-based trigger levels, which are executed on a computer farm. The L2 trigger, which uses only part of the event information and the EF, which uses all available event information and provides the final trigger decision. In this thesis, the main focus will be on the muon and jet trigger. A detailed description of all algorithms used to find trigger signatures in ATLAS is found in [4].

The algorithms of the L2 trigger are seeded by the RoI of the L1 trigger. Due to the average allowed processing time of about 40 ms per event, the L2 algorithms can use detector data within the RoI and fast track finding algorithms are applied to Inner Detector hits as well as to MDT hits in the Muon System. A fast combination of tracks found in the Inner Detector and the Muon System is performed for the muon trigger.

The jet trigger also uses the detector information of the RoI provided by the L1 trigger. The energy deposition and the η-ϕ coordinates of the trigger towers inside a rectangular around the RoI are read out. The width $\Delta\eta$ and $\Delta\phi$ of the rectangular is defined at trigger configuration time. A cone jet finding algorithm is used to reconstruct the jet energy and coordinates, depending on the tunable parameter

ΔR. Afterwards, the reconstructed jet energy is corrected for the hadronic shower components.
Hypothesis algorithms are running in order to determine, whether the event is fulfilling a selection criteria like energy thresholds or physics signatures, as defined by the selection algorithms.
The final trigger decision is made by the EF. In the last trigger step, adapted offline reconstruction algorithms are used. In the EF, the full event information is available and can be used by the EF algorithms. For the muon trigger, tracks in the Muon System around the reconstructed muon from L2 are reconstructed and then combined with reconstructed tracks in the Inner Detector. The jet EF consists also of an adapted offline jet reconstruction algorithm. The jet EF reconstructs all jets in the event, runs a jet energy calibration algorithm and removes jets below a given transverse energy threshold.
The EF trigger efficiency as a function of the jet energy, reconstructed by offline jet reconstruction algorithms, is shown in Fig. 2.8. In Fig. 2.8(a) the thresholds $E_T^{L1} > 10$ GeV, $E_T^{L2} > 30$ GeV and $E_T^{EF} > 50$ GeV are applied. In Fig. 2.8(b) the difference between the threshold values of the trigger levels is larger. The corresponding thresholds values are $E_T^{L1} > 70$ GeV, $E_T^{L2} > 150$ GeV and $E_T^{EF} > 255$ GeV. In case of smaller threshold steps from L1 to EF, the selection performance (width of the turn-on curve) of the EF is dominated by the transverse energy resolution of the L1 trigger threshold. The performance of the EF jet trigger selection improves in case of significantly higher thresholds in the HLT compared to the L1 threshold value. Therefore, the different trigger thresholds from L1 to EF have to be tuned correctly to optimize the jet trigger selection in dependence of the transverse energy. The different jet trigger signatures used for the $b\bar{b}$ jet cross section measurement are described and studied in Section 8.1.

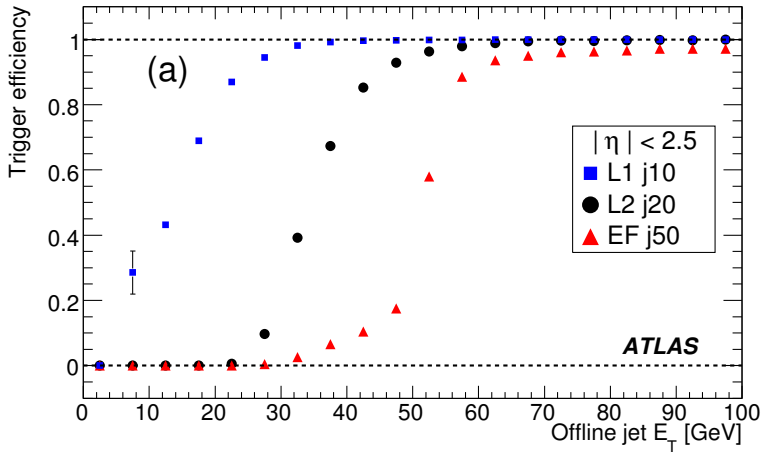

(a)

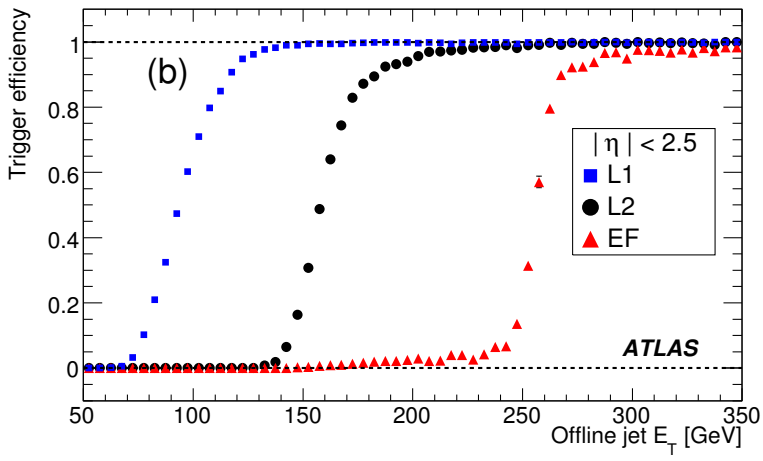

(b)

Figure 2.8: Trigger efficiency versus offline jet energy for different trigger thresholds [4].

Chapter 3

Theory of $b\bar{b}$ Production

This chapter provides the theoretical background of $b\bar{b}$ production. Up to now our understanding of the fundamental constituents and their interactions is well modeled in the Standard Model of Elementary Particle Physics. This chapter starts with the main aspects of this model, which are needed to understand the production of b-quarks.
Since within this thesis a measurement of the inclusive b-jet cross section will be prepared, Section 3.2 gives an introduction to the calculation of the $b\bar{b}$ production cross section using perturbative QCD. Although the cross section is calculated on parton level, b-quarks can only be measured as b-like hadrons, which will induce b-jets in the detector. Therefore, in Section 3.3 a phenomenological approach to the fragmentation process and jets is given. The chapter ends with an overview of the theoretical cross section as a function of the energy available.

3.1 Standard Model of Elementary Particle Physics

The Standard Model of Elementary Particle Physics (SM) is a Quantum Field Theory (QFT) based on the spontaneously broken (SSB) gauge symmetry group of

$$SU(3)_C \otimes SU(2)_L \otimes U(1)_Y \xrightarrow{SSB} SU(3)_C \otimes U(1)_{em}$$

where C denotes the color charge in the strong interaction, L represents the weak isospin and Y the hyper charge.
This theory describes the structure of matter as composed of spin-1/2 fermions as well as the interactions between the fermions, mediated by spin-1 gauge bosons [5, 6, 7].
In the SM 12 species of fermions exist, arranged in three families. Six kinds of fermions are given by the quarks q, which have an electric charge of 2/3 of an elementary charge e ($u,\ c,\ t$) and $-1/3e$ ($d,\ s,\ b$). The other six fermions are the leptons l. They have an electric charge of $-1e$ ($e,\ \mu,\ \tau$) or 0 ($\nu_e,\ \nu_\mu,\ \nu_{tau}$). In addition to every quark and lepton an antiparticle exists, which has the same mass but opposite electric charge. Up to now, this is the complete list of known fundamental point-like fermions:

$$\underbrace{\begin{pmatrix} u \\ d \end{pmatrix} \begin{pmatrix} c \\ s \end{pmatrix} \begin{pmatrix} t \\ b \end{pmatrix}}_{\text{quarks}} \qquad \underbrace{\begin{pmatrix} e^- \\ \nu_e \end{pmatrix} \begin{pmatrix} \mu^- \\ \nu_\mu \end{pmatrix} \begin{pmatrix} \tau^- \\ \nu_\tau \end{pmatrix}}_{\text{leptons}} .$$

In the SM three out of four fundamental forces are described, the strong-, the electromagnetic- and the weak force. These forces are described by the exchange of spin-1 bosons. Therefore, in addition to the 24 fundamental particles, there are exchange bosons.

Only quarks are participating in the strong interaction. It is described by the theory of Quantum Chromodynamics (QCD). The gluon g is the exchange boson, which carries the charge of the strong interaction, called "color". QCD is a non-Abelian gauge theory and the corresponding coupling constant of the strong interaction α_s is a "running coupling constant", i.e. the value of α_s depends on the exchanged momentum Q^2. α_s is expressed by

$$\alpha_s(Q^2) = \frac{12\pi}{(33 - 2N_f)\ln(Q^2/\Lambda^2)} , \tag{3.1}$$

where Λ is the scale at which the strong coupling 'constant' becomes large and finally diverges ($\Lambda \approx 250$ MeV). N_f is the number of quark flavors.

For small distances, i.e. high Q^2 momentum exchange ($r \propto \frac{1}{\sqrt{Q^2}}$), α_s becomes small ($\alpha_s \ll 1$) and the interaction via single gluon exchange dominates. Since the gluon is massless, the potential of QCD at small distances looks like the electromagnetic potential, i.e. $V \propto \frac{1}{r}$. On the other hand the gluon itself carries color charge, i.e. it is not color neutral. These colored gluons lead to an increased potential between two quarks proportional to their spatial separation r. Therefore, the potential of the strong interaction can be parametrized by:

$$V_{\bar{q}q} = -\frac{4}{3}\frac{\alpha_s}{r} + \sigma r . \tag{3.2}$$

The parameter σ (string tension) describes the increase of the potential energy of two quarks as they separate further. The string tension was estimated from energy spectra of $b\bar{b}$- and $c\bar{c}$-particles to $\sigma \approx 0.9$ GeV/fm ([8], [9]). Due to the increase of the potential, it is not possible to detect a free quark (confinement). The potential would lead to the production of new $q\bar{q}$ or gg pairs, if the potential energy is sufficient to create these pairs. These new partons form a coupled state (hadron) with the other quark(s). At short distances ($\approx$ fm) and high energies, the first contribution of Eq. (3.2) prevails. Therefore, in high energy collider experiments, quarks are considered to be "free" quarks (asymptotic freedom).

The electromagnetic force is mediated by the photon γ as the exchange boson. It couples to the electrical charge of a particle. Thus, quarks, charged leptons and $W^\pm$ interact via the electromagnetic force. The photon itself has no electric charge. Therefore the electromagnetic potential decreases with $1/r$, like it is described by Quantum Electrodynamics (QED).

Almost all particles experience the weak interaction. There are three exchange bosons mediating the weak interaction. These are the neutral Z^0 and the charged

$W^{\pm}$. In contrast to the gluon and the photon, the weak interaction bosons are not massless. Due to their mass, the coupling constant of the weak interaction is much smaller compared to the electromagnetic coupling constant.
In contrast to the strong and the electromagnetic interaction, the weak interaction distinguishes between left- and right-handed particles ($V-A$ theory), i.e. the interaction bosons only couple to left-handed particles. Almost all long-living hadrons decay via the weak interaction. Comparing weak decays with $\Delta s = 1$ (s-quark decay) to $\Delta s = 0$ transitions, the former are suppressed by a factor of about ≈ 20. This was considered historically by introducing the Cabibbo angle θ_C [10], which connects the d and s-quark to the mass eigenstate d' of the weak interaction

$$d' = d\cos\theta_C + s\sin\theta_C \ . \tag{3.3}$$

The weak mass eigenstates are arranged as doublets of the weak isospin I (analog to the proton-neutron isospin). The third component of the weak isospin for the leptons and the weak mass eigenstates u and d' is

$$I_3 = \begin{matrix} +1/2 \\ -1/2 \end{matrix} \quad \text{for} \quad \begin{pmatrix} \nu_l \\ l^- \end{pmatrix}_L \begin{pmatrix} u \\ d' \end{pmatrix}_L , \tag{3.4}$$

where L indicates the coupling to left handed particles only.
The isospin formalism would lead to flavor changing neutral currents (FCNC), which are measured in experiments to be strongly suppressed. In order to avoid FCNC at tree-level, the GIM (Glashow, Iliopoulos, Maiani [11]) mechanism was introduced, which predicted a fourth quark, the c-quark. The GIM mechanism introduces orthogonal mass eigenstates d' and s', which are both connected to the quarks via the Cabibbo angle. In order to take the third quark family into account, the GIM mechanism was generalized to the Cabibbo-Kobayashi-Maskawa matrix (CKM matrix) V_{CKM} [12]:

$$\begin{pmatrix} d' \\ s' \\ b' \end{pmatrix}_L = V_{CKM} \begin{pmatrix} d \\ s \\ b \end{pmatrix}_L = (V_{qq'}) \begin{pmatrix} d \\ s \\ b \end{pmatrix}_L \ . \tag{3.5}$$

The matrix elements $V_{q'q}$ cannot be predicted by theory from first principles, but are measured by different experiments. Without the mixing of the different quarks in the weak interaction, hadrons containing b-quarks would be stable. Calculating the transition probability of quarks (e.g. $b \to c$), the V_{CKM} matrix element has to be added to the common vertex of a W and a $q\bar{q}$ pair. Since the matrix element is $V_{cb} \approx 0.04 > 0$, the decay $b \to c$ is possible, but the lifetimes of the b-flavored particles are larger compared to c-flavored particles. The longer lifetime can be used to identify particles and jets containing a b-quark (Chapter 8.3).
Although the SM is confirmed by many experiments, several questions are still open. For example, the different masses of different particles cannot be explained by the SM.
To consider the different masses within the SM, the Higgs mechanism [13, 14, 15] is introduced, employing the principle of the spontaneous symmetry breaking. This

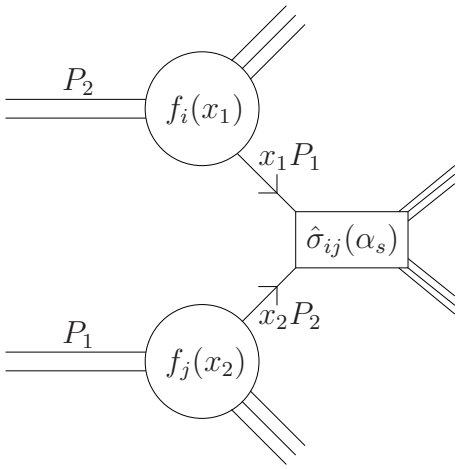

Figure 3.1: Description of a two parton scattering [16].

leads to the Higgs-field and to an additional fundamental particle, the Higgs boson. Although the Higgs boson explains the masses of the particles, its mass is a free parameter of the theory. It will be one of the main topics of the experiments at the LHC to search for a possible Higgs boson.
In addition to the open question about the different masses of the particles, the SM can neither explain the asymmetry of matter and antimatter nor can gravity be included into the model as the last fundamental force. Furthermore, the different energy scales of the different interactions as well as the different masses of particles, especially a Higgs boson with a relatively low mass, are unsolved problems in the SM. Therefore, theories beyond the SM like Super Symmetry (SUSY) are developed, which partially solves these problems. SUSY models will be tested at the LHC.

3.2 Inclusive Production of $b\bar{b}$ Quarks in pp-Collisions

At the LHC heavy quarks will be produced in proton-proton scattering. Due to the high energy available at the LHC, the scattering of protons is theoretically described by scattering of individual partons like qq- or gg-scattering (Section 3.1). Therefore, quarks or gluons, originating from the two incoming interacting protons, initialize the heavy quark production. The total cross section σ for a hard scattering process initiated by two protons with four-momenta P_1 and P_2 is written as

$$\sigma(P_1, P_2) = \sum_{i,j} \int dx_1 dx_2 f_i(x_1, \mu^2) f_j(x_2, \mu^2) \hat{\sigma}_{ij}(p_1, p_2, \alpha_s(\mu^2), Q^2/\mu^2)\,, \qquad (3.6)$$

where μ is the renormalization scale. $f_i(x_1, \mu^2)$ and $f_j(x_2, \mu^2)$ are the proton structure functions, which describe the momentum distributions of the quarks or gluons in the proton, i.e. the probability, that partons carry momentum fractions $p_1 = x_1 P_1$ and $p_2 = x_2 P_2$ participate. $\hat{\sigma}_{ij}$ is the short distance cross section of the interacting partons.
The cross section for heavy quark production is calculated in perturbation theory as a series in the coupling constant α_s:

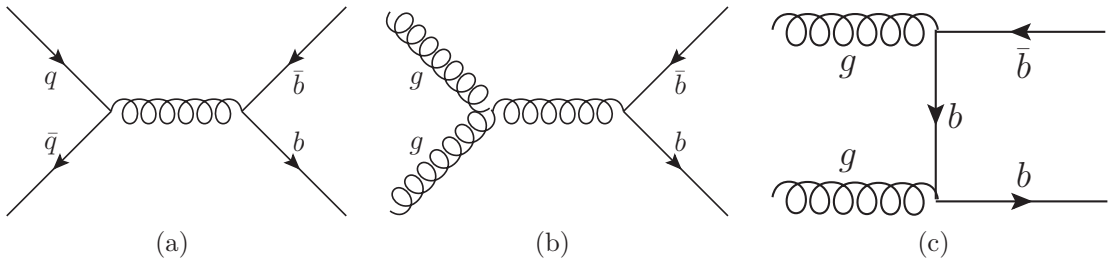

Figure 3.2: Feynman diagrams for LO heavy quark production.

$$\hat{\sigma}_{ij} = \alpha_s^2 \sum_{m=0}^{n} \alpha_s^m \hat{\sigma}_m \tag{3.7}$$

where the coefficients $\hat{\sigma}_m$ represent the contributions of the m^{th} order to the heavy quark production. Therefore, $m = 0$ is called leading order (LO) in the cross section calculation. The indices i and j specify the type of the incoming particles.
In LO order $b\bar{b}$ pairs will be produced by the flavor creation (FC) mechanism. In FC two incoming gluons or two incoming quarks annihilate to produce heavy quarks as outgoing particles. Examples of Feynman diagrams of FC are shown in Fig. 3.2.
In NLO the production mechanisms of gluon splitting (GS) and flavor excitation (FEX) have to be taken into account. In GS an outgoing gluon of a $2 \to 2$ process, splits into a $b\bar{b}$ pair. In case of FEX at least one of the b-quarks will be scattered into the detector by e.g. a gluon. Examples of Feynman diagrams of GS and FC are shown in Fig. 3.3.
In more detail, the short distance cross section $\hat{\sigma}_{ij}$ is described by

$$\hat{\sigma}_{ij}(s, m^2, \mu^2) = \frac{\alpha_s^2(\mu^2)}{m^2} F_{ij}(\rho, \frac{\mu^2}{m^2}) \tag{3.8}$$

where $\rho = \frac{4m^2}{\hat{s}}$. The dimensionless function $F_{ij}(\rho, \frac{\mu^2}{m^2})$ is written as a power series expansion

$$F_{ij}(\rho, \frac{\mu^2}{m^2}) = \underbrace{F_{ij}^{(0)}(\rho)}_{\propto \sigma_0} + 4\pi\alpha_s(\mu^2) \underbrace{\left[F_{ij}^{(1)}(\rho) + \bar{F}_{ij}^{(1)}(\rho) \log(\frac{\mu^2}{m^2}) \right]}_{\propto \sigma_1} + \mathcal{O}(\alpha_s^2)\,. \tag{3.9}$$

The lowest order $F_{ij}^0(\rho)$ corresponds to the LO cross section. The LO cross section can be obtained by integrating the equation

$$d\hat{\sigma}_{ij} = \frac{1}{\hat{s}} \frac{d^3p_3}{(2\pi)^3 2E_3} \frac{d^3p_4}{(2\pi)^3 2E_4} (2\pi)^4 \delta^4(p_1 + p_2 - p_3 - p_4) \sum |M_{ij}|^2 \tag{3.10}$$

over the phase space, using the invariant matrix element M_{ij} of leading order processes of the scattering of the two incoming partons. $\hat{s}$ is the center of mass energy squared and the δ-function provides energy and momentum conservation.
It can be shown, that $\bar{F}_{ij}^{(1)}(\rho)$ is completely fixed by the lower order term $F_{ij}^{(0)}(\rho)$, while $F_{ij}^{(1)}(\rho)$ has to be calculated considering the different types of Feynman diagrams of the next order.

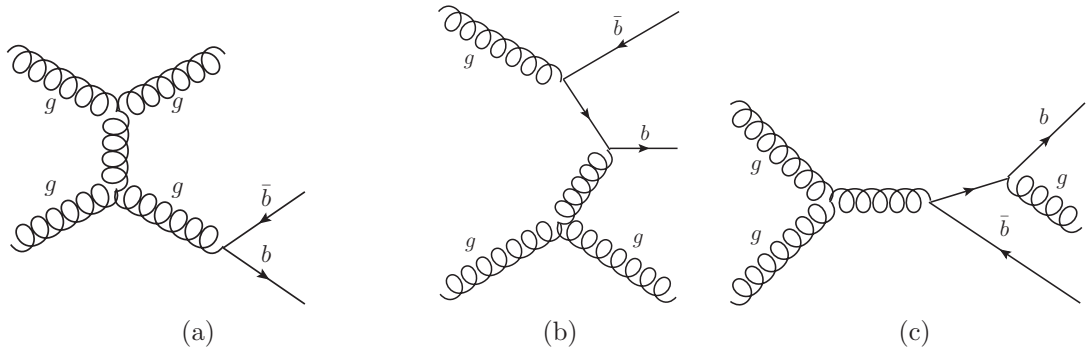

Figure 3.3: Examples of Feynman diagrams for NLO heavy quark production via (a) gluon splitting, (b) flavor excitation. An example for radiative corrections to the heavy quark cross section by NLO processes is shown in (c).

Already at NLO, logarithmic terms appear in the calculation of the short distance cross section, which depend on the choice of the renormalization scale. In an high-energy environment, μ has to be chosen of the same order as p_T, $\mu \approx p_{\mathrm{T}}$ and the convergence of the perturbative series is spoilt by large logarithms like $\log\left(\frac{p_T^2}{m^2}\right)$. This leads to differences between the QCD prediction of the $b\bar{b}$ production cross section and measurements at Tevatron, Fermilab (Chapter 4.2). In order to solve this problem, techniques to resum logarithms are developed. At leading log (LL) level the $\alpha_s^n \log\left(\frac{p_T^2}{m^2}\right)^n$ contributions are resumed, at next-to leading-log (NLL) $\alpha_s^n \log\left(\frac{p_T^2}{m^2}\right)^{n-1}$ contributions are resumed, etc.. These fixed-order plus next-to-leading logarithm (FONLL) [17] calculations result in a better agreement of theory and measurements.

3.3 b-Jets

Due to the confinement, b-quarks cannot be measured as free partons. The increase of the potential of the strong interaction proportional to the spatial separation $\propto r$ of the quarks is responsible for the creation of new $q\bar{q}$ pairs. These quarks will form a bound state (hadron) with the b-quarks. Therefore, during hadronization, $q\bar{q}$ states (mesons) or qqq states (baryons) arise.
The creation of quark pairs and their hadronization is called fragmentation. The fragmentation process cannot be calculated analytically and thus must be modeled phenomenologically. The fragmentation process leads to a small deceleration of a heavy quark. This is modeled by the Peterson fragmentation function $f(z)$, which describes the momentum zp of the hadron, p being the momentum of the heavy quark Q,

$$f(z) \propto \frac{1}{z\left(1 - \frac{1}{z} - \frac{\epsilon_Q}{1-z}\right)^2}. \tag{3.11}$$

Theoretically the factor ϵ_Q is given by the mass ratio of the light and the heavy

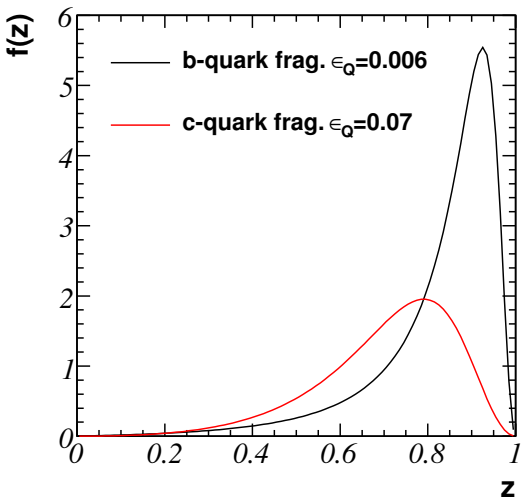

Figure 3.4: Peterson function used to model the fragmentation of heavy quarks.

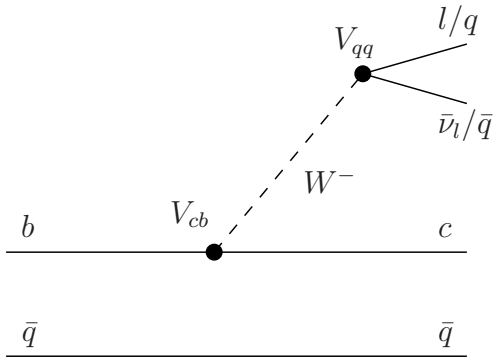

Figure 3.5: Example of a weak b-hadron decay.

quark, but in practice it is often used to tune the fragmentation process w.r.t. to experimental data. In the simulation of Monte Carlo events (Chapter 5.1), it was set to $\epsilon_Q = 0.006$ for the fragmentation of b-quarks and $\epsilon_Q = 0.07$ for c-quarks. In Fig. 3.4 the Peterson fragmentation function for $\epsilon_Q = 0.006$ is shown. Most of the momentum of the fragmentation hadron is provided by the heavy quark.

The decay of hadrons with at least one b-quark (b-hadrons) is mediated by the weak interaction. Due to the CKM-suppressed decay modes, the B-mesons have a mean lifetime $\tau = (1.58 \pm 0.14)$ ps [18], which is a long lifetime compared to the lifetime of c-hadrons or light quark resonances. Since the value $V_{cb} = 0.0412 \pm 0.0011$ is larger by one order of magnitude compared to $V_{ub} = 0.0039 \pm 0.0004$ [18], the b-quark will preferably decay to a c-quark by radiating a W-boson. An example of such a b-hadron decay is shown in Fig. 3.5.

The c-hadron itself will also decay, such that a cascade of particle decays is initiated. In the center-of-mass system of the individual decays, the momentum direction of the daughter particles is back-to-back, but due to the large boost of the system, the momentum direction of the daughter particles in the laboratory system will be close to each other. The particles will be measured as a jet in the detector. One

commonly used definition of a jet is a concentration of energy (deposited in the calorimeter) inside a cone of a fixed radius r in the η-ϕ-plane around the jet axis (cone jets). This definition is used in this thesis. The algorithm to reconstruct cone jets is explained in Chapter 6.1.

3.4 Theoretical $b\bar{b}$ Cross Section

The $b\bar{b}$ cross section $\sigma_{b\bar{b}}$ is a measure for the rate of $b\bar{b}$ pair production within proton-proton collisions with the instantaneous luminosity $\mathcal{L}$. As described in the previous sections, the expected cross section depends on the available phase space and therefore depends on the center-of-mass energy (CME) $\sqrt{s}$ of the colliding protons. In Fig. 3.6, the total $b\bar{b}$ cross section for various physics processes as a function of the CME is shown.
At the nominal LHC energy of $\sqrt{s} = 14$ TeV the expected $b\bar{b}$-cross section is $\sigma_{b\bar{b}} \sim 500\,\mu$b which leads to a production rate of approximately 10^6 Hz at a instantaneous luminosity of 10^{34} cm^{-2}s^{-1}. At lower CME, e.g. in the start-up phase of the LHC, the production cross section will be a bit smaller and therefore a smaller rate of $b\bar{b}$ pairs is expected, as shown in Fig. 3.6.
Although the rate of expected $b\bar{b}$ pairs is large, the total cross section for pp interactions is even larger by at least two orders of magnitude. Therefore, background processes have to be suppressed by at least two orders of magnitude in order to measure the $b\bar{b}$ production or b-jet cross section.

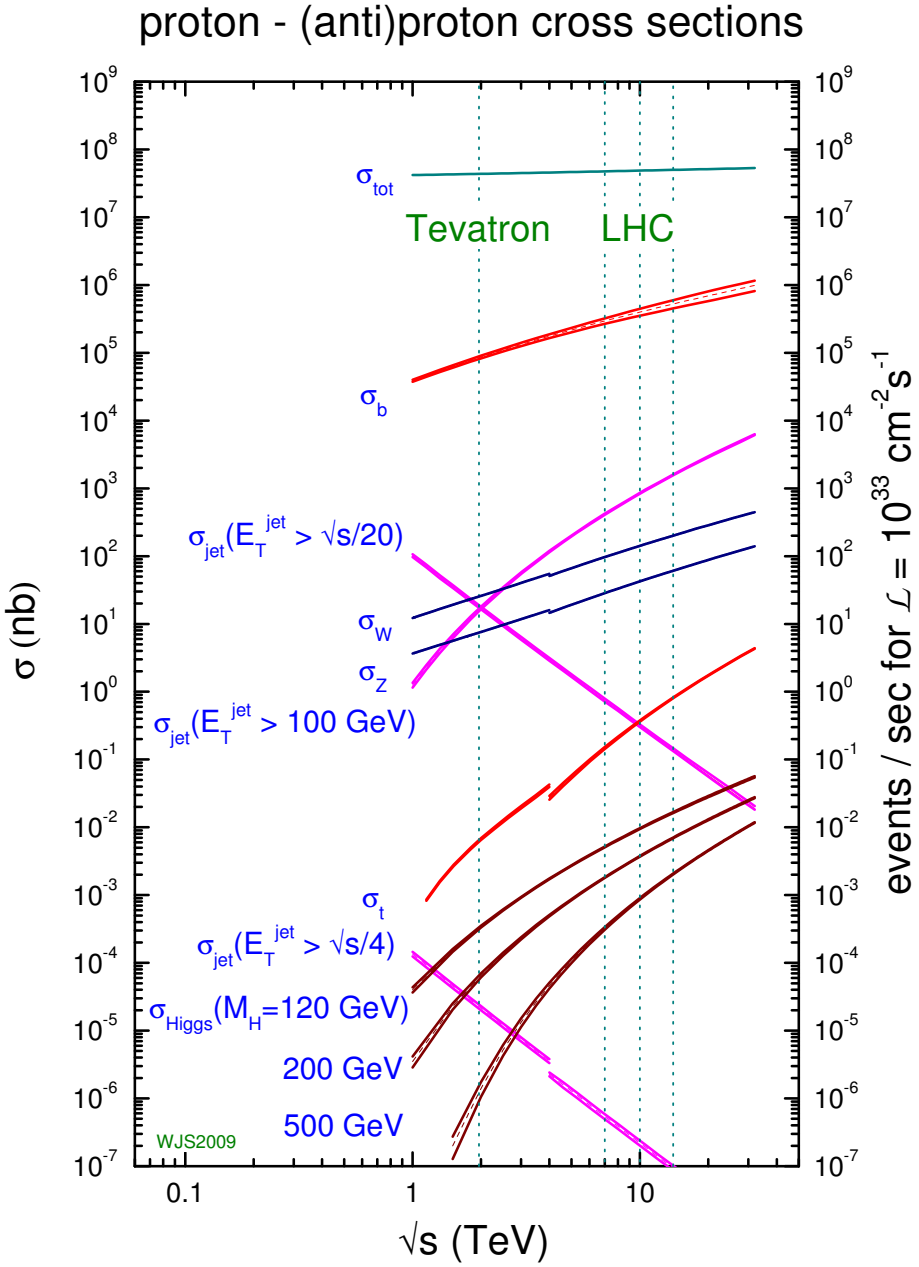

Figure 3.6: Expected cross sections for various processes as a function of the CME [19].

Chapter 4

$b\bar{b}$ Cross Section Measurements

The inclusive b-jet production cross section has been measured several times at lower energies. After motivating such a measurement at the LHC (Section 4.1), a short introduction into previous measurements and recent results follows in Section 4.2. At the end of this chapter (Section 4.3) the strategy to measure the differential b-jet cross section $\frac{d\sigma_{b-jet}}{dp_{\mathrm{T}}}$ at LHC energies within the ATLAS experiment is presented.

4.1 Motivation

The production cross section of $b\bar{b}$ pairs as well as the shape of their p_{T} spectrum can be calculated within perturbative QCD. Up to now, the results agree with the theoretical predictions. The high center-of-mass energy of $\sqrt{s} = 14$ TeV ($\sqrt{s} = 7$ TeV in the beginning) leads to possibilities to test QCD calculations at higher energies than before. An inclusive b-jet measurement is especially appropriate to probe QCD calculations. Since jets only weakly depend on fragmentation effects, a b-jet cross section can be unfolded to parton level and then easier compared to QCD calculations (systematic errors depending on fragmentation are negligible) in contrast to cross section measurements using an exclusive b-hadron decay channel. Due to the large expected event number, QCD can also be tested in more detail and with higher accuracy than before. The large p_{T} range of b-jets available, allows to separate the different production mechanisms (FC, FEX, GS, see Section 3.2) of b-quark production, since the contributions of the different mechanisms depend on the available energy. This will improve the phenomenology of heavy quark production. The understanding of b-jets, the identification of b induced jets as well as their production and fragmentation is an important input for many other measurements, like Higgs searches. Here one of the most important channels is the production of a SM Higgs boson in association with two top-quarks, which leads to four b-jets in the final state. Also in top physics b-jets play an important role since almost all top quarks decay to a b-quark and therefore induce a b-jet. Furthermore, in searches for New Physics like looking for Super Symmetry or exotic phenomena, (high p_{T}) b-jets play a key role. Especially the SM cross section has to be well known in order to differentiate between b-jet content compatible with SM expectation and b-production due to New Physics phenomena. Therefore, a good understanding of

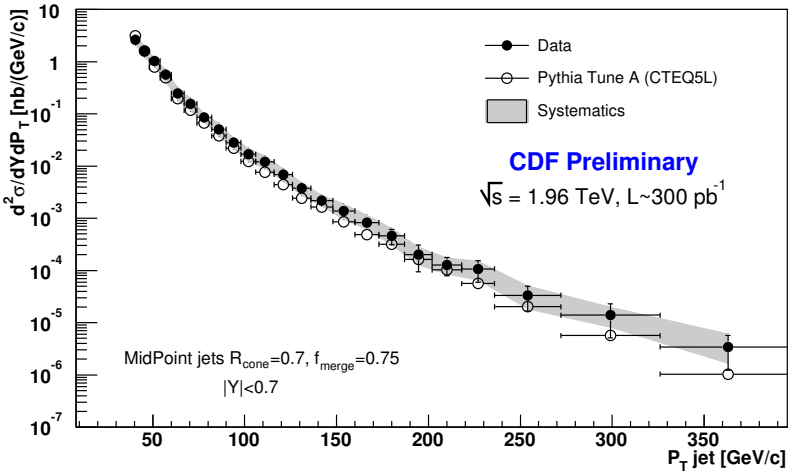

Figure 4.1: Inclusive b-jet p_{T} spectrum measured at Tevatron [23].

b-jets is essential.

4.2 Current Experimental Results

First $b\bar{b}$ cross section measurements were performed at the UA1 experiment [20], followed by many other experiments. In the past 15 years, many measurements were done at Tevatron, which are reviewed in [21]. Already with Run 0, CDF measured the b-production cross section via the decay channel $B^{+/-} \rightarrow J/\Psi K^{+/-}$ [22]. This first measurement showed discrepancies between the measured cross section and the one expected according to the theory of perturbative QCD, but with large errors ($30\%_{stat}$, $40\%_{syst}$) due to limited statistics and systematic uncertainties.
At Run I, the difference between theoretical calculations of the cross sections and the improved measurements decreased, but still a factor of nearly two remained. At Run II two different measurements became possible, due to a (better) secondary vertex reconstruction, b-hadron identification as well as higher available event statistics. The first method of a cross section measurement used an exclusive decay channel and an explicit reconstruction of the b-hadron. The advantage of these measurements is the large event statistics available, but the p_{T} reach of $(0-25)$ GeV is very limited. The second method is based on measuring inclusive b-jets (see e.g. [23]). Here the jet-p_{T} limit is around 500 GeV, but the statistics in the higher p_{T} region is low. These measurements use b-tagging algorithms, which are similar to the algorithms described in Section 8.3.
Also theoretical calculations of the cross section improved. Actually, FONLL provides the best description of the $b\bar{b}$ production cross section. The FONLL calculation matches NLO calculations and resummations of log $\left(p_{\mathrm{T}}^{b}/m_{b}\right)^{i}$ contributions ([17] and Section 3.2).
After taking updated PDFs with a higher value of α_s as well as improved fragmentation functions, the results of data and theory agree within errors. The actual result

of the b-jet cross section measurement of CDF is shown in Fig.4.1.
At the LHC a new pp center-of-mass energy region will become accessible. The $b\bar{b}$ production cross section will be measured by ATLAS and CMS. A measurement of the inclusive b-jet cross section in the high $p_{\mathrm{T}} > 50\,\mathrm{GeV}$ region at CMS is foreseen [24]. In this inclusive measurement, b-tagged jets (based on secondary vertex reconstruction) with at least one muon matched to a b-jet, will be used.
In ATLAS cross section measurements are planned in the low as well as in the high p_{T} region. In the low p_{T} region two methods are studied.
A first measurement of the production cross section will use the exclusive decay channel $B^+ \to J/\Psi K^+$ [4]. The analysis will be performed by explicit reconstruction of the B^+-mass and a fit to the spectrum in order to estimate the number of signal events. The second method [25] studied at ATLAS enriches the b content by using the shape of the spectrum of the relative momentum of a muon w.r.t. the matched jet-axis p_{T}^{rel}. On average p_{T}^{rel} is larger for b-quark induced jets compared to other jets.
The preparation of a measurement of the inclusive b-jet cross section in a higher jet p_{T} region is the aim of this thesis.

4.3 Strategy of the differential p_{T} b-Jet Cross Section Measurement

The measurement of the b-jet cross section requires counting the number of b-jets N_{bJet} in an event sample to calculate the cross section $\sigma_{b\bar{b}}$ considering the integrated luminosity $\mathcal{L}$ of the data sample:

$$\sigma_{b-jet} = \frac{N_{bJet}}{\mathcal{L}}\,. \tag{4.1}$$

Since an inclusive b-jet cross section measurement is prepared, it is not necessary to reconstruct hadrons explicitly, which contain b-quarks. The decay products of the b-hadron form a jet in the detector, which is measured in the calorimeter and identified using b-tagging methods. Therefore, the inclusive b-jet cross section is measured by the number of b-jets in the event sample.
In the measurement process not all b-jets will be identified. At first events have to be triggered by the jet trigger. The efficiency ϵ_{Tr} to trigger a b-jet event is given by:

$$\epsilon_{Tr} = \frac{N_{Tr.bJet}}{N_{bJet}}\,, \tag{4.2}$$

where $N_{Tr.bJet}$ is the number of triggered b-jet events out of N_{bJet} events containing b-jets. In the reconstruction step some jets might not be or will be wrongly reconstructed. Only $N_{RecbJet}$ b-jets of the triggered b-jets are reconstructed, which leads to the reconstruction efficiency ϵ_{Rec}. Furthermore, reconstructed b-jets might miss a corresponding b-jet reconstructed taking Monte Carlo truth particles as input (truth b-jet). This is reflected in ϵ_{Ghost}, i.e. the probability to reconstruct a fake b-jet. The

purity of the reconstructed jet sample is then given by $P_{bJetRec} = 1 - \epsilon_{fakeJet}$. The following definitions are used throughout this thesis:

$$\epsilon_{Rec} = \frac{N_{Rec.bJet}}{N_{Tr.bJet}} \quad , \tag{4.3}$$

$$P_{Rec} = 1 - \epsilon_{Ghost} \quad = \frac{N_{Rec.bJet}}{N_{bAllRec}} \, . \tag{4.4}$$

The identification of the b-jets again leads to a loss of events or jets. The tagging efficiency ϵ_{Tag} is defined as the ratio of correctly identified b-jets $N_{btagged}$ and the number of b-jets $N_{bAllRec}$ in the event sample. On the other hand, background events will be misidentified. Therefore, the purity of the tagging reflects the fraction of correctly identified b-jets $N_{btagged}$ to the number of selected events N_{Sel} after the b-tagging procedure. The b-tagging efficiency and purity will be taken into account by:

$$\epsilon_{Tag} \quad = \frac{N_{btagged}}{N_{bAllRec}} \, , \tag{4.5}$$

$$P_{Tag} \quad = \frac{N_{btagged}}{N_{Sel}} \, . \tag{4.6}$$

In summary, the b-jet cross section will be measured by

$$\sigma_{b-jet} = \frac{P_{Rec} P_{Tag} N_{Sel}}{\epsilon_{Tr} \epsilon_{Rec} \epsilon_{Tag} \mathcal{L}} \, . \tag{4.7}$$

In order to measure a differential b-jet cross section $\frac{d\sigma_{b-jet}}{dp_{\mathrm{T}}}$, the p_{T} spectrum of the jets has to be divided into bins. The bin width of the individual bins in the spectrum depends on one hand on the expected event statistics as a function of p_{T} and on the other hand on the jet p_{T} resolution of the calorimeter. In order to correct for detector jet p_{T} resolution effects on the differential cross section, an unfolding algorithm has to be applied to the result. The unfolding algorithm, based on matrix inversion of the response matrix derived from the simulation of the detector effects on simulated b-jets, is described in Section 8.4.
The differential b-jet cross section will be measured in two scenarios. In the first, the cross section will be given in terms of the leading jet of an event, i.e. the hardest (b-)jet determines the p_{T} bin. The second type of measurement will consider all jets inside each event.

Chapter 5

Monte Carlo Event Sample

In order to prepare the analysis of experimental data taking with the ATLAS detector, Monte Carlo (MC) events are used to develop analysis strategies and reconstruction algorithms and to improve existing analyses. The general description of the generation and simulation of MC events is given in Section 5.1. Section 5.2 describes in detail the event samples, which are used to prepare the measurement of the b-jet cross section. All simulated events are generated in the official ATLAS MC data production, in which the simulation software packages configured for ATLAS are used. The simulation software packages as well as their configurations are validated by the ATLAS collaboration.

5.1 Simulation of Monte Carlo Events

Monte Carlo events play a key role in the development of reconstruction and analysis algorithms. Different event samples were produced to estimate the physics performance of ATLAS. The production of MC events is done in several steps, which are shown in Fig. 5.1. The first step is to generate events on parton level followed by fragmentation and hadronization of the partons. This first step is implemented by event generators. A commonly used event generator is Pythia [26], which is discussed in Section 5.1.1. The second step of the MC event production is the simulation of the interaction of the particles with the detector material (Section 5.1.2) followed by the digitization of the detector response (Section 5.1.3). Simulated and digitized events have the same data structure as real data taken directly with the ATLAS detector. The reconstruction of the simulated events is described in detail in Chapter 6.

5.1.1 Pythia Event Generator

The aim of the Pythia event generator is to simulate a pp-collision on parton level, followed by the fragmentation and hadronization of partons to hadrons and the decay of unstable hadrons, which do not reach the first detector layer. For the generation of events, Pythia version 6.415 inside the ATLAS software framework Athena [27] release 14.2.0.1 is used. At the point of time this study was started, a data taking

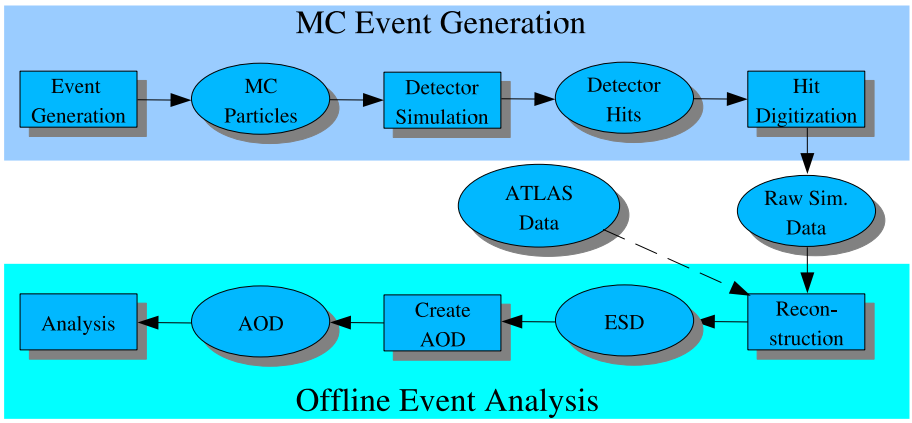

Figure 5.1: Different steps in Monte Carlo event simulation.

run at a center-of-mass energy of $\sqrt{s} = 10\,\text{TeV}$ was planned. Therefore, within this thesis this center-of-mass energy is assumed.

The event generation starts with the two incoming protons, each with a parton momentum distribution parametrized by a particle density function (PDF) (Eq. 3.6). The PDFs are the results of fits to experimental data. For the event generation the PDF set CTEQ6L1 in LHAPDF 5.3.0 [28] is used. The incoming partons of the protons may radiate other partons, like $g \to gg$ or $q \to qg$, and create the initial showers (initial state radiation, ISR). Then two partons enter the hard scattering process (HSP). The HSP determines the main characteristics of the generated event. For example, an increase of the transferred momentum in the HSP typically leads to jets with higher p_T in the final state of the event.

The properties of the HSP itself are determined by the short distance cross section described by Eq. (3.10). Pythia uses matrix elements calculated in leading order (LO) for the different processes.

After the determination of the properties of the HSP, possibly created resonances will decay. Also each of the partons may again radiate further partons, a process which is called final state radiation (FSR). In addition to the HSP, additional scattering processes in the event are expected. Since the cross section of scattering processes drops at higher p_T, several scattering processes with transferred momenta less than in the HSP can occur. These additional scattering processes form the underlying event, i.e. interactions between other constituents of the protons or ISR partons. All partons from the HSP, ISR, FSR and the underlying event form the final state of the parton event.

In QCD, interactions assuming the assumption of colored partons are valid at short distance. For long distances perturbative QCD becomes strongly interacting and will fail to describe the interaction. Therefore, color carrying partons have to be transformed into color neutral particles. The fragmentation and hadronization step cannot be calculated from first principles. Phenomenological models are employed for the event generation. In Pythia the Lund-string-model for fragmentation is the default choice. This model starts with the assumption of a linear potential between two colored particles. Once these two colored particles move away from each other,

the potential energy in the string between them increases by ~ 1 GeV/fm. Above some potential energy, the string may break due to the production of additional partons $q'\bar{q}'$. At the end, in the hadronization the partons are arranged in color neutral particles, the hadrons.

After hadronization of all partons, unstable hadron decays are simulated like e.g. B-meson decays. All particles, which will not decay further until they reach the detector, are passed to the detector simulation.

5.1.2 Detector Simulation using Geant4

Particles, which enter the detector, will interact with the detector material. The simulation is performed using Geant4 [29] accessed via Athena release 14.2.25.8 . Therefore, a map of the ATLAS detector material (passive and active material) and magnetic field is necessary. The ATLAS geometry tag ATLAS-GEO-02-01-00 is used for simulation. The field and material map includes also the simulation of misalignment in the detector and introduces a beam spot shift from $(0\text{ mm}, 0\text{ mm}, 0\text{ mm})$ to $(1.5\text{ mm}, 2.5\text{ mm}, -9\text{ mm})$.

All particles passed on by the event generator are tracked through the detector material in a tunable step width, which was set to 30 μm in the ATLAS event simulation.

Different physics processes are included and simulated for each particle. Particle decays are considered as well as secondary particle production from decays or interactions. For each particle also the energy loss due to e.g. bremsstrahlung, multiple interaction or scattering is calculated. Characteristics of the material like coefficients of the Bethe-Bloch formula are taken from the element or mixture of elements given by the material map.

For hadronic particles a list of processes is implemented. The cross section for each process is calculated. Interactions of the hadrons due to multiple scattering are estimated and resulting hadronic showers are simulated.

Every interacting particle causes an electronic signal in the sensitive material of the detector, simulated as energy deposition in the active volume. The signals have to be digitized to form a hit or an energy cluster in the detector.

5.1.3 Digitization

In this step of the event simulation, the Geant4 energy depositions, estimated in the detector simulation, are transformed into an output similar to the electronic signals recorded by the real ATLAS detector. Therefore, Geant4 energy depositions have to be transformed into a hit- or cluster-information of the corresponding sensitive detector component. At this point signal thresholds or electronic noise of the detector system have to be considered. The digitization step transforms the simulated information of the detector into an analog hit signal.

The digitization step uses the same Athena release as the detector simulation.

5.2 Simulation of QCD-Events

For the preparation of the b-jet cross section measurement, event samples of QCD events in different p_{T} regions are used. The events consist of the signal b-jets and other QCD jets. These other QCD jets are the main background for the cross section measurement and will be further called QCD jets, i.e. jets induced by gluons or quarks except b- or t-quarks. Both, signal and background events are included in the jet event samples.

ISUB	Subprocess
11	$q + q' \to q + q'$
12	$q + \bar{q} \to q' + \bar{q}'$
13	$q + \bar{q} \to g + g$
28	$q + g \to q + g$
53	$g + g \to q + \bar{q}$
68	$g + g \to g + g$

Table 5.1: List of processes used in the Pythia QCD event generation.

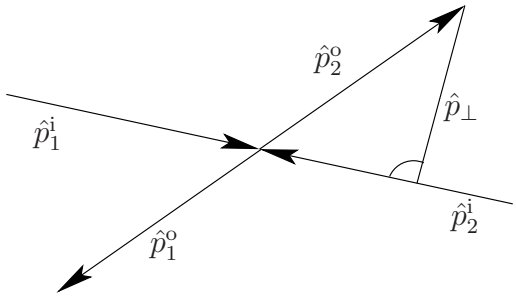

Figure 5.2: Definition of $\hat{p}_\perp$ in the rest frame of the two incoming particles with the momenta $\hat{p}_1^{\mathrm{i}}$ and $\hat{p}_2^{\mathrm{i}}$.

The event generator Pythia uses LO matrix elements in the calculation of the HSP. Thus only the LO Feynman diagrams (see Section 3.2) are included. A list of possible processes in the HSP is given in Tab. 5.1, where q denotes any quark flavor (except top), g gluons and ISUB is the number of the subprocess in the Pythia numbering scheme.
The NLO contributions from gluon splitting (GS) and flavor excitation (FEX) (Section 3.2) are not considered directly, but are simulated by Pythia in the parton showering algorithm after the HSP. For example, GS will be simulated by subprocess 68 followed by one of the outgoing gluons splitting into a $b\bar{b}$ pair.
In order to generate a sufficient number of events also in the higher p_{T} region, the samples are split into sub-samples with different settings for the momenta transferred in the HSP. The momentum transferred in the HSP is steered in Pythia by the options *ckin* 3 and *ckin* 4, which are the lower and upper values of $\hat{p}_\perp$. $\hat{p}_\perp$ is defined in the restframe of the HSP as the momentum transferred perpendicular to the momentum direction of the two incoming partons (Fig. 5.2). The choice of *ckin* 3 and *ckin* 4 determines the phase space available for the event generation and therefore influences the effective cross section, which is calculated by Pythia.
In total, seven QCD sub-samples with different *ckin* 3 and *ckin* 4 settings are chosen. All event samples are produced in the MC08 ATLAS event production. Tab. 5.2 lists the different QCD event samples used throughout this thesis, including the settings of *ckin* 3 as lower and *ckin* 4 as upper limit on $\hat{p}_\perp$. The lower and upper cut on $\hat{p}_\perp$ ensure, that the generated event sub-samples are disjunct w.r.t. the phase space. In the last column the resulting cross section σ_{QCD} as estimated by Pythia, for each event sub-sample is given. Errors on σ_{QCD} represents the statistical uncertainty on the cross section only.

Name	number of events ($\times 10^3$)	$ckin\ 3 - ckin\ 4$ [GeV]	σ_{QCD} $[pb]$
J1	850	17 - 35	$(867 +/- 2)\times 10^6$
J2	500	35 - 70	$(56.04 +/- 0.07)\times 10^6$
J3	500	70 - 140	$(3.273 +/- 0.004)\times 10^6$
J4	400	140 - 280	$(151.2 +/- 0.2)\times 10^3$
J5	400	280 - 560	$(5.150 +/- 0.006)\times 10^3$
J6	200	560 - 1120	$112.1 +/- 0.1$
J7	200	1120 - 2240	$1.073 +/- 0.001$

Table 5.2: QCD event samples used throughout this thesis.

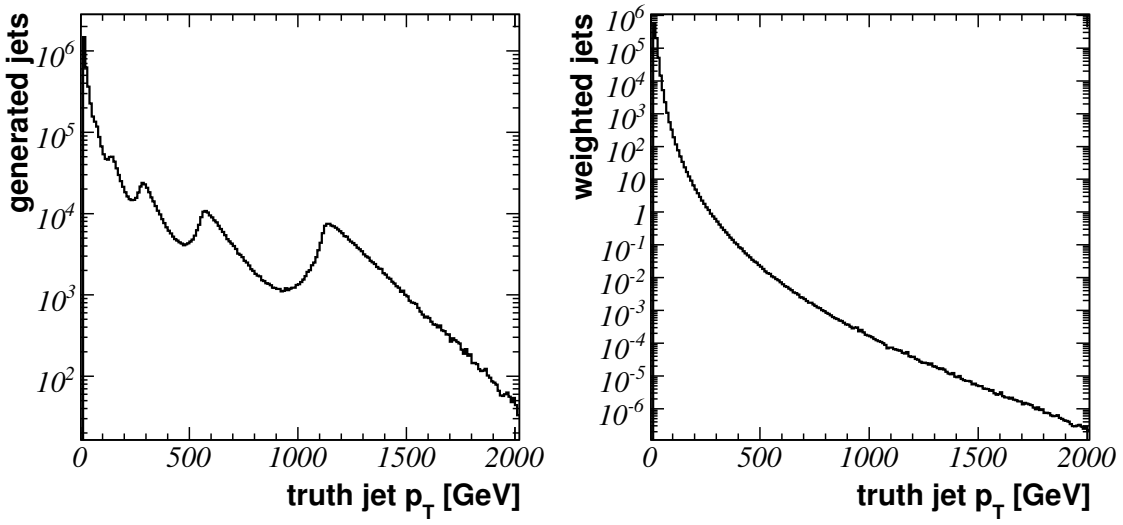

(a) (b)

Figure 5.3: Cone4 jet p_{T} spectrum of (a) generated events and (b) events weighted with respect to the calculated QCD cross sections of the sub-samples.

5.2.1 Weighting of Simulated Events

Due to different event statistics in the different p_{T} regions, the events have to be weighted to reflect the p_{T} dependence of the cross section of QCD jet events. The generated jet p_{T} spectrum is shown in Fig. 5.3(a). Therefore all jets of the events, using a narrow cone size of $\Delta R_{cone} = 0.4$ for jet reconstruction (Section 6.1), are considered. The different $\hat{p}_{\perp}$ ranges of the sub-samples cause the steps observed in the p_{T} spectrum. Because of the setting of $\hat{p}_{\perp}$ on the parton level, the steps are smeared for the jet p_{T} spectrum in the ATLAS laboratory system and no hard cut is visible.

The events of each event sub-sample are weighted differently. The first event sub-sample is the reference sample and is assigned the event weight $\omega_{J1} = 1$. The event weight of an event of sub-sample i depends on the number of events j in this sub-sample and the number of events k in the reference sub-sample weighted by the cross sections:

$$\omega_{Ji} = \frac{k_{J1}\sigma_{Ji}}{j_{Ji}\sigma_{J1}} \,. \tag{5.1}$$

Sub-sample	event weight ω_i
J1	1
J2	0.1094 +/− 0.0003
J3	0.006395 +/− 0.000017
J4	$(37.14 +/- 0.10)\times10^{-5}$
J5	$(12.59 +/- 0.03)\times10^{-6}$
J6	$(54.90 +/- 0.14)\times10^{-8}$
J7	$(52.49 +/- 0.13)\times10^{-10}$

Table 5.3: Weights of different sub-samples, which reflect the p_{T} cross section of QCD events.

The weight ω_i assigned to each event in sub-sample i is given in Tab. 5.3. The jet p_{T} spectrum of all jets taking the weights into account is shown in Fig. 5.3(b). The spectrum exhibits the expected behavior of the fast and continuous drop with increasing p_{T}.

5.2.2 Labeling of (Leading) b-Jets

On parton level the b-quark is the initiator of a b-jet. The definition to label a jet as a b-jet is based on geometrical matching of the flight direction of a b-quark to the jet axis of truth and reconstructed jets, respectively.
For the inclusive $b\bar{b}$ jet cross section measurement jets have to fulfill the following cuts

- $p_{Tjet} > 10$ GeV ,
- $|\eta_{jet}| < 2.5$

in order to be considered in the analysis. In case of a b-quark with $p_{Tb-quark} > 5$ GeV in the generated event, it is attempted to match this b-quark to a truth and a reconstructed jet. If $\Delta R < 0.3$, with ΔR being the opening angle between the jet axis and the flight direction of the b-quark, the jet is labeled a b-jet. In case of more than one matched jet, the jet with the smallest ΔR is labeled a b-jet initiated by this b-quark. If a jet cannot be matched to a b-quark, this jet is labeled a background jet and called QCD jet in the further analysis.
For the leading jet analysis (Section 4.3) an additional step is necessary. Fig. 5.4 shows the flowchart for finding the leading b-jet in an event. First a quark-to-jet matching is done as described above. The leading b-jet is then defined as the truth jet with the hardest p_{T}. If another truth b-jet is found in the same p_{T} bin, the leading truth b-jet will be the hardest jet according to the reconstructed jet p_{T} value. The assignment of a truth and a reconstructed jet is also based of a geometrical matching by the opening angle $\Delta R < 0.2$ of the two jet axes (see Section 6.1).

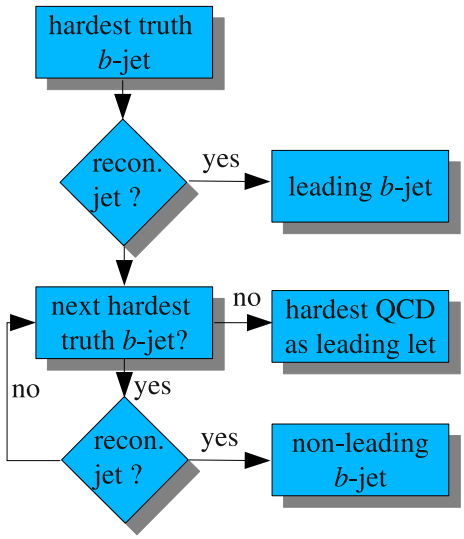

Figure 5.4: Algorithm for labeling the hardest p_{T} jet as leading jet.

In case the leading truth b-jet is not matched to a reconstructed jet the labeling algorithm will take another truth b-jet from the same p_{T} bin, if available. Otherwise other truth b-jets will be investigated in decreasing p_{T} order and tried to be matched to a reconstructed jet. If there is a truth b-jet with a matched reconstructed jet inside the event, this b-jet is taken as the hardest p_{T} b-jet, but labeled as non-leading b-jet, which will be considered in the efficiency and purity determination of the reconstruction of the selected jets used for the cross section measurement.
In case of b-quarks without a matched reconstructed jet in the event, the hardest QCD-jet is taken as leading jet, but labeled fake-leading jet. This fake-leading jet will also be considered in the efficiency and purity determination of the jet reconstruction.

5.2.3 b-Jet Cross Section and QCD-Jet Background

After the weighting of events w.r.t. to the QCD sub-sample‘s cross section and the labeling procedure of b-jets are applied, the differential MC cross section $\frac{d\sigma_{b-jet}}{dp_{\mathrm{T}}}$ of b-jets is derived. In dependence of the binning in p_{T} a differential cross section of b-jets and QCD background jets versus p_{T} can be estimated. In Fig. 5.5 and Appendix A the differential cross section for all jets of the events is given in the region of 30 GeV $< p_{Tjet} <$ 1130 GeV for both the b-jets and the QCD background jets. The differential cross section is provided for jets using a narrow cone size of $\Delta R_{cone} = 0.4$ (cone4 jets) and a wide cone size of $\Delta R_{cone} = 0.7$ (cone7 jets) (Section 6.1).
The horizontal error bars indicate the bin width, whilst the vertical error bars on the cross section reflect the statistical uncertainty due to limited MC event statistics. The number of entries per p_{T} bin is normalized to the number of entries per 20 GeV. The cross section drops by $\approx$ 10 orders of magnitude over the range from $p_{\mathrm{T}} =$ 30 GeV to approximately $p_{\mathrm{T}} =$ 1130 GeV. Therefore the number of expected events will decrease by the same order. This leads to increased statistical uncertainties for

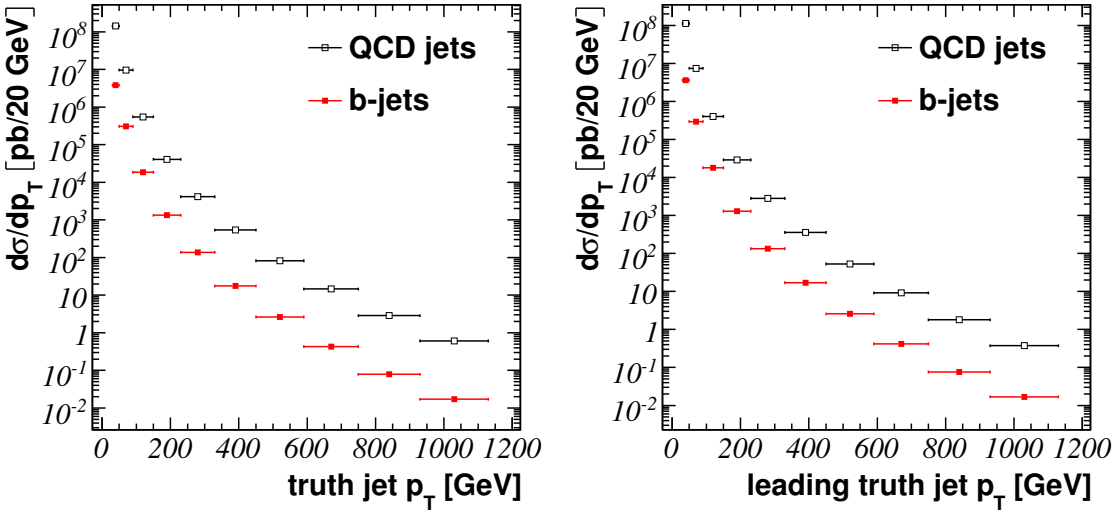

(a) (b)

Figure 5.5: Differential p_{T} cross sections for (a) all cone4 jets and (b) leading cone4 jets on truth level in the region of 30 GeV $< p_{\mathrm{T}_{jet}} <$ 1130 GeV.

jets with higher p_{T}. As expected, the QCD background is larger by a factor of about 30 (lower p_{T} region) to 20 (higher p_{T} region) compared to the cross section of b-jets. b-tagging algorithms will be used to reduce the background keeping the b-jet signal. The differential cross sections of cone7 jets are larger compared to the differential cross sections of cone4 jets. The larger cone size of cone7 jets leads to a shift in the differential jet spectrum compared to the differential cone4 jet spectrum, since on average more particles are considered in the larger cone size of the cone7 jets.
The cross section in the case of the leading b-jet scenario is lower compared to the cross section in the case considering all b-jets inside the event. This reduction of the cross section is due to the fact, that for the leading jet analysis at most one b-jet per event is considered. For the b-jet signal, the difference of the jet and the leading jet cross section spectrum is decreasing towards higher p_{T}. This reflects the probability that a $b\bar{b}$ pair results in two or more high p_{T} jets. In case of e.g. FEX often only one b-quark is scattered into the detector while the other b-quark is collinear to the beamline and hence lost for the measurement. In case of GS the decay angle of the two b-quarks in the laboratory system is very small, so that these b-quarks initiate a single jet in the detector only. This leads to smaller differences of the leading b-jet and the b-jet production cross sections.
In comparison to the signal cross section, the difference in the QCD background cross section decreases with increasing p_{T}. In most of the events, the simulation of the HSP by a $2 \rightarrow 2$ process in Pythia results in two jets in the detector. In the lower p_{T} part of the spectrum, the transferred momentum is smaller, which leads to jets which cannot be measured due to the detector acceptance.

Chapter 6

Offline Reconstruction of Event Data

With the ATLAS detector hits and clusters of particles of an event in the various sub-detector systems are measured. Triggered events are written to a data storage system. Then the events will be reconstructed, i.e. the measured information will be transformed into objects relevant for physics analysis. Pattern recognition algorithms are implemented in the ATLAS software framework Athena. These algorithms combine different detector information to obtain objects, which are interpreted e.g. as tracks traversing the detector or energy depositions caused by a particle jet.

For the b-jet cross section measurement different reconstructed physics analysis objects are needed. The reconstruction algorithms of the analysis objects used throughout this thesis as well as their performances are presented in this chapter.

The most relevant objects for the differential b-jet cross section measurement are jets. Within this analysis, jets reconstructed by a cone based algorithm are used. The cone based algorithm as well as the performance of the jet reconstruction are discussed in Section 6.1. In order to distinguish between jets initiated by a b-quark and jets initiated by other QCD processes (QCD jets), tracks are used to search for long living particles within these jets. Precise and effective track reconstruction algorithms are necessary to reconstruct tracks even in the dense environment of jets consisting of many particles. The track finding is presented in Section 6.2. In Section 6.3 the algorithm to reconstruct the primary interaction point of the two colliding protons (primary vertex) is discussed. The knowledge about the primary vertex will improve the ability to identify b-jets.

6.1 Jet Reconstruction

Partons from the hard scattering process (HSP) will initiate jets in the detector. After fragmentation and showering, particles will first form a particle jet in the Inner Detector and then a calorimeter jet by depositing energy in different calorimeter sections.

A jet finding algorithm has to fulfill several experimental and theoretical requirements [4].
From the theoretical point of view, the jet finding should be

- infrared safe: Additional soft particles not originating from the fragmentation of the hard scattered partons should not affect the number of reconstructed jets. The same holds for the absence of such soft particles.
- collinear safe: The result should be the same whether the transverse momentum is carried by one particle or whether this particle splits into different particles.
- order independent: The jet reconstruction algorithm should find the same jets at parton-, particle- and detector-level.

The experimental required attributes of a jet algorithm are

- detector technology independence: The performance of the algorithm should not strongly depend on the design of the detector, which provides the data. Therefore, detector specific signal event characteristics must be corrected for as much as possible.
- environment independence: Jets interesting for physics have to be efficiently reconstructed independently of the instantaneous luminosity, multiple interactions and underlying event activities.
- full and fast implementation: The jet algorithm must be fully specified (configuration e.g. selection cuts) and should be efficient to minimize the required computing time and memory consumption.

Within the ATLAS data reconstruction two different measured calorimeter information are used as seeds for the jet reconstruction: Calorimeter towers and topological calorimeter clusters. The calorimeter towers are cell projections onto a regular $\Delta\eta \times \Delta\phi = 0.1 \times 0.1$ grid covering the whole detector region of ATLAS. The energies of the cells within the tower are summed. Reconstructed jets seeded by calorimeter towers are used within this thesis.
The topological cell clusters are three dimensional energy depositions in the calorimeters. A calorimeter cell forms a seed cell for a cell cluster in case of an energy deposition above a certain threshold. Neighboring cells above a certain secondary signal threshold are added to the calorimeter cluster. After adding the energies of all relevant cells to the cluster, the cluster is investigated for possible local maxima and split into two jet seeds if more than one local maximum is found.
The cell clusters or the calorimeter towers from a calorimeter jet are used as input seeds for the jet finding algorithms. In ATLAS cone based as well as sequential recombination algorithms are implemented for the jet reconstruction.
The standard seeded cone based algorithm takes a p_{T} ordered list of calorimeter objects (calorimeter towers or cell clusters) as input. If the highest p_{T} object exceeds

the threshold of $p_{\mathrm{T}} > 1$ GeV, this object is taken as a seed. Calorimeter objects within a cone of ΔR_{cone} are added to the seed and a new four momentum vector for the sum of the objects is calculated. Every contribution is weighted by the p_{T} of the object. After that, objects within the ΔR_{cone} are iteratively summed until the direction of the cone is considered stable. The resulting four momentum of the cone forms a jet. Different cone sizes are preferred for different physics measurements. In order to measure the full parton kinematics including small angle gluon radiations in inclusive cross section measurements, wider cone sizes are preferred. For measurements of events with busy final states narrow cone sizes are taken. In the ATLAS standard reconstruction a narrow cone size of $\Delta R_{cone} = 0.4$ (cone4 jets) and a wide cone size of $\Delta R_{cone} = 0.7$ (cone7 jets) are available.

The cone algorithm is not infrared safe. In order to increase the infrared stability, a split-and-merge algorithm is added to the jet finding algorithm. Overlapping jets, which share more than a certain splitting fraction f_s of p_T constituents are merged into one jet. Otherwise they are split into two jets. The fraction f_s is set to $f_s = 0.5$ in the standard ATLAS reconstruction.

The reconstructed jet energy is on average smaller than the energy of the truth jet. The truth jet information is estimated by applying the jet reconstruction algorithm to generated MC particles (except neutrinos and muons). The difference in energy is mainly due to the calorimeter response depending on the particle type (larger energy deposition for electrons or photons in comparison to hadrons), dead material in the calorimeter or low p_{T} particles leaving the cone due to the magnetic field. In order to correct for these effects, the calorimeter response has to be calibrated. In the ATLAS reconstruction a calibration method based on the approach developed in the CDHS [30] and later used in the H1 experiment [31] is applied.

The aim of the calibration is to minimize the differences in the jet four momentum of the reconstructed jet compared to the corresponding truth jet. The characteristic of the electromagnetic component of a jet is a larger energy density in the calorimeter compared to the energy density of the hadronic component. Therefore, all cells or towers, which contribute to the jet, are assigned a weighting function. The weighting function w_i of a calorimeter cell i depends on the energy density $\rho_i = E_i/V_i$, i.e. the measured energy E_i divided by the cell volume V_i, and the cell location $\vec{X}_i$. The calibrated four momentum $(E_{jet}, \vec{p}_{jet})$ of the jet is then calculated by

$$(E_{jet}, \vec{p}_{jet}) = \left(\sum_i^{N_{Cell}} w(\rho_i, \vec{X}_i) E_i, \sum_i^{N_{Cell}} w(\rho_i, \vec{X}_i) \vec{p}_i \right) . \tag{6.1}$$

The weighting functions are estimated from fully simulated QCD events by fits of the reconstructed jet energy to the MC truth level jet energy.

The result of the jet reconstruction and calibration is given as the jet axis direction in pseudorapidity η_{jet} and azimuth ϕ_{jet} as well as the four-momentum, assuming a massless particle:

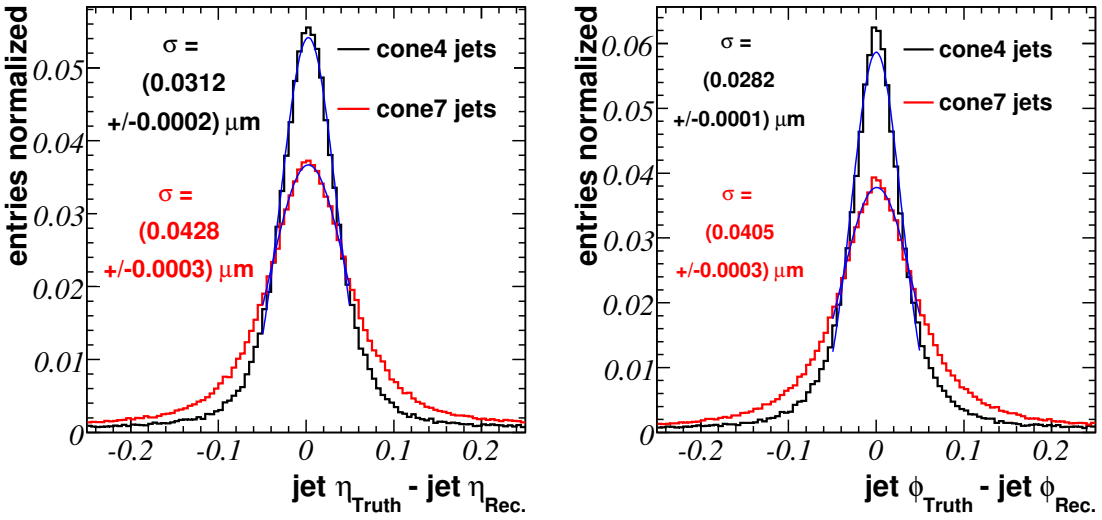

(a) (b)

Figure 6.1: Residual distribution of (a) η_{jet} and (b) ϕ_{jet} for cone4 and cone7 jets of nearest reconstructed and truth jet pairs.

$$\begin{aligned} E_{jet} &= |\vec{p}_{jet}| = \sqrt{p_x^2 + p_y^2 + p_z^2}\,, \\ p_x &= p\frac{\cos\phi}{\cosh\eta}\,, \\ p_y &= p\frac{\sin\phi}{\cosh\eta}\,, \\ p_z &= p\tanh\eta\,. \end{aligned} \tag{6.2}$$

In order to estimate the performance of reconstructing the kinematic jet variables as well as the jet p_{T} after calibration, the reconstructed jets are compared to the truth jets. Every reconstructed jet is assigned to the nearest truth jet, i.e. the one with the smallest opening angle ΔR between the reconstructed jet axis and the truth jet axis. Fig. 6.1(a) and 6.1(b) present the distributions of the kinematic jet variables $\Delta\eta = \eta_{truth\,jet} - \eta_{rec\,jet}$ and $\Delta\phi = \phi_{truth\,jet} - \phi_{rec\,jet}$ (residual distribution) of the reconstructed and truth jet pairs for cone4 and cone7 jets.
The distributions are symmetric around zero and wider in case of cone7 jets due to the larger cone size. The resolution of the jet reconstruction on η_{jet} or ϕ_{jet} is estimated by the width of a Gaussian distribution fitted to the residual distribution. The fit range is chosen from -0.05 to 0.05 in $\Delta\eta$ and $\Delta\phi$. In Fig. 6.2(a) and 6.2(b) the resolutions in η_{jet} and ϕ_{jet} as a function of the truth jet p_{T} are presented. The slightly worse resolution in the jet η_{jet} reconstruction at larger truth jet p_{T} is due to the binning in truth jet p_{T} and is not seen if the spectrum is plotted versus the truth jet energy.
The resolution of the jet direction reconstruction improves with larger jet p_{T}. Since the resolution is in the same order for both variables, η and ϕ, a cut on the opening angle ΔR is applied in order to match reconstructed and truth jets. The distribution

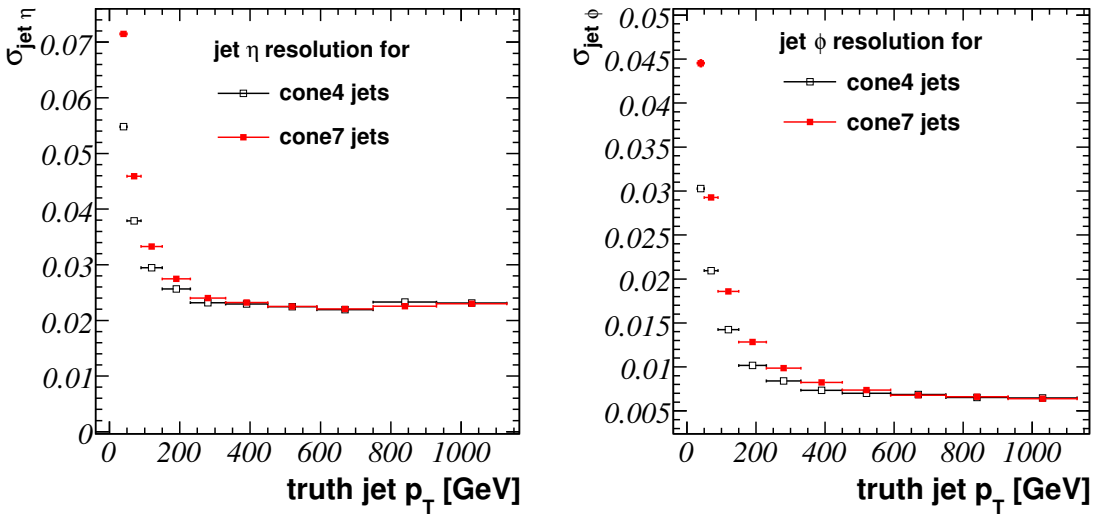

(a) (b)

Figure 6.2: Jet reconstruction resolution in (a) η_{jet} and (b) ϕ_{jet} for cone4 and cone7 jets as a function of the truth jet p_{T}.

of the opening angle ΔR between truth and reconstructed jet pairs is shown in Fig. 6.3 (a). Fig. 6.3 (b) shows the mean values of the ΔR distributions in the different jet p_{T} bins. The upper and the lower line give the square root of the squared mean residual (RMS) deviation for each jet p_{T} bin ΔR distribution.
The mean of the opening angle distribution is $\Delta R < 0.1$ over the jet p_{T} range considered. A truth jet is matched to a reconstructed jet in case the opening angle is $\Delta R < 0.2$. After applying this matching cut, the performance of the jet reconstruction is derived. The efficiency ϵ_{JetRec} of the jet reconstruction is the fraction of truth jets with a matched reconstructed jet $N_{rec\,truth\,jet}$ divided by the number of truth jets $N_{truth\,jet}$. The portion of reconstructed jets without a matched truth jet (fake jet) $N_{fake\,jet}$ is reflected in the purity P_{JetRec} of the jet reconstruction:

$$\epsilon_{JetRec} = \frac{N_{rec\,truth\,jet}}{N_{truth\,jet}} \quad , \tag{6.3}$$

$$P_{JetRec} = 1 - \epsilon_{fake} = \frac{N_{Rec} - N_{fake\,jet}}{N_{Rec}} \, . \tag{6.4}$$

The efficiency and the purity of cone4 and cone7 jets as a function of the truth jet p_{T} are shown in Fig. 6.4.
Both purity and efficiency increase as a function of the (truth) jet p_{T} and is about $\approx 95\%$ at (truth) jet $p_{\mathrm{T}} = 90\,\mathrm{GeV}$. The efficiency as well as the purity reaches a plateau of $> 98\%$ at a (truth) jet $p_{\mathrm{T}} > 230\,\mathrm{GeV}$ for both chosen cone sizes. The lower efficiency of the cone7 jet algorithm compared to the cone4 jet algorithm is due to the differences in the resolutions of the kinematic variables of the jet axis. This leads to the broader ΔR distribution (Fig. 6.3 (b)) of the reconstructed-to-truth jet matching mainly in the lower jet p_{T} region and therefore to a lower efficiency and purity for the cone7 jet algorithm, as a consequence of the $\Delta R < 0.2$ cut. Due the

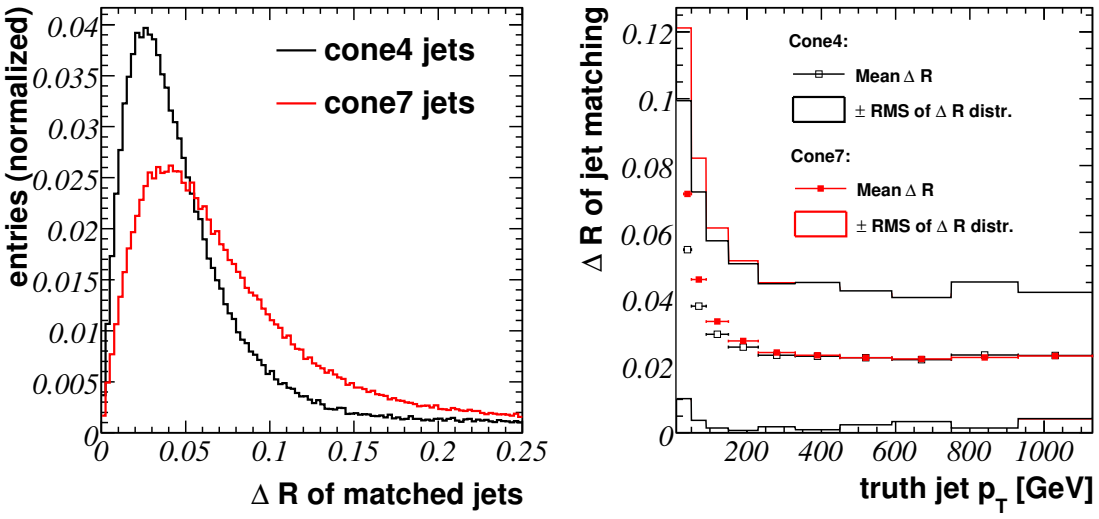

(a) (b)

Figure 6.3: (a) Distribution of the opening angle ΔR of truth and reconstructed jet pairs. (b) Mean value of the ΔR distributions as a function of the truth jet p_{T}. The area between the lower and upper line represents the ±RMS of the mean value.

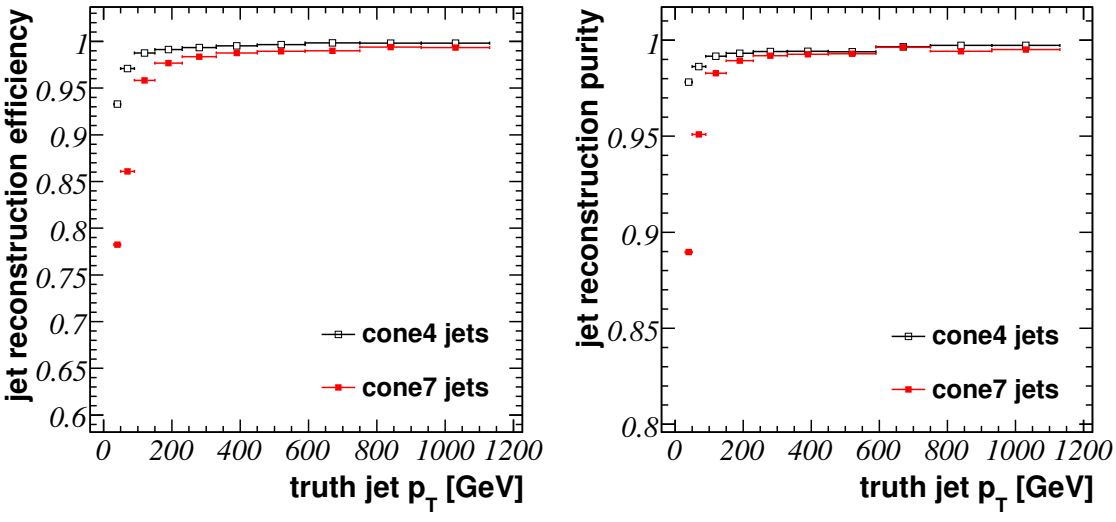

(a) (b)

Figure 6.4: (a) Efficiency and (b) purity of the jet reconstruction for cone4 and cone7 jets.

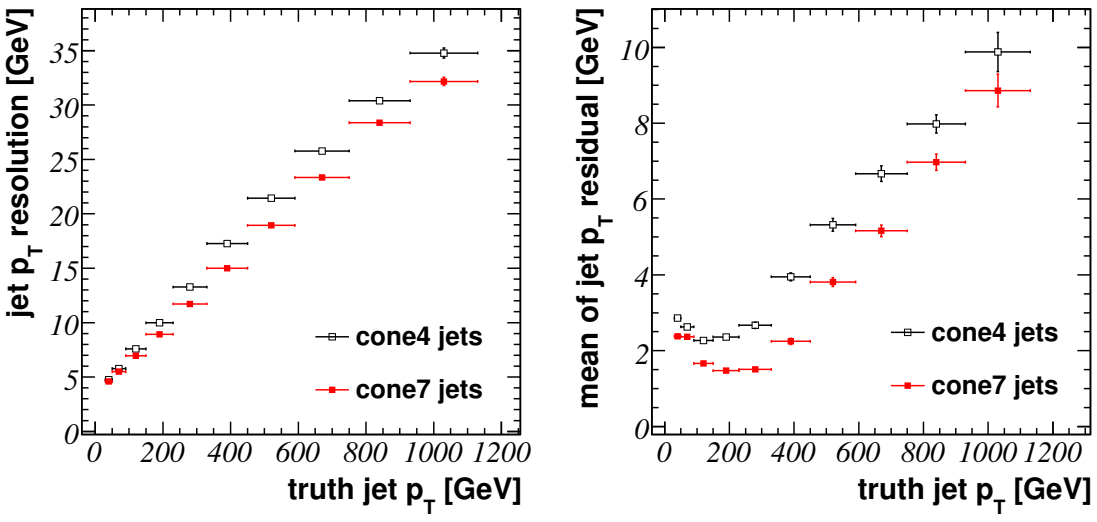

(a) (b)

Figure 6.5: (a) Jet p_{T} reconstruction resolutions $\sigma_{p_{\mathrm{T}}}$ and (b) mean values $\mu_{p_{\mathrm{T}}}$ of the residual distributions for cone4 and cone7 jets for the different jet p_{T} bins.

high efficiency and purity of the jet reconstruction, the loss of jets in the b-jet cross section measurement as well as the background contribution due to fake jets, are expected to be small.

The resolution of the jet p_{T} is important for the differential jet p_{T} cross section measurement. The resolution of the jet p_{T} reconstruction is determined explicitly in each jet p_{T} bin as the width $\sigma_{p_{\mathrm{T}}}$ of a Gaussian distribution fitted to the residual distribution of the truth jet p_{T} minus the matched reconstructed jet p_{T}. A fit range of $\pm 80\,\mathrm{GeV}$ is taken in each jet p_{T} bin. The resolution widths $\sigma_{p_{\mathrm{T}}}$ and the mean values $\mu_{p_{\mathrm{T}}}$ of the Gaussian distribution fits as a function of the truth jet p_{T} are shown in Fig. 6.5(a) and (b), respectively. Since the calorimeter energy resolution is proportional to the energy of the jet (Tab. 2.1), it is expected, that the jet p_{T} resolution also becomes worse with increasing jet p_{T}. Therefore, the jet p_{T} bin width is broadened towards higher jet p_{T} to take both the decreasing event number due to the falling cross section and the calorimeter resolution into account. The bin width is about a factor of 2-5 larger than the resolution width $\sigma_{p_{\mathrm{T}}}$, which suppresses large bin-to-bin migrations in the measured jet p_{T} spectrum. The mean values $\mu_{p_{\mathrm{T}}}$ of the jet p_{T} residual distributions move to larger positive values with larger truth jet p_{T}, i.e. the reconstructed jet p_{T} is on average about 1% lower than the truth jet p_{T}. This shift is caused by the jet calibration of the calorimeter and will be corrected for by the unfolding algorithm.

6.2 Track Reconstruction

Particles traversing the different parts of the Inner Detector deposit energy in the detector elements. These energy deposits are recorded as hits. The track reconstruction algorithms combine different hits to estimate particle trajectories, called

tracks.
For the b-jet cross section measurement tracks reconstructed by the ATLAS algorithm New Tracking [32] are taken. The ATLAS New Tracking uses the hit information of the Pixel Detector, the SCT as well as the TRT. It starts with a global search for seeds followed by a local search for additional hits, which are matched to track candidates.
Two different approaches are used to find a seed for a track and furthermore a track candidate. Firstly an inside-out and secondly an outside-in strategy for track finding will be described.

Inside-Out Track Reconstruction

The inside-out strategy starts with a seed finding using the precision hits in the Pixel Detector. Two seed finding algorithms are available. The seed search with z vertex constraint combines pairs of space points, constructed from measured hit information of the Pixel Detector, and extrapolates the direction in the primary interaction region keeping a given momentum and transverse impact range. From these pairs z vertices are built and filled into a histogram. A fast primary vertex search is performed. This vertex constrains the seeds with three or more space points.
The unconstrained seed search combines three space point objects within a given momentum and transverse impact range. This approach results in a larger number of seeds and a more time consuming track finding. However, it is more efficient in finding tracks in events with loosely constraint primary vertices.
The seeds contain the directional information of a possible track candidate, such that a road through the detector layers is defined. Along this road, further hits are searched for and, if certain requirements are fulfilled, added to the seed. A KalmanFilter algorithm [33] is used to update the track fit after each layer step and to predict the position of an expected hit in the next detector layer. After all layers are passed, the seed forms a track candidate.
The seeded track finding ends with a high multiplicity of track candidates, which include still a lot of fake tracks. In order to reduce the number of fake tracks, track candidates are ranked due to their likelihood (track score) to describe real trajectories of particles traversing the detector. The track score is calculated for each track candidate considering quality criteria. The fit quality, the number of hits on the track as well as the number of missing hits in detector layers are taken into account with different weights according to the type of the (missing) hit. In case of hits shared between two or more track candidates, the hit is assigned to the track candidate with the higher track score. Track candidates with a quality less than a given quality cut, are rejected and not considered in further track reconstruction.
All remaining tracks (silicon tracks) are extrapolated into the Transition Radiation Tracker (TRT) and form a road in the TRT. Track extensions for the different silicon tracks are searched for by performing a line fit to hits in the road using the r-ϕ hit coordinates in order to estimate, whether a TRT hit is compatible with a silicon track extrapolation. This results in an extended track. After a refit of the

combined track (silicon track and the extended track), the track quality ranking of the combined track is compared to the quality of the initial silicon track. In case of a worse track ranking of the combined track compared to the initial silicon track (e.g. Pixel Detector hits may be labeled as outlier hits after the refit), the initial silicon track is kept while the TRT hits are labeled as outlier measurements w.r.t. this track.

Outside-In Track Reconstruction

The outside-in track reconstruction strategy is seeded by TRT track segments. It is more efficient in case of secondary particles coming from conversions or for decays of long lived particles.
TRT segment finding starts with the projections of the TRT hits in the r-ϕ-plane (r-z plane in the end-cap region). In this projection, track segments from tracks originating roughly from the primary interaction region, appear as almost straight lines. In order to find these straight lines, the projection plane r-ϕ is transformed into the parameter space of straight lines, like the initial azimuthal angle ϕ_0 and the inverse momentum c_T (Hough transform [34]). Hit points associated to the same line in the r-ϕ plane will be transformed into the same cell (two-dimensional histogram) in the line parameter plane, since they satisfy the same line parametrization. The TRT track segment finding is reduced to a local maximum finding in the two-dimensional histogram. The final TRT track segments are extrapolated into the silicon detectors.

The resulting tracks of both, the inside-out and the outside-in reconstruction strategy, are parametrized as a helix with five parameters ϕ, θ, d_0, z_0, $\frac{q}{p}$ (perigee parametrization [35]):

- d_0: impact parameter in the transverse plane,
- z_0: impact parameter in the longitudinal direction (z coordinate of the track),
- ϕ: azimuthal angle,
- θ: polar angle,
- $\frac{q}{p}$: charge divided by the momentum of the track.

The parameters are defined at the point of closest approach to the nominal interaction point.
For track reconstruction performance studies a MC particle track is matched to a reconstructed track if 80% of its hits are created by the MC particle.
In Fig. 6.6 the resolutions of the transverse impact parameter d_0 and the longitudinal impact parameter $z_0 \times \sin\theta$ as a function of η are shown. The resolution depends on the p_{T} and the η direction of the track. While the resolution improves with larger p_{T}, it worsens with larger η.
For the tracking performance study presented here, isolated pions are taken [4]. The resolution is determined by the RMS of the residual distribution.

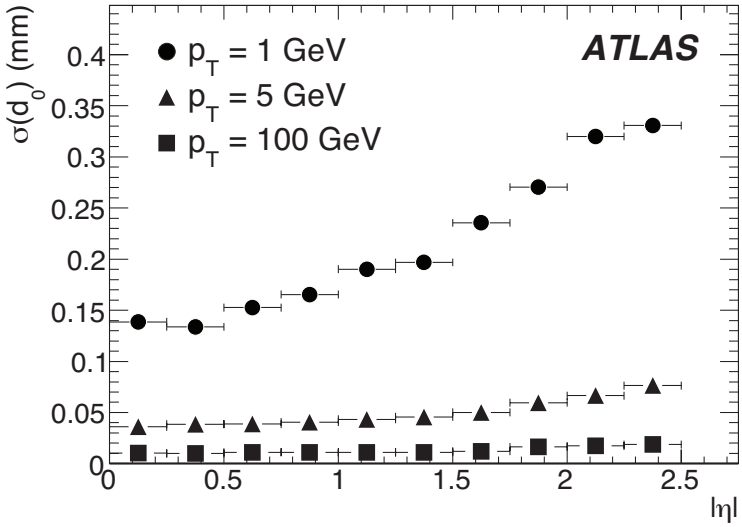

(a)

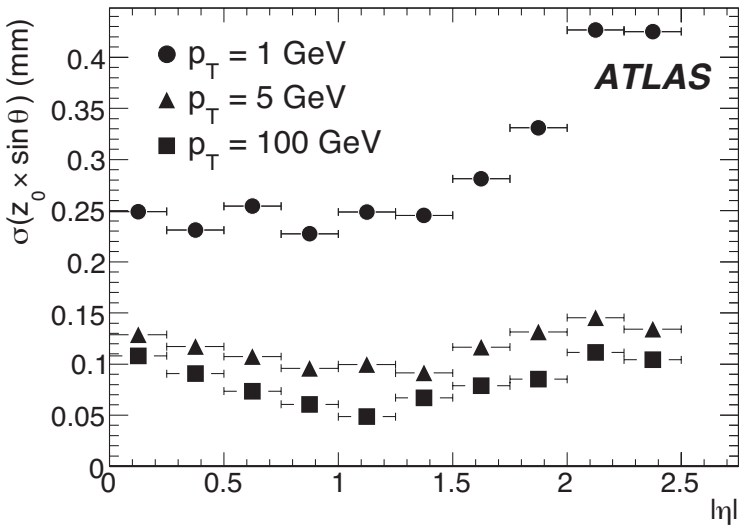

(b)

Figure 6.6: Expected resolution of the reconstruction of the (a) transverse impact parameter d_0 and (b) the longitudinal impact parameter $z_0 \times \sin\theta$ of tracks for different p_{T} and η regions. For this study isolated pions are taken [4].

The resolution of track parameter X_i as function of p_{T} is parametrized by

$$\sigma_{X_i}(p_{\mathrm{T}}) = \sigma_{X_i}(\infty)(1 \oplus p_{X_i}/p_{\mathrm{T}})\,. \tag{6.5}$$

For track parameter i, $\sigma_{X_i}(\infty)$ is the expected asymptotic resolution at infinite momentum and p_{X_i} is a constant p_{T} value, at which the intrinsic detector resolution is equal to the resolution due to multiple scattering. In Tab. 6.1 the expected momentum (direction) resolution (ϕ, $\cot\theta$, $\frac{q}{p}$) for isolated muons and the impact parameter resolutions for d_0 and z_0 for isolated pions are listed.

track parameter	$0.25 < \lvert\eta\rvert < 0.50$		$1.5 < \lvert\eta\rvert < 1.75$	
	$\sigma_X(\infty)$	p_X(GeV)	$\sigma_X(\infty)$	p_X(GeV)
inverse transverse momentum (q/p_{T})	$0.34\,\mathrm{TeV}^{-1}$	44	$0.41\,\mathrm{TeV}^{-1}$	80
azimuthal angle ϕ	$70\,\mu$rad	39	$92\,\mu$rad	49
polar angle ($\cot\theta$)	0.7×10^{-3}	5.0	1.2×10^{-3}	10.0
transverse IP (d_0)	$10\,\mu$m	14	$12\,\mu$m	20
longitudinal IP ($z_0 \times \sin\theta$)	$91\,\mu$m	2.3	$71\,\mu$m	3.7

Table 6.1: Expected track parameter resolution in two η regions. Isolated muons are taken for the angular and momentum resolutions as well as isolated pions for the estimation of impact parameter resolution [4].

Different quality cuts are applied on the reconstructed tracks in order to reduce the number of fake tracks while keeping the efficiency as high as possible. Only tracks with $p_{\mathrm{T}} > 1\,\mathrm{GeV}$ and $|\eta| < 2.5$ are considered for performance studies. In addition, reconstructed tracks have to have seven precision hits (pixel and SCT). A cut on the impact parameter of $d_0 < 2\,\mathrm{mm}$ and $|z_0 - z_v| \times \sin\theta < 10\,\mathrm{mm}$ is applied. In order to tune the track selection w.r.t. b-tagging, a second, more strict set of cuts is applied. The impact parameter cuts change to $d_0 < 1\,\mathrm{mm}$ and $|z_0 - z_v| \times \sin\theta < 1.5\,\mathrm{mm}$ and at least two hits in the Pixel Detector are required, of which one hit has to be in the innermost layer (b-layer) for a reconstructed track.
The efficiency of track reconstruction is defined as the portion of MC particles with a matched reconstructed track, whilst the fake rate is estimated by the fraction of reconstructed tracks without a matching MC particle track. The efficiency and fake rate for the reconstruction of pion tracks in top-quark initiated jets are shown in Fig. 6.7.
The track reconstruction efficiency for isolated pions with standard cuts is $\approx 90\%$ in the central region and drops to $\approx 80\%$ in the end-cap region of the Inner Detector. The fake rate increases towards higher η by a factor of about two. Using b-tagging quality cuts, the efficiency is lower by about 5% across the η range compared to standard cut selection, but also the fake track rate is lower by a factor of about two in the barrel up to a factor of 2.5 in the end-cap region.

6.3 Primary Vertex Reconstruction

The interaction region of the ATLAS experiment is the region in which two proton bunches cross each other. The primary vertex is the interaction point of two protons,

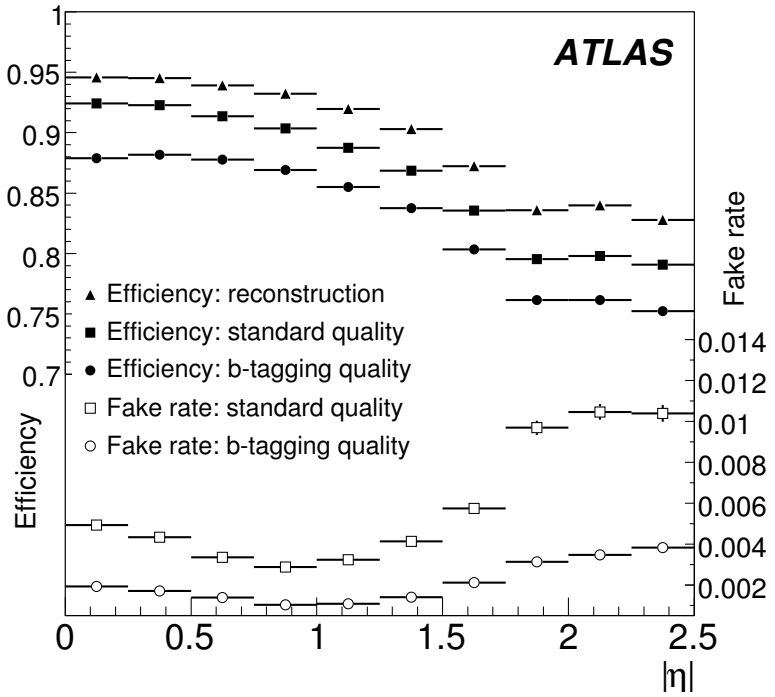

Figure 6.7: Fake track rate and track reconstruction efficiency for isolated pions in $t\bar{t}$ events using different sets of track quality cuts [4].

which initiate the physics event of interest. Due to possibly more than one collision in one bunch crossing, several interaction points may exist and have to be reconstructed. The interaction points are randomly distributed over the interaction region (beam spot) according to a Gaussian distribution, which has a width of $\sigma_{xy} \approx 15\,\mu$m in the transverse plane and $\sigma_z \approx 56$ mm in the longitudinal plane. The mean point of the beam spot is simulated at fixed coordinates (1.5 mm, 2.5 mm, -9 mm) (Fig. 6.8). The width of the beam spot in the transverse plane σ_{xy} is more precise than in the longitudinal direction. Therefore, the improvement of the knowledge of the primary interaction point due to an explicit reconstruction is mainly expected in the z direction.

The reconstruction of the primary vertex is performed in two steps: Vertex finding and vertex fitting. In the vertex finding step tracks are associated with a primary vertex candidate. In the second step a vertex fit is performed using the tracks associated to the primary vertex candidate.

Within this thesis, primary vertices are determined using an adaptive vertex fitter technique [36] as well as the expansion of the algorithm to fit several vertices simultaneously [37]. The algorithm is implemented in the ATLAS software framework as InDetAdaptiveMultiPriVxFinder [38].

The vertex reconstruction starts with the selection of tracks, which fulfill the cuts listed in Tab. 6.2.

Cuts on the impact parameter (and its error) of the tracks prevent, that tracks from secondary vertices participate in the primary vertex fit. The track quality cuts

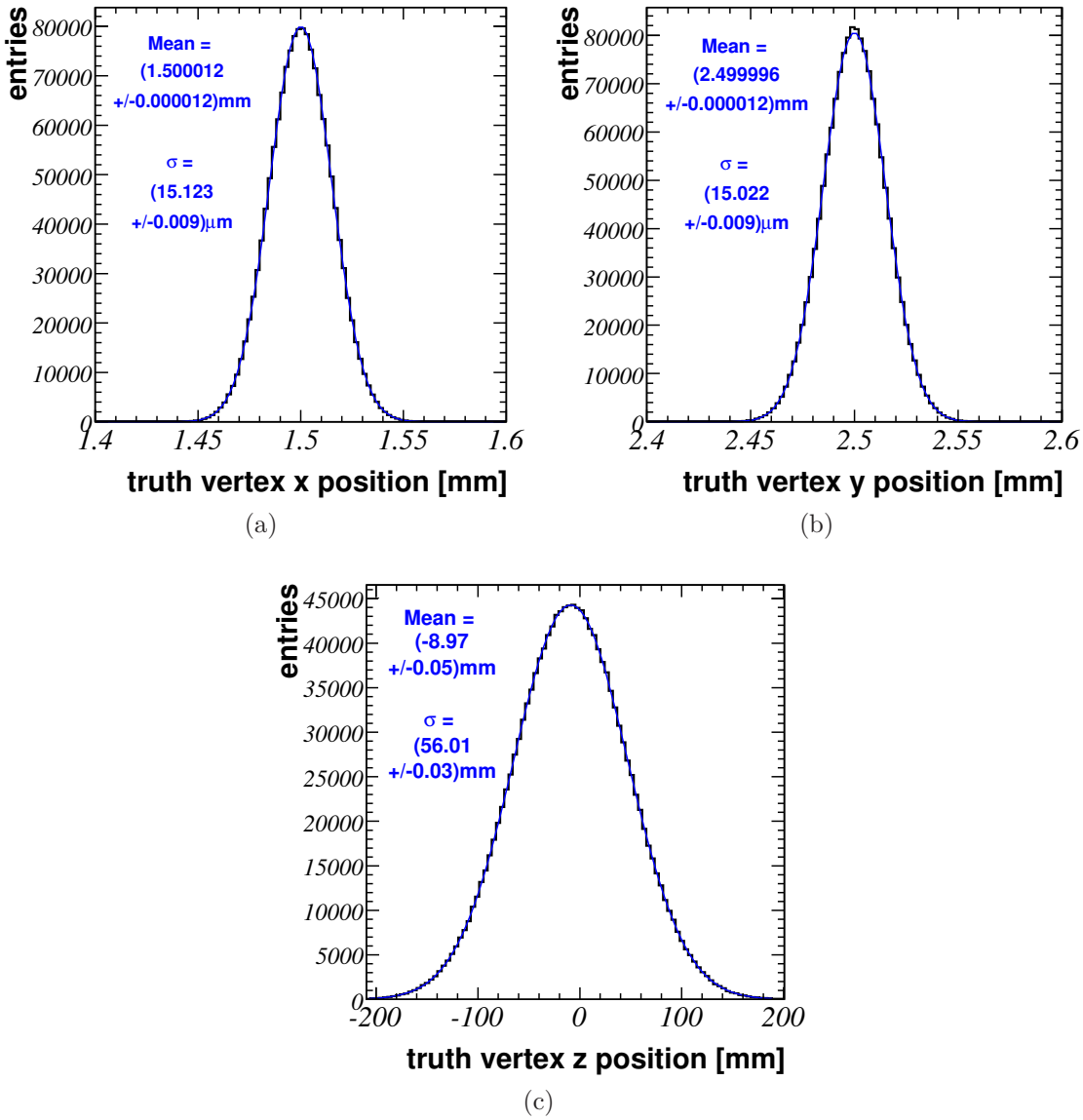

Figure 6.8: Simulated x, y and z position of the primary vertex.

track selection cut	cut expression
transverse momentum	$p_{\mathrm{T}} > 0.5\,\mathrm{GeV}$
maximum transverse impact parameter	$\lvert d_0 \rvert < 1\,\mathrm{mm}$
uncertainty of transverse impact parameter	$\sigma_{d_0} < 0.35\,\mathrm{mm}$
uncertainty of longitudinal impact parameter	$\sigma_{z_0} < 2.5\,\mathrm{mm}$
maximum significance of transverse impact parameter	$\frac{\lvert d_0 \rvert}{\sigma_{d_0}} < 4$
number of pixel and SCT hits	$n_{Si} \geq 7$
SCT hits	$n_{SCT} \geq 5$
pixel hits	$n_{pix} \geq 1$
quality of the track fit	$\chi^2/ndf < 3.5$

Table 6.2: Track selection cuts for primary vertex reconstruction.

ensure that every track has a sufficient number of precision Inner Detector hits.
Before the vertex fit, a seed finder estimates a first vertex position by clustering tracks using their longitudinal impact parameter w.r.t. the beam spot. After track selection and seed finding, a first fit is performed based on a χ^2_{vertex} minimization of a quantity formed by the track residuals w.r.t. the estimated primary vertex position, divided by the track errors. Also the beam spot position is taken into account (beam spot constraint). Tracks, which are incompatible with the fitted vertex position (outlier tracks) create a new vertex seed. In the next iteration two vertex fits are performed simultaneously. Vertices, which are not separated significantly are merged and used again in the next iteration of the fit.
In order to reduce the influence of outlier tracks on the vertex fit, an additional weight for each track (w.r.t. to each vertex seed) is introduced. The weighting factors are estimated from the χ^2 contribution of the track to the last vertex fit. The influence of a track with a higher χ^2 contribution is therefore down-weighted in the next iteration of the fit.
The number of vertex candidates will grow in each iteration step and all vertex candidates compete with each other to obtain tracks until no tracks are left.
Since this procedure depends strongly on the first estimated vertex position, an annealing procedure is added to the vertex fitting. A thermodynamic annealing is introduced to the weights of the different tracks selected for the vertex fit. The track weight $w(\chi^2, T)$ depends on the χ^2 contribution to the fit and additionally on a 'temperature' T, which is expressed in the form of a Fermi function:

$$w(\chi^2, T) = \frac{1}{1 + e^{(\frac{\chi^2 - \chi^2_c}{2T})}}\,. \tag{6.6}$$

This temperature is set to a high value in the beginning and decreases with every iteration of the vertex fit. For $T \to 0$ the weight function of the tracks is a step function and all tracks with a χ^2 over a given cutoff value $\chi^2 \geq \chi^2_c$ are rejected.
The efficiency of the primary vertex reconstruction is the fraction of events in which a primary vertex is reconstructed. The efficiency to find a primary vertex in QCD jet events is $(99.937 \pm 0.002)\%$. A primary vertex, which is reconstructed wrongly,

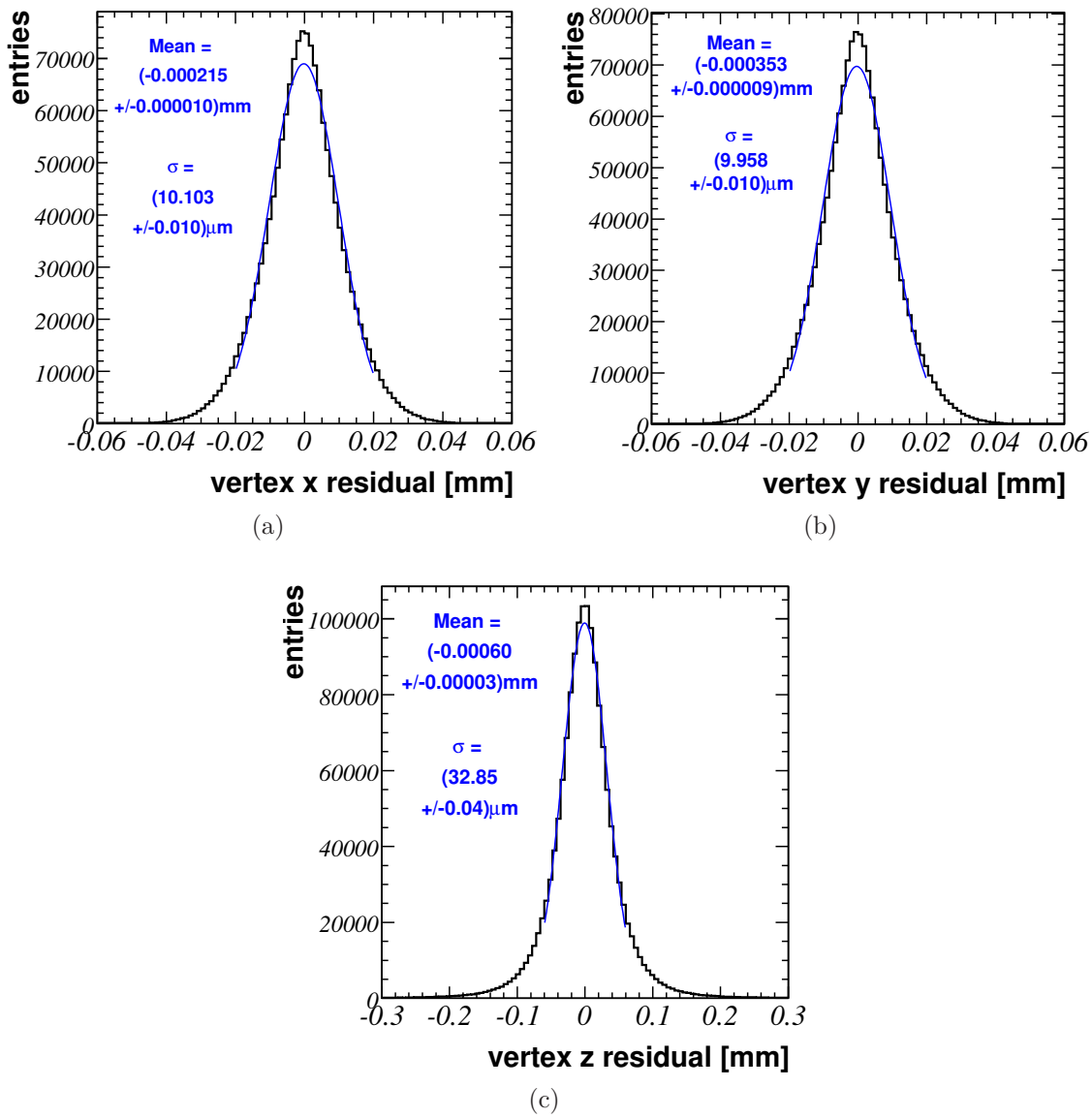

Figure 6.9: Residuals for x, y and z of reconstructed vertices. The resolution of the vertex reconstruction is determined by a fit of a Gaussian distribution.

i.e. far away from the simulated position, leads to a wrong determination of impact parameters of tracks w.r.t. this fake primary vertex and therefore would decrease the efficiency to identify b-jets. The percentage of outlier primary vertices, defined by the distance of the reconstructed and MC z-coordinate of the primary vertex $|z_{VRec} - z_{VSim}| > 0.5\,\text{mm}$, is $(0.136 \pm 0.003)\%$.
The resolution of the primary vertex reconstruction is estimated by a fit of a Gaussian distribution to the residual distribution of reconstructed to truth primary vertices (Fig. 6.9). The fit range is about 2σ of the Gaussian fit around the maximum, thus not considering the non-Gaussian tails of the distribution. As expected, the resolution of the reconstructed vertex in the x and the y position is similar. The precision of the primary vertex reconstruction in the transverse plane is already constraint to the beam spot width and only a small improvement is expected from $\sigma_{beam} \approx 15\,\mu\text{m}$ to $\sigma_{xy} \approx 10\,\mu\text{m}$. The resolution of the z position of the primary vertex is $\sigma_z = (32.85 \pm 0.04)\,\mu\text{m}$ and therefore more precise than the beam spot of the two intersecting proton bunches.
The more precise knowledge of the z position improves the identification of b-jets. Also cuts on the longitudinal impact parameter of tracks w.r.t. the reconstructed primary vertex reject contributions originating from pile-up events (additional proton-proton collisions in the same bunch crossing).

Chapter 7

Luminosity Determination

In high energy physics experiments different kinds of interactions between elementary particles are studied. The probability for a special kind of event to happen is given by the cross section, which depends on the energy available. On the other hand the luminosity is a property of the particle collider. The instantaneous luminosity $\mathcal{L}$ is defined such, that the production rate $R = \frac{dN}{dt}$ of events per second is the product of the production cross section σ_p and the luminosity:

$$R = \frac{dN}{dt} = \sigma_p \mathcal{L} \,. \tag{7.1}$$

The unit of the luminosity is $\mathrm{cm}^{-2}\mathrm{s}^{-1}$, while the unit of the cross section is barn ($1\,\mathrm{b} = 10^{-24}\,\mathrm{cm}^2$). A general expression to calculate the luminosity of particle colliders is given in Section 7.1.
While the instantaneous luminosity gives the production rate, the integrated luminosity $\mathcal{L}_{int}$

$$\mathcal{L}_{int} = \int_0^T \mathcal{L}(t)\, dt \tag{7.2}$$

is directly proportional to the number of produced events N_{exp} during the measuring time T, with the production cross section σ_p:

$$N_{exp} = \sigma_p \mathcal{L}_{int} \,. \tag{7.3}$$

The instantaneous luminosity is typically time dependent, due to the decrease of the beam intensity with time. The time dependence of the instantaneous luminosity is modeled by an exponential decrease with a time constant τ

$$\mathcal{L} \to \mathcal{L}_0 e^{-\frac{t}{\tau}} \,. \tag{7.4}$$

At the LHC the nominal time constant of the beam is expected to be in the order of $\tau \approx 14\,\mathrm{h}$, which means that after 10 minutes 1% of instantaneous luminosity is lost. In practice the data taking periods of the ATLAS detector are divided into luminosity blocks. The luminosity blocks are time periods short enough to consider the measurement conditions to be stable, but long enough to determine the integrated luminosity. The time corresponding to a luminosity block is of the order

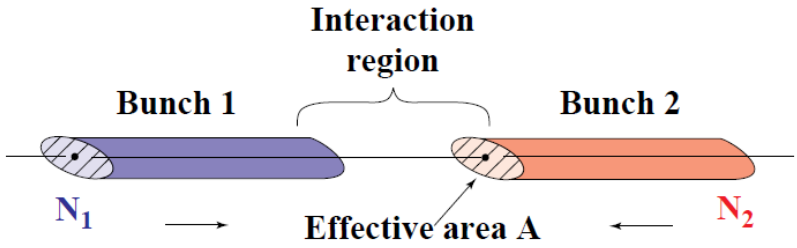

Figure 7.1: Head-on collision of two proton bunches [40].

of $\mathcal{O}(\text{min})$. During this time, effects should be negligible. The luminosity has to be explicitly measured for each luminosity block. Different methods of luminosity measurements are discussed in Section 7.2.

7.1 Luminosity of a Collider

In this section, the calculation of the luminosity for a collider with bunched beams is presented (following [39]).
The beams of the LHC consist of several bunches of N protons per bunch. The bunches of the two different beams are accelerated in opposite directions and collide head-on in a cross sectional area A, shown in Fig. 7.1.
For a simple approximation a uniform distribution of the protons in the bunches projected onto the cross sectional area is assumed. In this case, a single proton of the first bunch has an effective cross sectional region of $\frac{N_2}{A}\sigma_{int}$ due to the N_2 protons in the other bunch. The number of interactions per bunch crossing is then $\frac{N_1 N_2}{A}\sigma_{int}$ since the first bunch contains N_1 protons. The interaction rate R, taking the beam revolution frequency f and the number of bunches N_b per beam stored in the collider into account, is written as:

$$R = \frac{dN}{dt} = f\frac{N_b N_1 N_2}{A}\sigma_{int}. \tag{7.5}$$

The luminosity $\mathcal{L}$ as the interaction rate per unit cross section is then given by

$$\mathcal{L} = f\frac{N_b N_1 N_2}{A}. \tag{7.6}$$

In reality, the proton density distribution is not uniform over the transverse beam profile. A more realistic assumption is a Gaussian distribution of the protons in the transverse plane about the midpoint of the beam profile in each direction, which leads to a Rayleigh distributed density of the protons $N_i(r)$ (for N_1 and N_2):

$$dN_i(r) = \frac{N_i r}{\sigma^2} e^{-r^2/2\sigma^2}\, dr. \tag{7.7}$$

Contributions to the luminosity $\mathcal{L}$ from cross sectional rings at r with a thickness of dr are estimated from (7.6) to

$$d\mathcal{L} = f\frac{N_b\, dN_1\, dN_2}{2\pi r\, dr}. \tag{7.8}$$

The integral $\int d\mathcal{L}(r)$ over r is the overlap integral of the two beam proton density distributions. Using (7.7) and integrating over the radius r, the instantaneous luminosity for a collider is written as:

$$\mathcal{L} = f\frac{N_b N_1 N_2}{4\pi\sigma^2} = f\frac{N_b N_1 N_2}{4\pi\sigma_x\sigma_y}. \tag{7.9}$$

The last part explicitly takes the extension of the two beams in the x and y direction σ_x,σ_y into account. As seen in (7.9), the instantaneous luminosity increases with the proton density in the bunches, since $\mathcal{L}$ rises with the number of protons and drops with larger transverse beam extensions.
The luminosity calculated by (7.9) is valid for the ideal case with beams of Gaussian beam profiles colliding head-on. In practice the beam profile differs from the ideal case and modifications to (7.9) are necessary.
One effect, which reduces the luminosity given by (7.9), is a crossing angle of the two proton bunches. In case of head-on bunch collisions and small gaps between bunches, unwanted proton-proton collisions due to additional bunch crossings outside the nominal interaction region can appear. In order to avoid these collisions, the bunches at the LHC collide at a crossing angle of $\phi = 285\,\mu$rad, which reduces the area in which the interactions can take place. In the calculation of the luminosity the crossing angle is introduced as two rotations in the coordinate system of each beam by $\phi/2$. The coordinates x and s (longitudinal coordinate along the beam pipe) for the two bunches are written as:

$$x_1 = x\cos\frac{\phi}{2} - s\sin\frac{\phi}{2},\;\; s_1 = s\cos\frac{\phi}{2} + s\sin\frac{\phi}{2}\,, \tag{7.10}$$

$$x_2 = x\cos\frac{\phi}{2} + s\sin\frac{\phi}{2},\;\; s_2 = s\cos\frac{\phi}{2} - s\sin\frac{\phi}{2}\,. \tag{7.11}$$

$$\tag{7.12}$$

Using the rotated coordinates in the density of the protons (7.8) results in

$$\mathcal{L} = f\frac{N_b N_1 N_2}{4\pi\sigma_x\sigma_y}S \tag{7.13}$$

where S is

$$S = \frac{1}{\sqrt{1+\left(\frac{\sigma_s}{\sigma_x}\tan\frac{\phi}{2}\right)^2}} \approx \frac{1}{\sqrt{1+\left(\frac{\sigma_s}{\sigma_x}\frac{\phi}{2}\right)^2}}\,. \tag{7.14}$$

In addition to the crossing angle a spatial offset of the colliding beams will reduce the luminosity. In case of a transverse offset along the x-axis of d_1 and d_2 of bunch 1 and 2, respectively, the luminosity is given by [41]:

$$\mathcal{L} = f\frac{N_b N_1 N_2}{4\pi\sigma_x\sigma_y} S W e^{\frac{B^2}{A}} \tag{7.15}$$

with

$$W = e^{-\frac{(d_2-d_1)^2}{4\sigma_x^2}}, \tag{7.16}$$

$$A = \frac{\sin^2\frac{\phi}{2}}{\sigma_x^2} + \frac{\cos^2\frac{\phi}{2}}{\sigma_s^2},\ B = \frac{(d_2-d_1)\sin\frac{\phi}{2}}{2\sigma_x^2}. \tag{7.17}$$

The last exponential term in (7.15) only contributes in the non-trivial case of a simultaneous offset of the beams in addition to a crossing angle between the colliding bunches. In the start-up phase of the LHC, the number of bunches will be small and a crossing angle will not be necessary.

7.2 Measurements of the Luminosity

The (instantaneous) luminosity is measured by different methods. Not all methods are available in the first data taking periods of the LHC. In this chapter four different luminosity measurements are discussed. One of the first measurements will be the estimation of the luminosity from beam parameters (Section 7.2.1). Later on a measurement of the absolute luminosity is performed by the ALFA detector, which results in a better accuracy (Section 7.2.2), but needs special beam conditions and lower luminosity. Online monitoring of the luminosity will be provided by the LUCID detector, which then gives a relative luminosity measurement. This measurement needs to be calibrated by an absolute luminosity estimation (Section 7.2.3). However, it is also feasible at higher luminosities. In Section 7.2.4 the possibility of an offline determination of the luminosity is discussed.

7.2.1 Determination of the Luminosity from LHC Machine Parameters

The determination of the luminosity from LHC machine parameters will be one of the first measurements of the luminosity. In order to determine the luminosity from (7.9), the number of protons per bunch as well as the transverse beam size have to be measured. The other variables are well known in a data taking run.
The number of protons will be measured by e.g. beam current transformers, which integrate the beam current for each bunch. The principle of the beam current transformer is shown in Fig. 7.2.
The beam current transformer interacts with the magnetic field of the beam. The beam current I_B generates an output voltage at the winding of $V = L\,dI_B/dt$. The output waveform closely resembles the beam intensity distribution with an added DC offset due to the transformer droop (which is corrected for on electronic or on software level). The accuracy of the beam current measurement for nominal beam with $1.15 \cdot 10^{11}$ protons per bunch is expected to be better than 1%.

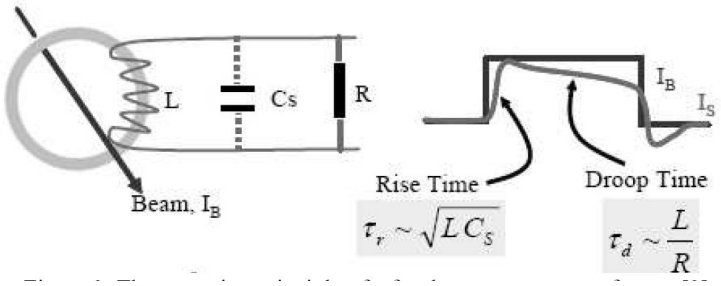

Figure 7.2: Measurement principle of the fast current transformer [42].

Several methods to determine the beam profile are available. One method will be to vary the displacement d of the two beams relative to each other and to monitor the relative luminosity. Measuring the relative luminosity $\mathcal{L}(d)/\mathcal{L}_0$ is equivalent to a measurement of W in (7.15) assuming Gaussian beam profiles in the transverse plane. Fitting the term

$$W = e^{-\frac{d^2}{4\sigma^2}} \tag{7.18}$$

to the relative luminosity as a function of d gives an estimate of the beam size. The scans will be performed separately with a vertical and a horizontal displacement to estimate the beam size σ_x and σ_y from the fits. Such separation scans are known as Van-der-Meer scans.
Other possibilities to measure the beam profile are:

- Wire scanners: A wire is moved vertically and horizontally through the beam. Beam particles hitting the wire and ionize the atoms. This results in a current in the wire. The current is measured as a function of the wire position.

- Scintillator monitors: A thin metal screen (doped aluminum foil) is placed in the beam path. Beam particles produce scintillating photons, which are observed on a screen.

- Optical transition radiation monitors: A titanium screen in the beam path leads to transition radiation photons produced by the beam particles due to the transition from vacuum to metal. These photons are collected and observed on a screen.

- Synchrotron light monitors: Synchrotron light of the beam is produced with undulators. The emitted synchrotron photons are recorded with a camera and provide a two dimensional image of the beam.

The beam current and beam size measurements together with the well known beam parameters allow the determination of the luminosity. The expected accuracy of the luminosity measurement using beam parameters is $\Delta\mathcal{L}/\mathcal{L} = 5$ to 10% [43].

7.2.2 Absolute Luminosity Measurement

At the LHC dedicated detectors like in the TOTEM [44] experiment or the ALFA detector [1] measure the absolute luminosity. The measurement of the absolute luminosity used in the TOTEM experiment is based on a measurement of the elastic scattering rate. The total cross section is connected to the number of elastic and inelastic scattering events via the luminosity

$$N_{inel} + N_{el} = \sigma_{tot}\mathcal{L}\,. \tag{7.19}$$

The elastic cross section is related to the total cross section by using the optical theorem. For small values of the Mandelstam variable $t = (p_1 - p_3)^2$ (p_1, p_2 are the momenta of the incoming and p_3, p_4 of the outgoing particles of the scattering process) the scattering process follows:

$$\lim_{t\to 0}\frac{d\sigma_{el}}{dt} = (1+\rho^2)\frac{\sigma_{tot}^2}{16\pi} = \frac{1}{\mathcal{L}}\frac{dN_{el}}{dt}|_{t=0}\,, \tag{7.20}$$

where ρ is the ratio of the imaginary and the real part of the nuclear scattering amplitude. Therefore, the luminosity is measured by the total event rate $N_{inel}+N_{el}$ and the differential elastic scattering event rate $\frac{dN_{el}}{dt}$:

$$\mathcal{L} = \frac{(1+\rho^2)}{16\pi}\frac{(N_{inel}+N_{el})^2}{\frac{dN_{el}}{dt}|_{t=0}}\,. \tag{7.21}$$

A similar method of measuring the absolute luminosity will use the Coulomb scattering amplitude. Within the ATLAS experiment, the ALFA detector is used to measure the absolute luminosity using this strategy. The design of the ALFA detector is explained in Section 2.4. The elastic scattering amplitude is a superposition of the Coulomb f_c and the strong f_s scattering amplitude.
The differential elastic cross section is written as [41]

$$\lim_{t\to 0}\frac{d\sigma_{el}}{dt} = \frac{1}{\mathcal{L}}\frac{dN_{el}}{dt}|_{t=0} = \pi|f_c+f_s|^2 = \frac{4\pi\alpha_{em}^2}{|t|^2} - \frac{\alpha_{em}\rho\sigma_{tot}}{|t|}e^{\frac{-B|t|}{2}} + \frac{\sigma_{tot}^2(1+\rho^2)}{16\pi}e^{-B|t|} \tag{7.22}$$

where ρ is the ratio of the imaginary and real part of the nuclear scattering amplitude and B the nuclear slope parameter. The measurement of the luminosity is reduced to the measurement of the t spectrum of the elastic scattering. The parameters σ_{tot}, $\mathcal{L}$, ρ and B are derived from a fit to the measured t spectrum. The t spectrum will be measured in a range of about $(0.00055 < -t < 0.055)\,\mathrm{GeV}^2$. The luminosity is converted into an average instantaneous luminosity by taking the duration of the measurement into account.
Details of the t spectrum measurement are found in [45]. In Fig. 7.3 the resulting fit to the t spectrum is shown.
Special beam conditions are necessary due to the measurement at very small scattering angles. A small emittance and a high β^* (betatron-function value of the beam, i.e. small beam oscillations) are necessary and special LHC runs with lower luminosity in the order of $\mathcal{L} = 10^{-27}\mathrm{cm}^{-2}\mathrm{s}^{-1}$ are needed. This method is expected

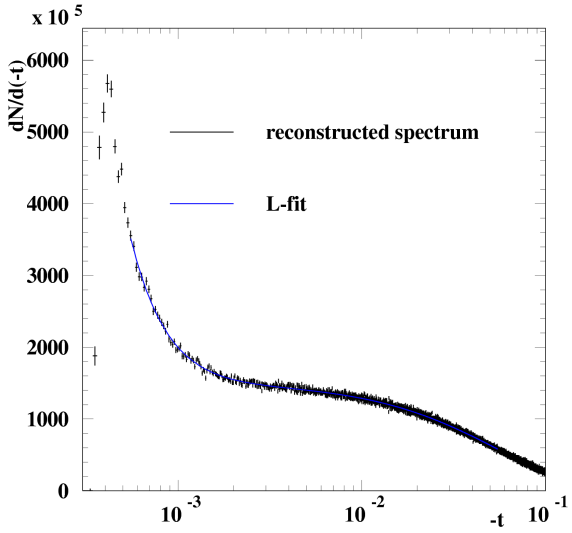

Figure 7.3: Luminosity fit on a reconstructed MC data t spectrum [45].

to give the best precision with an estimated uncertainty of $\Delta\mathcal{L}/\mathcal{L} = 2\%$ to 3% on the absolute luminosity [43]. Since the absolute luminosity measurements need special beam conditions, they have to be complemented by relative online luminosity measurements.

7.2.3 Relative Luminosity Measurement

Relative luminosity measurements by the LUCID detector [1] (Section 2.4), which is part of the ATLAS detector, will complement the absolute luminosity measurements. The time resolution of the LUCID detector is short enough to measure the luminosity for each bunch crossing (BC).
The number of inelastic interactions μ in a BC is expressed as

$$\mu = \sigma_{inel} L_B \,, \tag{7.23}$$

the product of the inelastic cross section σ_{inel} and the bunch crossing luminosity L_B. A determination of the relative luminosity is obtained by measuring the mean number $< M >$ of particles in the detector, which is directly proportional to the mean number of inelastic interactions:

$$< M >=< C > \epsilon_{pp}\mu =< C > \epsilon_{pp}\sigma_{inel} L_B \,. \tag{7.24}$$

The number $< C >$ represents the particles in the detector measured in a calibration run and ϵ_{pp} the efficiency to detect them. The product $< C > \epsilon_{pp}$ describes the number of particles detected in a calibration run, in which the absolute luminosity is measured by e.g. the ALFA detector or using the machine parameters. This term is then considered to be fixed.

The linear relationship in (7.24) is used to extrapolate the luminosity calibrated at $\mathcal{L} = 10^{-27}\text{cm}^{-2}\text{s}^{-1}$ to higher luminosities up to the design luminosity of $\mathcal{L} = 10^{-34}\text{cm}^{-2}\text{s}^{-1}$ taking the inelastic cross section of $\sigma_{inel} = 79.2\,\text{mb}$ into account.
The effects of non linearities on the relative luminosity measurement, due to higher particle rates at higher luminosity of the LHC, are studied in [46].

7.2.4 Offline Luminosity Determination

Several methods are available to determine the luminosity via offline methods. Assuming a precise knowledge of the parton cross section of a specific physics process, the luminosity is determined by counting the number of such events, recorded in a suitable data taking run. Physics processes include J/Ψ, W and Z production. Physics processes with muons or electrons in the final state are preferred since it is relatively easy to separate them from possible background events.
Counting the rate of produced W/Z events is used to calculate the luminosity. For luminosities of $\mathcal{L} > 10^{33}\,\text{cm}^{-2}\text{s}^{-1}$ the relatively large cross section expected for W/Z production will allow a luminosity estimation with small statistical uncertainties. The overall error on the luminosity estimation will be dominated by the systematic uncertainty of the proton density function. This systematic uncertainty will be reduced, when the proton density function is better constrained due to new LHC measurements. The accuracy of the absolute luminosity calculation is expected to be in the order of $\Delta\mathcal{L}/\mathcal{L} = 5\%$ to 10%. The relative luminosity calculation will reach an accuracy of $\Delta\mathcal{L}/\mathcal{L} = 1\%$ to 5% [43].
Other possibilities of offline luminosity determinations are counting the number of silicon space points per event, which is expected to scale with the luminosity. Also the Poisson distributed number of reconstructed primary vertices of inelastic events λ scales with the luminosity

$$\lambda = \sigma_{inel}\mathcal{L}_B\,, \tag{7.25}$$

where $\mathcal{L}_B$ is the luminosity for a specific bunch. For this luminosity determination the cross section σ_{inel} of inelastic events has to be measured independently (e.g. by LUCID or by the TOTEM experiment [44]).

Chapter 8

Measurement of the Differential b-Jet Cross Section

In order to measure the differential b-jet cross section, b-jets measured by the ATLAS detector have to be separated from other QCD-jet background (jets not initiated by a b-quark). The general strategy for measuring the b-jet cross section has already been presented in Section 4.3. The different efficiencies and purities of the event selection in the b-jet cross section formula (4.7):

$$\sigma_{b-jet} = \frac{P_{Rec} P_{Tag} N_{Sel}}{\epsilon_{Tr} \epsilon_{Rec} \epsilon_{Tag} \mathcal{L}} \tag{8.1}$$

have to be estimated. The integrated luminosity is given by the luminosity measurements described in Chapter 7, while the estimations of the purities and the efficiencies are discussed in this chapter. Since the measurement of the differential b-jet cross section is based on measured and reconstructed jets, an unfolding algorithm has to be applied in order to reduce the effect of the jet p_{T} smearing, i.e. of bin-to-bin migrations. Therefore, the unfolding algorithm includes a step of transforming the measured reconstructed b-jet p_{T} spectrum into the truth b-jet p_{T} spectrum w.r.t. to the jet p_{T} binning. Not all efficiencies and purities are estimated for the reconstructed jet p_{T} binning. The trigger efficiency ϵ_{Tr} as well as the efficiency to reconstruct b-jets ϵ_{Rec} are calculated using the MC truth jet p_{T}, since in data recorded by the detector reconstructed jets are not available for non-reconstructed or non-triggered b-jet events. These efficiencies will be used to estimate the b-jet cross section after the unfolding procedure. The efficiencies have to be validated with data by comparing the jet p_{T} spectra from MC events to those of measured events.

In the calculation of the purity of the b-jet reconstruction P_{Rec} as well as the efficiency ϵ_{Tag} and the purity P_{Tag}, reconstructed jets are used. Therefore, these quantities are estimated using the reconstructed jet p_{T} for the binning. They will be applied to the cross section calculation before the unfolding procedure.

The first step of the event selection is to trigger the events containing a b-jet signal. Within this thesis the combination of single jet triggers is used, as discussed in Section 8.1. The triggered b-jets have to be reconstructed, which results in the

efficiency of the b-jet reconstruction ϵ_{Rec} as well as the purity of the reconstructed b-jets P_{Rec}. The purity reflects possible fake jets and wrongly reconstructed leading b-jets (Section 8.2). For the selection of b-jets different b-tagging algorithms are used (Section 8.3), combined and optimized to select b-jets over the whole jet p_{T} range considered.
After the event selection, an unfolding algorithm is applied to the measured b-jet spectrum in order to reduce the effects of the jet p_{T} smearing during the measurement and reconstruction processes (Section 8.4). Systematic errors of the measurement, like the uncertainty of the jet energy scale of the calorimeter as well as the expected precision of the tagging efficiency and purity based on calibration on data, are taken into account in Section 8.5.
The result for the differential b-jet cross section is given in Section 8.6.

8.1 Trigger Selection

The first step of the b-jet cross section measurement is to trigger the events containing a b-jet signal. The design and the algorithms of the ATLAS trigger system are explained in Section 2.7. To estimate the trigger efficiencies for signal and background events, MC truth jet p_{T} information are used. Hence the p_{T} binning is based on the truth jet p_{T}, the trigger efficiency will be applied on the measured b-jet p_{T} spectrum after the unfolding of the measured spectrum.
Events, which contain at least one b-quark will produce at least one jet, which is initiated by the b-quark. Therefore, the signal signature requires at least one jet in the detector. In the ATLAS trigger menu a set of jet triggers, which is used within this thesis, are available to trigger on jet events. The exact configurations of the jet triggers, like thresholds, prescale factors or jet cone sizes, depend on the instantaneous luminosity as well as the center of mass energy of the collisions and will be adjusted to the actual beam conditions. Within this thesis a jet trigger menu is chosen, which is optimized for an instantaneous luminosity of $10^{31}\,\mathrm{cm}^{-2}\mathrm{s}^{-1}$.
The overall bandwidth for storing triggered events on tape is estimated to ≈ 24 Hz for the combination of all jet triggers. Because of the limited bandwidth, the triggers have to be prescaled by a prescale factor PF, i.e. only one event out of PF events, which fulfill the trigger condition, is written to tape (triggered). The prescale factors are chosen to trigger events such, that high p_{T} jet events (lower cross section compared to the lower p_{T} events) are triggered as efficiently as possible, i.e. lower prescale factors are used. Lower p_{T} jet events are triggered by trigger items, which have prescale factor such, that the complete available bandwidth is used. Therefore, jet trigger items with lower thresholds have a higher prescale factor. In Tab. 8.1 the different single jet trigger items are listed, which are combined to trigger jet events as efficiently as possible. The number in the trigger name indicates the jet E_{T} threshold set for this trigger item.
The overall trigger efficiency ϵ_{Tr} represents the probability for an event (with at least one jet) to be triggered by the jet trigger menu. Therefore ϵ_{Tr} will be estimated for each jet p_{T} bin considering the leading jet of an event and will then be used to

	L1	L2	EF	Prescale Factor
J10	L1_J10	L2_J10	EF_J10	42000
J80	L1_J18	L2_J50	EF_J80	6000
J115	L1_J23	L2_J60	EF_J115	2000
J140	L1_35	L2_J80	EF_J140	500
J180	L1_J42	L2_J110	EF_J180	100
J265	L1_J70	L2_J150	EF_J265	15
J350	L1_J120	L2_J205	EF_J350	1

Table 8.1: Different single jet trigger and prescale factors. The trigger menu is foreseen for an instantaneous luminosity of $10^{31}\,\mathrm{cm}^{-2}\mathrm{s}^{-1}$ [4].

re-weight the MC events to reflect not only the cross section but also the trigger selection (including prescale factors) of these events. After re-weighting, the trigger efficiency (including prescale factors) for the measurement of the b-jet cross section considering all b-jets in the events is calculated. Possible differences of triggering b-jet events compared to QCD background events have to be considered. Therefore, the overall trigger efficiency is estimated separately for signal b-jet events and QCD background.

In order to estimate the overall trigger efficiency of the combination of the single jet triggers, the trigger efficiency $\epsilon_{\mathrm{JetTrigger}}$ as a function of the truth jet p_{T} for each trigger item has be determined. The trigger efficiency $\epsilon^{i}_{\mathrm{JetTrigger_j}}$ for the jet trigger i is defined as the portion of triggered events $N^{i}_{triggered_j}$ out of $N^{i}_{events_j}$ events in the truth jet p_{T} bin j and therefore represents the probability of an event to be triggered by the jet trigger i, not taking prescale factors into account:

$$\epsilon^{i}_{\mathrm{JetTrigger_j}} = \frac{N^{i}_{triggered_j}}{N^{i}_{events_j}}\,. \tag{8.2}$$

The trigger efficiencies for the different single jet trigger as a function of the truth jet p_{T} are shown in Fig. B.1 in App. B.

The trigger efficiency is low in case of jets below the threshold and increases to over 99% for each trigger in case the jet energy exceeds the trigger threshold (turn-on curve). The trigger efficiency around the trigger threshold is higher in case of cone4 jets compared to cone7 jets (Section 6.1), although the same trigger configuration is chosen. Thus the differences are not due to the used trigger item itself. The differences originate from the different cone sizes, which are used to estimate the truth p_{T} of a jet. For cone7 jets a wider cone is used, which results in a higher truth jet p_{T} and therefore in some cases in a higher jet p_{T} bin. The turn-on curve of any jet trigger is shifted to higher truth jet p_{T} for cone7 jets.

The statistical uncertainty on the trigger efficiency is calculated as described in App. C. Because always the larger uncertainty of the asymmetric errors is taken, trigger efficiencies including errors can exceed a value of one. This is in a sense unphysical, but in this way the uncertainty of the trigger efficiency is not underestimated in case of high trigger efficiencies and therefore constitutes a conservative estimate of the uncertainty.

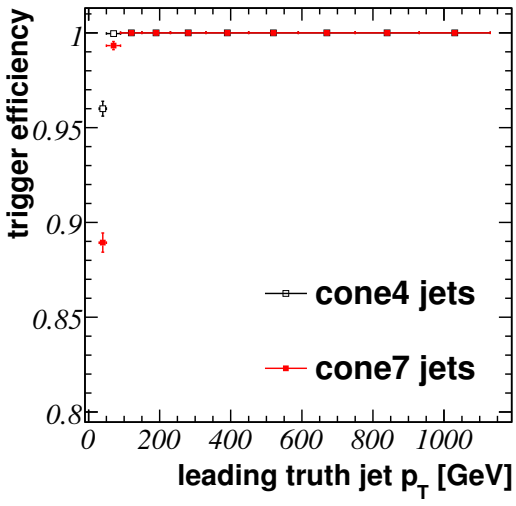

Figure 8.1: Trigger efficiency for b-jet events as a function of the leading truth jet p_{T}.

The trigger efficiency of all jet triggers reflects the probability of an event to be triggered by at least one of the jet triggers. The combined trigger efficiency as a function of the leading truth jet p_{T} is shown in Fig. 8.1. The trigger efficiency is only in the first jet p_{T} bin below 99% as expected from the individual trigger efficiencies of the separate jet triggers.
The trigger rate R_j^i is the expected frequency of each jet trigger item i to trigger an event in jet p_{T} bin j, without taking prescale factors into account. It depends on the efficiency of the trigger item, the instantaneous luminosity as well as the cross section for obtaining events in bin j. The rate R_j^i for an instantaneous luminosity $\mathcal{L}$ is estimated by

$$R_j^i = \epsilon_j^i \mathcal{L} \sigma_{b-jetEvent} \,. \tag{8.3}$$

The trigger rates for each trigger item are shown in Fig. B.2 in App. B. The trigger rate as a function of the leading truth jet p_{T} increases for each trigger after exceeding the trigger threshold because the efficiency to trigger on such events increases. The falling shape of the trigger rate as a function of the jet p_{T} after the threshold is due to the falling cross section of such events towards higher jet p_{T}. The trigger rate contribution of the higher p_{T} jet trigger item, e.g. J350, in jet p_{T} bins far below the trigger threshold is due to the fact, that the leading b-jet in the event may not be the hardest jet in the event, i.e. the event is triggered by a harder QCD jet, but filled into a lower jet p_{T} bin due to the lower jet p_{T} of the leading b-jet. The trigger rate contributions of jet trigger items below the trigger threshold for cone4 jets is always larger than for cone7 jets, which is again an effect of the truth jet p_{T} shift due to the different cone sizes. As soon as jet events exceed the trigger threshold, the cone7 trigger rate is larger compared to the cone4 rate.
The individual single jet trigger items are prescaled to trigger low energy jet events as well as higher energy jet events within the given bandwidth limit of the jet trigger menu. The prescale factors have to be taken into account for the overall efficiency of

the jet trigger. The probability P_i^j of an event in a truth jet p_{T} bin j to be triggered by a jet trigger i, which is prescaled by a factor PF_i is given by

$$P_i^j = \frac{\epsilon^i_{\mathrm{JetTrigger_j}}}{PF_i} \,. \tag{8.4}$$

Jet events may fulfill several jet trigger conditions. Therefore the probability P_{il} of an event to be triggered by a combination of two jet trigger i and l is

$$P_{il}^j = P_i^j + P_l^j - P_i^j P_l^j \,. \tag{8.5}$$

The probability to be triggered by a combination of jet triggers is the sum of the probabilities to be triggered by at least one of the jet triggers minus the probability to be triggered by both trigger items. The last term reflects the correlations between the different jet triggers. In case of the combination of more than two jet triggers, the overall probability for an event to be triggered is estimated recursively taking the different trigger efficiencies and prescale factors into account. This probability is taken as the effective trigger efficiency ϵ_{Tr} and represents the probability of an event to be triggered by the combination of all jet triggers. The estimated trigger efficiency ϵ_{Tr} for b-jet events as well as for QCD background events (jet events without b-jet content) is listed in Tab. 8.2 for cone7 and in Tab. 8.3 for cone4 jets.
The effective trigger efficiency for cone4 jets is higher in the lower truth jet p_{T} region compared to the cone7 trigger efficiency. This reflects the larger truth jet p_{T} of cone7 jets due to the larger cone size, which causes jet events (possibly with a larger prescale factor) to be filled into a higher jet p_{T} bin compared to those of cone4 jets. In the higher jet p_{T} region, the events are almost always triggered by the J350 trigger (Fig. B.1(g)), which is not prescaled. There the difference in the trigger efficiency ϵ_{Tr} between both cone sizes vanishes.
The effective trigger efficiency for b-jet events is higher compared to the trigger efficiency of QCD background events, which is related to the definition of a b-jet event. The b-jet does not need to be the hardest p_{T} jet in the event, i.e. a jet trigger with a higher threshold may trigger the event due to a harder light quark jet. The lower prescale factor of this jet trigger item increases the probability for such an event to be triggered. Due to the (possibly lower) leading truth b-jet p_{T}, the event assigned to the lower jet p_{T} region is triggered with higher probability. This is the main cause for the difference in the trigger efficiencies for b-jet and QCD events.
The trigger rate for b-jet events R_j in truth jet p_{T} bin j is estimated by

$$R_j = \mathcal{L}\sigma_{b-jetEvent}\epsilon_{Tr} \tag{8.6}$$

and shown in Fig. 8.2 for an instantaneous luminosity of $\mathcal{L} = 10^{31}\,\mathrm{cm}^{-2}\mathrm{s}^{-1}$.
The trigger rate is flat in the jet p_{T} region, where the jet triggers are prescaled. In the higher jet p_{T} region, the trigger rate reflects the cross section of b-jet events. The effect of the different cone sizes is amplified, because jets reconstructed using cone4 with a possibly lower prescale factor are shifted to lower jet p_{T} bins compared to jets reconstructed with cone7 (same prescale factor, but higher truth jet p_{T}). Thus, the average prescale factor in truth jet p_{T} bin j is lower for the cone4 jets. In jet

p_{T} range [GeV]		cone7 trigger efficiency	
		b-jets	QCD jets
$30-50$	trigger ϵ_{Tr}	$(27.0 \pm 0.3) \cdot 10^{-6}$	$(18.94 \pm 0.03) \cdot 10^{-6}$
	trigger rate [Hz]	0.172 ± 0.003	4.53 ± 0.02
$50-90$	trigger ϵ_{Tr}	$(83 \pm 2) \cdot 10^{-6}$	$(30.94 \pm 0.18) \cdot 10^{-6}$
	trigger rate [Hz]	0.078 ± 0.003	0.921 ± 0.015
$90-150$	trigger ϵ_{Tr}	$(1.02 \pm 0.03) \cdot 10^{-3}$	$(0.397 \pm 0.003) \cdot 10^{-3}$
	trigger rate [Hz]	0.075 ± 0.003	0.717 ± 0.014
$150-230$	trigger ϵ_{Tr}	$(10.9 \pm 0.3) \cdot 10^{-3}$	$(5.97 \pm 0.03) \cdot 10^{-3}$
	trigger rate [Hz]	0.077 ± 0.003	0.936 ± 0.012
$230-330$	trigger ϵ_{Tr}	0.087 ± 0.003	0.0401 ± 0.0003
	trigger rate [Hz]	0.076 ± 0.004	0.717 ± 0.011
$330-450$	trigger ϵ_{Tr}	0.778 ± 0.015	0.680 ± 0.004
	trigger rate [Hz]	0.105 ± 0.004	1.79 ± 0.02
$450-590$	trigger ϵ_{Tr}	0.9989 ± 0.0017	0.9981 ± 0.0004
	trigger rate [Hz]	0.0226 ± 0.0007	0.446 ± 0.004
$590-750$	trigger ϵ_{Tr}	0.9997 ± 0.0018	0.99995 ± 0.00011
	trigger rate [Hz]	$(4.09 \pm 0.17) \cdot 10^{-3}$	$(87.0 \pm 0.9) \cdot 10^{-3}$
$750-930$	trigger ϵ_{Tr}	1 ± 0.0014	0.9998 ± 0.0002
	trigger rate [Hz]	$(0.83 \pm 0.03) \cdot 10^{-3}$	$(18.5 \pm 0.2) \cdot 10^{-3}$
$930-1130$	trigger ϵ_{Tr}	1 ± 0.005	1 ± 0.0004
	trigger rate [Hz]	$(0.234 \pm 0.016) \cdot 10^{-3}$	$(4.288 \pm 0.09) \cdot 10^{-3}$
> 1130	trigger ϵ_{Tr}	1 ± 0.005	0.9999 ± 0.0003
	trigger rate [Hz]	$(0.056 \pm 0.004) \cdot 10^{-3}$	$(1.27 \pm 0.02) \cdot 10^{-3}$

Table 8.2: Trigger efficiency of leading cone7 b-jet signal events and leading cone7 QCD-jet background events as a function of the leading truth jet p_{T}.

p_{T} bins, in which mostly the same prescale factor is used, the cone7 trigger rate is larger due to the larger cross section compared to cone4 jets. This can be seen in the higher jet p_{T} bins as well as in the first bin, in which almost all events are prescaled by $PF = 42000$.

The effective trigger efficiency, which includes prescale factors, is used to re-weight MC events. Up to now the weight ω_i of an event i reflected the cross section (Chapter 5.2.1). In order to consider also the probability of an event to be triggered by the prescaled jet trigger menu, the events are re-weighted by

$$\omega^i_{triggered} = \omega_i \frac{\epsilon^j_{Tr.}}{\epsilon_{j,Raw}} \,, \tag{8.7}$$

where $\epsilon_{j,Raw}$ denotes the trigger efficiency not taking prescale factors into account. Hence $\omega^i_{triggered}$ reflects the different prescale factors of the jet trigger.

The overall trigger efficiency for the b-jet cross section measurement taking all jets into account is estimated after re-weighting. The overall trigger efficiencies of each p_{T} bin for b-jets and QCD background jets are estimated by summing up the triggered

p_{T} range [GeV]		cone4 trigger efficiency	
		b-jets	QCD jets
$30-50$	trigger ϵ_{Tr}	$(35.3 \pm 0.4) \cdot 10^{-6}$	$(22.63 \pm 0.02) \cdot 10^{-6}$
	trigger rate [Hz]	0.127 ± 0.003	2.26 ± 0.02
$50-90$	trigger ϵ_{Tr}	$(0.151 \pm 0.005) \cdot 10^{-3}$	$(0.0462 \pm 0.0003) \cdot 10^{-3}$
	trigger rate [Hz]	0.089 ± 0.004	0.685 ± 0.017
$90-150$	trigger ϵ_{Tr}	$(1.60 \pm 0.06) \cdot 10^{-3}$	$(0.604 \pm 0.004) \cdot 10^{-3}$
	trigger rate [Hz]	0.086 ± 0.004	0.728 ± 0.015
$150-230$	trigger ϵ_{Tr}	$(15.8 \pm 0.6) \cdot 10^{-3}$	$(7.69 \pm 0.05) \cdot 10^{-3}$
	trigger rate [Hz]	0.081 ± 0.004	0.885 ± 0.014
$230-330$	trigger ϵ_{Tr}	0.121 ± 0.005	0.0585 ± 0.0009
	trigger rate [Hz]	0.080 ± 0.005	0.818 ± 0.018
$330-450$	trigger ϵ_{Tr}	0.858 ± 0.015	0.782 ± 0.004
	trigger rate [Hz]	0.087 ± 0.004	1.67 ± 0.02
$450-590$	trigger ϵ_{Tr}	0.9999 ± 0.0019	0.9995 ± 0.0003
	trigger rate [Hz]	0.0179 ± 0.0008	0.368 ± 0.004
$590-750$	trigger ϵ_{Tr}	1 ± 0.003	0.9999 ± 0.0002
	trigger rate [Hz]	$(3.32 \pm 0.17) \cdot 10^{-3}$	$(73.1 \pm 0.9) \cdot 10^{-3}$
$750-930$	trigger ϵ_{Tr}	1 ± 0.0017	0.9998 ± 0.0003
	trigger rate [Hz]	$(0.68 \pm 0.03) \cdot 10^{-3}$	$(16.1 \pm 0.2) \cdot 10^{-3}$
$930-1130$	trigger ϵ_{Tr}	1 ± 0.006	1 ± 0.0006
	trigger rate [Hz]	$(0.168 \pm 0.013) \cdot 10^{-3}$	$(3.73 \pm 0.09) \cdot 10^{-3}$
>1130	trigger ϵ_{Tr}	1 ± 0.005	0.9999 ± 0.0003
	trigger rate [Hz]	$(0.046 \pm 0.003) \cdot 10^{-3}$	$(1.140 \pm 0.018) \cdot 10^{-3}$

Table 8.3: Trigger efficiency of leading cone4 b-jet signal events and leading cone4 QCD-jet background events as a function of the leading truth jet p_{T}.

jets weighted by $\omega^i_{triggered}$ and divided by the number of all ω_i weighted jets in the jet p_{T} bin. The resulting effective trigger efficiencies for jets are higher than the overall trigger efficiency of the leading jets. The higher trigger efficiency is due to the jet multiplicity and due to non-leading jets in events, which are triggered by higher jet triggers with smaller prescale factors. The effective trigger efficiencies for b-jets and QCD background jets are listed in Tab. B.1 for cone7 and in Tab. B.2 for cone4 jets (App. B).
The expected trigger efficiencies (without taking prescale factors into account) for b-jets are shown in Fig. 8.3(a). They show the same behavior as the trigger rates of leading jets. The trigger rate of b-jets (Fig. 8.3(b)) is larger compared to the event trigger rate due to several jets per event being counted separately.

8.2 b-Jet Reconstruction

Within this thesis a cone-based jet algorithm is used to reconstruct jets. The algorithm as well as the reconstruction performance for all QCD jets (including b-jets)

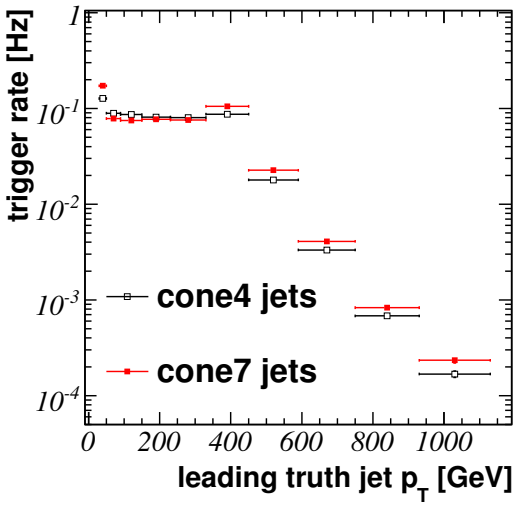

Figure 8.2: Trigger rate for b-jet events as a function of the jet truth p_{T} of the leading jet.

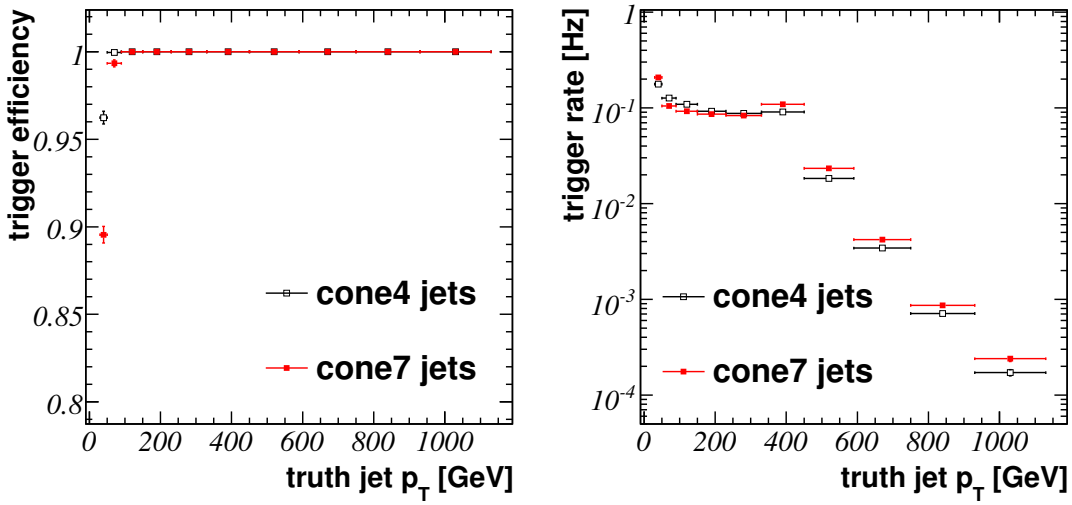

(a) (b)

Figure 8.3: Trigger efficiency for b-jets (a) as a function of the truth jet p_{T}. In (b) the expected b-jet trigger rate, estimated for an instantaneous luminosity of $\mathcal{L} = 10^{31}\,\mathrm{cm}^{-2}\mathrm{s}^{-1}$ is presented.

are explained in detail in Section 6.1. In order to measure the b-jet cross section, the efficiency ϵ_{Rec} to reconstruct b-jets in the sample of triggered events has to be estimated. The efficiency ϵ_{Rec} is defined as the portion of triggered truth b-jets with matched reconstructed b-jets $N_{RecbJet}$ divided by the triggered truth b-jets $N_{TrbJets}$:

$$\epsilon_{Rec} = \frac{N_{RecbJet}}{N_{TrbJets}} \,. \tag{8.8}$$

The jet reconstruction efficiency ϵ_{Rec} will be determined considering all b-jets in the triggered event sample as well as for the case considering only the leading b-jet of an event. The reconstruction efficiency ϵ_{Rec} has to be determined on MC truth level. As in Section 6.1 a $\Delta R < 0.2$ cut to associate a truth b-jet to a reconstructed b-jet is taken. The estimated efficiencies for cone4 and cone7 b-jets are listed in Tab. 8.4 and shown in Fig. 8.4(a) for the leading b-jet and in Fig. 8.4(b) for all b-jets in the event sample.

p_{T} range [GeV]		b-jet reconstruction efficiency leading b-jet	all b-jets
$30-50$	ϵ_{Rec} Cone4	0.959 ± 0.004	0.954 ± 0.004
	ϵ_{Rec} Cone7	0.929 ± 0.004	0.925 ± 0.004
$50-90$	ϵ_{Rec} Cone4	0.982 ± 0.004	0.980 ± 0.004
	ϵ_{Rec} Cone7	0.940 ± 0.006	0.948 ± 0.006
$90-150$	ϵ_{Rec} Cone4	0.987 ± 0.004	0.986 ± 0.004
	ϵ_{Rec} Cone7	0.983 ± 0.004	0.980 ± 0.004
$150-230$	ϵ_{Rec} Cone4	0.995 ± 0.002	0.994 ± 0.002
	ϵ_{Rec} Cone7	0.978 ± 0.004	0.988 ± 0.003
$230-330$	ϵ_{Rec} Cone4	0.994 ± 0.004	0.994 ± 0.003
	ϵ_{Rec} Cone7	0.993 ± 0.003	0.993 ± 0.003
$330-450$	ϵ_{Rec} Cone4	0.995 ± 0.004	0.995 ± 0.004
	ϵ_{Rec} Cone7	0.995 ± 0.003	0.995 ± 0.003
$450-590$	ϵ_{Rec} Cone4	0.997 ± 0.003	0.997 ± 0.003
	ϵ_{Rec} Cone7	0.989 ± 0.004	0.989 ± 0.004
$590-750$	ϵ_{Rec} Cone4	0.987 ± 0.007	0.987 ± 0.007
	ϵ_{Rec} Cone7	0.997 ± 0.003	0.997 ± 0.003
$750-930$	ϵ_{Rec} Cone4	0.997 ± 0.003	0.997 ± 0.003
	ϵ_{Rec} Cone7	0.996 ± 0.003	0.996 ± 0.003
$930-1130$	ϵ_{Rec} Cone4	0.993 ± 0.011	0.993 ± 0.011
	ϵ_{Rec} Cone7	0.985 ± 0.009	0.986 ± 0.009
>1130	ϵ_{Rec} Cone4	0.998 ± 0.007	0.998 ± 0.007
	ϵ_{Rec} Cone7	0.999 ± 0.007	0.999 ± 0.005

Table 8.4: Jet reconstruction efficiency for (leading) b-jets as a function of truth jet p_{T}.

As already seen for all QCD jets, the efficiency to reconstruct b-jets is about 99% in the jet p_{T} region considered. Only the efficiencies in the first jet p_{T} bin are lower for both chosen cone sizes, but still about 95%. The efficiencies for cone7 b-jets in the

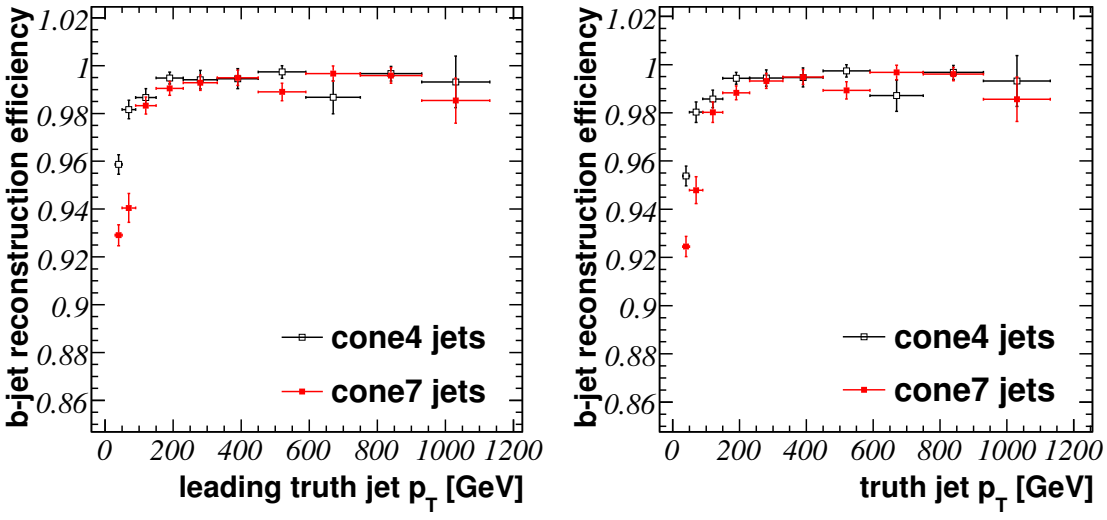

(a) (b)

Figure 8.4: b-jet reconstruction efficiency as a function of the truth jet p_{T} considering (a) the leading b-jet and (b) considering all b-jets in the event sample.

first two jet p_{T} bins are slightly smaller than for cone4 jets. This has already been seen in the efficiencies for all QCD jets as a consequence of the matching $\Delta R < 0.2$ cut and the shift of cone7 jets to higher jet p_{T}. The loss of b-jets for both cone sizes is therefore expected to be small. The uncertainties on the efficiency are estimated as described in App. C. The larger uncertainty of the two asymmetric errors is taken in the further calculation, which may lead to an unphysical uncertainty range of the efficiency above one.

The purity P_{Rec} of the reconstruction of b-jets takes fake b-jets into account. These fake b-jets have an associated b-quark but a missing matched truth b-jet. In case of the purity for the leading b-jet reconstruction, the purity also takes wrong leading b-jets into account. This means the reconstructed hardest p_{T} b-jet is associated to a truth b-jet in a lower jet p_{T} bin compared to the truth leading b-jet. This might be caused by a missing reconstructed truth leading b-jet as well as by a too low reconstructed p_{T} of the leading jet. The purity has to be estimated on reconstructed jet level in contrast to the reconstruction efficiency. In the measurement, the purity will be taken into account before the unfolding will be applied to the b-jet cross section spectrum. The efficiency of the b-jet reconstruction will be applied after the unfolding. The purity is defined as the ratio of b-jets with an associated truth b-jet $N_{RecbJet}$ to all reconstructed b-labeled jets $N_{bAllRec}$:

$$P_{Rec} = \frac{N_{RecbJet}}{N_{bAllRec}}\,. \tag{8.9}$$

In Tab. 8.5 the purities of the b-jet reconstruction for both cone sizes considering only the leading b-jet as well as all b-jets are listed. The purity as a function of the reconstructed jet p_{T} is shown in Fig. 8.5 for (a) leading b-jets and in (b) for all b-jets in the event sample.

p_{T} range [GeV]		b-jet reconstruction purity	
		leading b-jet	all b-jets
$30-50$	P_{Rec} Cone4	0.971 ± 0.004	0.979 ± 0.005
	P_{Rec} Cone7	0.912 ± 0.005	0.929 ± 0.004
$50-90$	P_{Rec} Cone4	0.984 ± 0.004	0.979 ± 0.004
	P_{Rec} Cone7	0.950 ± 0.005	0.972 ± 0.004
$90-150$	P_{Rec} Cone4	0.984 ± 0.004	0.976 ± 0.005
	P_{Rec} Cone7	0.959 ± 0.005	0.986 ± 0.004
$150-230$	P_{Rec} Cone4	0.992 ± 0.003	0.989 ± 0.003
	P_{Rec} Cone7	0.978 ± 0.004	0.986 ± 0.003
$230-330$	P_{Rec} Cone4	0.995 ± 0.004	0.995 ± 0.004
	P_{Rec} Cone7	0.981 ± 0.005	0.989 ± 0.004
$330-450$	P_{Rec} Cone4	0.996 ± 0.003	0.999 ± 0.003
	P_{Rec} Cone7	0.993 ± 0.004	0.998 ± 0.02
$450-590$	P_{Rec} Cone4	0.996 ± 0.003	0.999 ± 0.003
	P_{Rec} Cone7	0.987 ± 0.004	0.995 ± 0.003
$590-750$	P_{Rec} Cone4	0.998 ± 0.004	0.998 ± 0.004
	P_{Rec} Cone7	0.991 ± 0.005	0.996 ± 0.003
$750-930$	P_{Rec} Cone4	0.993 ± 0.004	0.995 ± 0.004
	P_{Rec} Cone7	0.994 ± 0.004	0.992 ± 0.004
$930-1130$	P_{Rec} Cone4	0.985 ± 0.013	0.992 ± 0.009
	P_{Rec} Cone7	0.983 ± 0.010	0.999 ± 0.005
>1130	P_{Rec} Cone4	0.996 ± 0.007	0.998 ± 0.009
	P_{Rec} Cone7	0.996 ± 0.009	0.981 ± 0.013

Table 8.5: Jet reconstruction purity for (leading) b-jets as a function of truth jet p_{T}.

The purity of the reconstructed b-jets is larger than 95% for jets of both cone sizes, except the first jet p_{T} bin for cone7 jets. Again, this difference is a consequence of the ΔR cut in the matching of the reconstructed to truth jets and the shift of cone7 jets towards higher jet p_{T} due to the broader cone size. The differences of the leading b-jet purity and the purity considering all b-jets in the event sample are due to the possibility that the hardest reconstructed b-jet is not associated to the hardest truth b-jet.

Due to the high purity of the reconstructed b-jets, the influence of fake b-jets is expected to be small. The error on the purity is estimated as described in App. C, which leads to asymmetric errors. The given uncertainties on the purities are the larger of the two uncertainties, which can lead to uncertainty ranges of the purity above one.

The performance of the p_{T} reconstruction of the b-jets is discussed in Section 8.4, since the jet p_{T} resolution is crucial for the unfolding.

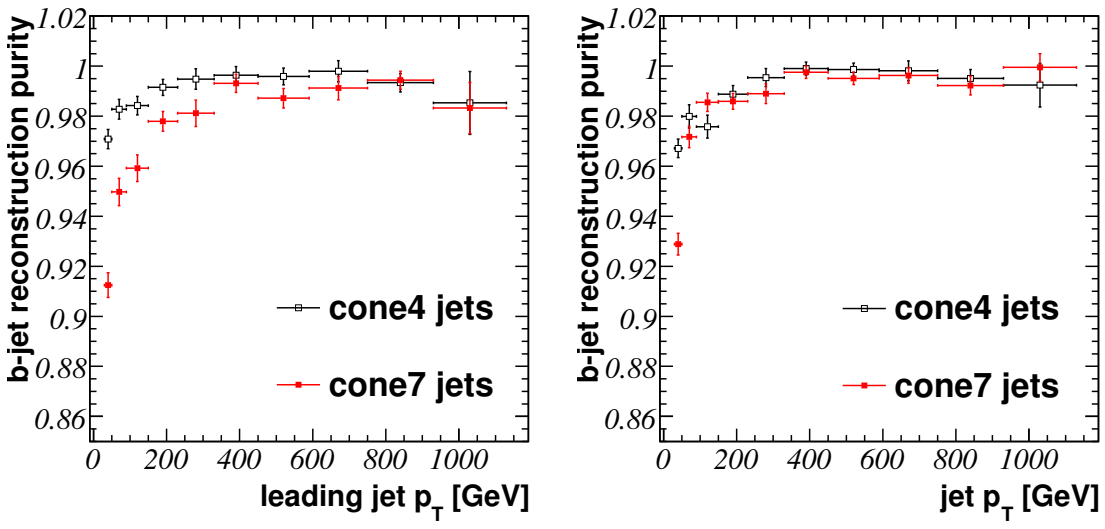

Figure 8.5: b-jet reconstruction purity as a function of the jet p_{T} considering (a) the leading b-jet and (b) considering all b-jets in the event sample.

8.3 Event Selection

Events containing jets initiated by a b-quark have to be selected from the triggered and reconstructed events. For this, the measurably long lifetime of the hadrons containing a b-quark (b-hadron) is used. Due to the longer lifetime, the b-hadrons decay after traveling some distance from the primary vertex. Often the b-hadron decays into a c-hadron, which in turn forms a tertiary vertex. The typical topology of a b-jet is therefore a cascade decay with two vertices separated from the primary vertex: The decay vertex of the b-hadron and the decay vertex of the c-hadron.

Therefore b-jets show on average larger impact parameters of particle tracks, which originate from the secondary or tertiary vertex, compared to particle tracks originating from the primary vertex. The larger impact parameter is used to calculate a b-tagging weight, which is proportional to the probability, that the track originates in a decay point of a b-hadron. The b-tagging algorithm based on impact parameter information is discussed in detail in Section 8.3.1. Hadrons containing a c-quark (not originating from a decay of a b-hadron) on average have a lower lifetime compared to b-hadrons. However, the lifetime of such c-like hadrons also allows the decay into other particles forming a secondary vertex. Therefore c-like hadrons form an important background for b-tagging. In this chapter the distributions of the discriminating variables are shown for b-jets, c-jets as well as for light quark jets (jets initiated by gluons or an u-,d- or s-quark). In addition to the impact parameter information, the secondary decay vertex of the b-hadron is reconstructed. Information of this secondary vertex is used on top of the lifetime based b-tagging in order to improve the selection of b-jets and the rejection of QCD background jets (c-quark and light quark jets). The algorithm to find secondary vertices in jets as well as the way to combine secondary vertex and lifetime based b-tagging are discussed in Section 8.3.2.

The resulting b-tagging weights of the jets are used as the discriminative variable for b-jets against c- and QCD jets. The resulting performance of the b-jet event selection for the sample using all b-jets as well as using leading b-jets is presented in Section 8.3.3.

8.3.1 Lifetime Based b-Tagging

The (on average) longer lifetime of b-hadrons leads to the decay of such particles in a secondary vertex at a certain distance to the primary vertex. Therefore, particles originating from this secondary vertex tend to have higher impact parameter w.r.t. to the primary vertex. The b-tagging methods discussed first use the impact parameters of tracks. In the ATLAS software, the lifetime based taggers are known as IP2D, which uses the transverse impact parameter as a discriminant variable for b-jets, and IP3D, which uses the longitudinal impact parameter information in addition.
In order to identify b-jets, the primary vertex, jets and tracks have to be reconstructed. The first step is the association of selected tracks to the different jets, since tracks carry the information needed by the b-tagging. The selection cuts on the tracks ensure a certain reconstruction quality of the tracks, i.e. a largest possible reduction of the fake track rate, while keeping the efficiency of track reconstruction high. The quality cuts for b-tagging are listed in Tab. 8.6.

track selection criterion	cut
transverse momentum	$p_{\mathrm{T}} > 1\,\mathrm{GeV}$
maximum transverse impact parameter	$\lvert d_0 \rvert < 1\,\mathrm{mm}$
maximum longitudinal impact parameter	$\lvert z_0 - z_{pv} \rvert \sin\theta < 1.5\,\mathrm{mm}$
number of pixel and SCT hits	$n_{Si} \geq 7$
pixel hits	$n_{pix} \geq 2$, one in the b-layer

Table 8.6: Track selection cuts for lifetime based b-tagging.

The association of the tracks to jets is based on geometrical ΔR_t matching of the tracks w.r.t. the reconstructed jet axis. The matching cut is chosen to be the same $\Delta R_t = 0.4$ for cone4 as well as for cone7 jets. In addition, the influence of a broader matching cone size $\Delta R_t = 0.7$ for tracks associated to cone7 jets will be discussed. In Fig. 8.6 the track multiplicities per jet are presented.
The track multiplicities of cone4 and cone7 jets are the same in the case both use $\Delta R_t = 0.4$, as expected. In case of $\Delta R_t = 0.7$ the track multiplicity increases. Due to the broader matching cone, more tracks are associated to a jet. The same behavior is seen for background jets. The track multiplicity changes for different p_{T} bins of the jet. Due to the higher energy per jet the average track multiplicity will increase towards higher p_{T} of a jet. As an example, the b-jet track multiplicity distribution for the lower p_{T} bin of $(50-90)\,\mathrm{GeV}$ as well as for the higher p_{T} bin of $(590-750)\,\mathrm{GeV}$ are shown in Fig. 8.7.
Tracks originating from a secondary vertex tend to have higher impact parameters d_0 w.r.t. the primary vertex than those originating from the primary vertex. In

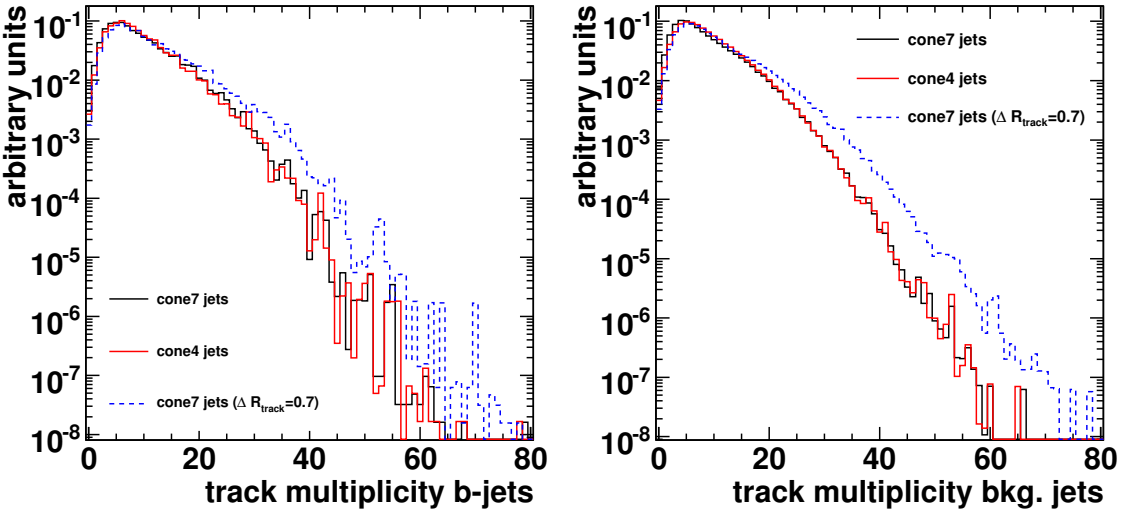

(a) (b)

Figure 8.6: Multiplicities of tracks associated to cone7 and cone4 jets for (a) b- and (b) QCD jets. For cone7 jets, two track matching cone sizes of $\Delta R_t = 0.4$ and $\Delta R_t = 0.7$ are presented.

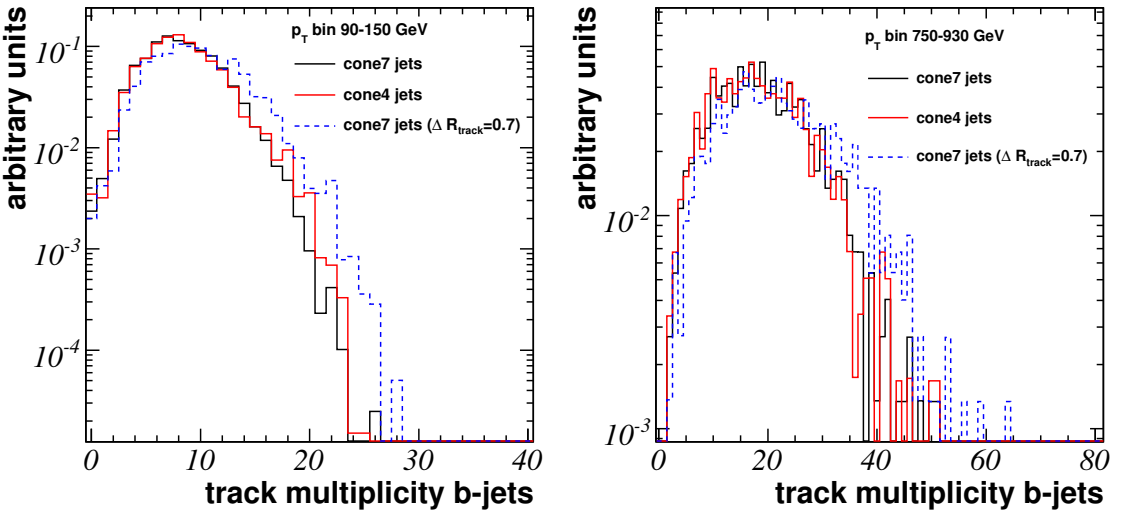

(a) (b)

Figure 8.7: b-jet track multiplicities for two different jet p_{T} regions.

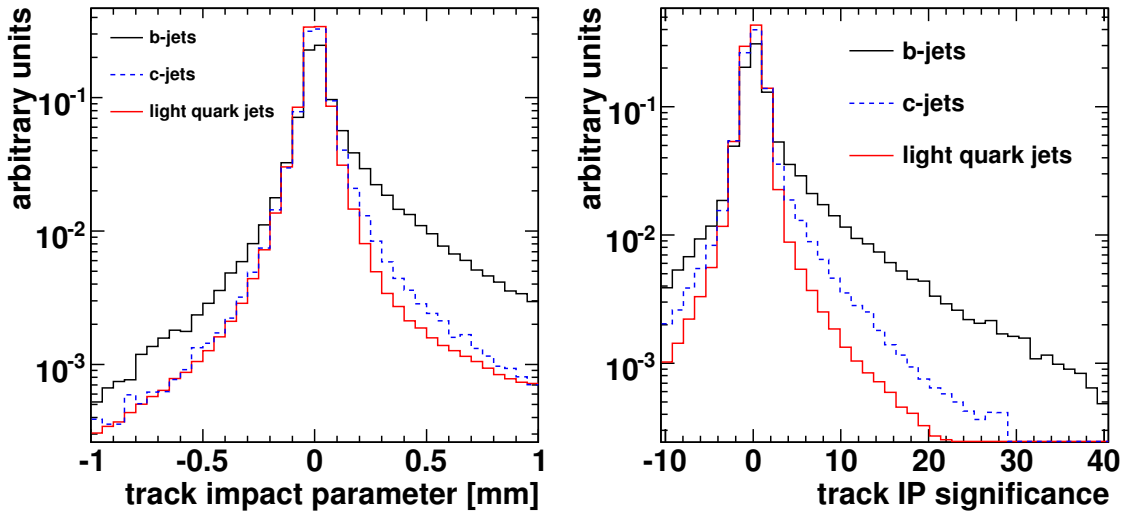

(a) (b)

Figure 8.8: (a) Signed impact parameter distributions of tracks in b-, c- and light quark jets. (b) Significance d_0/σ_{d_0} of tracks in b-, c- and light quark jets.

order to take into account, that the secondary decay vertex of the b-like hadron has to lie on its flight path, the impact parameter is signed. The sign of the impact parameter is defined by

$$sign(d_0) = sign((\vec{P}_j \times \vec{P}_t)(\vec{P}_t \times (\vec{X}_{pv} - \vec{X}_t))) \tag{8.10}$$

where $\vec{P}_t$ and $\vec{X}_t$ are the direction and the position of the track at the point of closest approach to the primary vertex. $\vec{P}_j$ denotes the reconstructed jet axis and $\vec{X}_{pv}$ the position of the reconstructed primary vertex. Therefore, the sign of the impact parameter is defined to be positive if the point of closest approach is in front (in the direction of the jet) of the plane perpendicular to the jet axis containing the primary vertex. The distributions of the track impact parameter for tracks in b-jets, c-jets and in light quark jets are shown in Fig. 8.8(a).
Tracks in light quark jets originate from the primary vertex and the distribution reflects the experimental resolution. Due to the longer lifetime b-jet tracks have a larger positive signed impact parameter, whereas the negative tail in the distributions reflects the experimental resolution. The surplus of c-jet tracks on the positive side is caused by the longer lifetime of c-hadrons. Since the tail of the b-jet tracks on the positive side is larger than for the background jets, the impact parameter is used to discriminate against QCD background jets.
In order to take the reconstruction precision of the track impact parameter into account, the significance $S = \frac{d_0}{\sigma_{d_0}}$ of each track is calculated. This results in a higher weight for more precisely reconstructed tracks. In Fig. 8.8(b) the significance S distributions for b-jet and background jet tracks are presented. As expected the distribution of b-jet tracks extends to higher significances compared to the one for tracks in light quark jets. The differences between the significance distributions will decrease towards higher jet p_{T} as can be seen in Fig. 8.9.

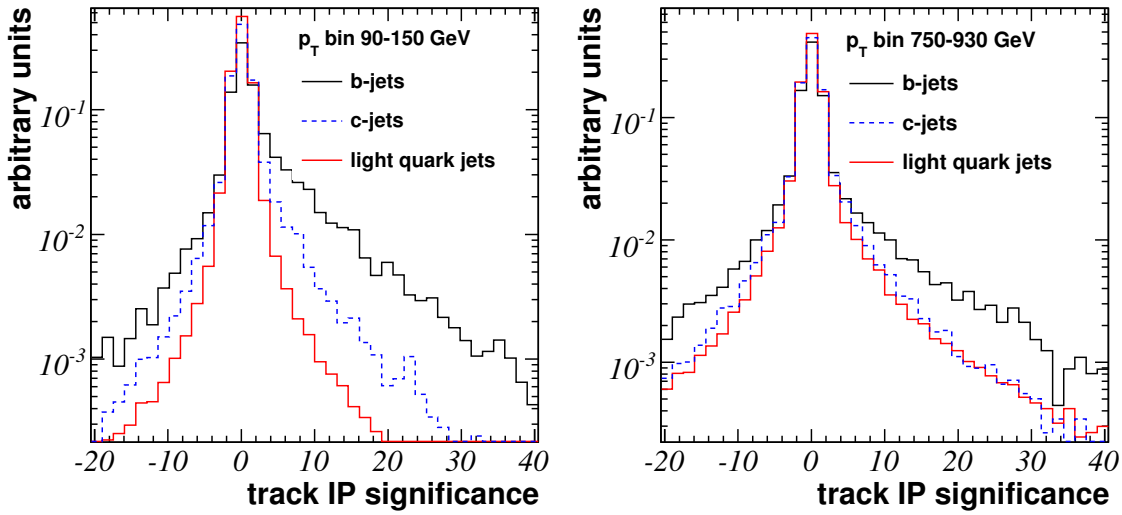

Figure 8.9: Distribution of the track significance S for signal and background cone7 jets (a) in jet p_{T} bin $(90 - 150)\,\mathrm{GeV}$ and (b) in jet p_{T} bin $(590 - 750)\,\mathrm{GeV}$.

Several reasons lead to the smaller differences for b-jet tracks and background jet tracks at higher jet p_{T}. The number of fragmentation tracks, which do not origin from the b-quark itself increases, which will decrease the b-tagging performance. The track density of such high energetic jets will increase and therefore the tracking efficiency will be lower. The number of fake tracks or tracks with shared hits (e.g. a pixel hit, which is assigned to more than one track) will be larger than for lower p_{T} jets. In addition, the Lorentz boost of high energetic b-hadrons can lead to a decay beyond the first pixel layer and tracks originating from this kind of b-hadron decay have a missing or shared hit in the first pixel layer. However, the interaction of the b-hadron with the first pixel layer is not included in the detector simulation and therefore the requirement of a pixel hit in the first detector layer will not be fulfilled. In order to take these effects in higher jet p_{T} regions into account, the track selection cuts are optimized to increase the b-tagging efficiency. This will be discussed in Section 8.3.3.

In order to calculate a jet weight, which is proportional to the probability for a jet to be initiated by a b-quark, the track significances are compared to calibration histograms. These two calibration histograms are simulated normalized distributions of tracks in b-jets as well as in background jets, i.e. the histograms are an approximation of the probability density function of a track to have a significance S for the cases of b-jet tracks and for background jet tracks. The track significance S_i of a track i of a jet of unknown flavor will be compared to the calibration distributions. The ratio of the probability $b(S_i)$ for the hypothesis of being a b-jet track divided by the background jet probability $u(S_i)$ is called the track weight w_i:

$$w_i = \frac{b(S_i)}{u(S_i)}\,. \tag{8.11}$$

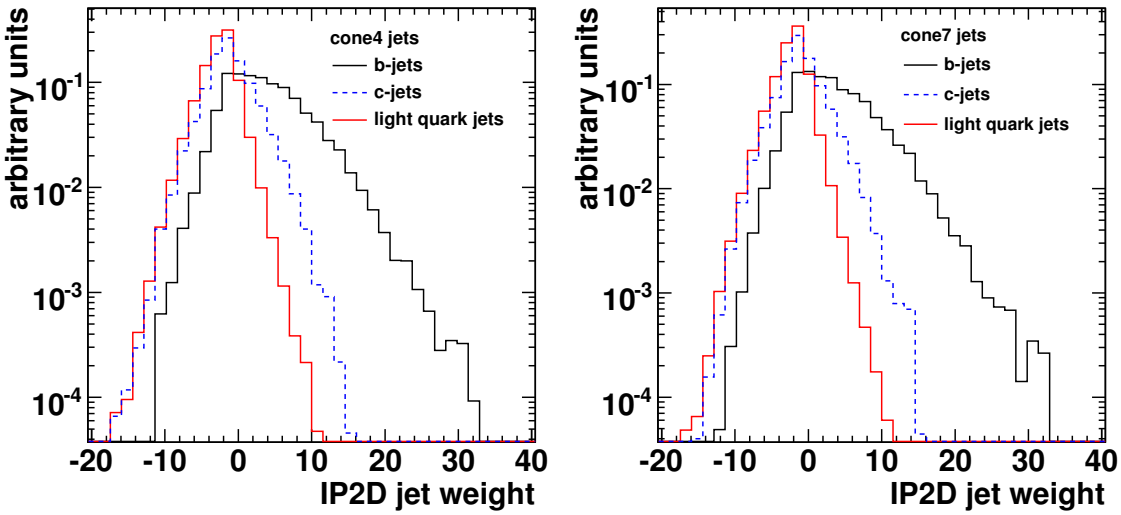

(a) (b)

Figure 8.10: IP2D jet weight distributions for signal and background jets using (a) cone4 and (b) cone7 jets.

The track weight is calculated for each track associated to a jet of unknown flavor. In order to calculate a jet weight W_{IP2D}, which is proportional to the probability, that the jet is initiated by a b-quark, all track weights are combined via

$$W_{IP2D} = \sum_i \ln w_i = \sum_i \ln \frac{b(S_i)}{u(S_i)} \,. \tag{8.12}$$

The jet weight distributions of b- and background cone4 and cone7 jets are shown in Fig. 8.10. The jet weights extend to higher values for b-jets, while the jet weights of light quark jets are distributed around zero. The c-jet weights also extend to higher values as expected from the previous discussion.
The jet weight distribution for background jets using the cone7 jet reconstruction algorithm is slightly broader compared to cone4 jets. This is due to the labeling procedure of b-jets. The broader cone size of cone7 jets leads to a more ambiguous labeling of a b-jet. For both cone algorithms, the same $\Delta R = 0.3$ matching cut between the b-quark direction and the jet axis is taken. Due to the broader cone size of cone7 jets it is more likely, that the b-quark direction differs by more than $\Delta R = 0.3$ from the reconstructed jet axis and hence the jet is labeled a background jet although there is b-content inside the cone radius. This effect is seen in the lowest jet p_{T} bin, but decreases towards higher jet p_{T} bins, since the tracks in the jets are more collinear. Therefore, the labeling algorithm for b-jets is kept the same for both cone sizes.
The jet weight distributions for two different jet p_{T} bins are shown in Fig. 8.11. The differences of the jet weights decrease towards higher jet p_{T}, since the jet weight distributions for background are broader and the b-jet distribution is becoming narrower. This will lead to a decrease of the b-tagging performance in higher jet p_{T} bins.

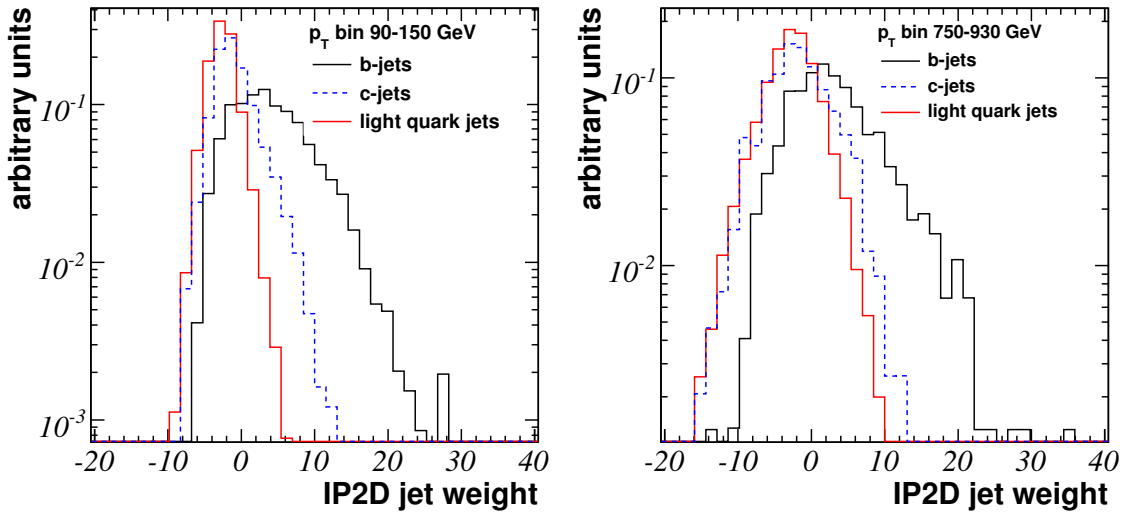

Figure 8.11: IP2D jet weight distributions for signal and background jets (a) in jet p_{T} bin $(90 - 150)$ GeV and (b) in jet p_{T} bin $(590 - 750)$ GeV

The IP2D algorithm takes only the impact parameter information in the transverse plane into account. To increase the b-tagging performance, in addition the longitudinal impact parameter from each track in a jet may be considered. The longitudinal impact parameter significance is added to the transverse impact parameter significance. This IP3D algorithm calculates a track weight for each track. In order to calculate a track weight analogously to the IP2D tagger, 2-dimensional calibration histograms are needed in order to take correlations of the impact parameter significances into account. The calibration histograms contain the transverse impact parameter significance versus the longitudinal impact parameter significance of b-jet tracks as well as for background jet tracks. Hence the calibration histograms represent an estimate of the probability density functions for tracks from b-jets and for tracks from background jets to have a certain 3-dimensional impact parameter significance S_{3D_i}. Like for the IP2D tagger, the track weight for a track i from a jet of unknown flavor is estimated by the ratio of the b-jet track hypothesis probability $b(S_{3D_i})$ and the background jet hypothesis probability $u(S_{3D_i})$ using (8.11). The final IP3D jet weight is calculated by (8.12).

The IP3D jet weight distributions for b-jets and background jets are shown in Fig. 8.12 for cone4 and cone7 jets.

Due to the additional information provided by the longitudinal impact parameter of the tracks, the jet weights of b-jets increase compared to the IP2D jet weight distribution. The b-tagging performance is expected to be higher than for IP2D although the main discriminating power is contained in the transverse impact parameter, since the hit precision in the transverse plane is better than in the longitudinal direction of the detector.

In order to distinguish between b-jets and background jets a cut on the jet weight has to be determined. Each jet above the cut is labeled a tagged b-jet. The cut

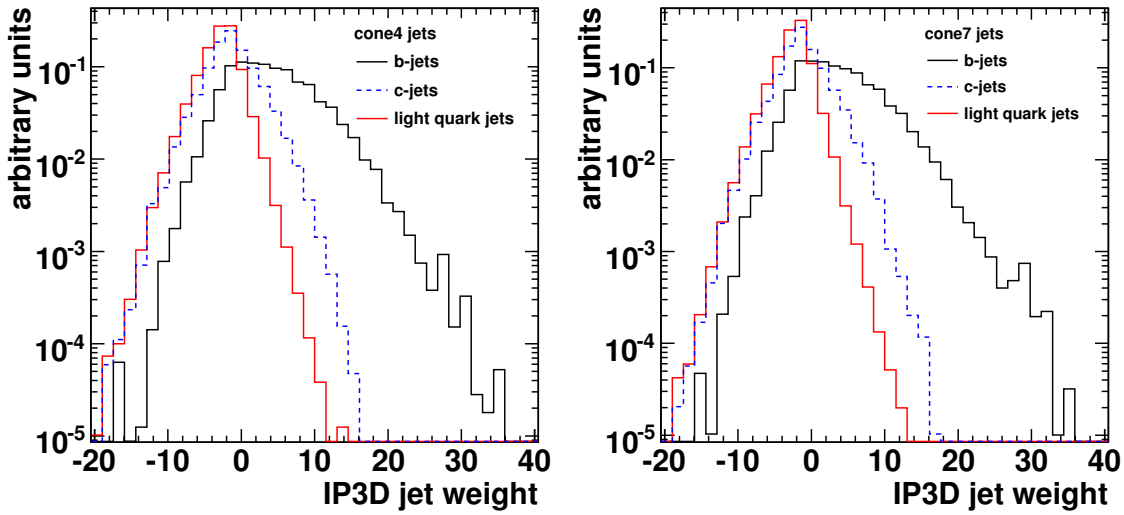

(a) (b)

Figure 8.12: IP3D jet weight distributions for b-jet signal and background jets using (a) cone4 and (b) cone7 jets.

value has to be optimized for the selection of jets associated with truth b-jets by minimizing the mistagging of background jets. The determination of the cut value on the jet weights is described in Section 8.3.3.

8.3.2 Secondary Vertex Based b-Tagging

The longer lifetime of the b-hadrons leads to a decay in a secondary vertex separated from the primary vertex. In addition to the impact parameter based b-tagging algorithms, the secondary vertex based algorithm reconstructs the secondary vertex explicitly. Additional information from the secondary vertex is used to increase the performance of the b-tagging. The algorithm is known in the ATLAS software as SV algorithm [47].

The secondary vertex based b-tagging starts with the search for a secondary vertex inside a jet. In b-jets often two vertices are present. The first one from the b-hadron decay (often to a c-hadron) and the second one from a c-hadron decay. It is difficult to reconstruct both decay vertices separately, since firstly the probability to have at least two charged particles coming from each vertex, which are reconstructed, is low. Secondly the resolution of the track parameters is not sufficiently good to resolve the two vertices, especially in the lower jet p_{T} region. For b-tagging it is important to reconstruct secondary vertices with high efficiency, while a complete reconstruction of the decay topology is not necessary. Therefore the SV algorithm is looking for one secondary vertex in an inclusive way. The aim for the secondary vertex finding is a gain in the b-tagging performance and not a reconstruction of a specific decay topology.

The secondary vertex finding is based on the software package VkalVrt [48]. The inclusive secondary vertex reconstruction starts with a selection of tracks out of all

tracks matched to the jet. The track requirements are listed in Tab. 8.7.

track selection criterion	cut
transverse momentum	$p_{\mathrm{T}} > 0.3\,\mathrm{GeV}$
maximum transverse impact parameter	$\lvert d_0\rvert < 5\,\mathrm{mm}$
uncertainty of transverse impact parameter	$\sigma_{d_0} < 1.0\,\mathrm{mm}$
number of pixel and SCT hits	$n_{Si} \geq 7$
SCT hits	$n_{SCT} \geq$
pixel hits	$n_{pix} \geq 1$
quality of the track fit	$\chi^2/ndf < 3.0$

Table 8.7: Track selection cuts for secondary vertex reconstruction.

The secondary vertex search starts with the determination of two-track vertices inside the jet with a maximum $\chi^2 < 4.5$. In addition both tracks have to have a distance to the primary vertex divided by the error of greater than 2.5, whereas the sum of both significances must be greater than 6.0. Some of the two-track vertices originate from K^0_S or Λ^0 decays as well as photon conversions $\gamma \to e^+e^-$ or hadronic interactions with the detector material. The invariant mass of a two-track vertex is calculated using a $\pi^-\pi^+$ hypothesis for K^0_s-decays and a $p\pi^-$ hypothesis for a Λ^0-decay. In case the invariant mass of such a two-track vertex corresponds to the K^0_s or Λ^0 mass, the tracks are rejected for further secondary vertex searches. Also the tracks from a two-track vertex with a transverse distance to the primary vertex, which is compatible to the positions of detector layers, are not considered further.
The remaining tracks matched to the jet are used for a secondary vertex fit based on a Kalman filter approach. The resulting χ^2_{vertex} of the secondary vertex fit is compared to a certain χ^2_{acc}. If the χ^2_{vertex} of the vertex fit is larger than the cut value, the track with the highest χ^2_{track} contribution is removed from the list of tracks for the fit and the vertex is fitted again until the vertex χ^2_{vertex} is below the cut or no tracks are left for vertex fitting.
In Fig. 8.13 the efficiencies ϵ_b, ϵ_c, and ϵ_u to reconstruct a secondary vertex in a b-, c- and light quark jet as a function of the jet p_{T} are presented. The efficiency ϵ_b is above 60% for the whole p_{T} region considered and rises above 80% for a jet p_{T} of about 100 to 400 GeV. The number of (fake) secondary vertices in light quark jets increases towards higher jet p_{T}. In the lower jet p_{T} region, ϵ_u is smaller than 10% while it increases to 60% for very high jet p_{T} due to higher track density and higher track multiplicity. Therefore the discrimination between b-jets and background jets due to a reconstructed vertex inside the jet itself will decrease. A higher track p_{T} cut in the track selection and a larger cut on the significance of the distance of two-track vertices to the primary vertex as well as a smaller cone size around the jet axis, in which tracks are taken for the secondary vertex reconstruction, will decrease the number of fake vertices.
In order to increase the performance of b-tagging on top of the impact parameter based b-tagging algorithms, additional discriminating variables have to be constructed. The distance of the primary to the secondary vertex already results in the

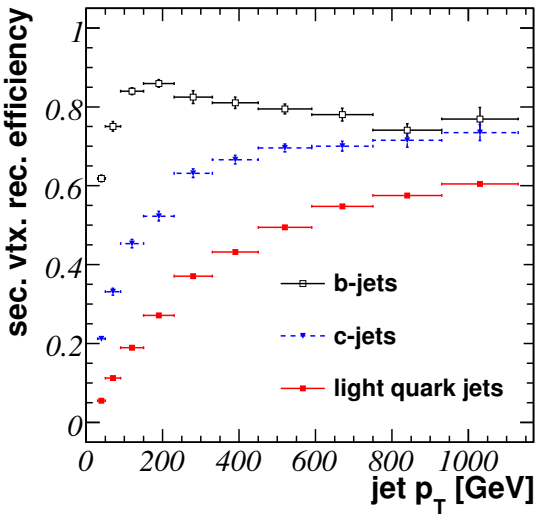

Figure 8.13: Secondary vertex reconstruction efficiency in b-, c- and light quark jets as a function of jet p_{T}.

larger impact parameter of tracks coming from a b-hadron decays w.r.t. primary vertex and will not lead to a gain in the performance of b-tagging, since this information is used in the IP3D algorithm. Therefore, the distance is not taken into account. The three discriminating variables in secondary vertex based b-tagging are

- the number of two-track vertices N: Due to the cascade-decay of a b-hadron, the number of two-track vertices tends to be higher in b-jets than in c-jets or for fake secondary vertices in light-quark jets,
- the invariant mass of the secondary vertex: The invariant mass of secondary vertices from b-hadron decays is significantly larger compared to the invariant mass of secondary vertices coming from a decay of a c-hadron or fake vertices in light quark jets due to the larger mass of the b-hadron,
- the fraction F of the energy sum of the tracks from the secondary vertex w.r.t. to the summed energy of all tracks in the jet. This variable is sensitive to the hard fragmentation function of b-quarks.

The distributions of the three discriminating variables are shown in Fig. 8.14.
For all three variables, the distributions for vertices in b-jets extend to higher values and are used to identify b-jets. The distributions for c-jets also extend to higher values compared to the light quark jet vertices, but less than for b-jets. Therefore the c-jet background will be suppressed using these variables. Since the invariant mass of any b-hadron is less than 6 GeV, the secondary vertex finding algorithm removes tracks from the track list in case the invariant mass would exceed this mass limit.
As already shown for the impact parameter based tagger, the distributions depend strongly on the jet p_{T} region. As an example the distributions for the variables in

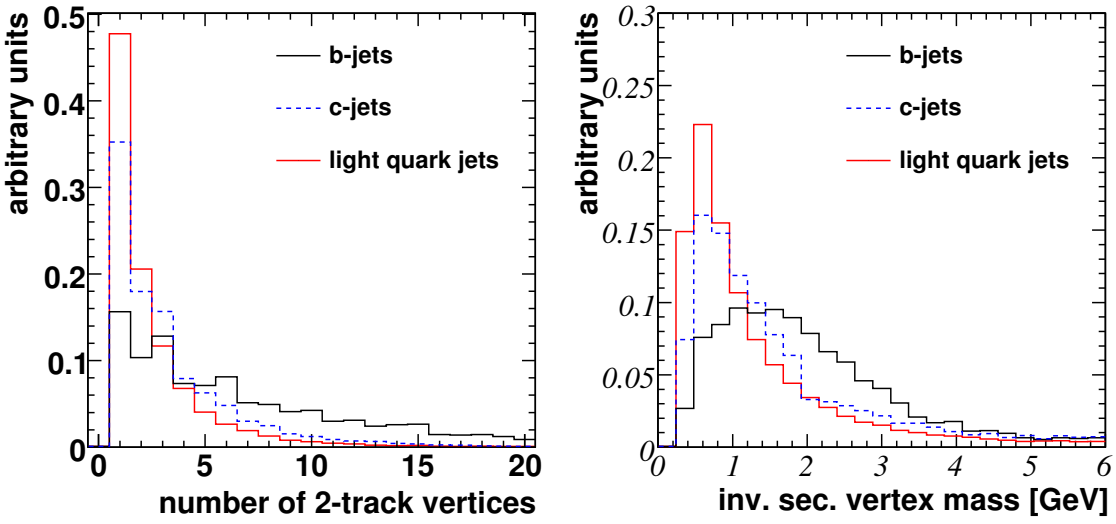

(a) (b)

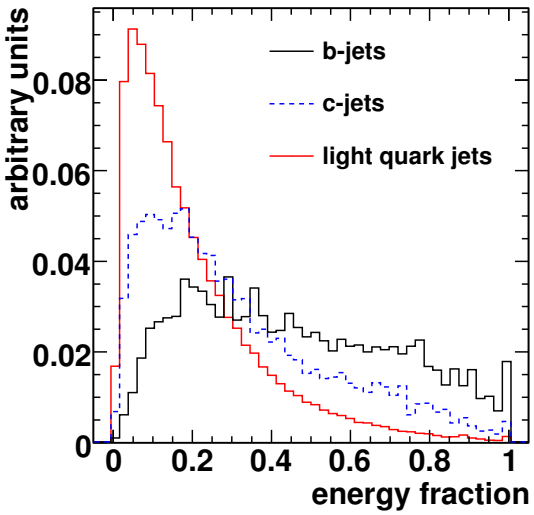

(c)

Figure 8.14: Variables used in secondary vertex based b-tagging: (a) Number of two-track vertices, (b) invariant mass of the secondary vertex and (c) fraction of the energy sum of tracks from the secondary vertex w.r.t. the energy sum of all tracks associated to the jet.

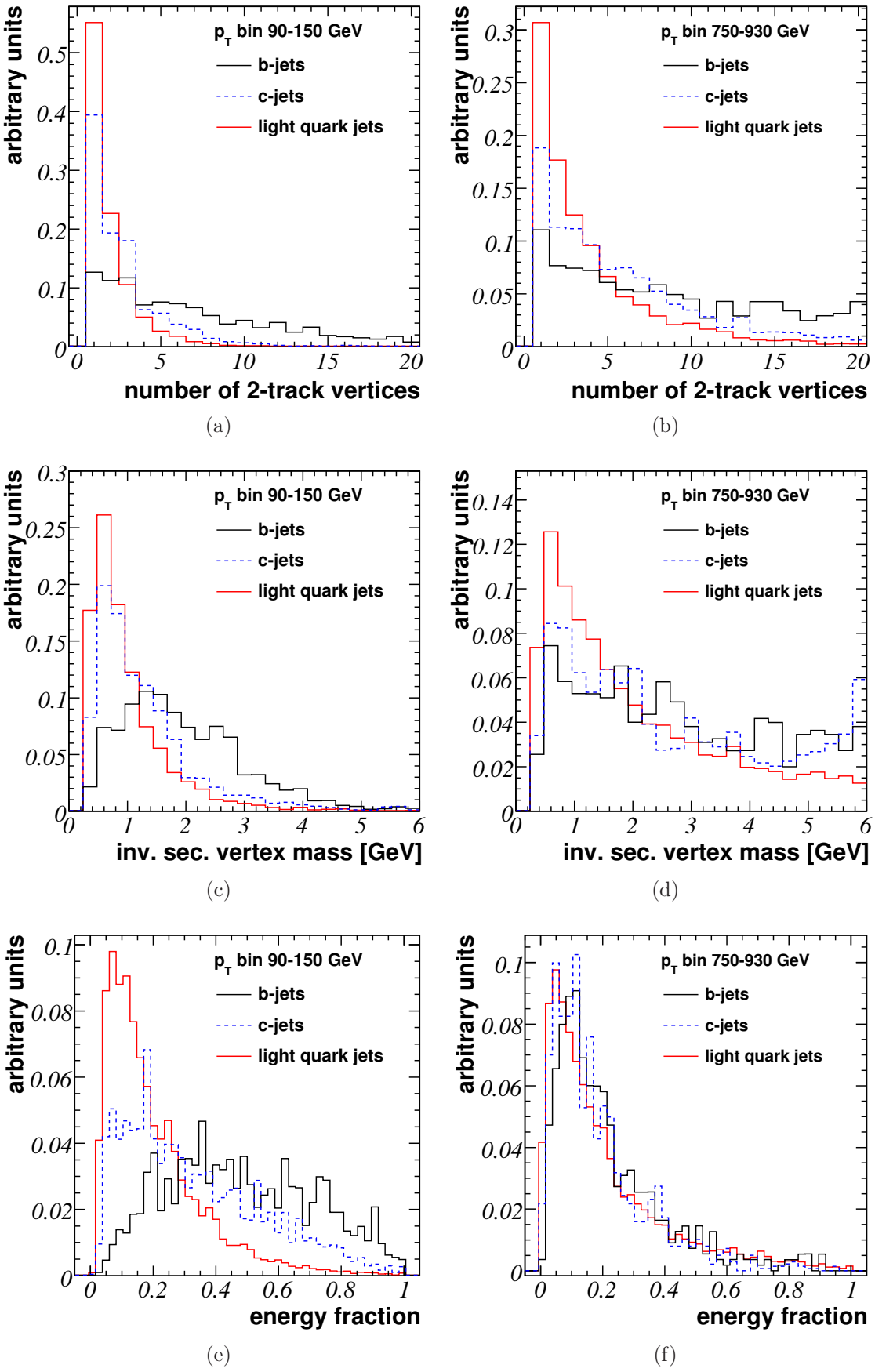

Figure 8.15: Secondary vertex based b-tagging variables for two different jet p_{T} bins.

the lower jet p_{T} bin of $(90-150)$ GeV and in the higher jet p_{T} bin of $(750-930)$ GeV are presented in Fig. 8.15(a)-(f).
The differences in the b-tagging variables become smaller towards higher jet p_{T}. In case of the energy fraction F, only small differences between b-jets and background jets are seen at high jet p_{T}. The discriminating power between b-jets and background jets will decrease and therefore the b-tagging performance will be worse in the higher jet p_{T} region in case the default configuration of the b-tagging algorithm is used. Tuning cuts for higher jet p_{T} will recover some of the b-tagging performance although the general performance will be worse. This is discussed in Section 8.3.3.
The three variables are combined to a jet weight, which will be used in addition to the impact parameter based jet weight from the IP3D algorithm. Thus the additional jet weight from the SV tagger should also be the logarithm of the ratio of the probability density functions for b-jets and background jets. Calibration events are used to produce calibration histograms for the different variables of interest. The histograms are, after smoothing, estimates of the probability density functions for the variables used in b-tagging. The number of events per bin should be as equal as possible in order to obtain similar statistical accuracy for the estimation of the probability density functions. In case of a steeply falling distribution, much higher event statistics is needed to provide a stable estimate for the probability density function. In order to cope with these problems, the chosen b-tagging variables are transformed:

- number of two-track vertices $N' = \log(n)$,
- invariant mass $M' = \frac{M}{M+1}$,
- energy fraction $F' = F^{0.7}$.

To take correlations of the three variables into account, the calibration histogram needs to be multidimensional. The probability density function is estimated from the multidimensional histogram using the ASH (Average Shifted Histograms) smoothing method [49] with linear extrapolations between the bins.
In addition to the discriminative variables, the efficiency ϵ to reconstruct a secondary vertex in the jet is used for the final probability density function:

$$PDF = (1-\epsilon)\delta(M', F', N') + \epsilon ASH(M', F', N')\,. \tag{8.13}$$

Since a three-dimensional calibration histogram requires a large number of events to be calibrated, two slightly different secondary vertex based b-tagging algorithms are implemented, known as SV1 and SV2. In the SV2 algorithm a three dimensional calibration histogram is used, while SV1 adds the information from the number of two-track vertices N' separately to a two-dimensional calibration histogram in M' and F'. Due to the large number of calibration events needed for the three-dimensional histogram for SV2, the combination of the IP3D and SV1 b-tagging algorithm is the default choice for b-tagging.

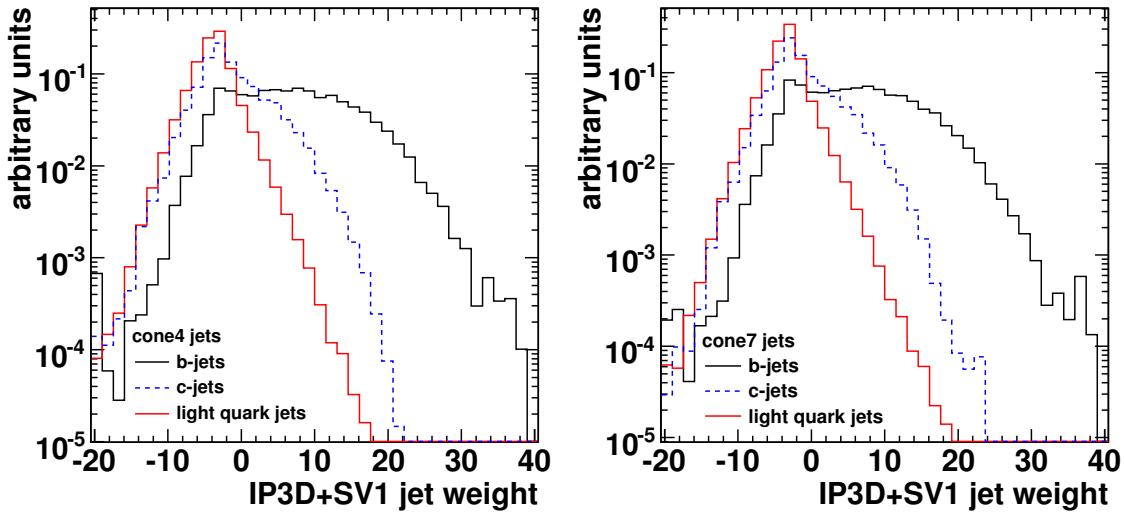

(a) (b)

Figure 8.16: Jet weight distributions of the IP3D+SV1 combination for signal and background jets reconstructed with (a) cone4 and (b) cone7 jet algorithm.

The jet weight w_{SV} for a jet of unknown flavor is the ratio of the value of the PDF for a b-jet hypothesis PDF_b to the PDF of a background jet hypothesis PDF_u evaluated at the point (M', F', N') for the jet considered:

$$\begin{aligned} w_{SV} &= \log\left(\frac{PDF_b(M', F', N')}{PDF_u(M', F', N')}\right) \\ &= \log\left(\frac{(1-\epsilon_b)\delta(M', F', N') + \epsilon ASH_b(M', F', N')}{(1-\epsilon_u)\delta(M', F', N') + \epsilon ASH_u(M', F', N')}\right) . \end{aligned} \tag{8.14}$$

In case of no secondary vertex is reconstructed, only the part with the δ-function contributes to the jet weight, which relates the probability to find no secondary vertex in a b-jet to the probability to find no secondary vertex in a background jet. The reconstruction efficiencies ϵ_b and ϵ_u are parameters also taken from calibration events ($\epsilon_b = 73.8\%$, $\epsilon_u = 7.3\%$ as default values) and will differ for different jet p_{T} regions as well as for different event topologies.
If a reconstructed secondary vertex inside the jet is found, again the ratio of the reconstruction efficiencies as well as the ratios of the probability density functions at the point (M', F', N') are taken into account. The jet weight w_{jet} of a jet of unknown flavor is the combination of the jet weight from the IP3D tagger and the SV tagger given by

$$w_{Jet} = w_{IP3D} + w_{SV} . \tag{8.15}$$

In Fig. 8.16 the jet weight distribution for the combination of the SV1 and IP3D taggers for b-, c- and light quark jets (cone7 and cone4 jets) is presented.
The jet weights of b-jets extend to higher values compared to the distributions for the impact parameter based tagger, which will result in a better performance of

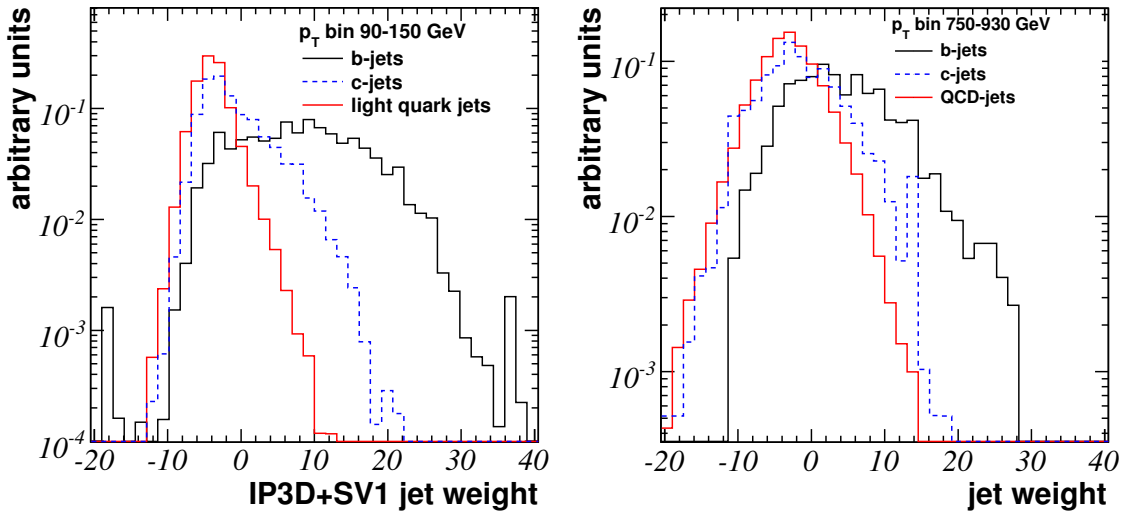

(a) (b)

Figure 8.17: SV1+IP3D jet weight distributions for signal and background jets reconstructed with cone7 jet algorithm for two different jet p_{T} bins.

b-tagging. The tail of positive jet weights for c-jets is (like for the impact parameter based tagger) larger compared to the light quark jet distribution, but still less than the b-jet distribution. Therefore the suppression of c-jet background will be less compared to the light quark jet background.
The distributions of jet weights for signal and background jets in two different jet p_{T} bins are shown in Fig. 8.17(a) and (b).
Again the widths of the jet weight distributions of b-jets become smaller towards higher jet p_{T}, while the background jet distributions become broader. This will reduce the b-tagging performance in the higher jet p_{T} region.

8.3.3 Performance of b-Tagging

The flavor of a measured jet is a priori unknown (jet with unknown flavor). The b-tagging algorithm IP3D+SV1 computes a jet weight w_{jet} for each jet, which statistically tends to higher values in case the jet is initiated by a b-quark compared to a c- or a light quark jet (Fig. 8.16). Therefore, the jet weights of jets with unknown flavor are used to select b-jets, rejecting c- and light quark jets.
For the b-jet cross section measurement a cut value w_{cut} on the jet weight has to be determined to label reconstructed jets as b-jets in case of a higher jet weight ($w_{jet} > w_{cut}$) and as a background jets otherwise ($w_{jet} \leq w_{cut}$). Different cut values will lead to different efficiencies of the b-tagging and different purity values for the sample of selected jets. Since the highest b-tagging performance (i.e. highest purity at a certain b-tagging efficiency) is expected for the combination of the secondary vertex and the impact parameter based b-tagging algorithms, the IP3D+SV1 jet weights are used to distinguish between signal and background jets.
The efficiency of b-jet identification is defined as

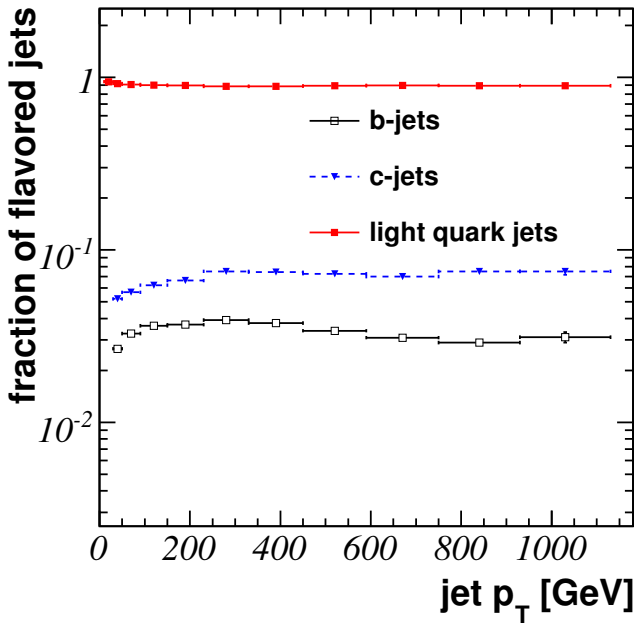

Figure 8.18: Fraction of different flavored jets in the jet sample.

$$\epsilon_{Tag} = \frac{N_{btagged}}{N_{bAllRec}}\,, \tag{8.16}$$

where $N_{btagged}$ is the number of tagged b-jets out of $N_{bAllRec}$ reconstructed and triggered b-jets. The purity is defined as the ratio of $N_{btagged}$ divided by all tagged jets N_{Sel},

$$P_{tag} = \frac{N_{btagged}}{N_{Sel}}\,. \tag{8.17}$$

The purity is equivalently expressed by the different fractions (f_b, f_c, f_u) of flavored jets in the event sample and the efficiency ϵ_{Tag} to tag a b-jet correctly as well as the misidentification rate (ϵ_c, ϵ_u) to tag a c- or light quark jet as a b-jet:

$$P_{Tag} = \frac{f_b\epsilon_{Tag}}{f_b\epsilon_b + f_c\epsilon_c + f_u\epsilon_u}\,. \tag{8.18}$$

The purity of the selected event sample depends on the cut value on the jet weights itself and on the ratio of background to signal events in the event sample, which is given by nature. In Fig. 8.18 the relative fractions of the different jets in the triggered and reconstructed jet sample are shown. The light quark ratio is about 90% across the whole jet p_{T} range, while the fraction of b-jets is lower by about a factor of 30. The c-jet fraction is slightly higher (by a factor ≈ 2) than the b-jet contribution. Due to the high background jet fraction, also low mistagging rates will lead to a decrease of the purity of the b-tagged event or jet sample.
In this section, the cut values w_{cut} will be determined, by optimizing the jet selection w.r.t. the efficiency, as well as the purity of the sample of selected (b-) jets. The cut values w_{cut} will be estimated by using all jets in the event sample for each jet

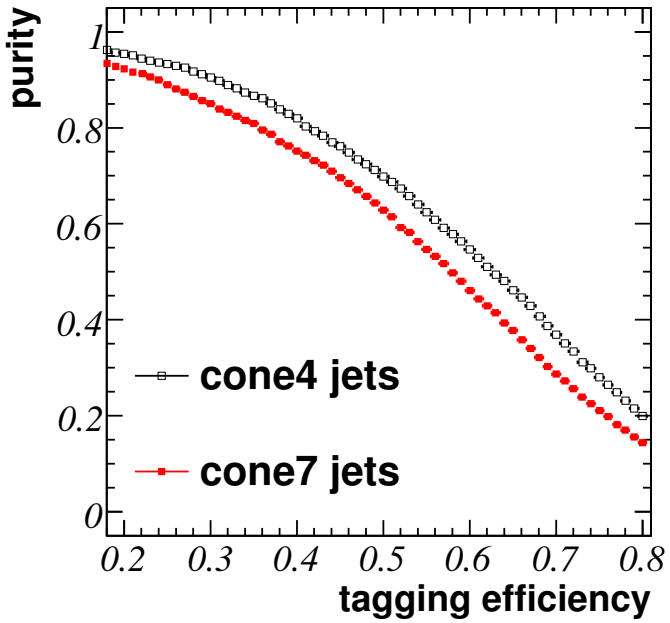

Figure 8.19: b-jet sample purity as a function of the efficiency to tag b-jets for cone7 and cone4 jets.

p_{T} bin separately. The same cut values will be used for the differential leading b-jet cross section measurement.

The b-tagging performance will not be uniform over the whole jet p_{T} range considered. Therefore, the optimal cut value on the jet weights will differ for each jet p_{T} bin. Since the calibration of b-tagging requires a certain minimum number of events, it will be difficult to calibrate the b-tagging algorithm for each jet p_{T} bin. For this reason the working point (w_{cut}) will be estimated for two fixed b-tagging efficiencies of $\epsilon_{Tag} = 50\%$ and $\epsilon_{Tag} = 60\%$ for each jet p_{T} bin. In addition, the choice of the working point will be optimized in the sense of a minimization of the statistical uncertainty of the differential b-jet cross section measurement. At the end of this section the cut values w_{cut} are listed, which lead to the different efficiencies and purities of the selected jets.

To estimate the purities P_{Tag} for different efficiencies ϵ_{Tag}, the jet weight distributions (e.g. Fig. 8.17) of the IP3D+SV1 tagger are taken. On the one hand a high cut value w_{cut} will lead to a small fraction of b-jets tagged and hence to a low b-tagging efficiency, but on the other hand a high purity of the selected jet sample is expected, since the mistagging rates will be low. In case of lower cut values w_{cut}, the efficiency to tag a b-jet increases, while the purity of the selected jets decreases. In Fig. 8.19 the purity is shown as a function of the b-jet efficiency.

As expected, for low selected efficiency values, a high purity of the selected events is achieved and vice versa. The performance of the b-tagging, i.e. the purity of the selected jets at the same b-tagging efficiency, is lower for cone7 jets compared to cone4 jets. This is caused mainly by the lowest jet p_{T} bin (due to the higher production cross section), where the truth quark labeling of the cone7 jets as b-jets

is more ambiguous than for higher jet p_{T} bins. The effect of a lower performance of b-tagging in higher jet p_{T} bins due to the labeling algorithm is negligible (discussed in Section 8.3.1). The purity of the selected jet sample as a function of the b-tagging efficiency for three different jet p_{T} bins is presented in Fig. 8.20 (a), (b) and (c). The estimated uncertainties of the purities as well as of the efficiencies are the statistical uncertainties due to the limited size of the MC event sample. The expected uncertainties of the efficiencies and the purities due to the calibration of b-tagging on data will be added to the results of the b-jet cross section measurement as a systematic error and discussed in Section 8.5.
The performance of b-tagging is higher in the lower jet p_{T} bin, as expected from the discussion of the jet weight distributions in Sections 8.3.1 and 8.3.2. Beside the effect of the more ambiguous truth quark labeling of cone7 jets as b- or background jets, the shift of reconstructed cone7 jets to higher jet p_{T} bins (broader cone size) influences the performance of b-tagging. Very low p_{T} jets are more difficult to tag as a b-jet. Some low p_{T} cone7 jets are filled into the first jet p_{T} bin, which are not considered for the cone4 jet spectrum due to the jet p_{T} cut. The b-tagging performance decreases, i.e. lower purity of the selected jet sample at the same b-tagging efficiency, compared to the case of taking cone4 jets. In the high jet p_{T} region, there is an opposite effect. Cone4 jets, which are located in a lower jet p_{T} bin and therefore in a preferred kinematic region better for b-tagging, are shifted to higher jet p_{T} bins in the case of cone7 jets. Hence the b-tagging performance in the higher jet p_{T} bin is better for cone7 jets compared to cone4 jets, which is shown in Fig. 8.20(b).
Due to the differences of lower and higher p_{T} jets, like e.g. different average track multiplicity per jet, the b-tagging cuts (used in the calculation of the jet weight) have to be tuned as a function of the jet p_{T}. For the impact parameter based tagger IP3D three different track selection cuts are varied:

- The Lorentz boost of a high energy b-hadron leads to an extended lifetime. At higher energy ($\approx 600\,\mathrm{GeV}$ of a b-hadron) and therefore higher b-jet p_{T}, the b-hadron may decay beyond the first pixel layer of the Pixel Detector. Hence tracks coming from the b-hadron decay will have no hit in the first layer and be cut if the default track selection is applied. This b-jet is more likely to have a smaller jet weight. To avoid the loss of b-jet tracks for b-jets above a certain jet p_{T}, a b-layer hit (b-hit) is no longer required.

- Towards higher jet p_{T} the track multiplicity increases. The b-tagging information is carried by tracks coming from the decay of the highly energetic b-hadron and tracks originating not from the b-hadron decay may worsen the performance of b-tagging. Thus the p_{T} track selection cut ($p_{\mathrm{T},IP}$) has to be tighter to increase the performance of b-tagging for high p_{T} jets.

- In the high jet p_{T} region, tracks coming from the b-hadron decay, are contained in a smaller cone radius due to the Lorentz boost, i.e. the tracks are more collinear. Therefore, the cone radius $\Delta R_{Tr.IP}$ of the track association to the jet is set to lower values for jets with higher p_{T}.

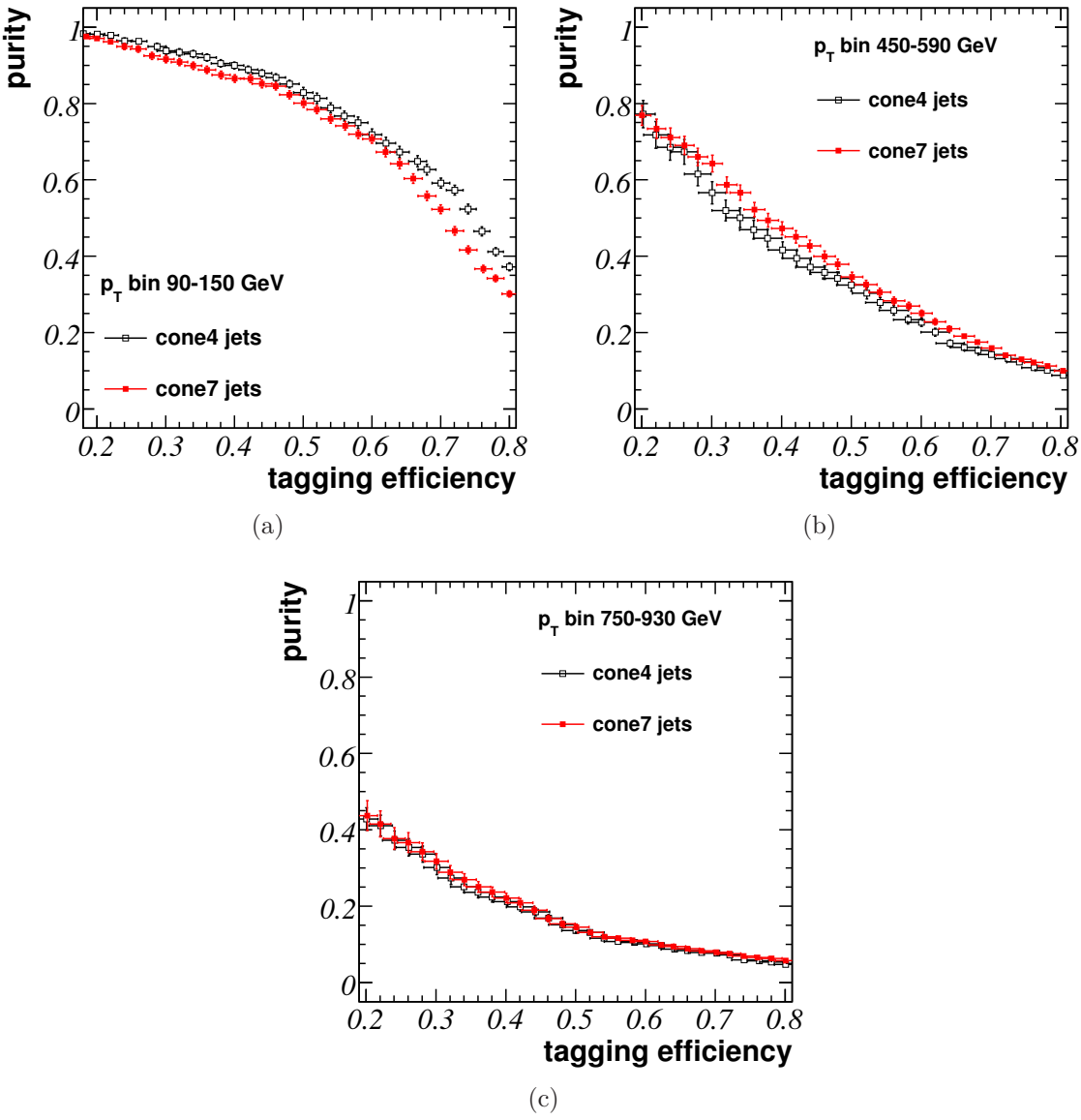

Figure 8.20: b-jet sample purity as a function of the efficiency to tag b-jets for the cone7 and cone4 jet algorithm in three different jet p_{T} bins.

In addition to the IP3D track selection cuts, selection cuts for the secondary vertex based b-tagger are varied. Again, three different variables are considered:

- The p_{T} cut ($p_{\mathrm{T},SV}$) value of the track selection for the secondary vertex reconstruction has to be increased (for the same reason as for the IP3D tagger).
- The cone radius $\Delta R_{Tr.SV}$ around the reconstructed jet axis, within which tracks are used to reconstruct a secondary vertex, has been chosen smaller in the high jet p_{T} region.
- Two-track vertices (Section 8.3.2), which originate from the b-hadron decays, have a larger distance to the primary vertex towards higher p_{T} of the b-hadron. Therefore, the cut on the significant distance $\sigma_{\mathrm{2Tr.Vert.}}$ to the primary vertex (distance between the primary and the two-track vertex divided by the uncertainty of the reconstructed two-track vertex) has to increase as a function of the jet p_{T}, which will also reduce the number of reconstructed (fake) vertices in light quark jets.

The cut values mentioned above have been varied separately and optimized for the highest purity for a given b-tagging efficiency. In Tab. 8.8 the resulting cut parameters for the IP3D+SV1 tagging algorithm are listed.

jet p_{T} bin	cut expression					
[GeV]	b-hit	$p_{\mathrm{T},IP}$ [GeV]	$\Delta R_{Tr.IP}$	$\sigma_{\mathrm{2Tr.Vert.}}$	$p_{\mathrm{T},SV}$ [GeV]	$\Delta R_{Tr.SV}$
$50-90$	1	1.0	0.4	3.5	0.3	0.4
$90-150$	1	1.0	0.4	3.5	0.3	0.4
$150-230$	1	1.0	0.4	4.5	0.3	0.4
$230-330$	1	1.0	0.4	5.0	0.5	0.4
$330-450$	1	2.0	0.4	6.0	0.5	0.4
$450-590$	1	3.0	0.4	7.0	1.5	0.4
$590-750$	0	3.0	0.4	7.0	1.5	0.4
$750-930$	0	3.0	0.4	7.0	2.0	0.4
$930-1130$	0	3.0	0.4	8.0	2.0	0.3
>1130	0	3.0	0.3	9.0	2.0	0.3

Table 8.8: Tuned cut values for different jet p_{T} bins.

The tuning of the significance of two track vertices in the SV1-tagging algorithm leads to a decrease of the number of (fake) vertices in light quark jets. In Fig. 8.21 the secondary vertex reconstruction efficiencies ϵ_{SV}, using the default and the optimized cut values listed in Tab. 8.8, inside b-jets (Fig. 8.21(a)) and inside background jets (Fig. 8.21(b)) are shown as a function of the jet p_{T}. Although ϵ_{SV} is worse for b-jets using the tuned cut values, the decrease of the number of secondary vertices in light quark and c-jets is larger. The larger decrease of the secondary vertex reconstruction efficiency in background jets yields a larger background event suppression and therefore a better b-tagging purity at a given b-tagging efficiency. Especially light

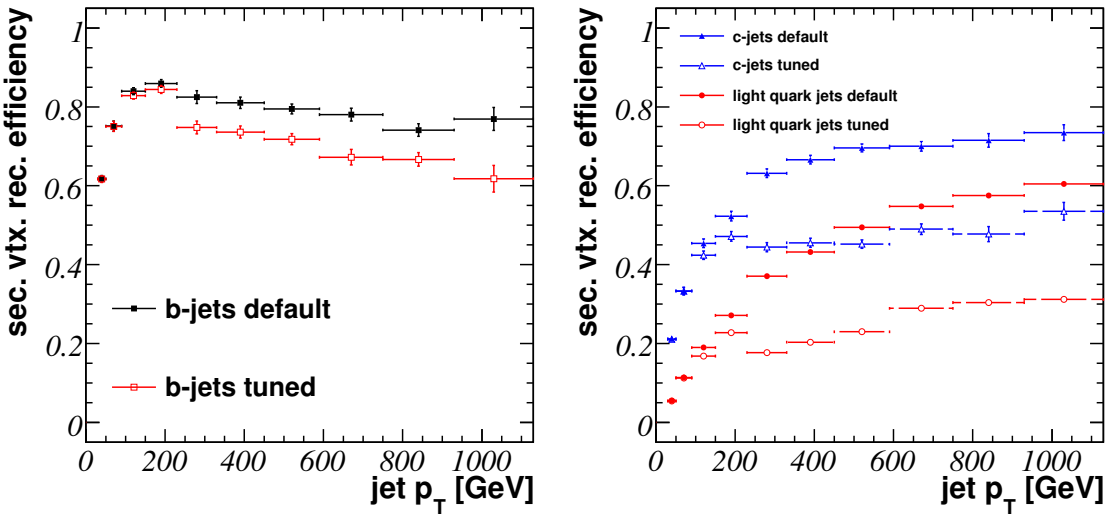

(a) (b)

Figure 8.21: Secondary vertex reconstruction efficiency inside (a) b-jets and (b) inside background jets as a function of the jet p_{T} for cone7 jets using two different set of cut values.

quark jet weights decrease since the probability to reconstruct a secondary vertex in high p_T jets decreases by a factor of about ≈ 2, which results in more background jets obtaining a smaller jet weight. The different estimated ϵ_{SV} to reconstruct a secondary vertex inside b-, c- and light quark jets are used in the calculation of the jet weight. This means instead of a constant ϵ_{SV} to reconstruct a secondary vertex, like in the default b-tagging algorithm configuration, a jet p_{T} dependent secondary vertex reconstruction efficiency (shown in Fig. 8.21) for b-jets as well as for background jets is used (8.14).

The cut values are chosen in order to maximize the purity for a given b-tagging efficiency. The ratio of the purities of the selected jet sample using the default cut compared to the tuned cut values are shown in Fig. 8.22. The ratio is given for b-tagging benchmark efficiencies of (a) 50% and (b) 60%.

In the lower jet p_{T} region, the default cut values are optimal (and also taken as tuned cut values). This is expected since the default cut values have been chosen to optimize the b-tagging performance in this jet p_{T} region. Towards higher jet p_{T} the tuning of cuts improves the b-tagging purity by a factor of up to ≈ 1.6 in the case of a b-tagging efficiency of 50%. For a b-tagging efficiency of $\epsilon_{Tag} = 60\%$ the improvement of the b-tagging purity is less, but it is still better than if the default cut values are taken. Therefore, an improvement of the b-tagging purity in the high jet p_{T} region (jet $p_{\mathrm{T}} > 330\,\mathrm{GeV}$) due to the cut tuning is expected. The purities of tagged jets for a fixed tagging efficiency of $\epsilon_{Tag} = 50\%$ and $\epsilon_{Tag} = 60\%$ are shown in Fig. 8.23 (a) and (b), respectively.

First the purity of the tagged jets increases with larger jet p_{T} and has its maximum in the jet p_{T} bin of $(150 - 230)\,\mathrm{GeV}$ with a purity $P_{Tag} > 0.8\,(0.7)$ for a tagging efficiency of $\epsilon_{Tag} = 50\%\,(60\%)$. Afterwards, as expected, the b-tagging performance

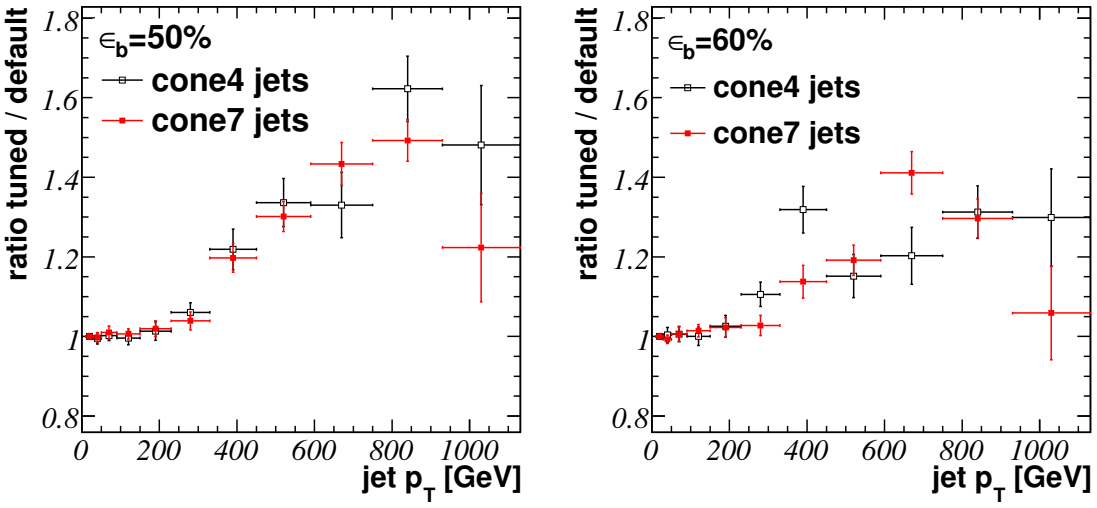

(a) (b)

Figure 8.22: Ratio of b-tagging purity values using default and tuned cut values at a fixed b-tagging efficiency of (a) 50% and (b) 60%.

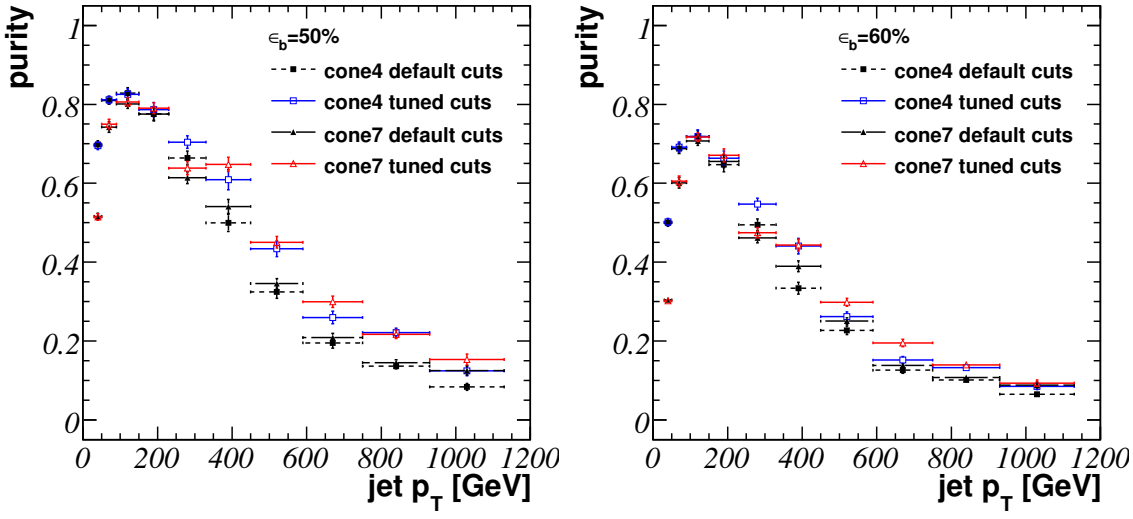

(a) (b)

Figure 8.23: b-jet sample purity using default and tuned cut values at fixed b-tagging efficiencies of (a) $\epsilon_{Tag} = 50\%$ and (b) $\epsilon_{Tag} = 60\%$.

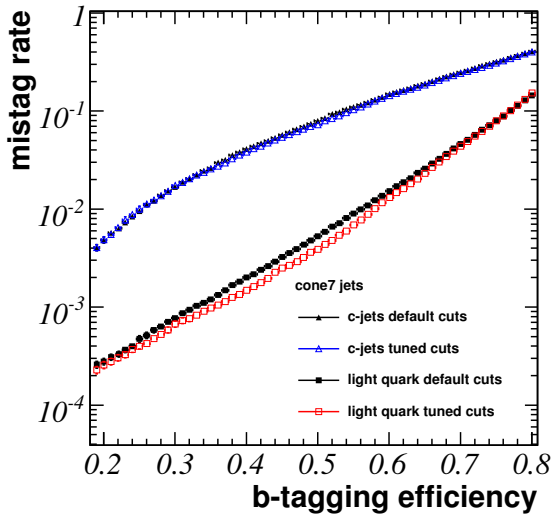

Figure 8.24: Mistagging rates for cone7 c-jets and for cone7 light quark jets as a function of the b-tagging efficiency taking default and tuned cut values.

decreases towards larger jet p_{T}. Although the performance is improved by taking the tuned cut values, the purity in the very high jet p_{T} region is less than $P_{Tag} \sim 0.2$. Therefore, the relative statistical error of the cross section measurement is expected to be larger due to the overall lower number of events and the higher mistagging rates. In Fig. 8.24 the mistagging rates for c-jets as well as for light quark jets taking the default and tuned cut values as a function of the b-tagging efficiency are shown. The misidentification rates determine the purity of the selected events according to (8.18).

The values of the b-jet sample purities at a fixed b-tagging efficiency of $\epsilon_{Tag} = 50\%$ and $\epsilon_{Tag} = 60\%$ taking all jets of the event sample into account, are listed in Tab. 8.9. The uncertainties of the purities are the statistical uncertainties due to the limited number of MC events.

For the b-jet cross section measurement taking only the leading (b-)jet of an event into account, the same set of tuning cuts as well as the same cuts on the jet weight as for the scenario, in which all jets are considered, are used. In this case the efficiency for b-tagging differs slightly from the fixed b-tagging efficiencies of $\epsilon_{Tag} = 50\%$ and $\epsilon_{Tag} = 60\%$ as used when all jets of the event sample are considered. In Fig. 8.25 the b-tagging efficiencies and in Fig. 8.26 the purities of the selected leading jet samples as a function of the leading jet p_{T} are shown. The purity of the selected leading jet sample is smaller than the purity values in case of taking all jets of the event sample into account. The smaller purity is due to events, for which the b-jet selection is missing the leading b-jet and takes another b-jet with lower jet p_{T} as tagged leading b-jet. These "additional" background jets decrease the purity values.

The optimal cut value w_{cut} on the b-tagging jet weight should minimize the expected error of the measured b-jet cross section. The calculation of the uncertainty on the b-jet cross section contributed by b-tagging will include the uncertainty on the purity, the uncertainty on the efficiency and the statistical uncertainty given by the number

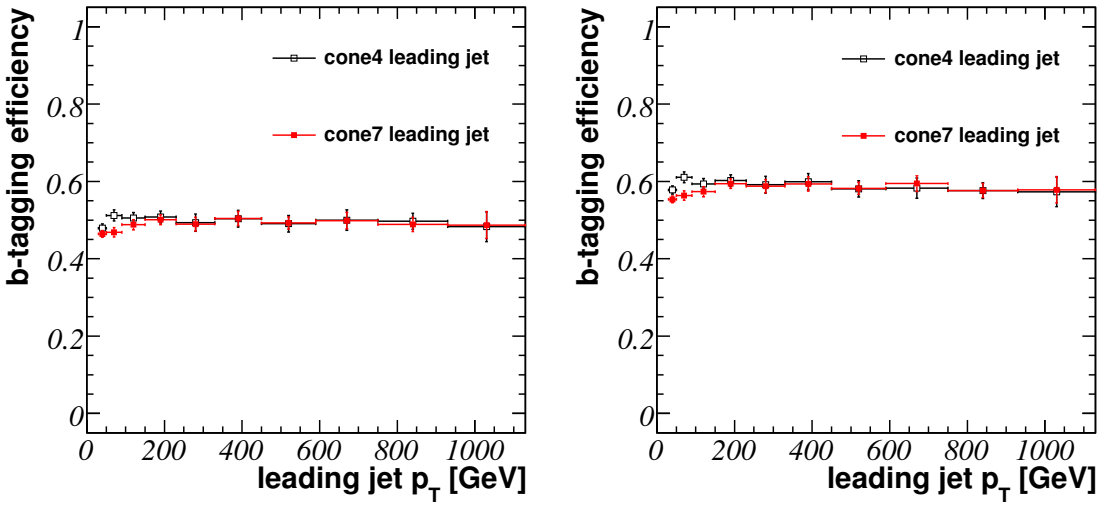

(a) (b)

Figure 8.25: Efficiencies for b-tagging for the leading jet scenario using the same cut values as for a fixed b-tagging efficiency of (a) $\epsilon_{Tag} = 50\%$ and (b) $\epsilon_{Tag} = 60\%$ in case of taking all jets in the event sample into account.

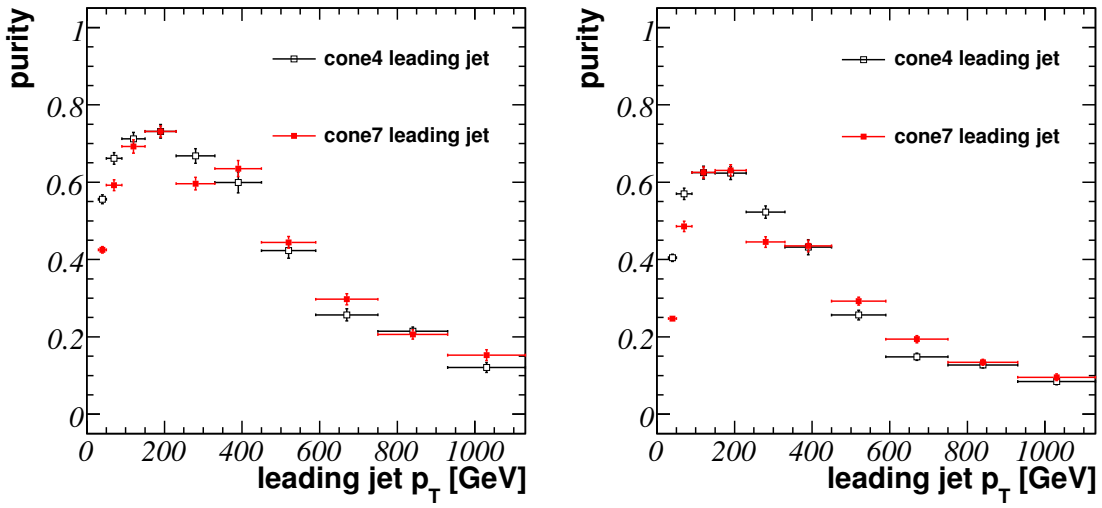

(a) (b)

Figure 8.26: Purity values for the sample of b-jets in the selected leading jet scenario using the same cut values for a fixed b-tagging efficiency of (a) $\epsilon_{Tag} = 50\%$ and (b) $\epsilon_{Tag} = 60\%$ in case of taking all jets of the event sample into account.

p_{T} range [GeV]		b-tagging purity at a fixed efficiency of 50%	60%
$30-50$	P_{Tag} Cone4	0.695 ± 0.010	0.502 ± 0.009
	P_{Tag} Cone7	0.515 ± 0.008	0.302 ± 0.005
$50-90$	P_{Tag} Cone4	0.811 ± 0.010	0.692 ± 0.013
	P_{Tag} Cone7	0.750 ± 0.012	0.605 ± 0.013
$90-150$	P_{Tag} Cone4	0.825 ± 0.014	0.719 ± 0.017
	P_{Tag} Cone7	0.806 ± 0.011	0.717 ± 0.011
$150-230$	P_{Tag} Cone4	0.787 ± 0.018	0.664 ± 0.018
	P_{Tag} Cone7	0.790 ± 0.014	0.671 ± 0.017
$230-330$	P_{Tag} Cone4	0.704 ± 0.016	0.547 ± 0.015
	P_{Tag} Cone7	0.638 ± 0.017	0.475 ± 0.013
$330-450$	P_{Tag} Cone4	0.61 ± 0.03	0.441 ± 0.019
	P_{Tag} Cone7	0.648 ± 0.018	0.443 ± 0.015
$450-590$	P_{Tag} Cone4	0.43 ± 0.02	0.262 ± 0.012
	P_{Tag} Cone7	0.450 ± 0.015	0.298 ± 0.010
$590-750$	P_{Tag} Cone4	0.260 ± 0.016	0.152 ± 0.009
	P_{Tag} Cone7	0.299 ± 0.015	0.195 ± 0.009
$750-930$	P_{Tag} Cone4	0.221 ± 0.011	0.132 ± 0.007
	P_{Tag} Cone7	0.217 ± 0.011	0.139 ± 0.006
$930-1130$	P_{Tag} Cone4	0.124 ± 0.013	0.0849 ± 0.008
	P_{Tag} Cone7	0.153 ± 0.014	0.094 ± 0.008
>1130	P_{Tag} Cone4	0.112 ± 0.013	0.083 ± 0.009
	P_{Tag} Cone7	0.150 ± 0.016	0.103 ± 0.010

Table 8.9: b-tagging purity values as a function of the jet p_{T} in the case of considering all jets in the event sample.

of selected events. Considering these contributions, the contribution to the relative uncertainty of the b-jet cross section measurement is estimated by

$$\frac{\Delta\sigma_b}{\sigma_b} = \sqrt{\left(\left(\frac{\Delta P_{Tag}}{P_{Tag}}\right)^2 + \left(\frac{\Delta\epsilon_{Tag}}{\epsilon_{Tag}}\right)^2 + \frac{1}{P_{Tag}\epsilon_{Tag}\mathcal{L}\sigma_b}\right)}. \tag{8.19}$$

The relative error on the cross section measurement has to be minimized. The contributions by the relative uncertainty of the purity and of the efficiency are determined by the number of available MC events or by the uncertainty of the b-tagging calibration. In order to optimize the measurement, these contributions will not be taken into account, since the number of MC events should be increased until the uncertainty will be negligible. The last term in (8.19) depends on the purity and the efficiency of b-tagging, while the cross section and the integrated luminosity are given. Therefore, the relative error $\frac{\Delta\sigma_b}{\sigma_b}$ will be minimized by maximizing the term $P_{Tag}\epsilon_{Tag}$.

Since the b-tagging performance is not uniform over the jet-p_{T} range considered,

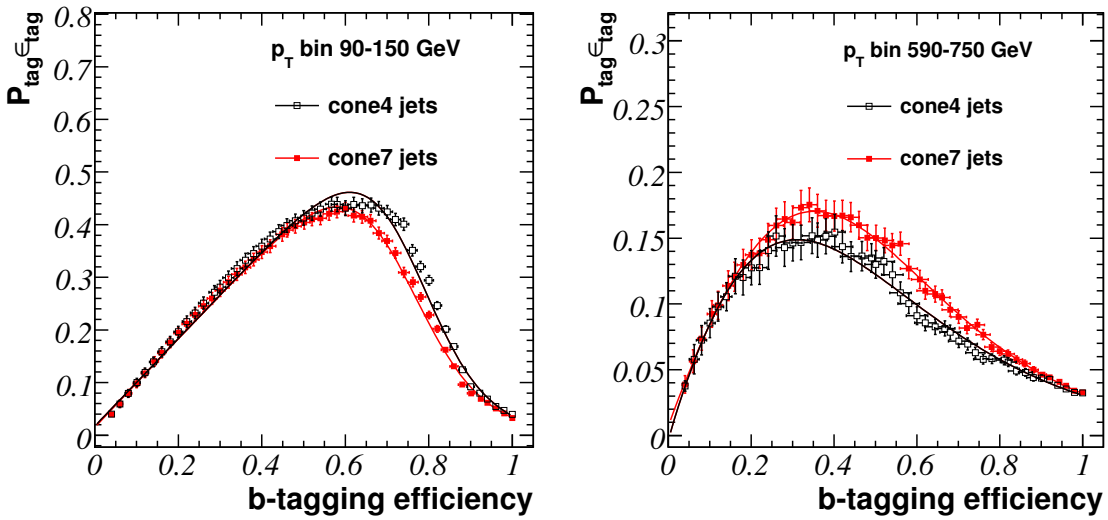

(a) (b)

Figure 8.27: Distributions of $P_{Tag}\epsilon_{Tag}$ as a function of the jet p_{T} for (a) $p_{\mathrm{T}}^{Jet} \in [90, 150]\,\mathrm{GeV}$ and (b) $p_{\mathrm{T}}^{Jet} \in [590, 750]\,\mathrm{GeV}$.

the optimal choice of the cut value w_{cut} on the jet weight distributions has to be determined for each jet p_{T} bin separately. As an example the distribution of $P_{Tag}\epsilon_{Tag}$ as a function of the b-tagging efficiency is shown in Fig. 8.27(a) for the jet p_{T} bin of 90 to 150 GeV and in Fig. 8.27(b) for the jet p_{T} bin of 590 to 750 GeV.
In order to smoothen the distribution, an empirical function

$$f(\epsilon_{Tag}) = \frac{\alpha + \beta\epsilon_{Tag}}{1 + e^{\gamma(\epsilon_{Tag} - \delta)}} \tag{8.20}$$

is fitted to the distribution with the parameters α, β, γ and δ. The function (8.20) does not reflect exactly the sharp of the distribution of $P_{Tag}\epsilon_{Tag}$. Therefore, a fit of the distribution is performed to determine its the maximum without depending on statistical bin-to-bin fluctuations. Without the fits, the optimization would result in a more fluctuating result of the optimal choice of efficiency and purity. This choice of the cut values would not be wrong, but would give the impression of larger differences in tuning between different bins and larger differences in tuning for cone4 and cone7 jets. A fit to find the maximum smoothes the statistical fluctuations. The values reflect the general behavior of the efficiency and purity as a function of the jet p_{T}.
The exact form of the distributions does not have to be reflected by the fit, only the maximum of the function has to be compatible with the maximum of the distributions (within the statistical uncertainty of $P_{Tag}\epsilon_{Tag}$). The maximum of the fitted function is used to give an estimate for the optimal choice of the b-tagging efficiency. The b-tagging efficiency in turn is used to calculate the purity of the selected events explicitly.
In Fig. 8.28(a) the optimal b-tagging efficiencies and in Fig. 8.28(b) the resulting purities for cone4 and cone7 jets are shown. Differences between efficiencies using

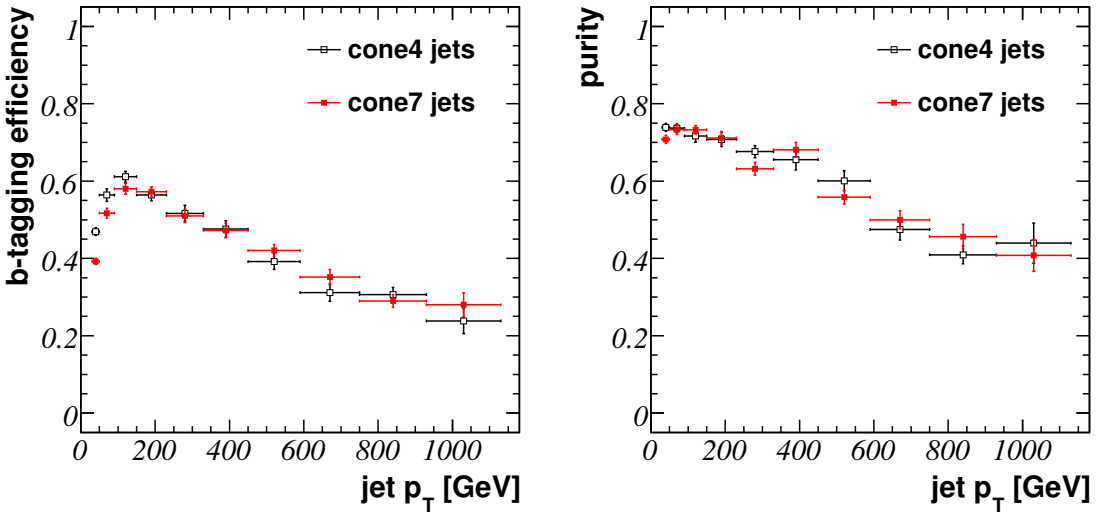

(a) (b)

Figure 8.28: Optimal working point for the b-tagging efficiency (a) and purity (b) in order to minimize the statistical uncertainty of the b-jet cross section measurement for cone4 and cone7 jets.

cone4 and cone7 jets are only seen in the first jet p_{T} bins. The optimal choice of the efficiencies for cone7 jets is lower compared to the one for cone4 jets, which is expected from the discussion above about differences in the b-tagging performance in the lower jet p_{T} region.

The b-tagging efficiency as well as the purity first increases and afterwards decreases as higher jet p_{T} is considered. Due to the decreasing efficiency, the purity in the higher jet p_{T} region is higher compared to the situation where a fixed b-tagging efficiency is taken, which results in a smaller statistical uncertainty of the measured b-jet cross section according to (8.19) compared to the scenario of taking a fixed b-tagging efficiency over the whole jet p_{T} range.

The same set of cuts is used to estimate the optimal choice for the b-tagging efficiencies when only the leading jets of events are taken into account. In Fig. 8.29(a) the b-tagging efficiency and in Fig. 8.29(b) the purity of the selected leading jets are shown.

In Tab. 8.10 the different jet weight cut values are summarized, which result in the different working points for a fixed b-tagging efficiency of $\epsilon_{Tag} = 50\%$ and $\epsilon_{Tag} = 60\%$ as well as for the optimized efficiency.

In the following section, the different efficiencies and purities are used to calculate the b-jet cross section as well as the expected uncertainty on the measurement as a function of the b-jet p_{T}.

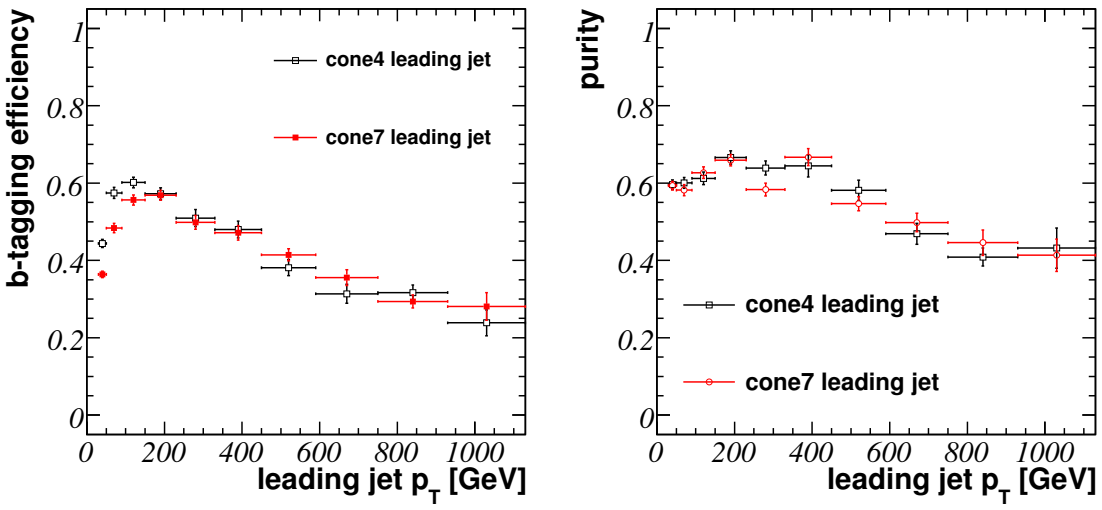

(a) (b)

Figure 8.29: Optimal working point for the b-tagging efficiency (a) and the purity (b) in order to minimize the statistical uncertainty of the b-jet cross section measurement taking only the leading jets into account for cone4 and cone7 jets.

8.4 Unfolding of the Differential b-Jet p_{T} Spectrum

The b-jet p_{T} is reconstructed from measured calorimeter information. Therefore, the reconstructed b-jet p_{T} differs from the truth b-jet p_{T} and the reconstructed b-jet p_{T} spectrum is smeared compared to the truth b-jet p_{T} spectrum. The resolution of the jet p_{T} reconstruction using calorimeter information after calibration will cause bin-to-bin migrations of the b-jets to lower or higher jet p_{T} bins w.r.t. the truth jet p_{T}. In order to correct for these detector effects, an unfolding algorithm is applied to obtain the truth b-jet cross section as a function of the jet p_{T}. This section starts with an introduction of the unfolding algorithm. After the introduction the transfer matrix is calculated and discussed. Then, the unfolding algorithm will be applied to the measured b-jet spectrum. For this purpose, two independent data samples are used. The first sample of events is used to calibrate the analysis to measure the b-jet spectrum, i.e. all efficiency and purity values as well as the transfer matrix are estimated using the first event sample. The second event sample is used to derive the estimated number of reconstructed and selected jets per jet p_{T} bin.

Due to the measurement the truth b-jet p_{T} spectrum $f(x)$ is smeared by the resolution function of the detector $t(x, x')$, which results in the measured reconstructed b-jet p_{T} spectrum $f'(x')$. Here x means the truth jet p_{T}, while x' represents the reconstructed jet p_{T} of the jets. The convolution [50, 51] is expressed by

$$f'(x') = \int_{-\infty}^{\infty} t(x, x') f(x) dx \,. \tag{8.21}$$

p_{T} range [GeV]		w_{cut} for ϵ_{Tag} of 50%	60%	optimal
$30-50$	Cone4	4.79	2.35	5.51
	Cone7	2.87	0.88	5.62
$50-90$	Cone4	6.84	4.43	5.2
	Cone7	6.07	3.76	5.75
$90-150$	Cone4	7.37	5.26	5.13
	Cone7	7.18	5.14	5.5
$150-230$	Cone4	6.87	4.56	5.44
	Cone7	6.81	4.78	5.4
$230-330$	Cone4	5.2	3.16	4.8
	Cone7	5.07	2.74	4.92
$330-450$	Cone4	5.28	3.14	5.86
	Cone7	5.25	2.9	5.81
$450-590$	Cone4	4.41	2.27	6.54
	Cone7	4.55	2.59	6.1
$590-750$	Cone4	3.51	1.54	6.65
	Cone7	3.97	2.22	6.65
$750-930$	Cone4	3.76	1.8	6.93
	Cone7	3.77	1.97	7.51
$930-1130$	Cone4	2.64	1.04	8.16
	Cone7	3.17	1.26	7.79
>1130	Cone4	3.27	1.93	7.85
	Cone7	3.8	2.18	7.33

Table 8.10: Jet weight cut values w_{cut} used for an b-tagging efficiency of 50% and 60% as well as for the optimal efficiency as defined in the text.

In the case of a spectrum being measured as a binned histogram, (8.21) has to be discretized. The bin content of the true histogram $\vec{\Theta}$ ($\Theta_i = \int_{Bin_i} f(x)dx$) is connected to the measured bin content in the histogram $\vec{d}$ ($d_i = \int_{Bin_i} f'(x')dx'$) by the transfer matrix $\mathbf{T}$

$$\vec{d} = \mathbf{T}\vec{\Theta}\,. \tag{8.22}$$

The element T_{ij} of the transfer matrix reflects the probability for an event generated in truth bin j to be measured in bin i. Therefore, the transfer matrix is written as

$$T_{ij} = \frac{\int_{Bin_i}\left(\int_{Bin_j} t(x,x')f(x)dx\right)dx'}{\int_{Bin_j} f(x)dx}\,. \tag{8.23}$$

Hence the transfer matrix depends on the (unknown) true distribution $f(x)$ and the transfer function $t(x,x')$. In order to estimate the transfer matrix, MC events are necessary, since the MC events contain the truth information as well as the simulated detector smearing. The result of the simulated data sample has to be compared to

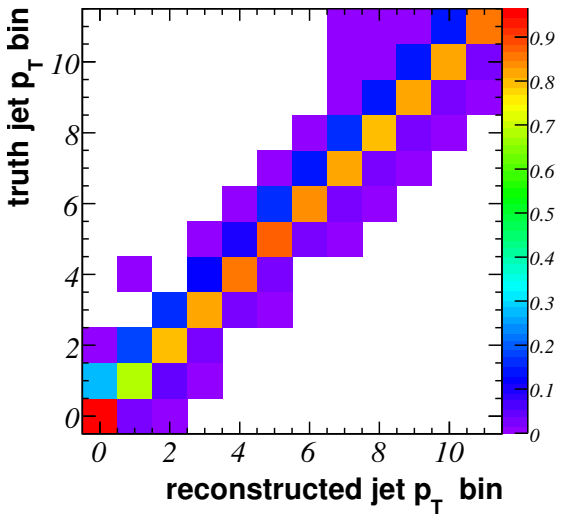

Figure 8.30: The transfer matrix, which describes the b-jet p_{T} bin-to-bin migration of cone7 jets.

data, i.e. the shape of the jet p_{T} spectrum or the p_{T} resolution of the simulated data to data taken by the ATLAS detector.
Therefore, the b-jet p_{T} resolution and the chosen jet p_{T} bin size determine the transfer matrix. The residual distributions of the jet p_{T} reconstruction for b-jets are shown in App. D. The residual distributions become broader towards higher jet p_{T} for both jet reconstruction cone sizes. Since the bin widths of the jet p_{T} bins also increase towards higher jet p_{T}, the width of the resolution distribution of the jet p_{T} reconstruction is more than a factor of ≈ 2 smaller than the chosen bin width. Hence, for most of the truth jets, the reconstructed jet p_{T} is in the same jet p_{T} bin as the truth jet p_{T}. Only few bin-to-bin migrations are expected. The estimated transfer matrix for cone7 b-jets is shown in Fig. 8.30. The transfer matrix is dominated by the diagonal entries, which reflects the probability of $\approx 80\%$ for reconstructed jets to be filled in the same jet p_{T} bin as the truth jet p_{T}. Bin-to-bin migrations of the jets are expected in the order of about 10% to 15%. The transfer matrix is asymmetric, which means the measured jet p_{T} tends to be smaller as the truth jet p_{T}.
Once the transfer matrix is derived, the true distribution is estimated by the inversion of (8.22)

$$\vec{\Theta} = \mathbf{T}^{-1}\vec{d}. \tag{8.24}$$

Relation (8.24) holds for the expected event numbers inside bins. The observed number of events $\hat{d}_i$ per jet p_{T} bin includes statistical fluctuations according to a Poisson distribution

$$P(\hat{d}_i) = \frac{e^{-d_i} d_i^{\hat{d}_i}}{\hat{d}_i!} \tag{8.25}$$

and the estimator for the true distribution $\hat{\vec{\Theta}}$ is therefore given by

$$\hat{\vec{\Theta}} = \mathbf{T}^{-1}\hat{\vec{d}}. \tag{8.26}$$

The result of the unfolding procedure provides an exact solution for the estimated true distribution. However, the result of the unfolding procedure by matrix inversion may contain strong fluctuations in the solution vector (and therefore large uncertainties), which can also result in negative (unphysical) bin contents. These fluctuations may be caused by (small) fluctuations in the transfer matrix, which are amplified due to the inversion of the matrix. The result of the unfolding procedure by matrix inversion is reasonable only for matrices with dominating diagonal entries. The size of the fluctuations in the result of the matrix inversion unfolding procedure is investigated by calculating the eigenvalues for the case of a symmetric transfer matrix and the singular values for the case of an asymmetric transfer matrix. Assuming a symmetric transfer matrix $\mathbf{T}$, the transfer matrix is decomposed by

$$\mathbf{T} = \mathbf{U}\mathbf{D}\mathbf{U}^T, \tag{8.27}$$

where $\mathbf{U}$ is a unitary matrix ($\mathbf{U}^T\mathbf{U} = \mathbf{1}$) containing the eigenvectors of the matrix $\mathbf{T}$. $\mathbf{D}$ is a diagonal matrix, which consists of the eigenvalues λ_i of the matrix $\mathbf{T}$ arranged in decreasing order. Rotating the system by multiplying (8.26) by $\mathbf{U}^T$ [52] the unfolding problem is expressed by

$$\underbrace{\mathbf{U}^T\hat{\vec{d}}}_{\vec{c}} = \mathbf{D}\,\underbrace{\mathbf{U}^T\hat{\vec{\Theta}}}_{\vec{b}}. \tag{8.28}$$

The matrix $\mathbf{U}$, containing the eigenvectors of the transfer matrix, transforms the truth vector and the measured vector to $\vec{c} = \mathbf{U}^T\hat{\vec{d}}$ and $\vec{b} = \mathbf{U}^T\hat{\vec{\Theta}}$, respectively. The folding step is expressed by $\vec{c} = \mathbf{D}\vec{b}$. Since the diagonal matrix $\mathbf{D}$ contains the eigenvalues λ_i, the unfolding step is given by

$$b_i = \frac{c_i}{\lambda_i}. \tag{8.29}$$

Therefore, the unfolded result B_i is obtained by a multiplication of the inverse eigenvalue λ_i with the coefficient c_i. In case of very small eigenvalues λ_i small statistical fluctuations in the coefficients c_i maybe amplified, which may lead to a result in the expectation values $\hat{\vec{\Theta}} = \mathbf{U}\vec{b}$ dominated by a few coefficients with very small eigenvalues. The jth eigenvector in the matrix $\mathbf{U}$ in general has j zero crossings. Hence, small eigenvalues not only lead to a strong amplification of statistical fluctuations, they also lead to an oscillating solution vector $\hat{\vec{\Theta}}$. To avoid these oscillations in the result of the unfolding procedure, different regularization methods have been developed [50, 51].

In case of an asymmetric transfer matrix, the singular values instead of the eigenvalues have to be estimated. The transfer matrix is decomposed by the singular value decomposition (SVD) to

$$\mathbf{T} = \mathbf{U}\mathbf{S}\mathbf{V}^T. \tag{8.30}$$

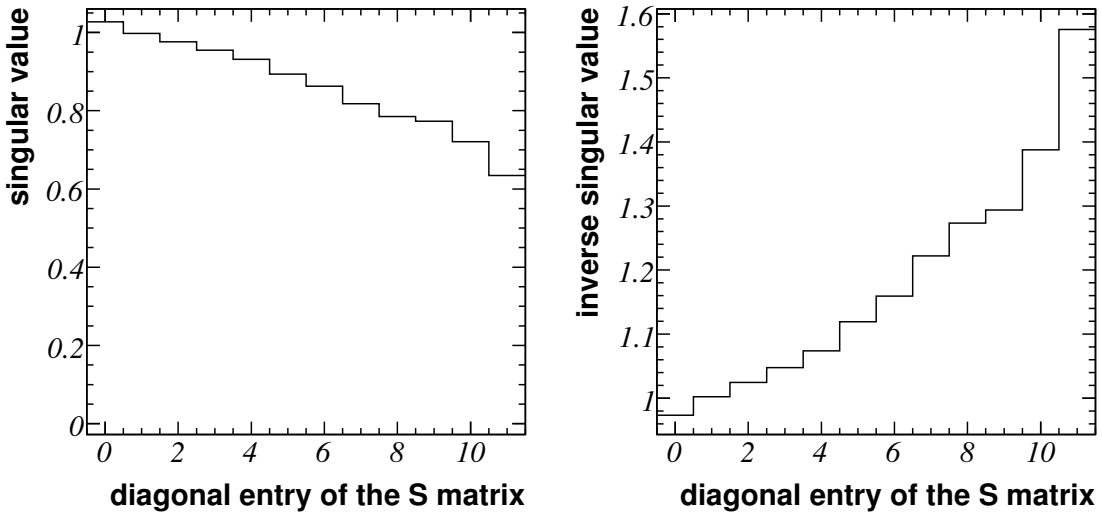

(a) (b)

Figure 8.31: (a) Singular values and (b) the inverse singular values of the transfer matrix **S** using cone7 jets.

The diagonal matrix **S** contains the singular values s_i and the matrices **U** and **V** are orthogonal matrices. Again, small singular values may lead to an amplification of statistical fluctuations, which may lead to the estimation of the expectation value for $\hat{\vec{\Theta}}$ being unacceptable. In order to avoid the oscillations in the result of the unfolding procedure, singular values, which represent contributions dominated by statistical fluctuations, are neglected and set to zero in the matrix **S**. After this "regularization", the pseudo-inverse of the matrix **T** is used to calculate the expectation value $\hat{\vec{\Theta}}$.
In Fig. 8.31 the singular values of the matrix **S** in decreasing order as well as the inverse singular values are shown. The smallest singular value is ≈ 0.58 and therefore the largest inverse singular value is ≈ 1.7. Since the singular values only slightly decrease over the whole range, statistical fluctuations will not be amplified strongly. Thus, an oscillation of the result of the unfolding procedure using the matrix inversion method is not expected and a regularization step is not necessary.
For the b-jet cross section measurement, the purity P_{Tag} and efficiency ϵ_{Tag} of the b-tagging as well as the purity of the jet reconstruction P_{Rec} have to be considered before the unfolding algorithm is applied, since these quantities depend on reconstructed jet p_{T} values. The number of triggered and reconstructed b-jets $\hat{d}_i$ in jet p_{T} bin i is

$$\hat{d}_i = \frac{P_{tag_i} P_{Rec,i}}{\epsilon_{tag,i}} N_{Sel,i}\,. \tag{8.31}$$

Consequently, the unfolded numbers of triggered and reconstructed truth b-jets $\hat{\vec{\Theta}}$ are

$$\hat{\vec{\Theta}} = \mathbf{V}\mathbf{S}^{-1}\mathbf{U}^T\hat{\vec{d}}. \tag{8.32}$$

For the determination of the b-jet cross section value $\sigma_{b,i}$ in bin i the trigger efficiency $\epsilon_{Tr,i}$ as well as the reconstruction efficiency of b-jets $\epsilon_{Rec,i}$ have to be taken into account

$$\sigma_{b-jet,i} = \frac{1}{\epsilon_{Tr,i}\epsilon_{Rec,i}\mathcal{L}}\hat{\Theta}_i \,. \tag{8.33}$$

In order to calculate the b-jet cross section from weighted events, the number of weighted b-jets are scaled to a certain luminosity $\mathcal{L}$. The errors have to be scaled as well. Since the number of MC events is fixed, the relative uncertainty of the b-jet cross section is independent of the scaling factor. Considering the estimated number of measured events as a function of the integrated luminosity, the relative error will be affected. The error estimation will be discussed in Section 8.6.
The covariance matrix $\mathbf{C}$ of the triggered and reconstructed numbers of b-jets contains the uncertainties of the ratios of the purity values divided by the efficiency values $\Delta(P_{Tag}/\epsilon_{Tag})$ of b-tagging as well as the statistical uncertainty of the number of measured jets N_{Sel} in the different jet p_{T} bins. These quantities depend on the reconstructed jet p_{T} and have to be considered before the unfolding algorithm is applied. The diagonal entries of the covariance matrix are calculated by

$$C_{ii} = \left(\frac{P_{Tag,i}P_{Rec,i}N_{Sel,i}}{\epsilon_{Tag,i}}\right)^2 \sqrt{\left(\frac{\Delta(P_{Tag,i}/\epsilon_{tag,i})}{(P_{Tag,i}/\epsilon_{Tag,i})}\right)^2 + \left(\frac{\Delta P_{Rec,i}}{P_{Rec,i}}\right)^2 + \frac{1}{P^2_{Tag,i}N_{Sel,i}}} \,. \tag{8.34}$$

Since weighted events are used, in the last term of (8.34) the effective number of events (App. C) is used to estimate the contribution to the computed uncertainty.
The covariance matrix $\mathbf{C_U}$ of the unfolded numbers of triggered and reconstructed b-jets is derived by error propagation

$$\mathbf{C_U} = \mathbf{V}\mathbf{S}^{-1}\mathbf{U}^T\mathbf{C}\mathbf{U}\mathbf{S}^{-1}\mathbf{V}^T \,. \tag{8.35}$$

To obtain the uncertainties of the b-jet cross section in the truth jet p_{T} bin i, the uncertainties of the trigger efficiency $\epsilon_{Tr,i}$ as well as the reconstruction efficiency $\epsilon_{Rec,i}$ have to be taken into account:

$$\Delta\sigma_{b-jet,i} = \sigma_{b-jet,i}\sqrt{\left(\frac{\sqrt{C_{U,ii}}}{\hat{\Theta}_i}\right)^2 + \left(\frac{\Delta\epsilon_{Tr,i}}{\epsilon_{Tr,i}}\right)^2 + \left(\frac{\Delta\epsilon_{Rec,i}}{\epsilon_{Rec,i}}\right)} \,. \tag{8.36}$$

The uncertainty of the luminosity will be considered as a systematic error and therefore added to the uncertainty of the b-jet cross section in Section 8.5. Since the number of events in the first data sample, which is used to derive the transfer matrix, is in the same order as the number of events in the second event sample, the statistical uncertainty of the transfer matrix is not negligible. This additional uncertainty will be added as the systematic uncertainty of the unfolding algorithm as discussed in Section 8.5.
In order to test the unfolding algorithm, two independent data samples are used. In case the first event sample is used to estimate the efficiencies, purities and the

transfer matrix as well as the number of b-jets per jet p_{T} bin, the true differential b-jet cross section distribution should be reproduced perfectly, since all quantities in (8.21) match the number of reconstructed jets. Therefore, on average the Poissonian distributed uncertainties of the reconstructed jet numbers cancel each other. In Fig. 8.32(a) the difference of the reconstructed b-jet cross section and the truth b-jet cross section, normalized to the truth cross section, taking only the first event sample into account, is shown. The quadratic points represent the reconstructed spectrum without unfolding, but taking also the trigger and reconstruction efficiencies estimated from the truth jet p_{T} spectrum into account. The uncertainties reflect the statistical errors. Since the bin width of the jet p_{T} spectrum is broader than the width of the resolution of the jet p_{T} reconstruction, only small corrections to the b-jet spectrum are necessary.
After application of the unfolding algorithm, the truth b-jet cross section is recovered as shown in Fig. 8.32(a). This is expected, since the reconstructed selected number of jets is taken from the same event sample, which is also used for the calibration of the unfolding algorithm. In Fig. 8.32(b), (c) and (d) the reconstructed and selected number of jets is taken from the second event sample. However, the same cut values are applied, e.g. on the jet weights, as estimated from the first event sample. Here the differential b-jet cross section is smeared a bit. The unfolding algorithm corrects the b-jet spectrum and improves the agreement of the measured and the true differential b-jet cross section. For a working point of $\epsilon_{Tag} = 60\%$ the reconstructed and unfolded b-jet cross section agrees within the uncertainty with the truth b-jet cross section. In case of a working point of $\epsilon_{Tag} = 50\%$ as well as for the optimized efficiencies the differences are within the uncertainty range, which is expected from the statistical point of view of Gaussian distributed uncertainties. Especially, the cross section bins at large jet p_{T} are dominated by statistical uncertainties on the numbers of selected jets. The statistical uncertainties, in the case the optimized working point of b-tagging is used, are smaller compared to the b-tagging scenarios with fixed ϵ_{Tag}, although the uncertainties of the b-tagging efficiency and purity values are larger in most of the jet p_{T} bins. In addition, the unfolding algorithm enlarges the uncertainties slightly.
In case an additional regularization is applied to the transfer matrix, the result of the differential b-jet cross section measurement worsens. Therefore, no regularization will be applied to the unfolding method. This will be different for smaller bin widths. In the case of a higher measured number of events (higher integrated luminosity), the jet p_{T} bin size will be reduced, the transfer matrix will contain larger off-diagonal elements and a regularization applied to the unfolding algorithm will become necessary.
In Fig. 8.33 the differences of the reconstructed and unfolded leading differential b-jet cross sections and the leading truth differential b-jet cross sections, normalized to the leading truth differential b-jet cross sections, are shown. Again, the first event sample is taken to estimate the efficiency and purity values and from the second event sample the number of selected leading (b-)jets is taken. The results are similar to the results of the differential b-jet cross section measurement taking all jets in the event sample into account. Within the statistical uncertainties, the results are

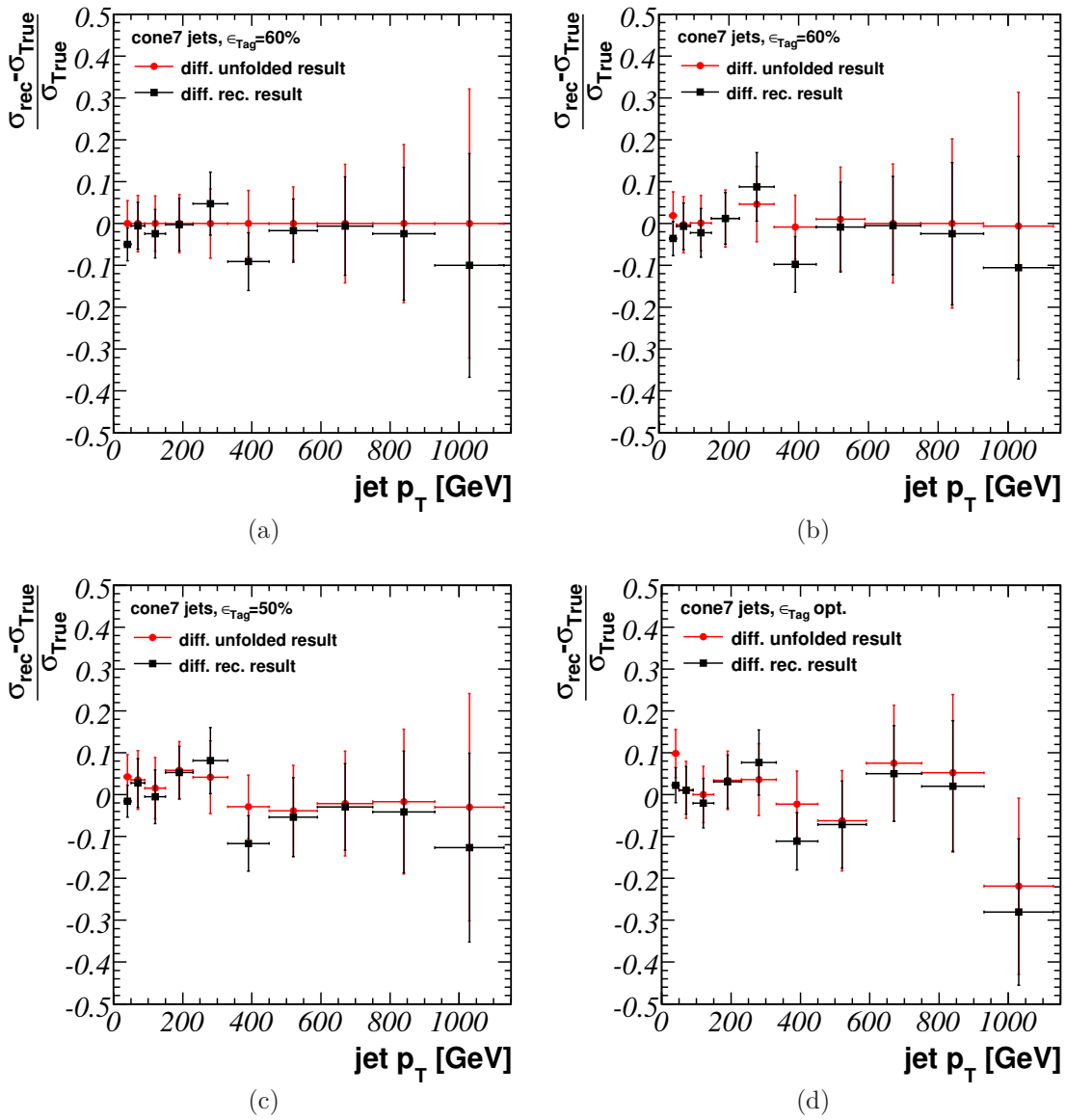

Figure 8.32: Differences of the reconstructed and truth cone7 b-jet cross sections as a function of the jet p_{T} normalized to the truth b-jet cross section. In (a) the same event sample is taken to estimate the purities, efficiencies, the transfer matrix as well as the reconstructed and selected jet numbers. The b-tagging efficiency is chosen at (b) $\epsilon_{Tag} = 60\%$, (c) $\epsilon_{Tag} = 50\%$ and (d) optimized as described in the text, taking a second event sample to estimate the reconstructed and selected number of events.

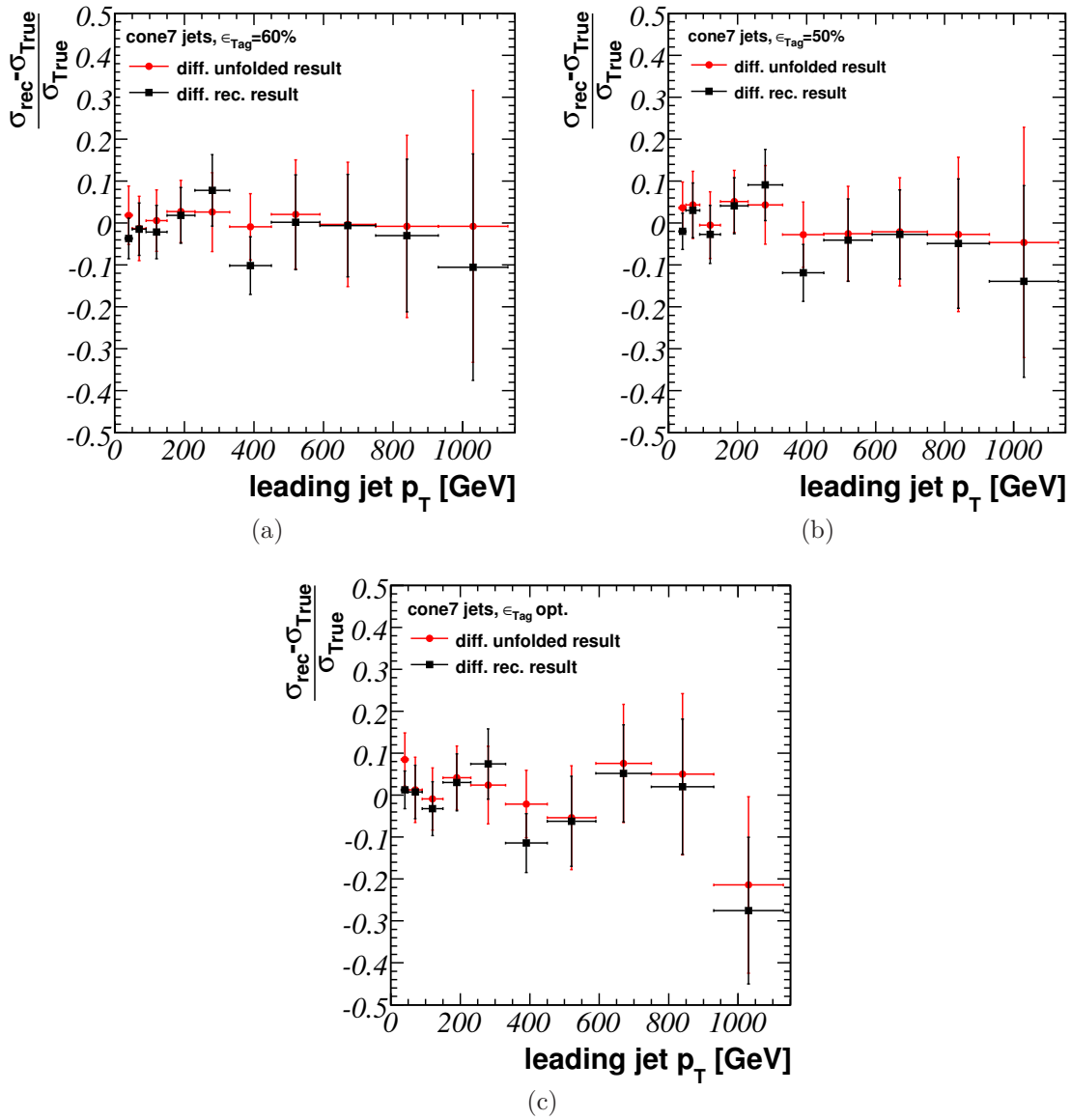

Figure 8.33: Differences of the reconstructed and cone7 leading truth b-jet cross sections as a function of the jet p_{T} normalized to the leading truth b-jet cross section. The b-tagging efficiency is chosen at (a) $\epsilon_{Tag} = 60\%$, (b) $\epsilon_{Tag} = 50\%$ and (c) optimized as described in the text, taking a second event sample to estimate the reconstructed and selected number of events.

compatible with the truth differential b-jet cross section. Within the uncertainty of the values, the largest differences are observed in the case of the optimized b-tagging efficiencies and purities. This is caused by smaller statistical errors as well as by the smaller number of selected events. Due to the higher purity values of the selected events, the overall statistical uncertainty nevertheless is smaller.
The differences of the differential unfolded and the truth differential b-jet cross sections, normalized to the truth differential b-jet cross sections using cone4 jets are presented in App. D. The results are comparable with the results of cone7 jets.

8.5 Systematic Uncertainties

Systematic uncertainties of the differential b-jet cross section measurement (e.g. from detector calibrations) have to be considered in addition to the statistical uncertainty of the measurement. Within this thesis, the following sources of systematic uncertainties are studied:

- the accuracy of the jet energy scale and the resolution of the jet p_{T} reconstruction,
- the uncertainties of the transfer matrix used in the unfolding algorithm,
- the uncertainties of the b-tagging efficiency as well as of the mistagging rates,
- the uncertainties of the integrated luminosity,
- the uncertainties of the jet reconstruction efficiency.

In order to study the impact of these systematic uncertainty sources on the differential b-jet cross section measurement, the affected input parameters are varied separately within the assumed accuracies. The difference of the differential b-jet cross section using a varied input parameter value compared to the b-jet cross section obtained with the original parameter value is taken as the systematic uncertainty contribution of the related parameter. In the following, the procedure to estimate the contributions of the different sources of systematic uncertainties to the differential b-jet cross section measurement is explained. The final systematic uncertainty is derived by the square root of the quadratic sum of all individual contributions. In order to avoid additional statistical effects due to the limited number of MC events, the systematic uncertainties are estimated using only the first event data sample (calibration sample). Since the first event data sample is also used for calibration (i.e. to estimate the efficiencies, purities as well as the transfer matrix), the analysis would result in a perfect reconstruction of the differential b-jet cross section in case the selected number of jets per bin is also taken from the calibration sample. In this case, that the different variations of input parameters are considered in the calibration using the calibration sample and the selected number of jets is also taken from this event sample, the effect of the resulting systematic uncertainty is mostly separated from the contributions due to statistical fluctuations.

The different systematic uncertainties are studied considering all jets in the event sample. The sources of the systematic uncertainties in the case of taking only the leading jet into account are the same. This assumption is justified since the differential leading b-jet cross section is similar to and shows the same behavior as the differential b-jet cross section taking all jets into account. Since the estimated efficiencies and purities of the leading jet analysis are of the same order (the leading jet sample is contained completely in the sample of all jets), the estimated contributions to the systematic uncertainties are not expected to be different within the available event statistics. Therefore, for both scenarios, the same systematic uncertainty is taken.

Uncertainty contribution by the jet energy scale

The measurements of the jet energy as well as of the jet p_{T} are provided by the ATLAS calorimeters. The energy calibration of the calorimeter may have a certain bias, which leads to a shift of the reconstructed jet energy as well as the jet p_{T} w.r.t. the truth jet p_{T}. The relative uncertainty of the jet energy scale (JES) is estimated to $\pm 5\%$ [4]. Therefore, to estimate the impact on the differential b-jet cross section, every reconstructed jet p_{T} is shifted by $\pm 5\%$. In measured event data, a shift of the jet p_{T} would be not known. Therefore, the $\pm 5\%$ shift has also to be taken into account in the calibration of other input parameters in the analysis. The resulting efficiencies and purities of the shifted jet p_{T} event sample are taken to estimate the contribution of the shift of the jet p_{T} to the systematic uncertainty. The differences of the resulting differential b-jet cross section of the shifted jet p_{T} spectrum compared to the non-shifted differential b-jet cross section are taken as an estimate for the contribution to the systematic uncertainty in each jet p_{T} bin.
The shift of the jet p_{T} by $\pm 5\%$ leads to bin-to-bin migrations of jets in the measured differential b-jet cross section spectrum. In Tab. 8.11, the estimated uncertainties due to the jet p_{T} shift are listed in the first column. Due to the steeply falling b-jet p_{T} spectrum, the absolute values of the systematic uncertainties are on average larger for the $+5\%$ jet p_{T} shift compared to the -5% jet p_{T} shift, which is reflected by asymmetric uncertainties. The uncertainty of the differential b-jet cross section due to the uncertainty of the JES varies from about 17% to larger than 40% towards higher jet p_{T} for both jet cone sizes. The limited number of MC events as well as the fact, that the estimation is done using a single event data sample, lead to fluctuations in the number of events affected by the bin-to-bin migrations and therefore to fluctuations in the contribution to the estimated systematic uncertainty in the different jet p_{T} bins on a percent level.

Uncertainty contribution by the jet p_{T} reconstruction resolution

The finite jet p_{T} reconstruction resolution leads to bin-to-bin migrations in the histogram of measured number of b-jets per jet p_{T} bin. The resolution of the jet p_{T} reconstruction $\sigma_{p_{\mathrm{T}}}$ is varied by $\pm 10\%$ in order to study the effect of a different jet

p_{T} range [GeV]		source of systematic uncertainty		
		jet p_{T} shift	$\sigma_{p_{\mathrm{T}}}$	unfolding
$30-50$	Cone4	$+18\%/-17\%$	$\pm 0.7\%$	$\pm 2.1\%$
	Cone7	$+21\%/-17\%$	$\pm 1.0\%$	$\pm 1.4\%$
$50-90$	Cone4	$+20\%/-20\%$	$\pm 0.6\%$	$\pm 2.4\%$
	Cone7	$+20\%/-17\%$	$\pm 2.0\%$	$\pm 2.3\%$
$90-150$	Cone4	$+29\%/-20\%$	$\pm 0.7\%$	$\pm 1.6\%$
	Cone7	$+24\%/-18\%$	$\pm 0.7\%$	$\pm 1.8\%$
$150-230$	Cone4	$+25\%/-20\%$	$\pm 2.4\%$	$\pm 1.2\%$
	Cone7	$+24\%/-20\%$	$\pm 0.5\%$	$\pm 1.6\%$
$230-330$	Cone4	$+20\%/-22\%$	$\pm 3.0\%$	$\pm 2.0\%$
	Cone7	$+25\%/-24\%$	$\pm 1.8\%$	$\pm 1.7\%$
$330-450$	Cone4	$+31\%/-21\%$	$\pm 1.7\%$	$\pm 1.9\%$
	Cone7	$+27\%/-22\%$	$\pm 1.4\%$	$\pm 1.5\%$
$450-590$	Cone4	$+37\%/-22\%$	$\pm 2.0\%$	$\pm 2.9\%$
	Cone7	$+33\%/-24\%$	$\pm 0.5\%$	$\pm 1.4\%$
$590-750$	Cone4	$+27\%/-33\%$	$\pm 0.9\%$	$\pm 2.7\%$
	Cone7	$+33\%/-33\%$	$\pm 1.2\%$	$\pm 2.8\%$
$750-930$	Cone4	$+37\%/-26\%$	$\pm 1.3\%$	$\pm 2.3\%$
	Cone7	$+34\%/-23\%$	$\pm 1.0\%$	$\pm 1.7\%$
$930-1130$	Cone4	$+41\%/-34\%$	$\pm 0.4\%$	$\pm 4.8\%$
	Cone7	$+37\%/-28\%$	$\pm 1.0\%$	$\pm 2.5\%$
>1130	Cone4	$+46\%/-40\%$	$\pm 0.6\%$	$\pm 6.1\%$
	Cone7	$+50\%/-47\%$	$\pm 0.8\%$	$\pm 4.6\%$

Table 8.11: Systematic error contributions of the differential b-jet cross section measurement due to a shift of $\pm 5\%$ of the reconstructed jet p_{T}, a variation of the jet p_{T} reconstruction resolution $\sigma_{p_{\mathrm{T}}}$ by $\pm 10\%$ and the statistical uncertainty of the transfer matrix.

p_{T} resolution. All reconstructed jet p_{T} values $p_{\mathrm{T}_{jet,rec}}$ are shifted by

$$p_{\mathrm{T}_{jet,rec}}^{\pm 10\%} = p_{\mathrm{T}_{jet,rec}} \pm 0.1(p_{\mathrm{T}_{jet,truth}} - p_{\mathrm{T}_{jet,rec}})\,, \tag{8.37}$$

where $p_{\mathrm{T}_{jet,truth}}$ denotes the truth jet p_{T}.
The systematic uncertainty due to the resolution of the jet p_{T} reconstruction is listed in the second column of Tab. 8.11. Since the bin-to-bin migrations of jets are partially canceling each other, the overall contribution is expected to be small ($\leq 3\%$) for both jet cone sizes.

Uncertainty contribution by the unfolding procedure

In the unfolding procedure (Chapter 8.4) the transfer matrix is derived from the calibration event sample, which contains approximately the same number of events compared to the second data sample (analysis sample), which is used as the analysis

event data sample. Since the number of events used to estimate the transfer matrix is of similar size as the number of events in the jet p_{T} spectrum, which will be unfolded, the uncertainty of the transfer matrix elements is not negligible. This reflects also the situation of a measurement with the ATLAS detector, since the MC event sample will not be larger than the number of events measured by the detector. In order to study the contribution to the systematic uncertainty introduced by the transfer matrix, the calibration sample is split into 10 sub-samples [53]. Each sub-sample is used to derive a transfer matrix, which contains 10 times less events compared to the original transfer matrix derived from the whole calibration data sample. Each of these ten transfer matrices is used to unfold the b-jet spectrum derived from events of the analysis event sample. The ten results of unfolding the differential b-jet cross section fluctuate. The statistical fluctuations are expected to be larger by a factor of $\sqrt{10}$ compared to the case when the transfer matrix estimated from the whole calibration data sample is used. Therefore, the root mean square of the results of the ten different unfolding procedures is expected to be larger by a factor of $\sqrt{10}$. In order to estimate the fluctuations of the original transfer matrix obtained from the full event statistics, the root mean square of the results, taking the ten transfer matrices from the sub-samples, is divided by $\sqrt{10}$ and taken as the contribution of the unfolding to the systematic uncertainty of the differential b-jet cross section measurement.
This estimation is performed for cone4 as well as for cone7 jets and the results are listed in the third column of Tab. 8.11. For both cone sizes, the uncertainties are observed to be on the percent level over the whole jet p_{T} region considered. Only in the highest jet p_{T} bin, the uncertainty is about $\approx 6\%$ for cone4 and $\approx 5\%$ for cone7 jets.

Uncertainty contribution by the b-tagging efficiency

The b-tagging efficiency will be estimated from the data with a certain accuracy. Within this thesis the relative precision of the b-tagging efficiency calibration is considered to be $\pm 5\%$ independent of the jet p_{T} like it is advised in [4]. The efficiency of the b-tagging ϵ_{Tag} is varied by increasing or decreasing the number of b-labeled b-jets by $\pm 5\% \times \epsilon_{Tag}$ in a certain jet p_{T} bin. This is equivalent to swapping, with a probability of $5\% \times \epsilon_{Tag}$, the status of the labeling of rejected (in case of $+5\% \times \epsilon_{Tag}$) or selected (in case of $-5\% \times \epsilon_{Tag}$) b-jets after tagging. Since the variation of ϵ_{Tag} depends on the estimated efficiency itself, the systematic uncertainty depends on the b-tagging efficiency working point (i.e. cut scenario). Hence, the impact on the b-jet measurement has to be estimated for the different cut scenarios of $\epsilon_{Tag} = 0.6$, $\epsilon_{Tag} = 0.5$ and the optimized efficiency $\epsilon_{Tag,opt}$ (Section 8.3.3).
In Tab. 8.12 the estimated contributions to the systematic uncertainty are listed. In the case of fixed b-tagging efficiencies, the uncertainties are larger in the lower jet p_{T} region and decrease towards higher jet p_{T}. In the region of a higher b-tagging performance most selected jets are b-jets and therefore the impact of these "additional" or "missing" b-jets is larger compared to the higher jet p_{T} region, where most of the selected jets are background jets. Hence the contribution to the

p_{T} range [GeV]		$\epsilon_{Tag} = 60\%$		$\epsilon_{Tag} = 50\%$		ϵ_{Tag} opt.	
		$\epsilon_{Tag} \pm 5\%$	$\epsilon_u \pm 10\%$	$\epsilon_{Tag} \pm 5\%$	$\epsilon_u \pm 10\%$	$\epsilon_{Tag} \pm 5\%$	$\epsilon_u \pm 10\%$
$30 - 50$	Cone4	$\pm 2.6\%$	$\pm 4.8\%$	$\pm 3.7\%$	$\pm 2.5\%$	$\pm 4.1\%$	$\pm 1.8\%$
	Cone7	$\pm 1.6\%$	$\pm 6.8\%$	$\pm 2.8\%$	$\pm 4.4\%$	$\pm 4.0\%$	$\pm 2.0\%$
$50 - 90$	Cone4	$\pm 3.5\%$	$\pm 3.0\%$	$\pm 4.1\%$	$\pm 1.9\%$	$\pm 3.7\%$	$\pm 2.7\%$
	Cone7	$\pm 3.1\%$	$\pm 3.9\%$	$\pm 3.8\%$	$\pm 2.4\%$	$\pm 3.6\%$	$\pm 2.7\%$
$90 - 150$	Cone4	$\pm 3.6\%$	$\pm 2.7\%$	$\pm 4.1\%$	$\pm 1.7\%$	$\pm 3.6\%$	$\pm 2.8\%$
	Cone7	$\pm 3.6\%$	$\pm 2.8\%$	$\pm 4.0\%$	$\pm 1.9\%$	$\pm 3.7\%$	$\pm 2.7\%$
$150 - 230$	Cone4	$\pm 3.4\%$	$\pm 3.3\%$	$\pm 4.0\%$	$\pm 2.1\%$	$\pm 3.6\%$	$\pm 2.9\%$
	Cone7	$\pm 3.4\%$	$\pm 3.1\%$	$\pm 4.0\%$	$\pm 1.9\%$	$\pm 3.6\%$	$\pm 2.8\%$
$230 - 330$	Cone4	$\pm 2.8\%$	$\pm 4.4\%$	$\pm 3.6\%$	$\pm 2.9\%$	$\pm 3.4\%$	$\pm 3.2\%$
	Cone7	$\pm 2.4\%$	$\pm 5.2\%$	$\pm 3.2\%$	$\pm 3.7\%$	$\pm 3.1\%$	$\pm 3.8\%$
$330 - 450$	Cone4	$\pm 2.2\%$	$\pm 5.6\%$	$\pm 3.1\%$	$\pm 3.9\%$	$\pm 3.3\%$	$\pm 3.4\%$
	Cone7	$\pm 2.2\%$	$\pm 5.5\%$	$\pm 3.3\%$	$\pm 3.5\%$	$\pm 3.4\%$	$\pm 3.1\%$
$450 - 590$	Cone4	$\pm 1.2\%$	$\pm 7.5\%$	$\pm 2.1\%$	$\pm 5.8\%$	$\pm 3.0\%$	$\pm 4.0\%$
	Cone7	$\pm 1.4\%$	$\pm 7.1\%$	$\pm 2.2\%$	$\pm 5.6\%$	$\pm 2.7\%$	$\pm 4.5\%$
$590 - 750$	Cone4	$\pm 0.7\%$	$\pm 8.6\%$	$\pm 1.2\%$	$\pm 7.7\%$	$\pm 2.3\%$	$\pm 5.4\%$
	Cone7	$\pm 0.9\%$	$\pm 8.2\%$	$\pm 1.4\%$	$\pm 7.2\%$	$\pm 2.5\%$	$\pm 5.1\%$
$750 - 930$	Cone4	$\pm 0.7\%$	$\pm 8.7\%$	$\pm 1.1\%$	$\pm 7.8\%$	$\pm 2.0\%$	$\pm 6.0\%$
	Cone7	$\pm 0.7\%$	$\pm 8.6\%$	$\pm 1.1\%$	$\pm 7.9\%$	$\pm 2.3\%$	$\pm 5.5\%$
$930 - 1130$	Cone4	$\pm 0.4\%$	$\pm 9.2\%$	$\pm 0.6\%$	$\pm 8.9\%$	$\pm 2.3\%$	$\pm 5.5\%$
	Cone7	$\pm 0.5\%$	$\pm 9.1\%$	$\pm 0.8\%$	$\pm 8.5\%$	$\pm 2.0\%$	$\pm 5.9\%$
> 1130	Cone4	$\pm 0.4\%$	$\pm 9.2\%$	$\pm 0.6\%$	$\pm 8.9\%$	$\pm 1.3\%$	$\pm 7.4\%$
	Cone7	$\pm 0.5\%$	$\pm 9.0\%$	$\pm 0.7\%$	$\pm 8.5\%$	$\pm 1.3\%$	$\pm 7.4\%$

Table 8.12: Systematic error contributions of the differential b-jet cross section measurement due to the uncertainty on the determination of the tagging efficiency ϵ_{Tag} of b-jets and mistagging rates ϵ_c and ϵ_{QCD} (summarized as ϵ_u) .

systematic uncertainty by the b-tagging efficiency variation is decreasing towards higher jet p_{T}. The contribution to the systematic uncertainty due to the b-tagging efficiency in the optimized b-tagging scenario is larger in the high jet p_{T} region compared to the scenario of fixed b-tagging efficiencies. This larger impact is due to the falling b-tagging efficiency towards higher jet p_{T}, as chosen in this tagging scenario.

The contribution to the systematic uncertainty by the b-tagging efficiency variation is expected to be less than 10% for both jet cone sizes. Although it will be more difficult to calibrate the b-tagging efficiency in the high jet p_{T} region, the contribution to the systematic uncertainty due to the b-tagging calibration is expected to be much smaller than the uncertainty due to the JES variation. This holds even if the relative b-tagging calibration accuracy will be worse than the assumed $\pm 5\%$ in the high jet p_{T} region.

Uncertainty contribution by the mistagging rates

The mistagging rates of c-jets ϵ_c and of QCD jets ϵ_{QCD} influence the purity of the selected jet sample according to (8.18) and hence the differential b-jet cross section measurement. The accuracy of the estimation of the mistagging rates on data is

expected to be $\pm 10\% \times \epsilon_{c,QCD}$ independent of the jet p_{T}[4].
Similarly to the b-tagging performance, the tagging labels of reconstructed background jets are swapped according to $\pm 10\% \times \epsilon_{c,QCD}$ of the estimated mistagging rates of c-jets ϵ_c and QCD jets ϵ_{QCD} (summarized as ϵ_u) in a jet p_{T} bin. Thus, the impact of the mistagging rate uncertainty on the systematic uncertainty is estimated for each cut scenario in the analysis. In Tab. 8.12 the different contributions to the systematic uncertainties due to a variation of the mistagging rates for the different cut scenarios are listed. The contribution to the systematic uncertainty due to the uncertainty of the mistagging rates is larger in the jet p_{T} region, in which the ratio of the selected background jets compared to signal jets is larger. Therefore, the highest contribution by the mistagging rate variation to the overall systematic uncertainty is larger in the region of very high jet p_{T}, but estimated to be less than 10% for each cut scenario. In the optimized b-tagging efficiency scenario, the purity is larger in the high jet p_{T} region and the contribution of the systematic uncertainty due to the mistagging rates is smaller compared to the scenarios with fixed b-tagging efficiencies.
Even though the contribution by the uncertainty of the mistagging rates in the very high p_{T} region is more difficult to estimate from data (and may be worse than the assumed $\pm 10\% \times \epsilon_{c,QCD}$), the estimated contribution to the systematic uncertainties is smaller than the uncertainty introduced by the shift in the JES.

Uncertainty contribution by the integrated luminosity

The integrated luminosity has to be measured to calculate the b-jet cross section. Dedicated detectors and offline algorithms are available to estimate the integrated luminosity providing measurements with different accuracies (Chapter 7). In order to estimate the overall systematic uncertainty of the differential b-jet cross section measurement, an uncertainty of $\pm 11\%$ of the integrated luminosity is used like it is measured with the ATLAS experiment [54] and added to the systematic uncertainty of the cross section measurement. Therefore, especially in the lower jet p_{T} region, the contribution by the uncertainty of the luminosity measurement is expected to be the second largest source of systematic uncertainty after the uncertainty due to a shift in the JES.

Uncertainty contribution by the jet reconstruction

The jet reconstruction efficiency enters directly in the calculation of the differential b-jet cross section. Missing jets due to a lower reconstruction efficiency of jets will lead to a smaller measured b-jet cross section. The uncertainty on the jet reconstruction efficiency is considered to be about 1%, which is added to the overall systematic uncertainty.

Overall systematic uncertainty

p_{T} range [GeV]	Summary of systematic uncertainty	
	Cone4 jets	Cone7 jets
$30 - 50$	$^{22\%}_{-21\%}$	$^{24\%}_{-21\%}$
$50 - 90$	$^{24\%}_{-23\%}$	$^{23\%}_{-21\%}$
$90 - 150$	$^{31\%}_{-23\%}$	$^{27\%}_{-22\%}$
$150 - 230$	$^{28\%}_{-23\%}$	$^{27\%}_{-23\%}$
$230 - 330$	$^{23\%}_{-25\%}$	$^{28\%}_{-27\%}$
$330 - 450$	$^{33\%}_{-24\%}$	$^{30\%}_{-25\%}$
$450 - 590$	$^{39\%}_{-25\%}$	$^{35\%}_{-27\%}$
$590 - 750$	$^{30\%}_{-35\%}$	$^{35\%}_{-35\%}$
$750 - 930$	$^{39\%}_{-29\%}$	$^{36\%}_{-26\%}$
$930 - 1130$	$^{43\%}_{-37\%}$	$^{39\%}_{-31\%}$
> 1130	$^{48\%}_{-43\%}$	$^{52\%}_{-49\%}$

Table 8.13: Summary of systematic uncertainties on the differential b-jet cross section measurement per jet p_{T} bin using cone4 and cone7 jets.

Tab. 8.13 summarizes the estimation of the overall systematic uncertainties in the different jet p_{T} bins. The uncertainties are calculated as the square root of the quadratic sum of all contributions listed above. The asymmetric errors reflect the asymmetric uncertainties due to the JES shift of the jet p_{T}, which is by far the dominant contribution to the systematic uncertainties. The overall systematic uncertainties increase for both jet cone size scenarios from about 20% to about 50% in the very high jet p_{T} region. The different contributions to the overall systematic uncertainties for different b-tagging efficiency scenarios do not result in sizable differences of the overall systematic uncertainties. Therefore, only the scenario with ϵ_{Tag} optimized is considered.

The contribution to the systematic uncertainties due to pile-up events is not included in this thesis, since MC event data samples including pile-up events are not available. The effect of additional events underlying the hard scattering process has to be studied in further analyses.

In addition to the overall systematic uncertainty, the uncertainty introduced by the choice of the MC model has to be considered as a MC model uncertainty. In order

to estimate the impact of the MC model uncertainty, results of the analysis using event samples generated by different MC generators have to be compared [4]. Also the input parameters to the event generators have to be varied and later on they should be tuned to data [4]. In order to provide an estimate for the MC model uncertainty, an uncertainty in the order of $\pm 10\%$ is assumed, following the results of detailed studies [4],[55].

8.6 Differential b-Jet Production Cross Section

The different contributions to the uncertainties of the differential b-jet cross section have been studied in Section 8.4 (statistical uncertainties of the MC event sample) and Section 8.5 (systematic uncertainties). In this section the different uncertainties will be summarized and an estimate of the statistical uncertainty of the measurement as a function of the integrated luminosity will be given.
In the upper plots of Fig. 8.34 (a) and (b) the reconstructed differential b-jet cross sections as a function of the jet p_{T} using (a) all cone7 jets and (b) using all cone4 jets in the event data sample are shown. The first data sample is used to calibrate the analysis and the second data sample is used for the analysis itself. The error bars indicate the statistical uncertainties obtained according to the MC event data sample's statistics and do not correspond to a certain integrated luminosity. The filled areas denote the obtained systematic uncertainties in the different jet p_{T} bins. The lower plots show the reconstructed b-jet cross section divided by the MC b-jet cross section per jet p_{T} bin. Again, the filled area represents the systematic uncertainty dominated by the contribution of the jet energy scale to the overall systematic uncertainty. In addition to the statistical and the systematic uncertainty, the uncertainty of the MC model of 10% has to be considered, which is not shown in the plots.
The expected statistical uncertainty of the differential b-jet cross section will decrease towards larger event numbers, i.e. will decrease with an increasing integrated luminosity. In addition, the statistical uncertainty depends on the chosen b-tagging efficiency (i.e. cut scenario). Hence the number of expected jets in the different jet p_{T} bins are scaled according to the integrated luminosity considering the different cut scenarios. The statistical uncertainties of the efficiencies and the purities due to the number of MC events used, are not taken into account for the estimations of the uncertainties as a function of the integrated luminosity. These uncertainties are due to calibration uncertainties of e.g. b-tagging and are considered as systematic uncertainties in the differential b-jet cross section measurement on data. As an example, the expected statistical uncertainty as a function of the integrated luminosity ($50\,\mathrm{pb}^{-1} \leq \mathcal{L} \leq 800\,\mathrm{pb}^{-1}$) is shown in Fig. 8.35 (a)-(d) using all cone7 jets in the event sample.
In Fig. 8.35(a) the expected statistical uncertainties of the lower jet p_{T} bins and in Fig. 8.35(b) of the higher jet p_{T} bins are shown for the cut scenario of a chosen b-tagging efficiency of $\epsilon_{Tag} = 0.6$. The statistical uncertainty is similar for all jet p_{T} bins, in which a prescaled jet trigger is used, since the differential b-jet spectrum

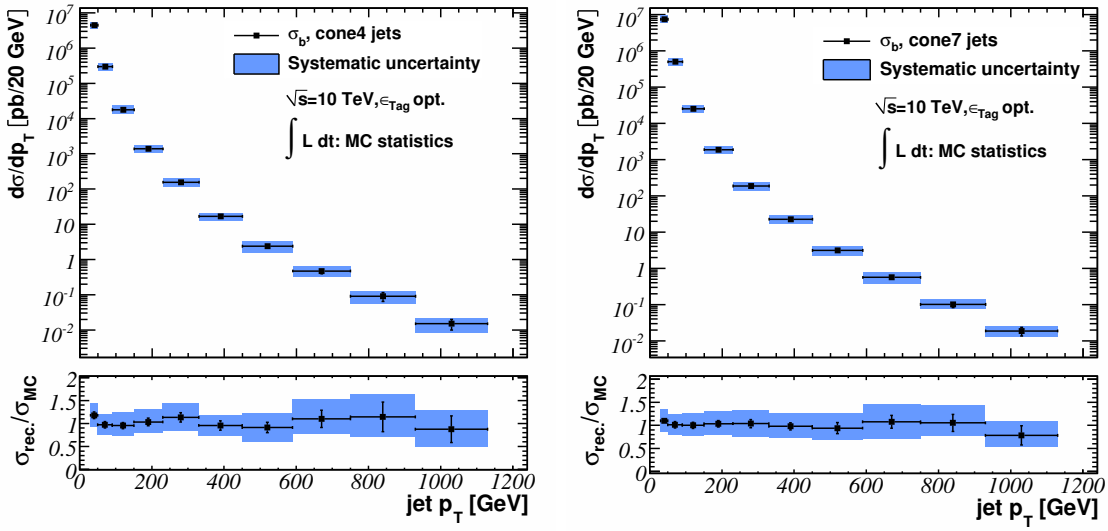

(a) (b)

Figure 8.34: Reconstructed differential b-jet cross section using (a) all cone4 jets and (b) all cone7 jets in the b-tagging scenario with an optimized b-tagging efficiency. The statistical uncertainties correspond to the available number of MC events.

is flattened due to the prescale factors. In the lower jet p_{T} bins, already for an integrated luminosity of $\mathcal{L} = 50\,\mathrm{pb}^{-1}$, the expected statistical uncertainties are smaller than the systematic uncertainties, which are above 20% for each jet p_{T} bin. Therefore, it is expected in the lower jet p_{T} bins, that the systematic uncertainty is the dominating uncertainty of the differential b-jet cross section measurement, even in case a smaller bin width is chosen for the measurement. Due to the b-jet cross section falling steeply with jet p_{T}, the relative statistical uncertainty increases. The relative statistical uncertainties in the higher jet p_{T} bins, as shown in Fig. 8.35(b), are larger. For comparison the (larger of the asymmetric) systematic uncertainties of the two highest jet p_{T} bins are marked as lines in the plot. For an integrated luminosity below the intersection point of the systematic and the statistical uncertainty, the statistical uncertainty is the dominant uncertainty of the measurement.

For the cut scenario with the optimized b-tagging efficiency the statistical uncertainty in the lower jet p_{T} region is also negligible in comparison to the systematic uncertainty (Fig. 8.35(c)). In the higher jet p_{T} region, the statistical uncertainty is less compared to the $\epsilon_{Tag} = 0.6$ cut scenario, which is expected since the b-tagging efficiency is optimized to reduce the statistical uncertainty for a certain integrated luminosity. Therefore, the integrated luminosity needed to reduce the statistical uncertainty below the systematic uncertainty is less compared to the scenarios with the fixed b-tagging efficiency. Nevertheless, the dominant uncertainty of the differential b-jet cross section will be the systematic uncertainty in most of the jet p_{T} bins considered.

The statistical uncertainties of the differential b-jet cross section measurement with $\epsilon_{Tag} = 0.5$ for all cone7 jets are shown in App. E. They show the same behavior

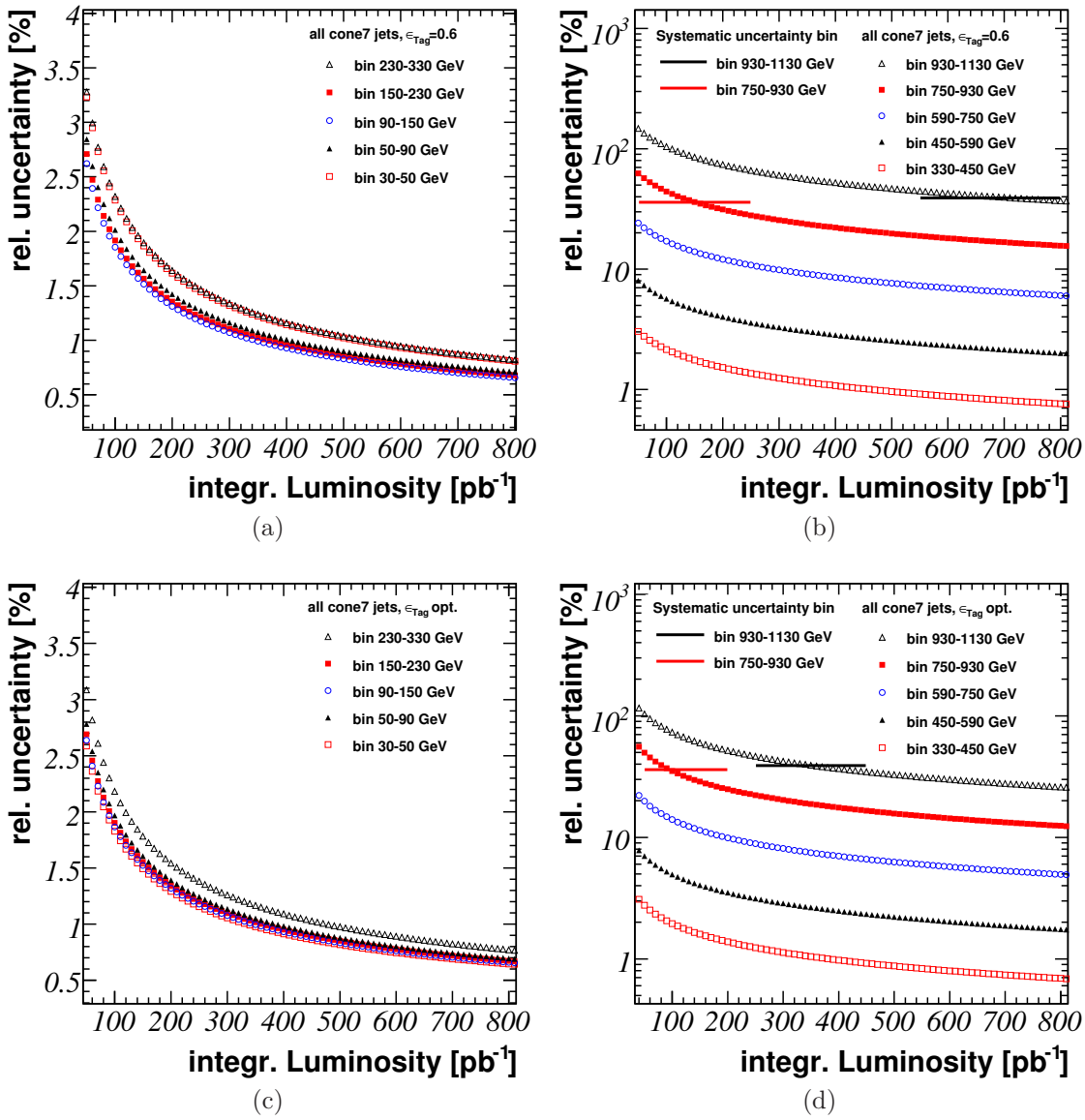

Figure 8.35: Statistical uncertainty of the differential b-jet cross section as a function of the integrated luminosity for cone7 jets. The b-tagging efficiency is chosen as $\epsilon_{Tag} = 0.6$ in (a) and (b) and to be ϵ_{Tag} opt. in (c) and (d). For comparison, the relevant systematic uncertainties for the two highest jet p_{T} bins are marked as lines in plots (b) and (c).

as for the fixed b-tagging efficiency of $\epsilon_{Tag} = 0.6$. Furthermore, the differences of the statistical uncertainty using cone4 jets (all cone4 jets as well as taking only the leading jet into account) are small and therefore, no separate plots are shown for these scenarios.

p_{T} range [GeV]		systematic uncertainty	ϵ_{Tag} opt., statistical uncertainty at MC stat.	$\mathcal{L} = 100\,\mathrm{pb}^{-1}$	$\mathcal{L} = 400\,\mathrm{pb}^{-1}$
$30 - 50$	Cone4	$^{+0.22}_{-0.21}$	0.06	0.02	0.01
	Cone7	$^{+0.24}_{-0.21}$	0.05	0.02	0.01
$50 - 90$	Cone4	$^{+0.24}_{-0.23}$	0.07	0.02	0.01
	Cone7	$^{+0.23}_{-0.21}$	0.07	0.02	0.01
$90 - 150$	Cone4	$^{+0.31}_{-0.23}$	0.07	0.02	0.01
	Cone7	$^{+0.27}_{-0.22}$	0.07	0.02	0.01
$150 - 230$	Cone4	$^{+0.28}_{-0.23}$	0.08	0.02	0.01
	Cone7	$^{+0.27}_{-0.23}$	0.07	0.02	0.01
$230 - 330$	Cone4	$^{+0.23}_{-0.25}$	0.09	0.02	0.01
	Cone7	$^{+0.28}_{-0.27}$	0.08	0.02	0.01
$330 - 450$	Cone4	$^{+0.33}_{-0.24}$	0.11	0.02	0.01
	Cone7	$^{+0.30}_{-0.25}$	0.08	0.02	0.01
$450 - 590$	Cone4	$^{+0.39}_{-0.25}$	0.12	0.06	0.03
	Cone7	$^{+0.35}_{-0.27}$	0.13	0.05	0.02
$590 - 750$	Cone4	$^{+0.30}_{-0.35}$	0.17	0.18	0.09
	Cone7	$^{+0.35}_{-0.35}$	0.13	0.14	0.07
$750 - 930$	Cone4	$^{+0.39}_{-0.29}$	0.28	0.42	0.21
	Cone7	$^{+0.36}_{-0.26}$	0.18	0.35	0.18
$930 - 1130$	Cone4	$^{+0.43}_{-0.37}$	0.33	0.92	0.46
	Cone7	$^{+0.39}_{-0.31}$	0.27	0.73	0.37
> 1130	Cone4	$^{+0.48}_{-0.43}$	0.29	-	-
	Cone7	$^{+0.52}_{-0.49}$	0.28	-	0.81

Table 8.14: Summary of different uncertainties on the differential b-jet cross section measurement using the optimized b-tagging efficiency taking all jets in the event sample into account. An entry "-" in a statistics column denotes insufficient statistics in the number of jets.

In Tab. 8.14 the different uncertainties on the differential b-jet cross section considering all jets in the event sample are listed for each jet p_{T} bin. The statistical uncertainties are given for three cases: the available MC event statistics, which do not correspond to a certain integrated luminosity and the expected statistical uncertainty scaled to an integrated luminosity of $\mathcal{L} = 100\,\mathrm{pb}^{-1}$ and $\mathcal{L} = 400\,\mathrm{pb}^{-1}$. In the lower jet p_{T} bins, the statistical errors are similar, since the prescale factors in the trigger flattened the b-jet spectrum. As mentioned above, the statistical uncertainties will be relevant only in the higher jet p_{T} region (about $p_{\mathrm{T}_{jet}} > 750\,\mathrm{GeV}$), where the statistical uncertainty is of the same order or larger than the systematic uncertainty of the differential b-jet cross section measurement. A entry of "-" in

the statistical uncertainty column means, that there is not sufficient integrated luminosity to measure the differential b-jet cross section in the particular jet p_{T} bin. Therefore, an integrated luminosity of about $\mathcal{L} = 400\,\mathrm{pb}^{-1}$ should be sufficient to measure the b-jet cross section in almost the entire jet p_{T} region, which is considered within this thesis, taking the optimized b-tagging efficiency scenario. The differential b-jet cross section measurement in the lower jet p_{T} regions is already possible with low event statistics, i.e. lower integrated luminosity, as shown in Fig. 8.35(c) and Fig. 8.35(d).
In most of the jet p_{T} bins, the statistical uncertainty is larger in case of using cone4 jets compared to using cone7 jets, which reflects the smaller differential cross section for cone4 jets in a certain jet p_{T} bin.

p_{T} range [GeV]		systematic uncertainty	ϵ_{Tag} opt., statistical uncertainty at MC stat.	$\mathcal{L} = 100\,\mathrm{pb}^{-1}$	$\mathcal{L} = 400\,\mathrm{pb}^{-1}$
$30 - 50$	Cone4	$^{+0.22}_{-0.21}$	0.07	0.03	0.01
	Cone7	$^{+0.24}_{-0.21}$	0.06	0.02	0.01
$50 - 90$	Cone4	$^{+0.24}_{-0.23}$	0.08	0.02	0.01
	Cone7	$^{+0.23}_{-0.21}$	0.08	0.03	0.01
$90 - 150$	Cone4	$^{+0.31}_{-0.23}$	0.08	0.02	0.01
	Cone7	$^{+0.27}_{-0.22}$	0.07	0.02	0.01
$150 - 230$	Cone4	$^{+0.28}_{-0.23}$	0.09	0.02	0.01
	Cone7	$^{+0.27}_{-0.23}$	0.07	0.02	0.01
$230 - 330$	Cone4	$^{+0.23}_{-0.25}$	0.09	0.02	0.01
	Cone7	$^{+0.28}_{-0.27}$	0.09	0.02	0.01
$330 - 450$	Cone4	$^{+0.33}_{-0.24}$	0.11	0.02	0.01
	Cone7	$^{+0.30}_{-0.25}$	0.08	0.02	0.01
$450 - 590$	Cone4	$^{+0.39}_{-0.25}$	0.13	0.06	0.03
	Cone7	$^{+0.35}_{-0.27}$	0.13	0.05	0.03
$590 - 750$	Cone4	$^{+0.30}_{-0.35}$	0.18	0.18	0.09
	Cone7	$^{+0.35}_{-0.35}$	0.13	0.14	0.07
$750 - 930$	Cone4	$^{+0.39}_{-0.29}$	0.28	0.42	0.21
	Cone7	$^{+0.36}_{-0.26}$	0.18	0.36	0.18
$930 - 1130$	Cone4	$^{+0.43}_{-0.37}$	0.34	0.95	0.47
	Cone7	$^{+0.39}_{-0.31}$	0.27	0.73	0.36
> 1130	Cone4	$^{+0.48}_{-0.43}$	0.29	-	-
	Cone7	$^{+0.52}_{-0.49}$	0.28	-	0.82

Table 8.15: Summary of different uncertainties on the differential b-jet cross section measurement using the optimized b-tagging efficiency taking only the leading jets into account. An entry "-" in a statistics column denotes insufficient statistics in the number of jets.

In Tab. 8.15 the different uncertainties on the differential b-jet cross section measurement considering only the leading jets of the cone4 as well as cone7 jet samples are listed. Like for the analysis considering all jets in the event sample, the statistical

uncertainties are relevant only in the higher jet p_{T} region, i.e. for the jet p_{T} bins with $p_{\mathrm{T}_{jet}} > 750\,\mathrm{GeV}$ (depending on the integrated luminosity).
The uncertainties for the cut scenarios with fixed b-tagging efficiencies of $\epsilon_{Tag} = 0.5$ and $\epsilon_{Tag} = 0.6$ for the differential b-jet cross section considering all jets as well as only the leading jets are given in App. E. As expected, the statistical uncertainties of the measurement are larger in the high jet p_{T} region taking a fixed b-tagging efficiency compared to the optimized b-tagging efficiency scenario. Therefore, for both fixed b-tagging efficiency scenarios of $\epsilon_{Tag} = 0.5$ and $\epsilon_{Tag} = 0.6$ a larger integrated luminosity is needed to measure the differential b-jet cross section. The statistical uncertainty of the measurement of the differential b-jet cross section using cone4 jets is larger compared to cone7 jets due to the smaller cross section of cone4 jets in a certain jet p_{T} bin.
In Fig. 8.36(a) the expected result of the differential b-jet cross section measurement with all cone7 in the event sample assuming an integrated luminosity of $\mathcal{L} = 100\,\mathrm{pb}^{-1}$ is shown. In the upper plot the reconstructed differential b-jet cross section is given. The lower plot shows the results normalized to the MC b-jet cross section. The corresponding result for the differential b-jet cross section measurement assuming an integrated luminosity of $\mathcal{L} = 400\,\mathrm{pb}^{-1}$ is shown in Fig. 8.36(b). The statistical uncertainties are far less than the systematic uncertainties in the lower jet p_{T} bins and become relevant only in the higher jet p_{T} bins at about $p_{\mathrm{T}_{jet}} > 750\,\mathrm{GeV}$.
The statistical fluctuations of the reconstructed differential b-jet cross section are expected to remain the same assuming different integrated luminosities. The number of jets per jet p_{T} bin will be scaled in order to correspond to the statistical uncertainty and therefore, the reconstructed cross section values stay the same independently of the assumed integrated luminosity.
In summary, the differential b-jet cross section, taking the optimized b-tagging efficiency scenario, can be measured with an integrated luminosity less than $\mathcal{L} = 100\,\mathrm{pb}^{-1}$ in the lower jet p_{T} region ($p_{\mathrm{T}_{jet}} < 750\,\mathrm{GeV}$) using cone4 or cone7 jets. Already at this integrated luminosity, the systematic uncertainty will be the dominant uncertainty. The statistical uncertainties of the measurement become relevant in the higher jet p_{T} bins and about $\mathcal{L} = 400\,\mathrm{pb}^{-1}$ is needed to reduce the statistical uncertainty to a similar size as the systematic uncertainty.

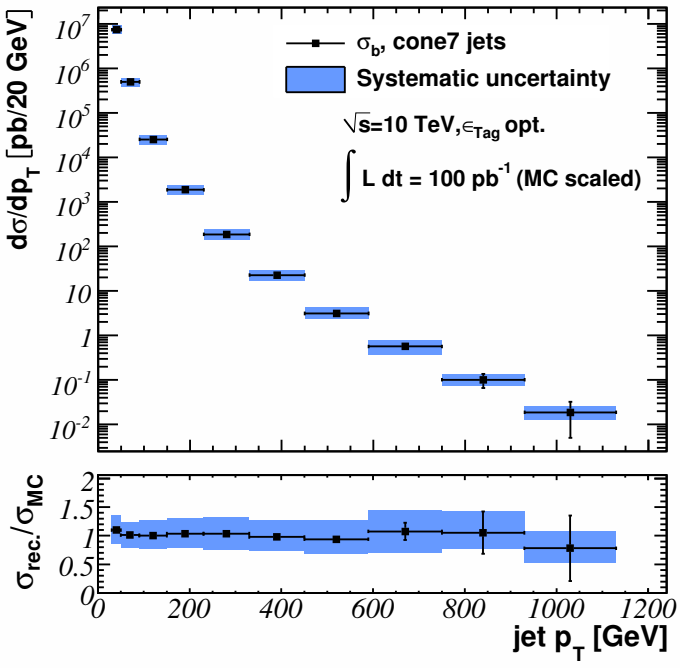

(a)

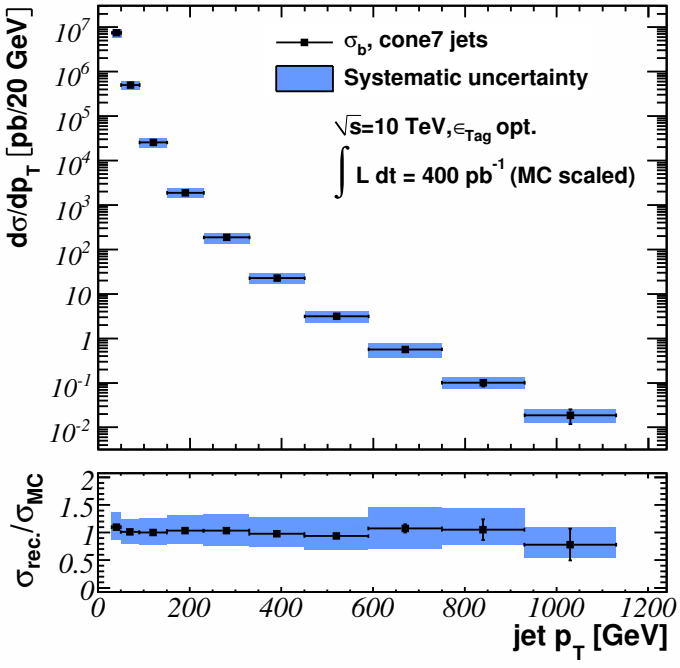

(b)

Figure 8.36: Obtained reconstructed differential b-jet cross section using all cone7 jets in the b-tagging scenario with an optimized b-tagging efficiency. The statistical uncertainties are scaled to the integrated luminosity of (a) $\mathcal{L} = 100\,\mathrm{pb}^{-1}$ and (b) $\mathcal{L} = 400\,\mathrm{pb}^{-1}$.

Chapter 9

Summary

In this thesis, the prospects of measuring the differential p_{T} b-jet cross section have been studied. The differential b-jet cross section depends on the center-of-mass energy and has been measured by previous experiments at lower energies. Up to now it has been extrapolated to the energy available at the Large Hadron Collider (LHC), but it should be measured at the LHC design center-of-mass energy of $\sqrt{s} = 14\,\mathrm{TeV}$. Such a measurement will be used to check the Standard Model of Elementary Particles (SM) and will serve as an important input to other analyses.

Currently, the LHC accelerates protons to an energy of 3.5 TeV resulting in a center-of-mass energy of $\sqrt{s} = 7\,\mathrm{TeV}$. At the time this study started, a data taking run with $\sqrt{s} = 10\,\mathrm{TeV}$ was planned and thus 10 TeV is assumed as the center-of-mass energy in this thesis. This thesis is based on Monte Carlo events, which simulate the production of b-quarks in proton-proton collisions as well as QCD background processes, which are the most important background contribution in the measurement of the differential b-jet cross section. The b-jets are identified on MC truth level by geometrical matching of the b-quark flight direction and the direction of the b-jet.

Jets reconstructed by the cone algorithm are studied for two different cone sizes, cone4 ($\Delta R = 0.4$) and cone7 ($\Delta R = 0.7$). The measurement of the differential b-jet cross section is prepared for two different cases, the first taking all jets in the MC event into account and the second taking only the leading p_{T} (b-)jet in the event.

The chosen trigger strategy is based on a combination of single jet trigger signatures. The simulated single jet trigger signatures with lower jet E_{T} thresholds are prescaled, which requires an appropriate reweighting of the MC events in the analysis. The prescale factors in the trigger menu, foreseen for an instantaneous luminosity of $10^{31}\,\mathrm{cm}^{-2}\mathrm{s}^{-1}$, decrease towards higher jet E_{T}. Starting at a threshold of $E_{\mathrm{T}} = 350\,\mathrm{GeV}$ no prescale factors are applied. The prescale factors cause, that the measured jet p_{T} spectrum shows a flat distribution up to $\approx 350\,\mathrm{GeV}$ and than decreases according to the falling production cross section. The trigger efficiency without taking prescale factors into account is found to be $\epsilon_{Tr} > 0.99$ except for the lowest p_{T} bin ($30\,\mathrm{GeV} < p_{\mathrm{T}_{jet}} < 50\,\mathrm{GeV}$), where the trigger efficiency is $\epsilon_{Tr} \approx 0.96$ for cone4 and $\epsilon_{Tr} \approx 0.89$ for cone7 jets.

The jet reconstruction efficiency is estimated by comparing the number of recon-

structed jets with the number of MC truth jets. The reconstruction efficiency is $\epsilon_{Rec} \approx 0.98$ for the jet p_{T} range considered except for the low jet p_{T} of $p_{\mathrm{T}_{jet}} < 90\,\mathrm{GeV}$, where ϵ_{Rec} is $0.92 < \epsilon_{Rec} < 0.95$ for cone7 jets and $0.95 < \epsilon_{Rec} < 0.98$ for cone4 jets. The loss of jets due to reconstruction is therefore expected to be small. The same behavior is observed for the purity of the jet reconstruction, which is a measure of fake jets due to the reconstruction. Again, the purity value is $P_{Rec} > 0.97$ for the jet p_{T} region considered except for the lowest jet p_{T} region, where the purity is $P_{Rec} \approx 0.92$ for cone7 jets ($P_{Rec} \approx 0.96$ for cone4 jets).
In order to select the b-jets and to reject background jets, b-tagging algorithms based on the fact, that on average the lifetime of b-hadrons (hadrons containing a b-quark) is longer compared to other hadrons, which decay before reaching the detector. Various cuts used in the b-tagging algorithms are tuned to maximize the b-tagging purity at a given b-tagging efficiency over the whole p_{T} range considered. In this thesis three different scenarios for the chosen b-tagging efficiency are studied. For the fixed b-tagging efficiency scenarios of $\epsilon_{Tag} = 0.5$ and $\epsilon_{Tag} = 0.6$, the b-tagging purity of the selected jets is decreasing towards higher jet p_{T}. The best performance of the b-tagging algorithms is observed in the jet p_T region of $50\,\mathrm{GeV} < p_{\mathrm{T}_{jet}} < 330\,\mathrm{GeV}$ where the b-tagging purity of the selected events is between $P_{Tag} \approx 0.7$ ($P_{Tag} \approx 0.5$) and $P_{Tag} \approx 0.8$ ($P_{Tag} \approx 0.7$) for $\epsilon_{Tag} = 0.5$ ($\epsilon_{Tag} = 0.6$). Towards higher jet p_{T} the purity decreases to the order of $P_{Tag} = 0.1$ for $p_{\mathrm{T}_{jet}} > 930\,\mathrm{GeV}$. Differences are seen for cone4 and cone7 jets, due to the shift of cone7 jets towards larger jet p_{T} caused by the larger cone size used in the reconstruction. In the optimized b-tagging efficiency scenario, the b-tagging efficiency as well as the b-tagging purity depend on the jet p_{T} and are chosen such, that the statistical uncertainty of the differential b-jet cross section is minimized, i.e. the product of $\epsilon_{Tag} \times P_{Tag}$ is maximized in each jet p_{T} bin. Therefore, the b-tagging efficiency as well as the b-tagging purity decrease towards higher jet p_{T}, but stay above the level of the fixed b-tagging efficiency scenarios.
An unfolding algorithm is applied to the measured b-jet p_{T} spectrum based on an inversion of the transfer matrix in order to correct for bin-to-bin migrations due to the smearing of the jet p_{T} in the measurement process. Since the chosen bin width is larger by more than a factor of two compared to the jet p_{T} resolution, only a small number of bin-to-bin migrations of jets are observed. Therefore, the transfer matrix is dominantly diagonal and an additional regularization of the unfolding algorithm will not provide any additional improvement.
The systematic uncertainties are studied using all cone4 or cone7 jets in the event sample. Since the cross section for the leading b-jet scenario follows the same behavior as the cross section for the all jets scenario, the same systematic uncertainties are assumed for the leading b-jet analysis. The uncertainty on the jet energy scale (JES) is by far the dominant contribution for the systematic uncertainty of the measurement of the differential b-jet cross section. A p_{T} independent uncertainty of the efficiency as well as of the purity of the b-tagging is assumed. However, it has to be calibrated on data (especially in the high p_{T} region). The contribution of pile-up events to the systematic uncertainty of the measurement will have to be studied in future analyses. The expected total systematic uncertainty varies from about 25% in the lower jet p_{T} region up to about 50% in the high jet p_{T} region. The differences

of the systematic uncertainties for the cone4 and cone7 jet scenarios are found to be small.
In order to extrapolate this study to an integrated luminosity of $100\,\mathrm{pb}^{-1}$, the expected statistical uncertainty is scaled as a function of the integrated luminosity. It will become relevant at a b-jet p_{T} of about $p_{\mathrm{T}_{jet}} > 750\,\mathrm{GeV}$ assuming the optimized b-tagging efficiency scenario. This holds for the analyses taking all cone4 or cone7 jets in an event into account as well as for the one taking only the leading (b-) jet in the event into account. Once an integrated luminosity of $400\,\mathrm{pb}^{-1}$ is collected, the differential b-jet cross section will be measured up to $750\,\mathrm{GeV} < p_{\mathrm{T}_{jet}} < 1.1\,\mathrm{TeV}$ with a statistical uncertainty which is on the same level as the systematic uncertainty. In this p_{T} region, the scenario with a fixed b-tagging efficiency needs a larger integrated luminosity (e.g. by a factor of ≈ 2 for $\epsilon_{Tag} = 0.6$) in order to reduce the statistical uncertainty to the same level as the systematic uncertainty.
Details are listed in Tab. 8.14, Tab. 8.15 and in App. E for the different scenarios. The result for the differential b-jet cross section distribution is shown in Fig. 8.36(a) and Fig. 8.36(b) for cone7 jets assuming an integrated luminosity of $100\,\mathrm{pb}^{-1}$ and $400\,\mathrm{pb}^{-1}$, respectively.

Appendix A

Monte Carlo Cross Sections

In this chapter the Monte Carlo jet cross sections for b-jet signal and QCD-jet background are given. Two different cone sizes $\Delta R = 0.4$ (cone4) and $\Delta R = 0.7$ (cone7) are used. The cross sections are given for the leading jet analysis as well as for the scenario in which all jets inside each event are considered.

p_{T} range [GeV]		cone4 jet cross section σ_{jet} [pb] leading jet	all jets
$30 - 50$	b-jet	$(3.68 \pm 0.05) \cdot 10^6$	$(3.90 \pm 0.05) \cdot 10^6$
	QCD bkg.	$(106.9 \pm 0.4) \cdot 10^6$	$(142.1 \pm 0.5) \cdot 10^6$
$50 - 90$	b-jet	$(584 \pm 11) \cdot 10^3$	$(611 \pm 11) \cdot 10^3$
	QCD bkg.	$(13.78 \pm 0.06) \cdot 10^6$	$(19.35 \pm 0.07) \cdot 10^6$
$90 - 150$	b-jet	$(52.6 \pm 1.1) \cdot 10^3$	$(54.5 \pm 1.1) \cdot 10^3$
	QCD bkg.	$(1.094 \pm 0.007) \cdot 10^6$	$(1.637 \pm 0.007) \cdot 10^6$
$150 - 230$	b-jet	$(5.23 \pm 0.12) \cdot 10^3$	$(5.42 \pm 0.12) \cdot 10^3$
	QCD bkg.	$(103.4 \pm 0.6) \cdot 10^3$	$(164.4 \pm 0.7) \cdot 10^3$
$230 - 330$	b-jet	661 ± 19	685 ± 19
	QCD bkg.	$(12.33 \pm 0.08) \cdot 10^3$	$(20.77 \pm 0.11) \cdot 10^3$
$330 - 450$	b-jet	102 ± 3	105 ± 3
	QCD bkg.	$(1.844 \pm 0.014) \cdot 10^3$	$(3.257 \pm 0.018) \cdot 10^3$
$450 - 590$	b-jet	17.6 ± 0.7	18.0 ± 0.7
	QCD bkg.	324 ± 3	581 ± 4
$590 - 750$	b-jet	3.43 ± 0.13	3.53 ± 0.13
	QCD bkg.	64.0 ± 0.6	117.4 ± 0.8
$750 - 930$	b-jet	0.70 ± 0.03	0.72 ± 0.03
	QCD bkg.	13.90 ± 0.16	25.9 ± 0.2
$930 - 1130$	b-jet	0.173 ± 0.009	0.177 ± 0.009
	QCD bkg.	3.17 ± 0.05	6.00 ± 0.07
> 1130	b-jet	0.046 ± 0.002	0.048 ± 0.002
	QCD bkg.	0.977 ± 0.012	1.874 ± 0.014

Table A.1: Cross section of cone4 b-jet signal and cone4 QCD-jet background as a function of the jet p_{T}.

p_{T} range [GeV]		cone7 jet cross section σ_{jet} [pb] leading jet	all jets
$30-50$	b-jet	$(6.45 \pm 0.07) \cdot 10^6$	$(6.87 \pm 0.08) \cdot 10^6$
	QCD bkg.	$(226.5 \pm 0.7) \cdot 10^6$	$(326.6 \pm 0.9) \cdot 10^6$
$50-90$	b-jet	$(947 \pm 16) \cdot 10^3$	$(987 \pm 17) \cdot 10^3$
	QCD bkg.	$(27.72 \pm 0.12) \cdot 10^6$	$(38.86 \pm 0.14) \cdot 10^6$
$90-150$	b-jet	$(73.8 \pm 1.4) \cdot 10^3$	$(76.5 \pm 1.4) \cdot 10^3$
	QCD bkg.	$(1.655 \pm 0.008) \cdot 10^6$	$(2.502 \pm 0.010) \cdot 10^6$
$150-230$	b-jet	$(7.02 \pm 0.13) \cdot 10^3$	$(7.27 \pm 0.13) \cdot 10^3$
	QCD bkg.	$(142.7 \pm 0.7) \cdot 10^3$	$(228.8 \pm 0.9) \cdot 10^3$
$230-330$	b-jet	862 ± 21	894 ± 21
	QCD bkg.	$(16.15 \pm 0.09) \cdot 10^3$	$(27.41 \pm 0.12) \cdot 10^3$
$330-450$	b-jet	131 ± 3	135 ± 3
	QCD bkg.	$(2.335 \pm 0.016) \cdot 10^3$	$(4.13 \pm 0.02) \cdot 10^3$
$450-590$	b-jet	22.5 ± 0.7	23.1 ± 0.7
	QCD bkg.	404 ± 3	729 ± 4
$590-750$	b-jet	4.12 ± 0.12	4.27 ± 0.12
	QCD bkg.	77.5 ± 0.6	143.8 ± 0.8
$750-930$	b-jet	0.82 ± 0.02	0.84 ± 0.02
	QCD bkg.	16.64 ± 0.17	30.9 ± 0.2
$930-1130$	b-jet	0.242 ± 0.017	0.247 ± 0.017
	QCD bkg.	3.74 ± 0.05	7.10 ± 0.07
>1130	b-jet	0.056 ± 0.003	0.058 ± 0.003
	QCD bkg.	1.133 ± 0.014	2.186 ± 0.017

Table A.2: Cross section of cone7 b-jet signal and cone7 QCD-jet background as a function of the jet p_{T}.

Appendix B

Jet Trigger

In this chapter the different trigger efficiencies (Fig. B.1 (a)-(h)) and trigger rates (Fig. B.2 (a)-(h)) are shown. The effective trigger efficiencies for the b-jet signal and QCD background using cone7 and cone4 jets are listed in Tab. B.1 and Tab. B.2.

p_{T} range [GeV]		jet cone7 trigger efficiency	
		b-jets	QCD jets
$30-50$	trigger ϵ_{Tr}	$(31.3 \pm 0.3) \cdot 10^{-6}$	$(26.77 \pm 0.06) \cdot 10^{-6}$
	trigger rate [Hz]	0.213 ± 0.004	8.78 ± 0.04
$50-90$	trigger ϵ_{Tr}	$(0.109 \pm 0.003) \cdot 10^{-3}$	$(0.8479 \pm 0.0007) \cdot 10^{-3}$
	trigger rate [Hz]	0.108 ± 0.004	3.29 ± 0.03
$90-150$	trigger ϵ_{Tr}	$(1.23 \pm 0.04) \cdot 10^{-3}$	$(0.980 \pm 0.008) \cdot 10^{-3}$
	trigger rate [Hz]	0.094 ± 0.004	2.46 ± 0.02
$150-230$	trigger ϵ_{Tr}	$(12.0 \pm 0.4) \cdot 10^{-3}$	$(10.2 \pm 0.3) \cdot 10^{-3}$
	trigger rate [Hz]	0.087 ± 0.003	2.32 ± 0.06
$230-330$	trigger ϵ_{Tr}	0.093 ± 0.003	0.0738 ± 0.0009
	trigger rate [Hz]	0.084 ± 0.004	2.01 ± 0.03
$330-450$	trigger ϵ_{Tr}	0.780 ± 0.014	0.665 ± 0.002
	trigger rate [Hz]	0.108 ± 0.004	2.74 ± 0.02
$450-590$	trigger ϵ_{Tr}	0.9990 ± 0.0013	0.9534 ± 0.0003
	trigger rate [Hz]	0.0233 ± 0.0007	0.685 ± 0.005
$590-750$	trigger ϵ_{Tr}	0.9998 ± 0.0017	0.9633 ± 0.00008
	trigger rate [Hz]	$(4.21 \pm 0.17) \cdot 10^{-3}$	$(136.4 \pm 1.0) \cdot 10^{-3}$
$750-930$	trigger ϵ_{Tr}	1 ± 0.0014	0.96771 ± 0.00015
	trigger rate [Hz]	$(0.86 \pm 0.03) \cdot 10^{-3}$	$(29.7 \pm 0.3) \cdot 10^{-3}$
$930-1130$	trigger ϵ_{Tr}	1 ± 0.005	0.9661 ± 0.0002
	trigger rate [Hz]	$(0.240 \pm 0.015) \cdot 10^{-3}$	$(6.92 \pm 0.10) \cdot 10^{-3}$
>1130	trigger ϵ_{Tr}	1 ± 0.005	0.96751 ± 0.00012
	trigger rate [Hz]	$(0.058 \pm 0.004) \cdot 10^{-3}$	$(2.13 \pm 0.02) \cdot 10^{-3}$

Table B.1: Trigger efficiency for all cone4 b- and QCD jets as a function of the truth jet p_{T}.

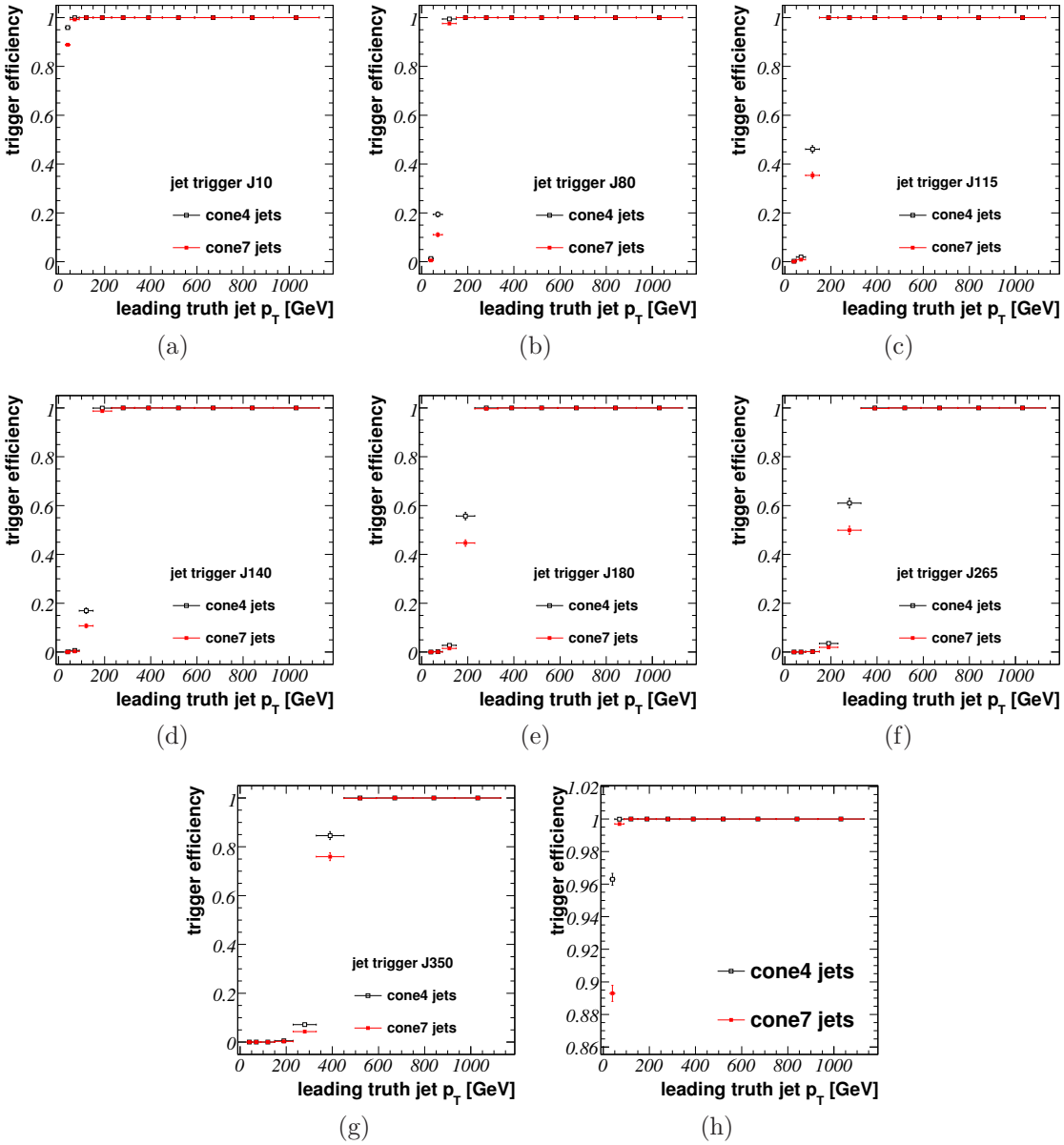

Figure B.1: Leading b-jet trigger efficiencies of different single jet triggers, without taking prescale factors into account.

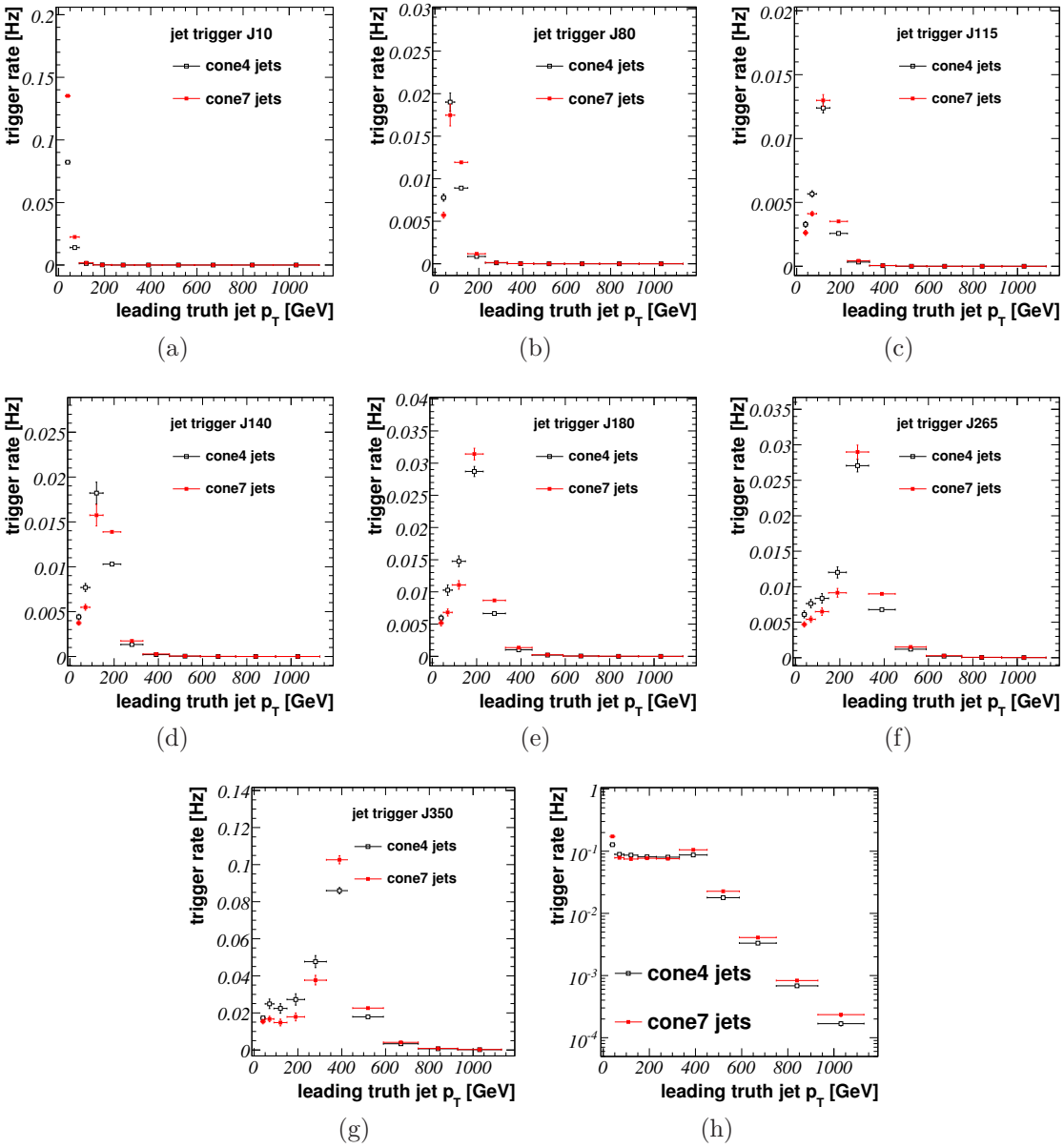

Figure B.2: Leading b-jet trigger rates of different single jet triggers, without correlations of the triggers into account.

p_{T} range [GeV]		cone4 jet trigger efficiency	
		b-jets	QCD jets
$30-50$	trigger ϵ_{Tr}	$(45.8 \pm 0.8) \cdot 10^{-6}$	$(40.34 \pm 0.16) \cdot 10^{-6}$
	trigger rate [Hz]	0.174 ± 0.004	5.75 ± 0.03
$50-90$	trigger ϵ_{Tr}	$(0.204 \pm 0.006) \cdot 10^{-3}$	$(0.161 \pm 0.002) \cdot 10^{-3}$
	trigger rate [Hz]	0.126 ± 0.005	3.13 ± 0.05
$90-150$	trigger ϵ_{Tr}	$(1.91 \pm 0.07) \cdot 10^{-3}$	$(1.55 \pm 0.02) \cdot 10^{-3}$
	trigger rate [Hz]	0.107 ± 0.005	2.54 ± 0.04
$150-230$	trigger ϵ_{Tr}	$(17.3 \pm 0.6) \cdot 10^{-3}$	$(13.9 \pm 0.04) \cdot 10^{-3}$
	trigger rate [Hz]	0.093 ± 0.004	2.28 ± 0.07
$230-330$	trigger ϵ_{Tr}	0.126 ± 0.005	0.0976 ± 0.0014
	trigger rate [Hz]	0.087 ± 0.005	2.02 ± 0.03
$330-450$	trigger ϵ_{Tr}	0.859 ± 0.015	0.751 ± 0.003
	trigger rate [Hz]	0.090 ± 0.004	2.43 ± 0.02
$450-590$	trigger ϵ_{Tr}	0.9999 ± 0.0018	0.948 ± 0.0002
	trigger rate [Hz]	0.0183 ± 0.0008	0.544 ± 0.005
$590-750$	trigger ϵ_{Tr}	1 ± 0.003	0.95223 ± 0.00013
	trigger rate [Hz]	$(3.43 \pm 0.17) \cdot 10^{-3}$	$(111.1 \pm 1.0) \cdot 10^{-3}$
$750-930$	trigger ϵ_{Tr}	1 ± 0.0017	0.96066 ± 0.00018
	trigger rate [Hz]	$(0.71 \pm 0.03) \cdot 10^{-3}$	$(24.7 \pm 0.3) \cdot 10^{-3}$
$930-1130$	trigger ϵ_{Tr}	1 ± 0.006	0.9578 ± 0.0003
	trigger rate [Hz]	$(0.171 \pm 0.013) \cdot 10^{-3}$	$(5.83 \pm 0.10) \cdot 10^{-3}$
>1130	trigger ϵ_{Tr}	1 ± 0.005	0.95838 ± 0.00015
	trigger rate [Hz]	$(0.047 \pm 0.003) \cdot 10^{-3}$	$(1.81 \pm 0.02) \cdot 10^{-3}$

Table B.2: Trigger efficiency for cone4 b-jets as a function of the truth jet p_{T}.

Appendix C

Statistical Error Estimation for Efficiencies

The efficiency ϵ of a certain condition is defined as

$$\epsilon = \frac{N_+}{N}\,, \tag{C.1}$$

where N_+ is the number of events that fulfills the condition (accepted events). For weighted events with event weights ω_i the efficiency is calculated by

$$\epsilon = \frac{\sum_+ \omega_j}{\sum \omega_i} = \frac{\sum_+ \omega_j}{\sum_+ \omega_j + \sum_- \omega_j}\,, \tag{C.2}$$

where $\sum_+$ $\left(\sum_-\right)$ represents the sum over weights of accepted (rejected) events. Assuming the total number of events N to be fixed, the number of accepted events is distributed according to the binomial distribution. This is fully equivalent to the ansatz, that accepted as well as rejected events are distributed according to the Poisson distribution ([56]). This leads to an estimation of the efficiency error using weighted events:

$$\Delta\epsilon = \frac{\sqrt{\sum_+ \omega_i^2 \left(\sum_- \omega_j\right)^2 + \sum_- \omega_i^2 \left(\sum_+ \omega_j\right)^2}}{\left(\sum \omega_i\right)^2}\,. \tag{C.3}$$

In case of a very low or a very high efficiency, the error given by (C.3) will become very small until it reaches $\Delta\epsilon = 0$ for $\sum_+ \omega_i = \sum \omega_i$ ($\epsilon = 1$) or $\sum_- \omega_i = \sum \omega_i$ ($\epsilon = 0$). This means, that the efficiency is exactly known independently of the number of events, which is available to estimate the efficiency.
In order to correctly estimate the statistical uncertainty of the efficiency in these extreme regions, the error is evaluated as described in [57]. The error estimation is based on a Bayesian approach assigning a prior to the efficiency probability density function (pdf). This ensures, for the efficiency: $0 \leq \epsilon \leq 1$. The resulting efficiency pdf $P(\epsilon; k, n)$ for a truth efficiency ϵ in case of k positive events out of n events in total is

$$P(\epsilon; k, n) = \frac{(n+1)!}{k!(n-k)!}\epsilon^k(1-\epsilon)^{n-k}\,. \tag{C.4}$$

The error of the "measured" efficiency is estimated by integrating over the efficiency pdf until 68.3% of the pdf's area is covered, the area being centered around the average value of the pdf. This results in asymmetric errors for the efficiency, but reasonable uncertainties, depending on the event statistics, in the extreme regions of $\epsilon \approx 1$ and $\epsilon \approx 0$.
To apply this method, which is implemented in the software framework ROOT [58] as the function TGraphAsymmErrors::BayesDivide(), in order to estimate errors of weighted events, the effective number of events n_{eff} with the same statistical significance as n unweighted events [50] is used. The distribution of unweighted events follows a Poissonian distribution with a mean value λ and a variance σ. To estimate the effective number of weighted events, it is assumed, that the distribution of weighted events follows a scaled Poissonian distribution with mean value $\tilde{\lambda}$ and variance $\sqrt{\tilde{\lambda}}$ such, that the ratio of the variance to the mean value is the same for both distributions:

$$\frac{\sqrt{\tilde{\lambda}}}{\tilde{\lambda}} = \frac{\sigma}{\lambda}\,. \tag{C.5}$$

Therefore, the effective number n_{eff} of events is given by

$$n_{eff} = \tilde{\lambda} = \frac{\left(\sum \omega\right)^2}{\sum \omega_i^2}\,. \tag{C.6}$$

The effective number of events and the efficiencies are used to estimate the error on the efficiencies using the Bayesian ansatz. Aside from the regions of extreme efficiency values ($\epsilon \approx 1$, $\epsilon \approx 0$), this gives similar results as (C.3), but provides non-zero uncertainties for very large or very small efficiencies.

Appendix D

Inputs and Results of the Unfolding Method

The finite resolution of the b-jet p_{T} reconstruction causes bin-to-bin migrations in the measurement of the differential b-jet cross section. The unfolding algorithm will correct for the detector effects. The residuals of the jet p_{T} reconstruction in the different jet p_{T} bins are shown in Fig. D.1. The results for the differential b-jet cross section as a function of the jet p_{T} using cone4 jets for the cases of taking all jets in the event sample into account (Fig. D.2) as well as taking only the leading (b-)jets into account (Fig. D.3) are presented.

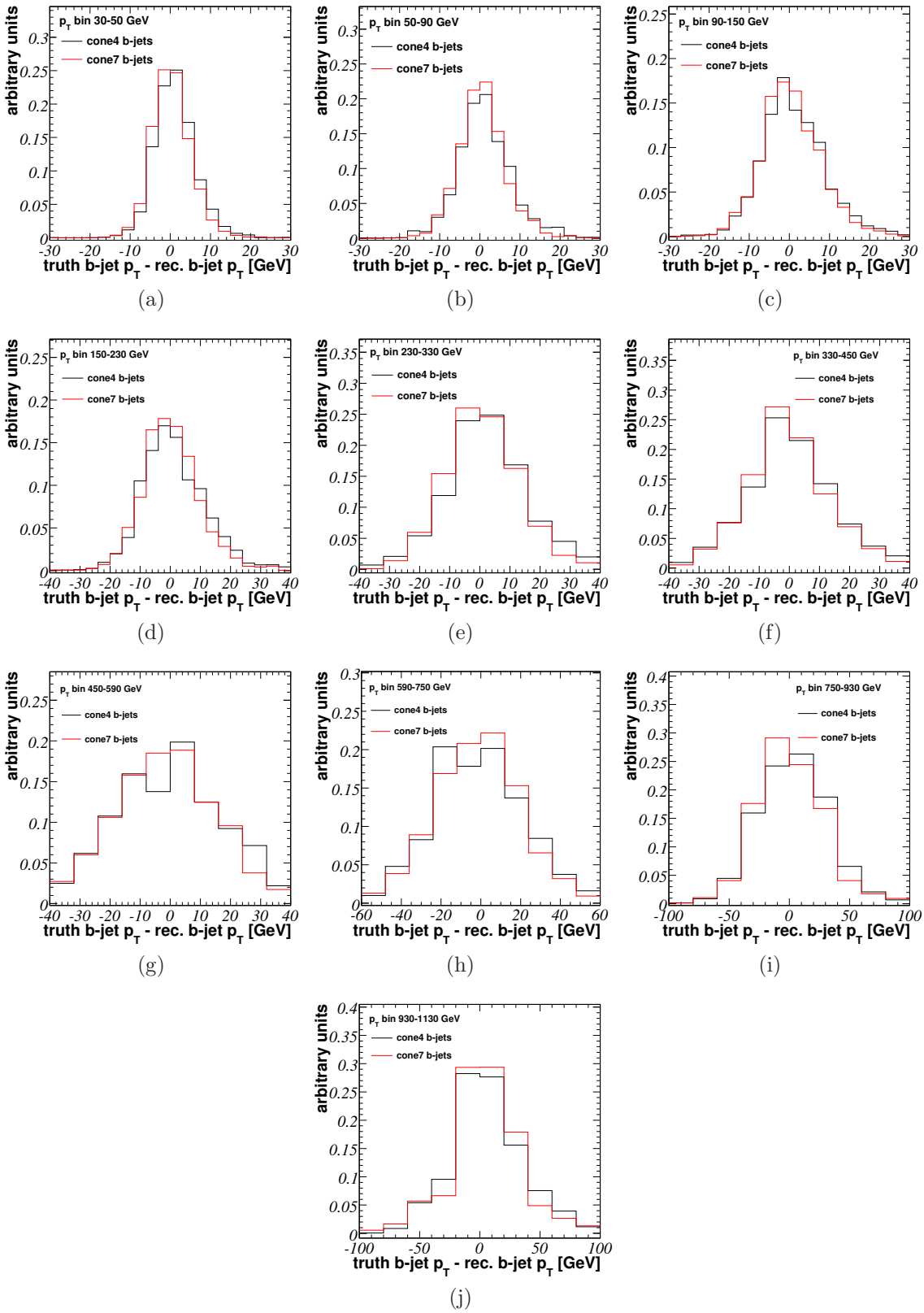

Figure D.1: b-jet p_{T} residuals in the different jet p_{T} bins for cone4 and cone7 b-jets.

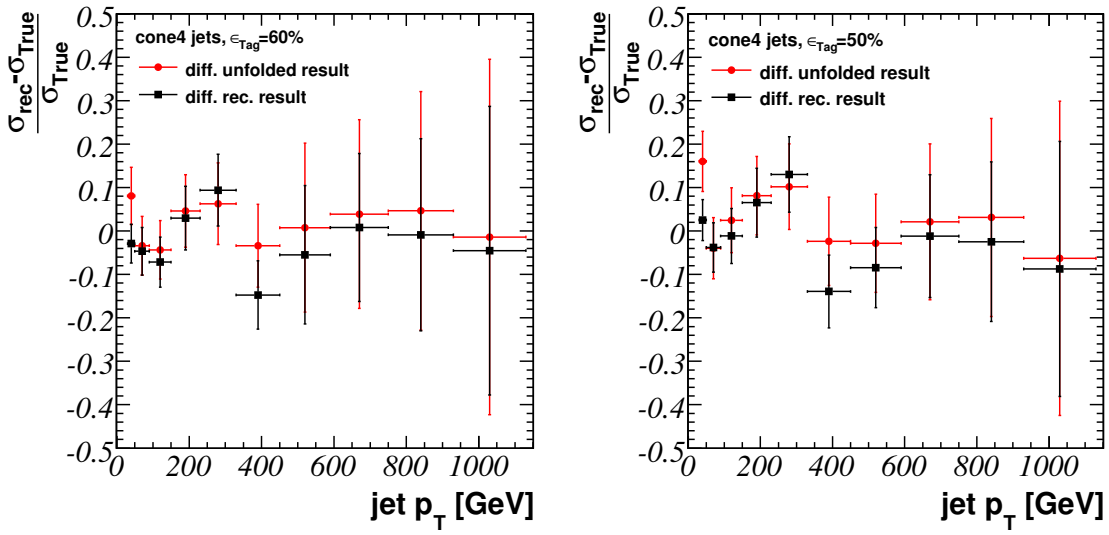

(a)

(b)

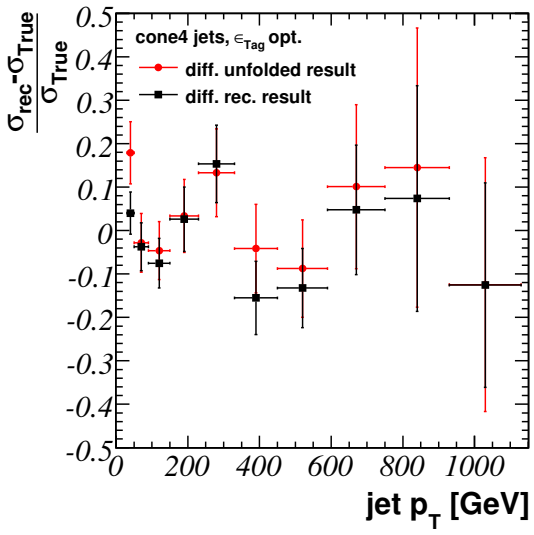

(c)

Figure D.2: Differences of the reconstructed and truth cone4 b-jet cross section as a function of the jet p_{T} normalized to the truth b-jet cross section. The b-tagging efficiency is chosen at (a) 60%, (b) 50% and (c) optimized w.r.t. the resulting statistical uncertainty, using the second event sample for the reconstructed and the selected event numbers.

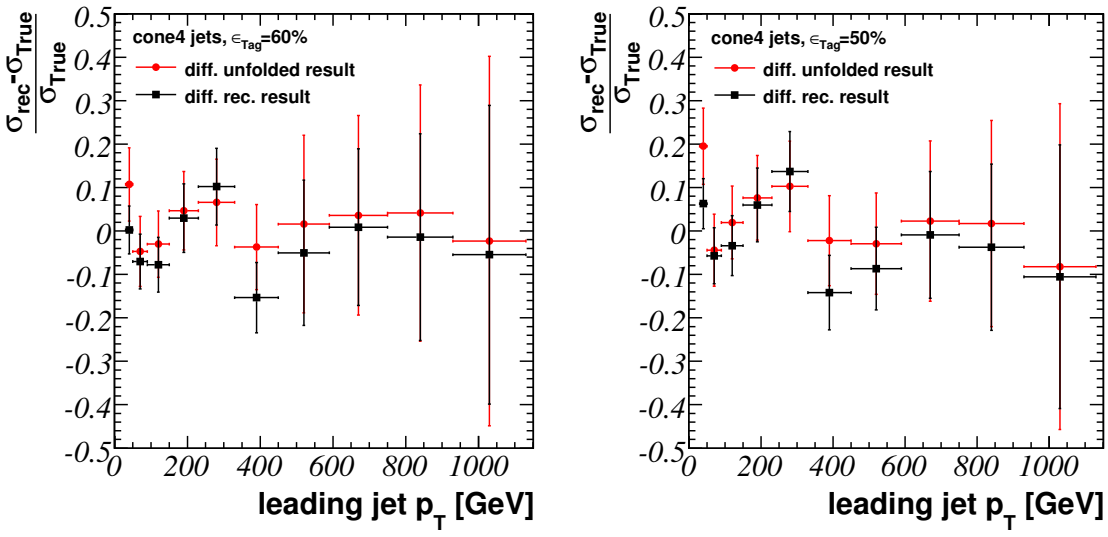

(a)

(b)

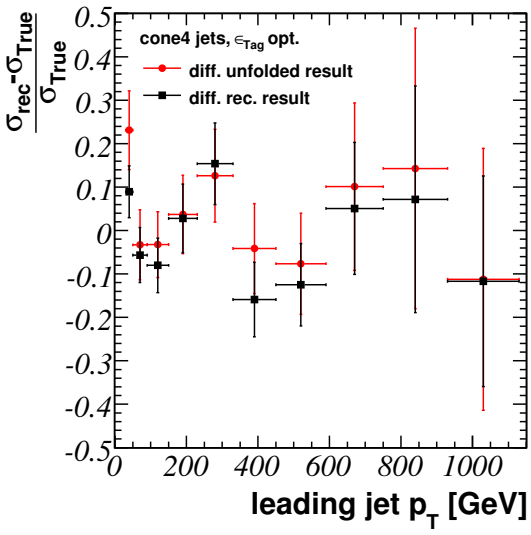

(c)

Figure D.3: Differences of the reconstructed and truth cone4 leading b-jet cross section as a function of the jet p_{T} normalized to the leading truth b-jet cross section. The b-tagging efficiency is chosen at (a) 60%, (b) 50% and (c) optimized w.r.t. the resulting statistical uncertainty, using the second event sample for the reconstructed and the selected event numbers.

Appendix E

Uncertainties of the Measurement for fixed b-Tagging Efficiencies

The expected statistical uncertainty of the differential b-jet cross section measurement depends on the chosen b-tagging scenario. In this appendix the scaled statistical uncertainties in dependence of the integrated luminosity for a fixed b-tagging efficiency of $\epsilon_{Tag} = 0.5$ are shown in Fig. E.1. In addition, the expected statistical uncertainties for the available MC event statistics and two different integrated luminosities on the differential b-jet cross section measurement using a fixed b-tagging efficiency of $\epsilon_{Tag} = 0.5$ taking all jets of the event sample into account (Tab. E.1) as well as for the leading jet analysis (Tab. E.2) are provided. In Tab. E.2 the uncertainties on the differential b-jet cross section measurement using a b-tagging scenario with $\epsilon_{Tag} = 0.6$ taking all jets of the event sample into account are listed. The uncertainties for the leading jet analysis are provided in Tab. E.3.

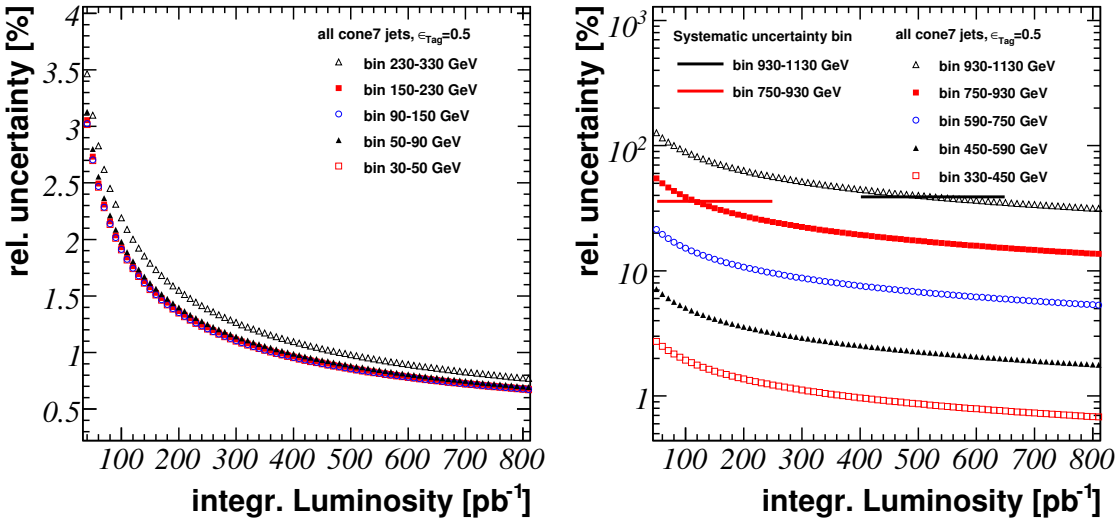

Figure E.1: Statistical uncertainty of the differential b-jet cross section as a function of the integrated luminosity for cone7 jets. The b-tagging efficiency is chosen at $\epsilon_{Tag} = 0.5$ in (a) and (b). For comparison, the relevant systematic uncertainties for the two highest jet p_{T} bins are marked as lines in plot (b).

p_{T} range [GeV]		systematic uncertainty	ϵ_{Tag}=0.5., statistical uncertainty at MC stat.	$\mathcal{L} = 100\,\mathrm{pb}^{-1}$	$\mathcal{L} = 400\,\mathrm{pb}^{-1}$
$30 - 50$	Cone4	$^{+0.22}_{-0.21}$	0.06	0.02	0.01
	Cone7	$^{+0.24}_{-0.21}$	0.05	0.02	0.01
$50 - 90$	Cone4	$^{+0.24}_{-0.23}$	0.07	0.02	0.01
	Cone7	$^{+0.23}_{-0.21}$	0.07	0.02	0.01
$90 - 150$	Cone4	$^{+0.31}_{-0.23}$	0.07	0.02	0.01
	Cone7	$^{+0.27}_{-0.22}$	0.07	0.02	0.01
$150 - 230$	Cone4	$^{+0.28}_{-0.23}$	0.08	0.02	0.01
	Cone7	$^{+0.27}_{-0.23}$	0.07	0.02	0.01
$230 - 330$	Cone4	$^{+0.23}_{-0.25}$	0.09	0.02	0.01
	Cone7	$^{+0.28}_{-0.27}$	0.08	0.02	0.01
$330 - 450$	Cone4	$^{+0.33}_{-0.24}$	0.10	0.02	0.01
	Cone7	$^{+0.30}_{-0.25}$	0.08	0.02	0.01
$450 - 590$	Cone4	$^{+0.39}_{-0.25}$	0.12	0.06	0.03
	Cone7	$^{+0.35}_{-0.27}$	0.11	0.05	0.03
$590 - 750$	Cone4	$^{+0.30}_{-0.35}$	0.18	0.19	0.10
	Cone7	$^{+0.35}_{-0.35}$	0.13	0.15	0.08
$750 - 930$	Cone4	$^{+0.39}_{-0.29}$	0.22	0.44	0.22
	Cone7	$^{+0.36}_{-0.26}$	0.18	0.39	0.19
$930 - 1130$	Cone4	$^{+0.43}_{-0.37}$	0.39	-	0.60
	Cone7	$^{+0.39}_{-0.31}$	0.28	0.89	0.45
> 1130	Cone4	$^{+0.48}_{-0.43}$	0.32	-	-
	Cone7	$^{+0.52}_{-0.49}$	0.26	-	0.83

Table E.1: Summary of different uncertainties on the differential b-jet cross section measurement using a fixed b-tagging efficiency of $\epsilon_{Tag} = 0.5$ taking all jets into account. An entry "-" in a statistics column denotes insufficient statistics in the number of jets.

p_{T} range [GeV]		systematic uncertainty	ϵ_{Tag}=0.5, statistical uncertainty at MC stat.	$\mathcal{L} = 100\,\mathrm{pb}^{-1}$	$\mathcal{L} = 400\,\mathrm{pb}^{-1}$
$30 - 50$	Cone4	$^{+0.22}_{-0.21}$	0.07	0.03	0.01
	Cone7	$^{+0.24}_{-0.21}$	0.06	0.02	0.01
$50 - 90$	Cone4	$^{+0.24}_{-0.23}$	0.09	0.02	0.01
	Cone7	$^{+0.23}_{-0.21}$	0.08	0.03	0.01
$90 - 150$	Cone4	$^{+0.31}_{-0.23}$	0.08	0.02	0.01
	Cone7	$^{+0.27}_{-0.22}$	0.08	0.02	0.01
$150 - 230$	Cone4	$^{+0.28}_{-0.23}$	0.09	0.02	0.01
	Cone7	$^{+0.27}_{-0.23}$	0.07	0.02	0.01
$230 - 330$	Cone4	$^{+0.23}_{-0.25}$	0.09	0.02	0.01
	Cone7	$^{+0.28}_{-0.27}$	0.09	0.02	0.01
$330 - 450$	Cone4	$^{+0.33}_{-0.24}$	0.11	0.02	0.01
	Cone7	$^{+0.30}_{-0.25}$	0.08	0.02	0.01
$450 - 590$	Cone4	$^{+0.39}_{-0.25}$	0.12	0.06	0.03
	Cone7	$^{+0.35}_{-0.27}$	0.12	0.05	0.03
$590 - 750$	Cone4	$^{+0.30}_{-0.35}$	0.18	0.19	0.10
	Cone7	$^{+0.35}_{-0.35}$	0.13	0.15	0.08
$750 - 930$	Cone4	$^{+0.39}_{-0.29}$	0.23	0.46	0.23
	Cone7	$^{+0.36}_{-0.26}$	0.19	0.41	0.21
$930 - 1130$	Cone4	$^{+0.43}_{-0.37}$	0.41	-	0.62
	Cone7	$^{+0.39}_{-0.31}$	0.29	0.91	0.45
> 1130	Cone4	$^{+0.48}_{-0.43}$	0.32	-	-
	Cone7	$^{+0.52}_{-0.49}$	0.27	-	0.85

Table E.2: Summary of different uncertainties on the differential b-jet cross section measurement using a fixed b-tagging efficiency of $\epsilon_{Tag} = 0.5$ taking only the leading jets into account. An entry "-" in a statistics column denotes insufficient statistics in the number of jets.

p_{T} range [GeV]		systematic uncertainty	ϵ_{Tag}=0.6, statistical uncertainty at MC stat.	$\mathcal{L} = 100\,\mathrm{pb}^{-1}$	$\mathcal{L} = 400\,\mathrm{pb}^{-1}$
$30 - 50$	Cone4	$^{+0.22}_{-0.21}$	0.06	0.02	0.01
	Cone7	$^{+0.24}_{-0.21}$	0.06	0.02	0.01
$50 - 90$	Cone4	$^{+0.24}_{-0.23}$	0.07	0.02	0.01
	Cone7	$^{+0.23}_{-0.21}$	0.07	0.02	0.01
$90 - 150$	Cone4	$^{+0.31}_{-0.23}$	0.07	0.02	0.01
	Cone7	$^{+0.27}_{-0.22}$	0.07	0.02	0.01
$150 - 230$	Cone4	$^{+0.28}_{-0.23}$	0.08	0.02	0.01
	Cone7	$^{+0.27}_{-0.23}$	0.07	0.02	0.01
$230 - 330$	Cone4	$^{+0.23}_{-0.25}$	0.09	0.02	0.01
	Cone7	$^{+0.28}_{-0.27}$	0.09	0.02	0.01
$330 - 450$	Cone4	$^{+0.33}_{-0.24}$	0.10	0.03	0.01
	Cone7	$^{+0.30}_{-0.25}$	0.08	0.02	0.01
$450 - 590$	Cone4	$^{+0.39}_{-0.25}$	0.19	0.07	0.04
	Cone7	$^{+0.35}_{-0.27}$	0.12	0.06	0.03
$590 - 750$	Cone4	$^{+0.30}_{-0.35}$	0.21	0.23	0.11
	Cone7	$^{+0.35}_{-0.35}$	0.14	0.17	0.09
$750 - 930$	Cone4	$^{+0.39}_{-0.29}$	0.26	0.52	0.26
	Cone7	$^{+0.36}_{-0.26}$	0.20	0.44	0.22
$930 - 1130$	Cone4	$^{+0.43}_{-0.37}$	0.42	-	0.66
	Cone7	$^{+0.39}_{-0.31}$	0.32	-	0.52
> 1130	Cone4	$^{+0.48}_{-0.43}$	0.33	-	-
	Cone7	$^{+0.52}_{-0.49}$	0.29	-	0.91

Table E.3: Summary of different uncertainties on the differential b-jet cross section measurement using a fixed b-tagging efficiency of $\epsilon_{Tag} = 0.6$ taking all jets into account. An entry "-" in a statistics column denotes insufficient statistics in the number of jets.

p_{T} range [GeV]		systematic uncertainty	ϵ_{Tag}=0.6, statistical uncertainty at MC stat.	$\mathcal{L} = 100\,\mathrm{pb}^{-1}$	$\mathcal{L} = 400\,\mathrm{pb}^{-1}$
$30 - 50$	Cone4	$^{+0.22}_{-0.21}$	0.08	0.02	0.01
	Cone7	$^{+0.24}_{-0.21}$	0.07	0.03	0.01
$50 - 90$	Cone4	$^{+0.24}_{-0.23}$	0.08	0.02	0.01
	Cone7	$^{+0.23}_{-0.21}$	0.08	0.03	0.01
$90 - 150$	Cone4	$^{+0.31}_{-0.23}$	0.08	0.02	0.01
	Cone7	$^{+0.27}_{-0.22}$	0.07	0.02	0.01
$150 - 230$	Cone4	$^{+0.28}_{-0.23}$	0.09	0.02	0.01
	Cone7	$^{+0.27}_{-0.23}$	0.07	0.03	0.01
$230 - 330$	Cone4	$^{+0.23}_{-0.25}$	0.09	0.02	0.01
	Cone7	$^{+0.28}_{-0.27}$	0.09	0.02	0.01
$330 - 450$	Cone4	$^{+0.33}_{-0.24}$	0.10	0.03	0.01
	Cone7	$^{+0.30}_{-0.25}$	0.08	0.02	0.01
$450 - 590$	Cone4	$^{+0.39}_{-0.25}$	0.20	0.08	0.04
	Cone7	$^{+0.35}_{-0.27}$	0.13	0.06	0.03
$590 - 750$	Cone4	$^{+0.30}_{-0.35}$	0.22	0.24	0.12
	Cone7	$^{+0.35}_{-0.35}$	0.15	0.18	0.09
$750 - 930$	Cone4	$^{+0.39}_{-0.29}$	0.28	0.56	0.28
	Cone7	$^{+0.36}_{-0.26}$	0.22	0.47	0.24
$930 - 1130$	Cone4	$^{+0.43}_{-0.37}$	0.43	-	0.68
	Cone7	$^{+0.39}_{-0.31}$	0.33	-	0.53
> 1130	Cone4	$^{+0.48}_{-0.43}$	0.35	-	-
	Cone7	$^{+0.52}_{-0.49}$	0.30	-	0.94

Table E.4: Summary of different uncertainties on the differential b-jet cross section measurement using a fixed b-tagging efficiency of $\epsilon_{Tag} = 0.6$ taking only the leading jets into account. An entry "-" in a statistics column denotes insufficient statistics in the number of jets.

Bibliography

[1] ATLAS Collaboration. *The ATLAS Experiment at the CERN Large Hadron Collider*. JINST 3 (2008) S08003, 2008

[2] CMS Collaboration. *The CMS experiment at the CERN LHC*. JINST 3 (2008) S08004, 2008

[3] ATLAS Collaboration. *ATLAS Level-1 Trigger Technical Design Report*. [ATLAS TDR-12],[CERN/LHCC//98-14], 1998

[4] ATLAS Collaboration. *Expected performance of the ATLAS experiment : detector, trigger and physics*. arXiv:0901.0512, CERN-OPEN-2008-020, 2008

[5] Sheldon L. Glashow . *Partial-symmetries of weak interactions*. Nuclear Physics 22:579-588., 1961

[6] S. Weinberg. *A Model of Leptons*. Physical Review Letters 19:1264-1266., 1967

[7] A. Salam, N. Svartholm ed. *Elementary Particle Physics: Relativistic Groups and Analyticity*. Eight Nobel Symposium. Stockholm: Almquvist and Wiksell. pp. 367, 1968

[8] E.J. Eichten at al. *Charmonium: Comparison with experiment*. Phys. Rev. D21 (1980) 203, 1980

[9] W. Buchmüller, G. Grunberg, S.-H.H. Tye. *Regge Slope and the Λ Parameter in Quantum Chromodynamics: An Empirical Approach via Quarkonia*. Phys. Rev. Lett. 45, 103, 1980

[10] N. Cabibbo. *Unitary Symmetry and Leptonic Decays*. Phys.Rev.Lett.,10(12):531-533, Jun. 1963

[11] S. L. Glashow, J. Iliopoulos, L. Maiani. *Weak Interactions with Lepton-Hadron Symmetry*. Phys. Rev. D2, 1970

[12] M. Kobayashi and T. Maskawa. *CP-Violation in the Renormalizable Theorie of Weak Interaction*. Progr. of Theor. Physics, 49(2):652-657, Sep. 1973

[13] P.W. Higgs. *Broken Symmetries and the Masses of Gauge Bosons*. Physical Review Letters 13: 508-509, 1964

[14] F. Englert and R. Brout. *Broken Symmetry and the Mass of Gauge Vector Mesons.* Physical Review Letters 13: 321-323, 1964

[15] G. S. Guralnik, C. R. Hagen, and T. W. B. Kibble. *Global Conservation Laws and Massless Particles.* Physical Review Letters 13: 585-587, 1964

[16] R.K. Ellis, W.J. Stirling, B.R. Webber . *QCD and Collider Physics.* Cambridge University Press, 1996

[17] M. Cacciari, M. Greco, P. Nason. *The p_T Spectrum in Heavy-Flavour Hadroproduction.* arXiv:hep-ph/9803400, 20 Mar 1998

[18] C. Amsler et al. *(Particle Data Group).* Physics Letters B667,1, (2008) and 2009 partial update for the 2010 edition

[19] W.J. Stirling. *, .* private communication

[20] C. Albajar et al. *[UA1].* Phys.Lett.B186,237(1987);Phys.Lett.B256,121(1991), 1991

[21] M.L. Mangano. *The saga of bottom production in $p\bar{p}$ collisions.* arXiv:hep-ph/0411020, 1 Nov 2004

[22] F. Abe et al., CDF. *Measurement of the B-meson and b-quark cross sections at $\sqrt{s}$ =1.8 TeV using the exclusive decay $B^{\pm} \to J/\Psi K^{\pm}$.* Phys. Rev. Lett. 68,3403, 1992

[23] M. D'Onofrio. *BEAUTY PRODUCTION CROSS SECTION MEASUREMENTS AT $E_{CM} = 1.96$ TeV.* arXiv:hep-ex/0505036, 13 May 2005

[24] V. Andreev, D. Cline, S. Otwinowski. *Measurement of open beauty production at LHC with CMS.* CMS NOTE-2006/120, 2006

[25] E. Lytken, M. zur Nedden. *Quarkonia and open beauty production in ATLAS.* ATL-PHYS-PROC-2008-048, Oct. 2008

[26] T. Sjostrand, S. Menna, and P. Skands. *PYTHIA 6.4 Physics and Manual.* JHEP 05(2006)026 arXiv:hep-ph/0603175, 2006

[27] G. Duckeck (ed.) et al.,(ATLAS Collaboration). *ATLAS Computing Technical Design Report.* ATLAS TDR-017, CERN-LHCC-2005-022, Jun. 2005

[28] J. Pumplin, D.R. Stump, J. Huston, H.L. Lai, P. Nadolsky, W.K. Tung. *CTEQ6L1 - LO with LO alpha s.* hep-ph/0201195

[29] J. Allison. *Geant4 - A Simulation Toolkit.* Nuclear Physics News, Volume 17 Issue 2, April 2007

[30] J.P. Dishaw. *, .* FERMILAB-THESIS-1979-08, 1979

[31] I. Abt et al. . Nucl. Instrum. Meth. A386, 348-396, 1997

[32] T.G. Cornelissen et al. *Concepts, design and implementations of the ATLAS new tracking.* ATLAS Note ATL-SOFT-PUB-2007-007, 2007

[33] R. Frühwirth et al. *Application of the Kalman Filtering to Track and Vertex Fitting.* Nucl. Inst. Meth., A 262, 1987

[34] R. Duda and P. Hart. *Use of the Hough Transformation to Detect Lines and Curves in Pictures.* Comm. ACM, Vol. 15, 1972

[35] F. Akesson, T. Atkinson, M.J. Costa, M. Elsing, S. Fleischmann, A. Gaponenko, W. Liebig, E. Moyse, A. Salzburger, M. Siebel. *ATLAS Tracking Event Data Model.* ATL-COM-SOFT-2006-005, 2006

[36] W. Waltenberger, R. Frühwirth, P. Vanlaer. *Adaptive vertex fitting.* J. Phys. G: Nucl. Part. Phys. 34 N343, 2007

[37] R. Frühwirth, W. Waltenberg. *Adaptive Multi-vertex fitting.* Proc. CHEP 2004, Interlaken, 2005

[38] E. Bouhova-Thaker et. al. *Vertex Reconstruction in the ATLAS Experiment at the LHC.* ATL-INDET-PUB-2009-001, 2009

[39] D.A. Edwards, M.J. Syphers. *An Introduction to the Physics of High Energy Accelerators.* Wiley, New York, 1993

[40] H. Burckhardt, P. Grafstrom. *Absolute Luminosity from Machine Parameters.* LHC Project Report 1019, May 2007

[41] W. Herr, B. Muratori. *Concept of Luminosity.* Proceedings CAS2003, CERN-2006-002, 2006

[42] R. Jones, H. Schmickler. *Introduction to beam instrumentation and diagnostics.* Proceedings CAS2003, CERN-2006-002, 2006

[43] S. Ask, D. Malon, T. Pauly and M. Shapiro. *Report from the Luminosity Task Force.* ATL-GEN-PUB-2006-002, July 2006

[44] The TOTEM Collaboration and G Anelli et al. *The TOTEM Experiment at the CERN Large Hadron Collider.* JINST 3 S08007, 2008

[45] H. Stenzel. *Luminosity calibration from elastic scattering.* ATL-LUM-PUB-2007-001, March 2007

[46] S. Ask. *Simulation of the Luminosity Monitoring in ATLAS.* ATL-LUM-PUB-2006-001, March 2006

[47] V. Kostyukhin. *Secondary vertex based b-tagging.* ATL-PHYS-2003-033, September 2003

[48] V. Kostyukhin. *VkalVrt - a package for vertex reconstruction in ATLAS.* ATL-PHYS-2003-031, August 2003

[49] D.W. Scott. *Multivariate density estimation theory, partice and visualization.* New York, NY Wiley, 1992

[50] G. Blohm, G. Zech. *Introduction to Statistics and Data Analysis for Physicists.* Deutsches Elektronen-Synchroton ISBN 978-3-935702-41-6, Februar 2010

[51] G. Cowan. *Statistical Data Analysis.* Clarendon Press, Oxford, 1998

[52] V. Blobel. *An unfolding method for high energy physics experiments.* arXiv:hep-ex/0208022v1, 2002

[53] G. Zech. *private communication*, October 2010

[54] The ATLAS Collaboration. *Luminosity Determination Using the ATLAS Detector.* ATLAS-CONF-2010-060, 2010

[55] The ATLAS Collaboration. *Measurement of inclusive jet and dijet cross sections in proton-proton collisions at 7 TeV centre-of-mass energy with the ATLAS detector.* arXiv:hep-ex/1009.5908v2, 1 Oct 2010

[56] B. List. *Statistical error on Efficiency Determination from Weighted events.* July 2003

[57] M. Paterno. *Calculating Efficiencies and Their Uncertainties.* May 2003

[58] R. Brun, F. Rademakers. *Root - An Object Oriented Data Analysis Framework.* Proceedings AIHENP'96 Workshop, Lausanne, September 1996

Danksagung

An erster Stelle möchte ich mich bei meinem Doktorvater Prof. Dr. Buchholz bedanken, der mir diese Arbeit ermöglicht hat und die Gelegenheit geboten hat viele interessante Erfahrungen in der Forschung wie auch der Lehre zu machen. Des weiteren möchte ich ihm dafür danken, dass er mich gerade in schwierigen Zeiten immer unterstützt hat.

Mein Dank gilt ebenfalls Prof. Dr. Grupen, der sich bereit erklärt hat, das Koreferat dieser Arbeit zu übernehmen.

Zudem möchte ich Dr. Wolfgang Walkowiak danken, der immer bereit war physikalische Probleme zu diskutieren und stets die Zeit aufbrachte mit Rat und Tat zur Seite zur stehen. Besonders möchte ich ihm für das Korrekturlesen dieser Arbeit danken, das ihn bestimmt mehrere Tage und einige Stifte gekostet hat.

Prof. Dr. Zech möchte ich für seine Bereitschaft danken, mir immer wieder Fragen zur statistische Datenauswertung zu beantworten und diese zu diskutieren.

Weiterhin möchte ich mich bei der ATLAS B-Physikgruppe bedanken. Stellvertretend hierfür seien Dr. Vato Kartvelishvili und Dr. Maria Smizanska genannt, die mir auch immer wieder bei Fragen zur Pythia Event Generierung behilflich war.

Mein Dank gilt auch auch der ATLAS b-Tagging-Gruppe für viele hilfreiche Diskussionen und Treffen. Hier möchte ich mich vor allem bei Dr. Christian Weiser, Dr. Giacinto Piacquadio, Dr. Vadim Kostyukhin und Dr. Andreas Wildauer bedanken, für die ganzen Denkanstöße und angenehme Abende.

Der experimentellen Teilchenphysik Gruppe Siegen und besonders meinem Bürokollegen Valentin Sipica möchte ich danken für all die großen und kleinen Gefallen, die mir erwiesen wurden sowie für das angenehme Arbeitsumfeld.

Ein Dank gebührt auch der “Theorieabteilung” in Person von Dr. Nils Offen, Dr. Martin Jung und Sven Faller für all die Zeit während des Studiums, die endlosen Diskussionen über Physik und andere Themen, sowie das Einführen des Campus-Grillens. Mein Dank gilt auch Dr. Tobias Huber für das Korrekturlesen des Theorieteils.

Ein besonderer Dank gilt meinen Eltern, die mich während des Studiums und auch während meiner Doktorandenzeit immer unterstützt haben.